Processing spatial and temporal information in cells using protein-based pattern formation

Manon Wigbers

A dissertation
submitted to the Faculty of Physics
at the Ludwig–Maximilians–Universität München
for the degree of
DOCTOR RERUM NATURALIUM

München 2021

Processing spatial and temporal information in cells using protein-based pattern formation

Dissertation
an der Fakultät für Physik
der Ludwig–Maximilians–Universität München

vorgelegt von
Manon Celia Wigbers
aus Amsterdam

München, den 15. Januar 2021

To my sister Fleur

Erstgutachter: Prof. Erwin Frey
Zweitgutachter: Prof. Joachim Rädler
Tag der mündlichen Prüfung: 23. März 2021

Zusammenfassung

Für lebende Zellen ist die präzise Koordination mehrer zellulärer Funktionen wie Zellwachstum, DNA-Synthese, Zellteilung und Zellmigration essentiell. Beispielsweise müssen Zellen während der Zellteilung das Zellwachstum, die Verdopplung und Trennung der DNA und die Septumbildung eng koordinieren, um zwei lebensfähige Tochterzellen zu erzeugen. Um solch eine robuste Koordination mehrerer zellulärer Funktionen zu gewährleisten muss die Zelle fortwährend räumliche und zeitliche Informationen verarbeiten. Diese räumliche und zeitliche Information ist mittels Proteindichteprofilen innerhalb der Zelle kodiert. Für eine zuverlässige Koordination mehrerer Zellfunktionen ist daher die robuste räumliche und zeitliche Regulierung solcher Proteinkonzentrationsprofile entscheidend.

In dieser Doktorarbeit haben wir mithilfe von Reaktionsdiffusionsmodellen untersucht, wie solche Proteinmuster aus einer Kombination von Protein-Protein-Wechselwirkungen und Proteintransport entstehen. Insbesondere haben wir untersucht, wie ein Proteinmuster die Bildung und den stationären Zustand eines nachgeschalteten Proteinmusters beeinflussen kann. Solche Prozesse, bei denen ein Proteinmuster als Vorlage für das nächste Muster dient, entsprechen der räumlichen Verarbeitung von Informationen. Hier stellen wir verschiedene Mechanismen der räumlichen und zeitlichen Informationsverarbeitung mittels proteinbasierter Musterbildung vor und zeigen, wie eine hierarchische Kopplung solcher Berechnungen bei Seesterneizellen einen Mechanismus zur Anpassung an die Form der Eizelle zur Folge hat.

In Kapitel 1 stellen wir die Grundprinzipien für die proteinbasierte Musterbildung vor. Wir werden zunächst einige grundlegende Mechanismen des Proteintransportes und der Proteininteraktionen in Zellen diskutieren und erklären, wie eine Kombination von Transport und Proteininteraktionen zu Proteinmustern führt. Im Anschluss daran werden wir untersuchen, wie solche Proteinmuster durch geometrische, mechanische und biochemische Reize beeinflusst werden. Insbesondere diskutieren wir wie Zellgröße, Zellform sowie mechanische Spannungen und Spannungen des Zellkortex die Bildung von Proteinmustern steuern können. Danach werden wir das Ziel dieser Arbeit – zu verstehen, wie ein Proteinmuster als Vorlage für nachgeschaltete Proteinmuster dienen kann – motivieren. Abschließend werden die Grundprinzipien der linearen Stabilitätsanalyse und der Theorie des lokalen Gleichgewichts vorgestellt, anhand derer wir die Bildung von Proteinmustern untersuchen.

In Kapitel 2 wird erläutert, wie ein vorübergehender Signalimpuls das Polaritätsmuster einer Zelle beeinflussen kann. Die Polarität der Zelle ist entscheidend für verschiedene zelluläre Prozesse, einschließlich Zellmigration. In diesem Kapitel untersuchen wir ein Po-

laritätsmodell für das Bakterium *Myxococcus xanthus*. Die Polarität von *M. xanthus* wird durch die asymmetrische Verteilung des Polaritätsproteins MglA definiert und bestimmt die Bewegungsrichtung. Die Polarität kann sich bei einem vorübergehendem Signal des vorgeschalteten Frz-Signalsystems umkehren. Wir untersuchen systematisch, wie sich die Amplitude und Dauer des Signals auf die dynamische Verteilung des Polaritätsmarkers auswirkt. Wir identifizieren vier qualitativ unterschiedliche Schaltmechanismen und diskutieren ihre Eigenschaften anhand nichtlinearer und stochastischer Dynamik.

In Kapitel 3 stellen wir einen Mechanismus vor, mit dem ein Protein eine Schwellenwert in einem flachen Konzentrationsgradienten finden kann. Als Beispiel nutzen wir in unserer Diskussion die Dynamik des Guanin-Austauschfaktors (GEF) Ect2. Ect2 kann einen Schwellenwert in einem Konzentrationsgradienten des Zellzyklusregulators Cdk1 in Seesterneizellen bestimmen (siehe auch Kapitel 6). In diesem Kapitel stellen wir zunächst ein Modell für Ect2 vor, das auf verfügbaren biochemischen Informationen über Ect2 basiert und das Bistabilität von Ect2 ermöglicht. Wir zeigen dann, dass die Bistabilität der Ect2-Aktivität zur Bildung eines Frontmusters führen kann, bei dem die Grenzschicht an dem Cdk1-Schwellenwert ausgerichtet ist. Somit kann eine Ect2-Front einen Cdk1-Schwellenwert markieren, indem Cdk1-Konzentrationen unter dem Schwellenwert durch eine hohe Ect2-Aktivität gekennzeichnet sind, während Cdk1-Konzentrationen über dem Schwellenwert durch eine niedrige Ect2-Aktivität gekennzeichnet sind. Schließlich zeigen wir, dass der Zerfall des Cdk1-Gradienten zur Verschiebung der Ect2-Front führt. Die in diesem Kapitel vorgestellten Ergebnisse bilden die Grundlage für den in Kapitel 6 vorgestellten Mechanismus zur Anpassung an die Form einer Zelle.

In Kapitel 4 wird ein Mechanismus vorgestellt, durch den die Aktivität eines Proteins nach der Aktivierung eines Signals vorübergehend erhöht wird. Dies entspricht einer zeitlichen Ableitung. Als Beispiel nutzen wir hier die Dynamik des Rho-Enzyms. Rho bildet ein Aktivitätsband, das sich an der Grenzfläche der Ect2-Front befindet und sich in Seesterneizellen über die Membran ausbreitet (siehe auch Kapitel 6). In diesem Kapitel stellen wir zunächst ein Modell für Rho vor, das auf den verfügbaren biochemischen Informationen für Rho basiert. Wir analysieren die Parameterregime des Modells mithilfe einer Phasenporträtanalyse und zeigen, dass Rho eine oszillatorische Dynamik aufweist. Wir zeigen, dass die Rho-Dynamik an einer zeitliche Ableitung entspricht, wenn die Reaktionsraten anregbar sind und nahe am Schwingungsregime liegen.

In Kapitel 5 stellen wir einen Mechanismus vor, bei dem sich die Konzentration eines Proteins am Rand eines vorgeschalteten stufenförmigen Proteinmusters ansammelt. Dies entspricht an einer räumlichen Ableitung. Um diesen Mechanismus zur Erkennung von Kanten zu demonstrieren, verwenden wir ein konzeptionelles eindimensionales Modell eines Proteins, das von der Membran ins Cytosol und umgekehrt wechseln kann, und fragen, wie sich eine vorgeschalteten Vorlage, die die Kinetik der Proteinreaktion beeinflusst, auf die Proteinmusterbildung auswirkt. Mit Hilfe lokaler Gleichgewichtstheorie können wir die stationären Muster im Phasenraum der Reaktionskinetik grafisch konstruieren. Als nächstes zeigen wir, dass die Vorlage eine regionale Instabilität der Massenumverteilung

in der Nähe von Kanten in der Vorlage auslöst, was zur Akkumulation von Proteinmasse und schließlich zu einer stationären Konzentrationspitze an Kanten in der Vorlage führt. Darüber hinaus zeigen wir, dass einfache geometrische Kriterien für die Form der reaktiven Nullkline vorhersagen, wann dieser Kantenerkennungsmechanismus funktionsfähig ist.

Kapitel 6 baut auf der Arbeit in Kapitel 3 und 4 auf. In diesem Kapitel fragen wir, wie sich Proteinmuster an die Zellform anpassen können, sodass ihre räumliche und zeitliche Dynamik unempfindlich gegenüber Variationen der Zellform ist. Zunächst präsentieren wir experimentelle Ergebnisse, bei denen wir Seesterneizellen in unterschiedlich geformten Kammern eingeschlossen haben, und zeigen, dass sich die Ausbreitung eines Bandes von Rho-Aktivität an die Zellform anpasst. Anschließend präsentieren wir einen Mechanismus zur Anpassung an die Form der Eizelle, der trotz drastischer Formänderungen eine robuste räumliche und zeitliche Dynamik von Proteinen auf der Membran gewährleistet. Der Mechanismus basiert auf der hierarchischen Kopplung eines cytosolischen Cdk1-Gradienten, einer bistabilen Ect2-Front und eines anregbaren Rho-Impulses. Wir zeigen, wie Informationen über die Zellform, die in einem cytosolischen Gradienten enthalten sind, durch Ect2 (einem bistabilen Regulator von Rho) decodiert werden können. Diese bistabile Front steuert wiederum präzise eine mechanochemische Reaktion, indem sie lokal die anregbare Dynamik von Rho auslöst. Unsere Theorie macht Vorhersagen über die Breite des Rho-Aktivitätsbandes und seine Ausbreitungsgeschwindigkeit, die wir experimentell bestätigen.

In Kapitel 7 verwenden wir dasselbe konzeptionelle eindimensionale Modell wie in Kapitel 5 und fragen, wie sich der cytosolische Fluss auf die räumliche und zeitliche Dynamik von Proteinmustern auf der Membran auswirkt. Wir kombinieren eine lineare Stabilitätsanalyse mit numerischen Simulationen, um zu zeigen, dass sich membrangebundene Proteinmuster gegen die Strömungsrichtung ausbreiten. Der Mechanismus, der der Musterausbreitung zugrunde liegt, beruht auf einem höheren Proteinzufluss auf der stromaufwärtigen Seite des Musters im Vergleich zur stromabwärtigen Seite. Darüber hinaus stellen wir fest, dass der cytosolische Fluss das Membranmuster qualitativ von einem spitzenförmigen Muster zu einem plateauförmigen Muster ändern kann. Schließlich zeigen unsere Untersuchungen, dass ein ungleichmäßiges Strömungsprofil die Musterbildung induzieren kann, indem eine regionale laterale Instabilität ausgelöst wird.

Abschließend diskutieren wir in Kapitel 8 die Auswirkungen der in dieser Arbeit vorgestellten Ergebnisse und machen einige Vorschläge für zukünftige Forschungen.

Summary

Living cells rely on the precise coordination of several cellular functions, such as cell growth, DNA synthesis, cell division and cell migration. For example during cell division, cells need to closely coordinate cell growth, the duplication and segregation of the DNA and septum formation to obtain two viable daughter cells. To obtain such a robust coordination of multiple cellular functions, the cell needs to constantly process spatial and temporal information. This spatiotemporal information is encoded in the concentration profiles of proteins inside the cell. Thus, to ensure a reliable coordination of multiple cellular functions, it is crucial that the concentration profiles of proteins are robustly regulated in space and time.

In this thesis, we study how such protein patterns arise from a combination of protein-protein interactions and protein transport, using reaction–diffusion models. In particular, we study how one protein pattern can affect the formation and steady state of a downstream protein pattern. Such processes, where one protein pattern serves as a template for the next pattern, are reminiscent of spatial computational operations. Here, we demonstrate several mechanisms for spatial and temporal computations based on protein-based pattern formation and show how a hierarchical coupling of such computations lead to a shape-adaptation mechanism is starfish oocytes.

In Chapter 1, we introduce the basic principles for protein based pattern formation. We will first discuss several basic mechanisms for protein transport and protein interactions that take place in cells and explain how a combination of transport and protein interactions leads to protein patterns. Next, we will review how such protein patterns are affected by geometric, mechanical and biochemical guiding cues. In particular, we discuss examples how cell size, cell shape, and mechanical stresses and tension of the cell cortex can guide protein pattern formation. We will then motivate the aim of this thesis, which is to understand how one protein pattern can serve as a template for downstream protein patterns. Finally, we will present the basic principles of linear stability analysis and local equilibria theory, which we use to study protein pattern formation.

Chapter 2 discusses how a transient signal can affect the polarity pattern of a cell. Cell polarity is crucial for several cellular processes including cell motility. In this chapter, we study a polarity model for the bacterium *Myxococcus xanthus*. The polarity of *M. xanthus* is marked by the asymmetric distribution of the polarity protein MglA, and determines the direction of motion. The polarity can reverse upon a transient signal from the upstream Frz signaling system. We systematically study how the amplitude and duration of the signal

affects the dynamic distribution of the polarity marker. We identify four qualitatively distinct switching mechanisms and discuss their characteristics based on the nonlinear and stochastic dynamics.

Chapter 3 presents a mechanism by which a protein can measure a threshold concentration in a shallow concentration gradient. As an example, our discussion is based on the dynamics of the guanine exchange factor (GEF) Ect2. Ect2 can measure a threshold value in a concentration gradient of the cell cycle regulator Cdk1 in starfish oocytes (see also Chapter 6). In this Chapter, we first introduce a model for Ect2 which is based on the available biochemical information of Ect2 and allows for Ect2 bistability. We then show that bistability of the Ect2 activity can lead to the formation of a front pattern, where the front interface is positioned at the Cdk1 threshold value. Thus, Ect2 can mark a Cdk1 threshold value, such that Cdk1 concentrations lower than the threshold are marked by high Ect2 activity and Cdk1 concentrations higher than the threshold are marked by low Ect2 activity. Finally, we show that the decay of the Cdk1 gradient leads to propagation of the Ect2 front. The results presented in this Chapter form the basis of the shape-adaptation mechanism presented in Chapter 6.

Chapter 4 presents a mechanism by which the activity of a protein is transiently increased after a signal is turned on. This is reminiscent of a temporal derivative. As an example, our discussion is based on the dynamics of the enzyme Rho. Rho forms a band of Rho activity that localizes at the interface of the Ect2 front, which propagates over the membrane in starfish oocytes (see also Chapter 6). In this Chapter, we first introduce a model for Rho which is based on the available biochemical information for Rho. We analyze the parameter regimes of the model using a phase portrait analysis and show that the Rho exhibits oscillatory dynamics. We show that the Rho dynamics is reminiscent of a temporal derivative when the reaction rates are excitable and close to the oscillatory regime.

In Chapter 5, we present a mechanism by which the concentration of a protein accumulates at the edge of an upstream steplike protein pattern. This is reminiscent of a spatial derivative. To demonstrate this edge-sensing mechanism, we use a conceptual one-dimensional model of a protein that cycles between the cytosol and membrane and ask how the protein pattern formation responds to an upstream template that affects the protein reaction kinetics. Using local equilibrium theory, we are able to graphically construct the stationary patterns in the phase space of the reaction kinetics. We next show that the template triggers a regional mass-redistribution instability near the template edge, leading to the accumulation of protein mass, which eventually results in a stationary peak at the template edge. Furthermore, we show that simple geometric criteria on the reactive nullcline's shape predict when this edge-sensing mechanism is operational.

Chapter 6 builds upon the work presented in Chapter 3 and 4. In this Chapter, we ask how protein patterns can adapt to cell shape, such that their spatiotemporal dynamics is insensitive to cell shape variations. First, we present experimental results where we confined starfish oocytes in differently shaped compartments, and show that the propagation of a Rho activity band adapts to the cell shape. We then present a shape-adaptation mechanism

that ensures robust spatiotemporal dynamics of proteins on the membrane despite drastic shape changes. The mechanism is based on the hierarchical coupling of a cytosolic Cdk1 gradient, a bistable Ect2 front and the excitable Rho pulse. We show how cell-shape information contained in a cytosolic gradient can be decoded by a bistable regulator of Rho, Ect2. In turn, this bistable front precisely controls a mechanochemical response by locally triggering excitable dynamics of Rho. Our theory makes predictions on the width of the Rho activity band and its propagation speed, which we experimentally confirm.

In Chapter 7, we use the same conceptual one-dimensional model as in Chapter 5 and ask how cytosolic flow affects the spatiotemporal dynamics of protein patterns on the membrane. We combine a linear stability analysis with numerical simulations to show that membrane-bound protein patterns propagate against the direction of the flow. The mechanism underlying the pattern propagation relies on a higher protein influx on the upstream side of the pattern compared to the downstream side. Furthermore, we find that cytosolic flow can change the membrane pattern qualitatively from a peak-shaped pattern to a mesa-shaped pattern. Finally, our study shows that a non-uniform flow profile can induce pattern formation by triggering a regional lateral instability.

Finally, in Chapter 8, we discuss the implications of the results presented in this thesis and make several suggestions for future research.

Contents

1 Introduction

"You can't connect the dots looking forward;
you can only connect them looking backwards.
So you have to trust that the dots will somehow
connect in your future."
– Steve Jobs

This Chapter is based on our manuscript "Control of protein pattern formation via geometric, mechanical and biochemical guiding cues", which is in preparation for publication. This work has been performed together with Tom Burkart, Laeschkir Würthner and Erwin Frey.

Living cells rely on the precise coordination of several cellular functions, such as cell growth, DNA synthesis, cell division and cell migration. For example during cell division, cells need to closely coordinate cell growth, the duplication and segregation of the DNA and septum formation to obtain two viable daughter cells. During cell migration, external signals from the cell's surroundings are transmitted by signaling proteins to polarity proteins to regulate the cells direction of motion. Thus, to obtain robust coordination of multiple cellular functions in space and time, the cell needs to process spatial and temporal information.

This spatiotemporal information is encoded in the concentration profiles of proteins that regulate these cellular functions, whereby each type of protein performs one specific task. Key examples are motor proteins that can generate small forces, and membrane receptor proteins that can transmit information from external signals. Remarkably, an individual protein is only a couple of nanometers in size, but collectively, multiple proteins can orchestrate processes on a much larger scale. In other words, to ensure such large scale coordination of cellular processes, it is crucial that protein concentration profiles are robustly regulated in space and time.

How do proteins find the right place at the right time inside a cell? The combination of protein transport and protein reactions can give rise to the self-organization of proteins inside cells. Such spontaneous *protein patterns* can be stationary or dynamic depending on the underlying transport and reaction properties of the proteins. In addition, the cellular substrates that the proteins are embedded in can affect protein transport and reactions due to variations in the viscosity or biochemical properties. Interestingly, the cell is not a static object itself but rather an active material that can dynamically adapt its size, shape and material properties, depending on its environment and the state of the cell cycle [1–5].

On the one hand, such properties are orchestrated by protein patterns, but on the other hand protein patterns also need to adapt to such dynamically varying cellular properties to ensure reliable functions.

Increasing number of theoretical and experimental studies [6–16] find that protein concentration profiles respond and adapt to cell shape, size and cell mechanics. In this chapter, we will review how protein patterns respond to such geometric and mechanical guiding cues. First, we give an overview of the types of transport and reactions proteins exhibit inside cells. Next, we will discuss how the transport and reaction can be affected by cell shape, size and cell mechanics.

In addition to cell geometry and cell mechanics, also previously established protein patterns affect the formation of downstream protein patterns, providing biochemical guidance of protein pattern formation [17–24]. However, the mechanisms that underlie such biochemical guidance remain poorly understood. In this thesis, we will discuss several biochemical guiding mechanism that process the spatial and temporal information contained in protein patterns. Finally in Sec. 1.4, we provide an outlook on the future research directions in this field.

1.1 Protein pattern formation

Protein transport

The transport of proteins within a cell is crucial to regulated spatial variations in protein concentration. In the following, we will discuss several mechanisms that underlie protein transport within cells.

Diffusion – Perhaps the most basic means of protein transport is diffusion. Diffusion arises from the Brownian motion of proteins and leads to the flattening of concentration gradients. In other words, diffusion leads to a net transport from regions with high concentration to regions with low concentration. The diffusion constant is given by the Stokes-Einstein relation $D = k_B T/(6\pi\eta r)$, where η is the viscosity of the surrounding substrate and r the size of the diffusing particle. Hence, the diffusion properties of a protein can vary between proteins and in different parts of the cell.

Flow – Apart from diffusion, also flow can lead to protein transport due to the friction between the proteins and the moving substrate. Flows generically arise from stress gradients, such that the substrate moves into the direction of higher contractile or lower extensile stresses. In cells, stress gradients can be generated by external forces that act on the cell, or by internal forces that are generated via contractions of the cytoskeleton. A prominent example for how flows are generated by internal forces in the cell is the cortical contractions in the *C. elegans* zygote [8, 13, 25]. Here, local depletion of the myosin concentration at

the cell cortex leads to a gradient of contractile stresses such that the cell cortex flows from the anterior to the posterior pole [26, 27].

Such cortical flows can also lead to flows in the cytoplasm or membrane due to the hydrodynamic coupling between the membrane, cortex and the cytoplasm [13]. In addition, cortical contractions can induce shape changes, leading to flows in the cytoplasm. Such cytoplasmic flows have been observed to be induced by surface contraction waves during maturation of starfish oocytes [28].

Proteins can be transported with the flow due to frictional coupling of the protein to the viscous medium. However, it is important to note that the transport of proteins is affected by diffusion and flow simultaneously. The relative impact of diffusion and flow on the transport of a protein can be quantified by the Péclet number $\mathrm{Pe} = \xi \cdot v/D$, where v is the velocity of a protein in the direction of the flow, D the diffusion constant and ξ a characteristic length scale. Large values of the Péclet number correspond to protein transport that is dominated by flow rather than diffusion. Thus, small proteins with large diffusion constant will have a small Péclet number, and are therefore less affected by flow, than large proteins with a small diffusion constant. Similarly, a protein that diffuses in the cytoplasm is less affected by flows than when it is bound to the more viscous membrane.

Active transport – So far we have discussed that diffusion and flow arise from concentration and stress gradients, respectively. Apart from these processes, proteins can also be transported via processes that consume energy in the form of ATP or GTP on the molecular scale. An example of such *active transport* is the treadmilling behavior of the tubulin-like filament FtsZ that constitutes the contractile ring during cell division in bacteria. FtsZ monomers can only bind to the plus end of FtsZ filaments and detach from the minus end, while the monomer turnover depends on the GTPase activity of FtsZ [29–31]. Thus, via the consumption of GTP, FtsZ filaments exhibit directed motion along the cell membrane.

In addition, proteins can be carried along cytoskeletal structures by molecular motors, such as kinesin [32]. Molecular motors also consume energy via ATP or GTP cycles, which leads to a stepping motion of the motor along microtubules or movement on actin fibres [32]. This leads to a directed transport of the cargo protein either towards the plus or minus end of the filaments, depending on the type of motor. Experiments *in vivo* and *in vitro* have highlighted the importance of this process for polarization of cells [33–39]. For example, during cell growth in fission yeast microtubules are aligned along the long axis of the cell and direct the active transport of the tip factors Tea1 and Tea4 towards the cell poles [34, 40–42]. These tip factors serve as a spatial cue for cell growth leading to the elongation of the cell along its long axis. Thus, the arrangement of microtubules directs the transport of proteins within the cell.

Protein reactions

The biochemical properties of proteins characterize the ability of proteins to associate with other proteins or cellular media. In the following, we discuss how such protein reaction kinetics can lead to the formation of protein patterns due to changes either in protein transport or in protein activity.

Attachment/detachment kinetics – One of the most basic protein reactions is the attachment of a protein to substrates in the cell, such as membranes. Since the material properties vary between different cellular substrates, the attachment and detachment kinetics can regulate the effective transport of a protein in the cell. It has been suggested that such a regulation of transport via attachment and detachment kinetics is playing a key role during directed motion in migrating cells [13]. During cell migration, a rearward flow of the cell cortex can lead to translocation of proteins from the front to the back of the cell. At the same time, flows in the cytoplasm are directed towards the cell frontier. Thus, proteins that are predominantly bound to the cell cortex accumulate at the cell rear, while proteins that predominantly diffuse freely in the cytosol would accumulate at the cell frontier [13, 43].

Aggregation – In addition to attachment kinetics to different substrates in the cell, proteins can also bind to other proteins and thereby form protein aggregations. The size of such aggregations range from nanometer scale protein dimers to micrometer scale oligomers and protein droplets [44–46]. Since the diffusion constant of a protein depends on its size, the formation of a protein aggregate changes the protein transport properties. Such an effect on protein transport has been suggested to play a role in the transport of PAR-3 proteins in the *C. elegans* embryo. Here, diffusive transport may dominate for PAR-3 monomers ($\mathrm{Pe} < 1$), while the transport of PAR-3 becomes dominated by flow ($\mathrm{Pe} > 1$) due to cell cycle dependent aggregation of PAR-3 [26, 47]. Thus, the protein clustering kinetics can affect the distribution of proteins in the cell.

Conformational state changes – So far we have discussed how protein reactions can affect the transport properties of the protein, which can lead to a non-uniform distribution of the protein concentration. We will now discuss protein reactions that do not alter the protein transport properties but rather its activity on downstream processes. Such reaction kinetics can lead to spatial patterns in protein activity rather than in the protein concentration. Key examples include molecular switches that can cycle between an active and inactive state due to phosphorylation and dephosphorylation, or nucleotide binding and hydrolysis.

Such reaction cycles can lead to spatial patterns in the proteins activity when the state changes only at a specific region in the cell, such as the cell membrane or the nucleoid in bacterial cells. To illustrate this, consider a protein that cycles between an active and an inactive state such that only the active state can bind the cell membrane. At the membrane the protein can undergo a conformational state change from the active to the inactive state, thereby detaching from the membrane. In the cytoplasm the inactive protein

diffuses freely until it gets activated and is able to bind to the membrane again. Since the protein only changes to an inactive state at the membrane, the membrane acts as a source into the cytoplasm for inactive proteins and as a sink for active proteins, leading to activity gradients in the cytoplasm. Thus, this source-degradation process of inactive proteins leads to spatial patterns of the protein activity, while the total concentration stays uniform [6, 21, 48, 49].

Nonlinear reaction kinetics and pattern forming instabilities – Some proteins have been suggested to amplify the attachment, clustering or activation kinetics, giving rise to nonlinear reaction kinetics. The combination of nonlinear reaction kinetics and protein transport can lead to the coexistence of multiple stable chemical equilibria, dynamic chemical equilibria and several pattern-forming instabilities. A pattern forming instability arises when a spatially uniform steady state is unstable against spatially inhomogeneous perturbations. An example of such a pattern forming instability is a mass-redistribution instability, which amplifies spatial variations in protein number, leading to a protein concentration pattern [49]. The dynamics and length scale of these patterns on short time scales is determined by the growth rate and wave length of the unstable modes. The wavelength of the fastest growing unstable mode determines the characteristic length scale of the initially growing pattern. The growth rate of the unstable modes depends on the specific reaction kinetics and transport properties of the dynamics. While the initial pattern is dominated by the dynamics of the unstable modes, the dynamics on longer timescales may be dominated by other processes such as coarsening [50] and non-linear reactions of the unstable modes far away from the linear regime.

In addition, several of such chemical equilibria can coexist for the same total protein concentration. This means that at different regions in the cell, the system can be at different chemical equilibria, giving rise to front-like protein activity patterns. Such front-like patterns can propagate, when one chemical equilibrium is more dominant than the other [51]. Moreover, unstable chemical equilibria can give rise to spatially homogeneous oscillations and traveling spiral waves [49, 52–55]. In general, nonlinear reaction kinetics and pattern forming instabilities play a central role for many of the pattern formation processes that we discuss in the following.

1.2 Guided pattern formation

1.2.1 Geometric guiding cues

On the most macroscopic scale, a cell is characterized by its size and shape, which confine protein transport and protein reaction kinetics. Both cell size and cell shape can affect protein pattern formation. For example, cell size provides a natural upper limit to the length scale of a pattern. In addition, for a constant protein concentration in the cell, an increasing cell size needs to be accompanied by a higher protein number, which has recently

been shown to be an important control parameter for the formation of protein patterns [49, 56]. Moreover, when the protein species cycle between the cytosol and the membrane, the cell shape can affect protein patterns due to local variations in the membrane curvature [57] and in the ratio between cytosolic volume to membrane surface [6].

In the following, we will first discuss how the cell size affects protein pattern formation. Next, we discuss how the shape of the cell affects the distribution of proteins on the membrane, either due to a curvature-dependent protein binding affinity or due to a curvature-dependent probability to encounter the membrane.

Size-dependent protein patterns

So far we have discussed that the biochemical reactions determine the chemical equilibria of the system and that nonlinear protein reactions in combination with protein transport can lead to pattern forming instabilities. Interestingly, several experimental studies show that, apart from reaction and transport properties of the cell, also the cell size affects protein patterns. Key examples include the transition of pole-to-pole oscillatory patterns to stripe patterns of MinD in filamentous *E. coli* cells [58] and the observation that the PAR proteins in *C. elegans* fail to polarize in small cells [16]. Here, we will review how the size of the cell affects both the chemical equilibria and the wave length of the initially growing unstable modes, and the final pattern that arise from a pattern forming instability.

To understand how the cell size affects chemical equilibria, consider a protein that cycles between a membrane-bound and cytosolic state. The chemical equilibrium is reached when the reactive fluxes between the two different states are balanced. The flux of the cytosolic component onto the membrane depends on the cytosolic diffusive flux towards the membrane as well as the reactive flux at the membrane. The reactive flux, in turn, depends on the total number of proteins in the cytosol. As the cell increases in size, while keeping the concentration constant, the total number of proteins in the cell increase. This implies a change of the balance between reactive membrane and cytosol fluxes, leading to a change of the chemical equilibrium. Such a change of the chemical equilibrium could either lead to a quantitative change in the membrane and cytosolic concentration, but can also qualitatively change the number of equilibria and their stability [49, 52].

In addition, cell size can also affect pattern forming instabilities. As explained above, a pattern forming instability arises when a spatially uniform steady state is unstable against spatially inhomogeneous perturbations. The characteristic length scale of the pattern that arises from such an unstable steady state is limited by the cell size: only unstable modes with a wavelength equal to the cell size or a fraction of the cell size can grow [59]. Thus, while a reaction network can lead to a pattern forming instability in large cells, it may only result in a stable and spatially uniform steady state in small cells. Indeed, this has been observed for the polarity pattern of PAR proteins in *C. elegans* [16].

Shape-dependent protein patterns

Over the last decades, an increasing number over experimental studies demonstrate the effect of cell shape on the distributions of proteins [15, 26, 27, 53, 58, 60]. These studies show that for a broad range of cells, ranging from bacteria to migrating fibroblasts to large zygotes, the cell shape and local membrane curvature serve as important guiding cues for the accumulation of proteins on the membrane. For example, during persistent motion, the curvature-sensitive protein BAIAP2 accumulates at curved membrane patches at the cell front, inducing the formation of lamellipodia [61]. Furthermore, in the rod-shaped bacterium *B. subtilis*, a curvature-sensitive protein DivIVA accumulates at the cell poles, where it recruits MinD to guide correct placement of the septum [62].

The mechanisms that underlie such curvature sensing rely on the interaction of proteins with the membrane. Note that the attachment of proteins to the membrane depends on (i) the probability of a protein to encounter the membrane (*hitting probability*) and (ii) the affinity of binding to the membrane. Both the hitting probability as well as the binding affinity can be affected by the shape of the membrane. In the following, we will review the mechanisms underlying a curvature-sensitive binding affinity and hitting probability.

Binding affinity – A prominent example of proteins that can sense the membrane curvature, are proteins that contain a curved Bin/Amphiphysin/Rvs (BAR) domains [60, 63, 64] Proteins that contain BAR-domains have a higher binding affinity to parts of the membrane that have a similar curvature as the domain, compared to their binding affinity to flat or oppositely curved membrane regions. The length of BAR-domains is approximately 20 nm, which limits their sensitivity to weakly curved surfaces.

Alternatively, membrane curvature can be sensed by proteins whose oligomerization is promoted by membrane curvature. A curved oligomer can more easily be formed on a membrane region with similar curvature compared to a flat membrane. This increased affinity of oligomers to curved membranes leads to enhanced protein accumulation. An example of such *collective curvature sensing* is provided by dynamin, which forms helical collars around the thin neck during bud formation in yeast due to curvature-induced oligomerization [57, 65, 66].

Finally, some proteins recognize membrane curvature via defects in membrane structure. This mechanism is well exemplified by proteins with ALPS motif. ALPS motifs do not have a defined structure in solution, but absorb into lipid bilayers by folding into an α-helix. It has been shown that ALPS motifs bind preferably to regions with low lipid packing density [57]. Such low-density packing can arise from membrane curvature, where the outer part of the lipid bilayer is stretched compared to a flat membrane. In experiments, ALPS motifs were found to bind strongly to sufficiently curved liposomes ($R < 50$ nm), and to weakly curved liposomes with a high concentration of conic-shaped lipids. This suggests that the attachment of proteins containing ALPS motifs can be promoted in regions of

negative membrane curvature in cells. Thus, curvature-dependent binding affinity can lead to predominant accumulation of proteins at curved membrane regions.

It has been reported that proteins that sense curvature can also deform the membrane. For example, the helical structure of dynamin oligomers induces membrane curvature during scission of the yeast bud [66–69]. Furthermore, proteins with BAR-domains play a curvature-sensing role at low concentrations, but stabilize membrane curvature at high protein concentrations [63, 64, 70]. Such a dual role can lead to a positive feedback loop, where a slightly curved membrane leads to the accumulation of curvature-sensitive proteins. These proteins, in turn, deform the membrane, leading to a further increase in the binding affinity. This has been proposed as a mechanochemical mechanism for protein recruitment [14].

Hitting probability – Recently, it has been shown that the distribution of proteins on the membrane can depend on the cell geometry even when the binding affinity of proteins does not depend on membrane curvature [6, 7, 53]. Theoretical studies have shown that the probability of proteins to encounter the membrane can become curvature-dependent for proteins whose rebinding to the membrane after detachment is delayed [6, 7]. Such a delay can arise for proteins that need to undergo a conformational state change between detachment and rebinding. This is a generic feature of NTPase cycles or phosphorylation cycles. The key insight to understand this curvature sensitivity is that the hitting probability depends on the distribution of proteins in the cytosol, which becomes inhomogeneous due to a delayed rebinding of proteins to the membrane. In the following, we will first discuss how a delayed rebinding of proteins to the membrane leads to an inhomogeneous distribution of proteins in the cytoplasm. Next, we will discuss how the hitting probability depends on the distribution of proteins in the cytoplasm.

To understand how a delayed rebinding leads to an inhomogeneous distribution of proteins in the cytosol, consider proteins that cycle between an active (NTP-bound) state and an inactive (NDP-bound) state, which can both bind to the membrane or diffuse in the cytosol. Furthermore, active membrane-bound proteins deactivate upon membrane detachment, and get reactivated with a rate λ in the cytosol [6]. This delayed activation leads to an exponentially decaying concentration of inactive proteins in the cytosol with a characteristic reactivation length scale $l = \sqrt{D_c/\lambda}$, where D_c is the diffusion constant in the cytosol. Thus, for a reactivation length scale l larger than the radius of membrane curvature R, but smaller than the system size L, the concentration of inactive proteins in the cytosol is increased close to membrane regions with stronger negative curvature (e.g. at cell poles). The strength of this effect depends on the reactivation length l and vanishes for a reactivation length smaller than the radius of membrane curvature ($l \ll R$) and larger than the system size ($l \gg L$). Such a locally increased concentration of inactive proteins in the cytosol at cell poles leads to an increased binding of inactive proteins to the negatively curved membrane.

In contrast, the concentration of active proteins exhibits a complementary concentration gradient perpendicular to the membrane, with its minimum at the membrane and its

maximum further away from the membrane, in the center of the cell [6]. Interestingly, this gradient of active proteins leads to an asymmetry of membrane attachment between curved and flat membrane regions that depends on the reactivation length [7]. For a large reactivation length ($l \sim L$), an active protein is more likely to hit the membrane in the middle of the cell due to the increased cytosolic concentration in the cell center. However, for a small reactivation length, active proteins have a higher probability to hit the cell poles, due to the increased ratio between membrane surface to cytosolic volume.

This argument based on the hitting probability of proteins to the membrane explains where proteins are most likely to encounter the membrane. However, the final protein pattern that forms on the membrane depends on the details of the protein reaction kinetics on the membrane. If a protein only binds to and detaches from the membrane, the increased hitting probability directly leads to an increase in the protein concentration at the poles. This is further enhanced when the protein promotes its own binding autocatalytically [6]. However, when two proteins mutually inhibit each others binding, an increased hitting probability leads to the formation of an interface between two protein domains on the membrane [7].

In addition to the inhomogeneous hitting probability, also other geometric factors may play a role during the formation of the protein patterns. For example, theoretical work on the polarization of the *C. elegans* zygote has suggested that the pattern formation dynamics is initially dominated by the curvature-dependent hitting probability [7]. However, the mechanism that underlies the positioning of the aPAR-pPAR interface on longer time scales is not completely understood, and may be largely determined by the minimization of the interface length [7] and other biochemical cues [26].

1.2.2 Mechanical guiding cues

In addition to the cell size and shape, also the mechanical properties of the cell can affect the transport and reaction kinetics of proteins. In the following, we will first discuss examples where local contractions of the cell cortex lead to the generation of stress gradients in the cell, leading to protein transport. Next, we discuss how the binding kinetics of proteins to the actin cortex can depend on the tension on the actin fibers.

Flow generation

As discussed in Section 1.1, flows arise from stress gradients. Recent work has demonstrated the generation of such stress gradients in the cytoplasm of starfish oocytes [28]. In these oocytes, a cortical *surface contraction wave* travels across the membrane along the animal-vegetal axis. These contractions lead to stress gradients in the cytoplasm, which results in cytoplasmic flows along the animal-vegetal axis. Similar observations were made for

Drosophila embryos, were apical constrictions instead of surface contraction waves lead to cytoplasmic flows [71]

In addition, instead of deforming the cell shape, cortex contractions can also lead to flows of the cortex as a direct consequence of spatially inhomogeneous contractions [8] or anisotropic cortical tension [72]. For example, cortical flows in *C. elegans* zygotes prior to PAR polarization arise due to nonuniform actomyosin activity [8]. Reduced actomyosin contractility at the posterior pole leads to anterior-directed cortical flow. Through hydrodynamical coupling, the cortical flow induces flows in the cytosol, leading to a posterior-directed cytoplasmic flow [26]. As discussed earlier, such flows can play a key role in the pattern formation process or serve as a symmetry-breaking cue. Thus, shape deformations as well as cortex contractions can act as a mechanical guiding cue for pattern formation.

Tension-dependent reaction kinetics

Forces acting on the actin cortex can also affect the reaction kinetics of proteins that bind to actin fibers. In the following, we will discuss two mechanism that underlie such tension-dependent reaction kinetics.

A first example is given by smooth muscle myosin. It has been observed that muscles liberate more heat, depending on the load applied to the muscle [73]. This so called 'Fenn effect' implies that the biochemistry of a shortening muscle, which is driven by acto-myosin contractions, responds to its mechanical conditions. A molecular mechanism for this load-dependent kinetics has been suggested by Huxley and Simmons, who proposed that the force-generating cycle of myosin proceeds slowly under load, while more quickly without load [74]. Indeed, *in vitro* studies showed that the binding life time of a single smooth muscle myosin to an actin filament is prolonged under higher load and decreases under low or negative load [75]. The same mechanism has been suggested as an underlying mechanism for the cooperative binding of non-muscle myosin II [76].

Another protein with tension-dependent binding kinetics is the actin-depolymerization factor cofilin [77]. Cofilin has been observed to preferentially accumulate on relaxed actin fibers [78, 79]. Since cofilin depolymerizes and severs actin fibers [80], it can locally alter the mechanical properties of the cortex depending on the local tension. The underlying mechanism for this tension-dependent binding has been hypothesized to rely on the degree of twist in the actin fiber [78, 79]. While spontaneous fluctuations can twist relaxed actin fibers [81], such fluctuations are suppressed in fibers under tension [82], leading to a preferred binding to relaxed fibers. In addition, the binding of cofilin itself can also induce a twist in relaxed actin fibers [78, 79]. This positive feedback loop has been suggested to induce cooperative binding of cofilin, which can lead to accumulation of cofilin to relaxed actin fibers. Thus, tension-dependent reaction kinetics can lead to the formation of protein patterns.

1.3 Aim of this thesis

In this introduction, we have have discussed how size, shape and mechanics of cells affect the formation and steady states of protein patterns inside cells. In other words, we discussed how the spatial and temporal information about the cell's geometry and mechanics can be encoded in protein concentration profiles. A third guiding cue to regulate the formation of protein patterns can be formed by biochemical signals. Such signals can originate from the external environment of the cell or from internal processes to coordinate multiple cellular functions. Cells process the information from these external and internal signals via biochemical signaling pathways.

To study such signaling pathways, the cell is often perceived as a computational unit that takes the concentration of external molecules as an input. Via membrane receptors and biochemical interactions inside the cell, these inputs lead to an output, such as the up- or down-regulation of the target protein or a change in its conformational state. The specific biochemical interactions between the membrane receptors and the target protein determine the decision-making response of the cell. For example, several theoretical and experimental studies have identified biochemical circuits that are able to perform logic operations, generate pulses, or act as noise-reduction filters [83–87]. In these examples, both the input and the output are considered to be homogeneous throughout the cell or, in other words, 'well-mixed'.

In contrast to such 'well-mixed' computational operations, both the input signals as well as the output can be spatially-dependent, leading to locally varying responses in the cell. Thus, these spatially-dependent signals are processed via protein patterns, such that the concentration profile of one protein serves as a *biochemical guiding cue* for the formation of a downstream protein pattern. Such spatially-dependent signal processing, where spatial protein patterns serve as inputs for downstream protein patterns, has been observed during many biological processes, ranging from the placement of the division site [17, 18, 20, 21, 23] to macropinocytosis [22, 24] and cellular wound healing [19]. However, the biophysical mechanisms that underlie these spatial computations remain poorly understood [88].

The general aim of this thesis is to uncover biophysical mechanisms by which proteins can process spatial and temporal information inside cells via protein-based pattern formation.

We will use mass-conserving reaction–diffusion models to study how protein patterns arise from a combination of protein-protein interactions and protein transport. In particular, we will ask how one protein pattern can affect the formation and steady state of a downstream protein pattern. Such processes, where the concentration profile of one protein serves as a template for the next pattern, is reminiscent of computational operations in cells. We will demonstrate several mechanisms for both spatial as well as temporal computations. To characterize the mechanisms for these computations, we will use biophysical analyses, such as a phase portrait analysis, linear stability analysis, and local equilibrium theory.

First, we characterize four mechanisms, that can switch the polarity of a cell upon a transient signal, using numerical simulations and a phase portrait analysis. Next, we use local equilibria theory to show how a protein can measure a threshold in a shallow gradient. We then demonstrate mechanisms of computations that are reminiscent of a temporal derivative and a spatial derivate. The mechanism of the temporal derivative demonstrates how a sudden increase in the concentration of the input leads to a transient, peak-like increase of the output. The spatial derivative shows how a step-like input leads to the formation of a peak at the edge of the step-like concentration profile. Then, we show that a hierarchical coupling of such computations lead to a shape-adaptation mechanism in starfish oocytes. Finally, we perform a linear stability analysis to show how flows in the cytoplasm of a cell can affect the protein concentration profiles of membrane-bound proteins.

1.4 Biophysical analysis

To describe the formation of protein patterns, reaction–diffusion models have proven useful [53, 89–104]. We will next give a brief overview of the mathematical methods to study such reaction–diffusion models.

1.4.1 Linear stability analysis

To study whether protein patterns can spontaneously arise from a homogeneous (or well-mixed) system, one can perform a linear stability analysis. The goal of linear stability analysis is to find whether a steady state is stable or unstable against small perturbations. In particular, one studies the time evolution of a small perturbations of the system in the vicinity of the steady state. When the amplitude of this perturbation grows, the system is unstable; and vice versa, a decaying amplitude implies a stable steady state.

To illustrate the general procedure of linear stability analysis we consider we consider the dynamics of one protein species on a one-dimensional domain of length L, as in Ref. [56]. The proteins can cycle between a membrane-bound state (concentration $m(x,t)$) and a cytosolic state (concentration $c(x,t)$), with diffusion constants D_m and D_c respectively. The reaction–diffusion equations for the membrane density m and the cytosolic density c read

$$\partial_t m(x,t) = D_m \partial_x^2 m + f(m,c), \tag{1.1a}$$
$$\partial_t c(x,t) = D_c \partial_x^2 c - f(m,c), \tag{1.1b}$$

where the reaction term $f(m, c)$ describes the attachment–detachment dynamics of the proteins. We consider reflective boundary conditions at $x = 0, L$, such that $\partial_x c|_{0,L} = \partial_x m|_{0,L}$. The dynamics conserves total protein density

$$\bar{n} = \frac{1}{L}\int_0^L \mathrm{d}x\; n(x,t), \tag{1.2}$$

with the local total density $n(x,t) = m(x,t) + c(x,t)$.

Following the standard procedure for linear stability analysis, we first find the homogeneous steady state $\mathbf{u}^* = (m^*, c^*)$ by solving $f(m^*, c^*) = 0$ and $\bar{n} = m^* + c^*$.

Next, we consider the dynamics for small perturbations $\mathbf{u}(x,t) = \mathbf{u}^* + \delta\mathbf{u}(x,t)$ around the homogeneous steady state. Expanding $\delta\mathbf{u}(x,t)$ in exponentially growing (or decaying) Fourier modes $\delta\mathbf{u} = \widehat{\mathbf{u}}_q\, e^{\sigma t} e^{iqx}$ leads to the eigenvalue problem

$$\mathcal{J}\widehat{\mathbf{u}}_q = \sigma\widehat{\mathbf{u}}_q, \tag{1.3}$$

with the Jacobian

$$\mathcal{J} = \begin{pmatrix} -D_c q^2 - f_c & -f_m \\ f_c & -D_m q^2 + f_m \end{pmatrix},$$

where $f_c = \partial_c f|_{\mathbf{u}^*}$ and $f_m = \partial_m f|_{\mathbf{u}^*}$ encode the linearized reaction kinetics. Thus, for each Fourier mode with wave number q, the eigenvalues $\sigma_{1,2}$ of the Jacobian $\mathcal{J}$ represent the growth rate of a the mode. The mode $q = 0$ correspond to spatially homogeneous perturbations, whereas the modes $q > 0$ correspond to spatially inhomogeneous perturbations. The eigenvalue with the largest real part determines the stability of the mode and indicates the mode's growth rate. For $\mathrm{Re}\,\sigma(q) > 0$, the mode with wave number q is unstable, whereas a mode is stable for $\mathrm{Re}\,\sigma(q) < 0$.

A typical dispersion relation with a band of unstable modes is shown in the inset of Fig. 1.1d. The mode q_c with the highest growth rate determines the wave length $\lambda = 2\pi/q_c$ of growing pattern on short time scales (see Fig. 1.1d). On longer timescales, the linear approximation of the dynamics may no longer hold. In this nonlinear regime, the system can be analyze using finite element simulations or local equilibrium theory, which we will further discuss in the next section.

1.4.2 Local equilibria theory

This section is based on Sec. I.B. from the paper "Pattern localization to a domain edge', which has been published in Physical Review E (Ref. [105]). This work has been performed together with Fridtjof Brauns, Tobias Hermann and Erwin Frey.

Recent work has developed a theoretical framework to study mass-conserving reaction–diffusion models in the nonlinear regime [49, 56]. In the following we review the key

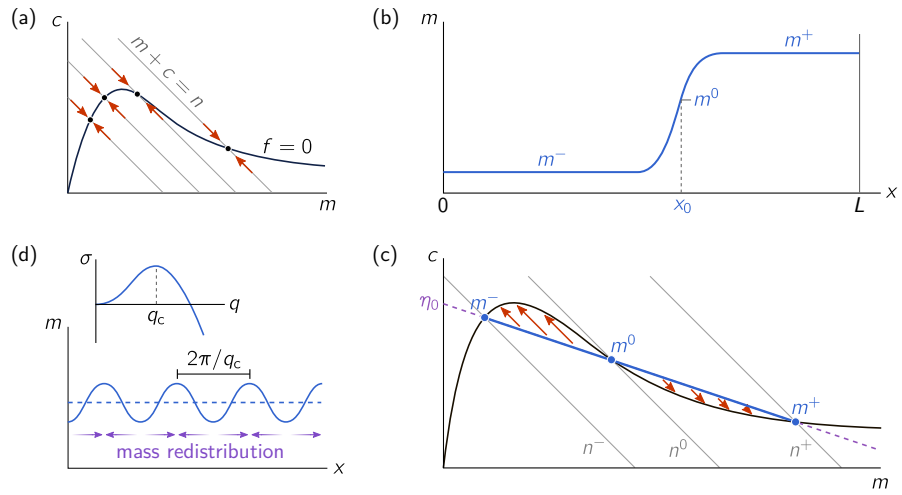

Figure 1.1 | Illustration of the phase-space geometric analysis for two-component McRD systems. (a) The reactive equilibria (black dots) are given by the intersections between the reactive subspaces $m + c = n$ (grey lines) and the reactive nullcline $f = 0$ (black line) in the (m, c)-phase space. Hence, the reactive nullcline encodes the qualitative structure of the reactive flow as illustrated by the red arrows. (b) Sketch of the membrane profile of a mesa pattern composed of a high- and low-density domains, m^+ and m^-, connected by a diffusive interface around the inflection point x_0. (c) Flux-balance construction of the mesa pattern in phase space (cf. (a)). The intersections of the flux-balance subspace (FBS) (purple dashed line) and the reactive nullcline yield the concentrations at the plateaus $m^\pm$ and the inflection point m^0. The balance of net reactive flows in the system (red arrows) determines the FBS-offset η_0. In the regime where the slope of the reactive nullcline is steeper than the slope of the FBS, an homogenous steady state is laterally unstable. (d) Linearization of the dynamics in the vicinity of the homogeneous steady state, yields a dispersion relation for growth rates of the eigenfunctions (Fourier modes indexed by wavenumber q). The fastest growing mode, q_c, dominates the length scale of the initial dynamics.

insights from this work and use these concepts and methods throughout the rest of the thesis.

To that end, we consider the dynamics of one protein species on a one-dimensional domain of length L, as in Ref. [56] and Sec. 1.4.1. The proteins can cycle between a membrane-bound state (concentration $m(x,t)$) and a cytosolic state (concentration $c(x,t)$), with diffusion constants D_m and D_c respectively. In cells, the diffusion constants of membrane-bound proteins and cytosolic proteins are typically widely different, such that $D_m \ll D_c$. The reaction–diffusion equations for the membrane density m and the cytosolic density c read

$$\partial_t m(x,t) = D_m \partial_x^2 m + f(m,c), \tag{1.4a}$$
$$\partial_t c(x,t) = D_c \partial_x^2 c - f(m,c), \tag{1.4b}$$

where the reaction term $f(m, c)$ describes the attachment–detachment dynamics of the proteins. Specific examples of such systems exhibiting self-organized pattern formation can be found in [91, 93, 94, 103]. At the boundaries, we impose no-flux conditions $D_c\partial_x c|_{0,L} = D_m\partial_x m|_{0,L} = 0$. The dynamics conserves total protein density

$$\bar{n} = \frac{1}{L}\int_0^L \mathrm{d}x\, n(x,t), \tag{1.5}$$

with the local total density $n(x,t) = m(x,t) + c(x,t)$.

To characterize the dynamics and steady states of McRD systems, we recently introduced a framework, termed *local equilibria theory* [49, 56]. This theory proposes to analyze spatially extended systems as a collection of small diffusively coupled compartments. The local reaction kinetics inside each of the compartments, then serves a proxy for the spatially extended dynamics, enabling a quantitative phase portrait analysis of the spatially extended system in the phase space of reaction kinetics [56]. In the following we briefly review the key results of local equilibria theory for the two-component McRD system and generalize this framework to analyze pattern formation in the presence of a spatial template. For a comprehensive analysis of the two-component McRD system on a homogeneous domain, we refer to Ref. [56].

The reaction kinetics of McRD systems conserves total protein mass, which implies that the reactive flow must point along the reactive phase spaces $n = c + m$, indicated by the gray lines in Fig. 1.1(a). The reactive flow vanishes along the *reactive nullcline* (NC), given by $f(m, c) = 0$. Intersections of the reactive nullcline with reactive phase spaces, given by the total density (mass) n, determine the reactive equilibria $(m^*(n), c^*(n))$ shown as black dots in Fig. 1.1(a). Hence, the shape of the nullcline encodes how the reactive equilibria move when total density n is changed, highlighting that the total density n is a *control parameter* for the reaction dynamics. Within each reactive phase space, the flow is directed towards a stable reactive equilibrium, as illustrated by the red arrows in Fig. 1.1(a).

In a spatially extended system, the total density $n(x,t) = m(x,t) + c(x,t)$ is generically inhomogeneous, and its dynamics is driven by diffusion, as can be seen by adding Eqs. (1.4a) and (1.4b)

$$\partial_t n(x,t) = D_c\partial_x^2\eta(x,t), \tag{1.6}$$

where we introduced the *mass-redistribution potential*, defined as [56]

$$\eta(x,t) := c(x,t) + \frac{D_m}{D_c}m(x,t). \tag{1.7}$$

To study the interplay of local reactions and diffusive mass-transport in spatially extended systems, local equilibria theory proposes to analyze such systems as a collection of diffusively coupled compartments. These notional compartments are chosen small enough that each of them can be regarded as well-mixed. Thus, local dynamics within each compartment can be characterized in the ODE phase space of reactions which is determined by

the density $n(x,t)$ within that compartment. In this characterization, the *local (reactive) equilibria* and their stability in each local phase space serve as proxies for the reactive dynamics in each compartment. This becomes clear when one imagines the compartments as isolated, for a given total density profile $n(x)$. Then each compartment will approach a stable local equilibrium, parametrized by the local density $n(x)$. In the spatially coupled system, the total density $n(x,t)$ is diffusively redistributed due to concentration gradients between the compartments (cf. Eq. (1.6)). Consequently, the local equilibria shift and their stability may change [56, 106]. This interplay between shifting local equilibria and mass transport is at the core of *local equilibria theory*.

In the remainder of this section, we recapitulate two key results from the phase-portrait analysis of two-component McRD systems [56]. We will later generalize this analysis to systems on a spatially heterogeneous domain.

Flux-balance construction. — From the dynamics of the total mass Eq. (1.6)–(1.7) it follows that, for any stationary pattern (denoted by $\widetilde{m}(x)$, $\widetilde{c}(x)$), $\widetilde{\eta}(x)$ must be constant in space on a domain with no-flux (or periodic) boundary conditions [56]:

$$\eta_0 = \widetilde{c}(x) + \frac{D_m}{D_c}\widetilde{m}(x) = \text{const.} \tag{1.8}$$

This relationship defines a linear subspace, termed *flux-balance subspace* (FBS), of the (m,c)-phase space of reaction kinetics (purple dashed line in Fig. 1.1(c)). Any stationary pattern must be embedded in a single FBS. This reflects that, in steady state, the diffusive fluxes in m and c are balanced against each other such that there is no net transport of mass.

We can use this condition, Eq. (1.8), to geometrically construct the steady state density profile in the (m,c)-phase space and from that estimate the real space density profile. The key insight is that we can approximate the concentrations at the plateaus, and the inflection point of the pattern by the local equilibria at the FBS-NC intersections (see Fig. 1.1(b)). We denote these intersection points by m^-, m^0 and m^+, where $m^\pm$ correspond to the concentrations at the plateaus and m^0 to the concentration at the inflection point of the pattern (Fig. 1.1(b,c)). Thus, the FBS-offset, η_0, fully determines these concentrations.

To determine the FBS-offset, η_0, one uses that in steady state the net reactive flow within the whole system must be balanced[1]:

$$\int_{m^-(\eta_0)}^{m^+(\eta_0)} \mathrm{d}m\, f\left(m, \eta_0 - \frac{D_m}{D_c}m\right) = 0, \tag{1.9}$$

where the plateau concentrations far away from the interface are approximated by the FBS-NC intersections $m^\pm(\eta_0)$. This *total turnover balance* condition implicitly determines the FBS-offset η_0. Note that on a large domain (much larger than the interface width,

[1]Note that before integration, Eq. (1.4a) is multiplied with $\partial_x \widetilde{m}(x)$ as a mathematical trick to substitute the integral over space by an integral over m.

where the approximation $m(0, L) \approx m_{\pm}$ holds), total turnover Eq. (1.9), and hence η_0, depends only on the function f and the ratio of the diffusion constants. This implies that η_0 is not dependent on the average mass $\bar{n}$ in this approximation.

We will show next that the average mass $\bar{n}$ determines the relative size of the low- and high-density regions and with that the position of the pattern's interface. This interface is marked by the position of the inflection point x_0 of the pattern profile. For a domain size much larger than the interface width, we can neglect the finite width of the interface region, such that the average mass can be approximated by

$$L\,\bar{n} \approx x_0\, n^-(\eta_0) + (L - x_0)\, n^+(\eta_0). \tag{1.10}$$

Conversely, x_0 can be determined for a given $\bar{n}$. Thus, this geometric construction, termed *flux-balance construction*, shows that significant features of the steady state profile are determined by the shape of the nullcline.

Mass-redistribution instability. — In addition to the construction of stationary patterns, it was shown in Ref. [56] that the nullcline shape determines the stability of a homogeneous steady state, and that the mechanism underlying lateral ("Turing") instability is a mass-redistribution cascade. Specifically, it was found that a homogenous steady state is laterally unstable when the *slope* of the nullcline $\chi(\bar{n}) := \partial_m c^*|_{\bar{n}}$ is steeper than the slope of the FBS (see Section II.D1 in Ref. [56] for a derivation),

$$\chi(\bar{n}) < -\frac{D_m}{D_c}, \tag{1.11}$$

which, using the mass-redistribution potential, Eq. (1.7), is equivalent to $\partial_n \eta^* < 0$. If this condition is fulfilled, high-density regions act as cytosolic sinks, leading to further accumulation of mass and hence a mass-redistribution cascade. This motivates the corresponding name *mass-redistribution instability*.

Starting from a homogeneous steady state with a small random perturbation, the initial dynamics is dominated by the fastest growing eigenfunction of the linearized dynamics. At the onset of this instability there is a dominant eigenfunction that determines the initial dynamics of the system. We can find this dominant eigenfunction by linearizing the system around its homogenous steady state (linear stability analysis). For a homogenous steady state, these eigenfunction are Fourier modes and their growth rates are given by the dispersion relation, shown as inset in Fig. 1.1(d). Due to mass-conservation, the real part of the growth rate goes to zero at $q = 0$, corresponding to a type II dispersion relation in the classification by Cross and Hohenberg [107]. The fastest growing mode, q_c, determines the length scale of the initially growing pattern as illustrated in Fig. 1.1(d)). Subsequently the pattern coarsens into a single peak [93, 94, 108, 109].

2 Polarity switching in response to a transient signal

"Non numeranda, sed ponderanda
sunt argumenta."
– Marcus Tullius Cicero

The mechanisms and design principles of regulatory systems establishing polarized protein patterns within cells are well studied. However, cells can also dynamically control their cell polarity. Here, we ask how an upstream signaling system can switch the orientation of a polarized pattern. We use a mathematical model of a core polarity system based on three proteins as the basis to study different mechanisms of signal-induced polarity switching. The analysis of this model reveals four general classes of switching mechanisms with qualitatively distinct behaviors: the transient oscillator switch, the reset switch, the prime-release switch, and the push switch. Each of these regulatory mechanisms effectively implements the function of a spatial toggle switch, however with different characteristics in their nonlinear and stochastic dynamics. We identify these characteristics and also discuss experimental signatures of each type of switching mechanism.

This Chapter is based on our paper "Four different switching mechanisms", which has been published in PloS Computational Biology [110]. This work has been performed together with Filipe Tostevin, Ulrich Gerland and Lotte Søgaard-Anderson.

2.1 Introduction

Cell polarity is manifested in molecular and morphological asymmetries of the cell. From bacterial to mammalian cells, cell polarity is essential in a multitude of functional contexts, including cell migration, asymmetric cell division and differentiation, cell-cell signaling, development and tissue homeostasis [111, 112]. One fundamental question related to cell polarity is how an initially symmetrical cell can establish a polarized state and subsequently maintain it [113]. However, cells are also known to dynamically change their polarity, e.g. reversing polarity in response to external or internal signals to control motility [114, 115]. This raises a second fundamental question: Which mechanisms permit reliable switching of cell polarity?

The first question, about establishing and maintaining cell polarity, is well studied, both on the conceptual level with theoretical approaches and on the experimental level by characterizing model systems. The polarization of an initially nonpolarized cell is a symmetry breaking phenomenon: In the case of essentially isotropic cells, e.g. budding yeast or epithelial cells [113], the continuous angular symmetry is broken by polarization, whereas discrete symmetry breaking occurs for rod-shaped bacterial cells [116]. Symmetry breaking can occur spontaneously [117], but is often controlled by upstream guiding cues [8]. While the detailed molecular mechanisms underlying cell polarization differ between organisms, they often incorporate conserved G-protein based signaling systems that use multiple feedback interactions to generate asymmetric distributions on the cell membrane via a Turing instability [118]. A class of simple networks that can achieve cell polarization was explored in a synthetic biology study [119], which first showed computationally that all such networks feature the three minimal motifs 'positive feedback', 'mutual inhibition', or 'inhibition with positive feedback', but that combinations of these motifs generally polarize more reliably. The study then corroborated the latter finding experimentally, recapitulating the basic principles underlying the establishment and maintenance of cell polarization in engineered systems. Taken together, these and other results address many aspects of the first question raised above. By comparison, significantly less is known about the second question on the dynamical control of cell polarity.

Dynamically changing cell polarity is widely observed and studied in eukaryotic model systems such as neutrophils [120], amoebae [115], and melanoma cells [121]. Depending on the system, its genetic makeup, and the environment, cells display a variety of dynamical patterns. For instance, melanoma cells either randomly polarize into frequently changing directions, or reverse cell polarity in an oscillatory fashion, or they persistently maintain cell polarity [121]. The dynamical control of cell polarity involves signaling. For instance, cell polarity changes can be coupled to internal signals, as in the case of yeast, where the dynamics of cell polarity is co-regulated by the cell cycle [122]. Often, cells get a directional cue from the environment governing the direction of their response [115]. However, cells can also respond to non-directional cues. For instance, a temporally decreasing chemoattractant signal triggers reversals of cell polarity in neutrophils, even in the absence of a

spatial concentration gradient [120]. Which mechanisms permit such reversals induced by a non-directional signal?

Rod-shaped bacteria display much of the eukaryotic phenomenology and serve as paradigmatic model systems. For instance, the Min system, used by *E*scherichia coli to localize the septum prior to cell division [123], constitutes a prime example of autonomous cell polarity oscillations. Its underlying molecular network, based on three Min proteins, was successfully reconstituted *i*n vitro [54]. On a conceptual level, the cell polarity oscillations of the Min system are analogous to those of the melanoma cells, also with respect to the basic regulatory scheme, whereby a bistable system can be turned into an oscillator via slow negative feedback [121, 124]. For signal-induced (rather than autonomous) polarity reversal, the Mgl system of *Myxococcus xanthus* constitutes a prime example. Here the cell polarity, marked by MglA, undergoes intermittent reversals, which are thought to be triggered by the upstream Frz signaling system [125]. The cell polarity reversals are accompanied by reversals in the direction of cell motion, enabling motility patterns that are crucial for predatory behavior and fruiting body formation [126].

Recently, Guzzo et al [127] identified the response regulator FrzX as a mediator of the Frz reversal signal to the Mgl system, and proposed a mechanism for how FrzX can interact with the three core polarity proteins to trigger polarity reversals. We take this study as a starting point to explore the question of signal-induced polarity switching on a more general level. Rather than focusing on one particular mechanism, we aim to identify the distinct classes of switching mechanisms and their underlying working principles. We find four distinct classes of mechanisms that can occur for different signaling regimes. We demonstrate that some are sensitive to the amplitude and duration of the input signal but relatively robust to intrinsic molecular noise, while others are less sensitive to signal variability but more susceptible to noise. These and other features allow us to identify experimental signatures that can be used to discriminate between the four classes of mechanisms *in vivo*.

2.2 Methods

We consider a cell polarity defined by an asymmetric distribution of a certain 'polarity marker' A. The polarity marker has the regulatory role to direct the spatial localization or activity of downstream processes. For instance, MglA in *M. xanthus* is a polarity marker that localizes at one of the cell poles and activates the motility machinery to determine the direction of cell motion [125]. Similarly, Cdc42 is a polarity marker in yeast and other eukaryotic cells [128]. A module consisting of the polarity marker and other regulatory proteins has the ability to establish and maintain a polarized distribution of A. This module, which we refer to as the 'core polarity system', receives input from a signaling pathway via a signaling protein X. We stipulate that the 'full polarity system' consisting of X and the core system can implement the function of signal-induced polarity switching (Fig. 2.1).

To explore mechanisms for signal-induced polarity switching, we consider a symmetric cell with a polarity marker that localizes only at its two cell poles '1' and '2' (Fig. 2.1A), while it rapidly diffuses in the cytoplasm. This simplest scenario is a good approximation for the *M. xanthus* polarity system [127] and suffices to reveal general principles of signal-induced polarity switching, as we will see below. The distribution of A is then characterized by quantifying its abundance at pole '1' and '2', as well as in the cytoplasm, and the time-dependent cell polarity can be defined as

$$\omega_A(t) = \frac{A_1(t) - A_2(t)}{A_1(t) + A_2(t)} , \tag{2.1}$$

where $A_1(t)$ and $A_2(t)$ are the time-dependent abundances of A at the poles. Hence, $\omega_A > 0$ corresponds to a higher abundance of A at pole 1 than at pole 2, and vice versa for $\omega_A < 0$, such that a reversal of cell polarity is marked by a change of sign in $\omega_A(t)$.

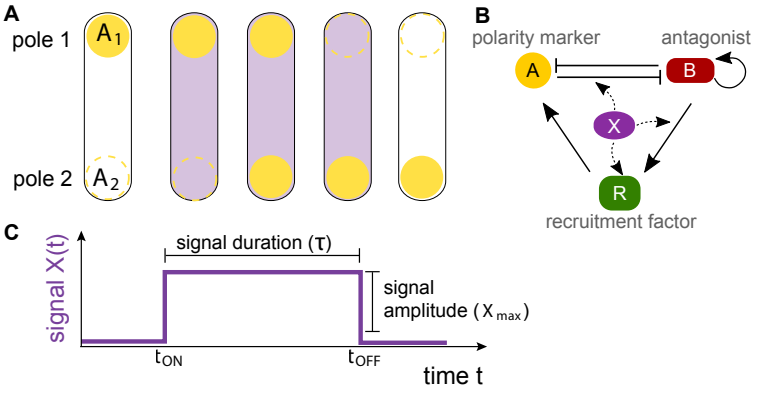

Figure 2.1 | Signal-induced polarity switching. **A** Schematic representation of a rod-shaped cell with polarity marker A shown in yellow. Proteins can either be bound to the poles or diffuse in the cytoplasm. The abundances of the polarity marker at the two poles are denoted by A_1 and A_2. The release of a signal protein X in the cytoplasm, shown in purple, can lead to a polarity reversal, such that the polarity marker switches from pole 1 to pole 2. **B** Schematic representation of the molecular interactions of the polarity model. The polarity marker A and its antagonist B inhibit each others binding to the pole. B can cooperatively recruit itself to the pole and promotes binding of the recruitment factor R, which in turn recruits A. Dashed lines indicate exemplary hypothetical interactions of the signal protein X with the polarity proteins. **C** The switching signal is implemented as a pulse in the total amount of X, parameterized by the signal duration τ and signal amplitude $X_{\max}$.

2.2.1 Model for a switchable polarity system

To obtain our working model, we generalize the recently proposed model of the *M. xanthus* polarity system [127]. This model involves the 'antagonist' B to the polarity marker A, as

well as a third protein species, the 'recruitment factor' R (representing MglB and RomR, respectively). The network of interactions between A, B, and R is shown in Fig. 2.1B. Besides the mutual inhibition between A and B, it involves self-recruitment of B, as well as indirect recruitment of A by B via R. The full dynamics of the interactions between A, B, and R at the poles is described by [127]

$$\begin{aligned}\frac{dA_i}{dt} &= k_{rA}(1-A_1-A_2)R_i - k_a A_i - k_{ba}A_i B_i^2 \\ \frac{dR_i}{dt} &= (1-R_1-R_2)(k_R + k_{bR}B_i) - k_r R_i \\ \frac{dB_i}{dt} &= (1-B_1-B_2)(k_B + k_{bB}B_i) - k_b \frac{k_M}{B_i+k_M} B_i \\ &\quad - k_{ab}A_i B_i^2 \ ,\end{aligned} \tag{2.2}$$

using the same convention for B and R as for A, i.e. B_i and R_i denote the abundances at the poles ($i = 1,2$). Eqs. 2.2 assume that the total abundances of A, B, and R in the cell are approximately constant, at least on the relevant timescale of polarity reversals. These total values are set to one by choosing appropriate units for the abundances. The dynamics in the cytoplasm is then obtained from the dynamics of the polar abundances, e.g. the cytoplasmic abundance of A is $1-A_1-A_2$. In total, the interactions between A, B, and R are specified by 10 rate constants and one saturation parameter. R binds to the cell poles with rate k_R where it locally recruits A with rate k_{rA}. B binds at the intrinsic rate k_B to the poles, where it recruits both itself, at rate k_{bB}, and R at rate k_{bR}. At the same time, A can displace B from the pole and vice versa with a rate k_{ab} and k_{ba}, respectively. All three proteins can also spontaneously unbind from the poles, with the corresponding rates k_a, k_r, and k_b, but the unbinding of B is slowed in presence of more B (with the saturation parameter k_M determining the characteristic abundance for this feedback effect).

The positive feedback from B onto its own localization together with the mutual inhibition of A and B allow this model to spontaneously generate a stable asymmetry in the protein abundances at the two poles. Polarity schemes based on mutual antagonism also play a role in polarity establishment of the PAR system [25] determining the anterior-posterior axis in *C. elegans*, and the Rac-Rho system regulating front-rear polarity in mammalian cells [121]. Here, we use Eq. 2.2 to describe the deterministic dynamics of the core polarity system. To explore noise effects due to the relatively low copy numbers of regulatory proteins within cells, we also devised a stochastic model based on stochastic differential equations, see Eqs. 2.6 in 'Materials and Methods'. These equations take the same form as Eqs. 2.2, but with an added noise term in each equation that depends on the state of the system. The noise strength in this model is determined by an effective "copy number" parameter N, with $N \to \infty$ recovering the deterministic dynamics and noise strength increasing with decreasing N.

The signaling protein X mediates a non-directional signal that interacts with the core polarity system (Fig. 2.1B) to induce polarity switching (in *M. xanthus*, X corresponds

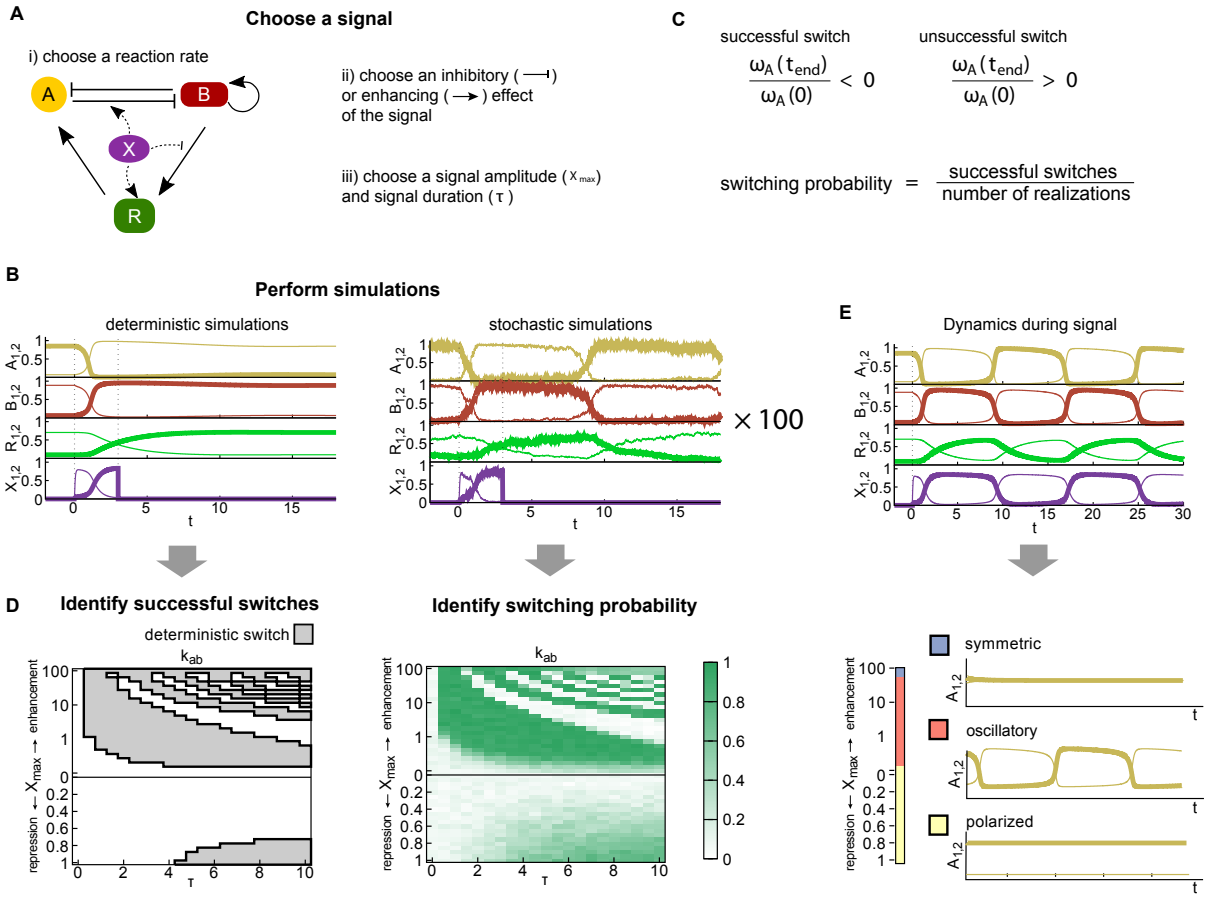

Figure 2.2 | Schematic representation of the workflow. **A** Switching signals are parameterized by the choice of i) a reaction rate it acts on, ii) an inhibitory or enhancing effect and iii) the amplitude $X_{\max}$ and duration τ of the transient signal. X can act on any of the 11 parameters of the polarity model. **B** Example of a deterministic and stochastic simulation before, during and after the signal. The signal is applied between $t = 0$ and $t = 3$. Thick lines indicate the concentrations of A (yellow), B (red), R (green) and X (purple) at pole 1, and thin lines at pole 2. **C** Switching is evaluated by comparing the signs of the asymmetry $\omega_A(t)$ in A before and after the switch. For the stochastic simulation a switching probability is calculated from 100 trajectories. **D** Switching regimes are plotted in phase space as a function of X_{max} and τ for the modification of each model parameter. For the deterministic model, successful switches are shown by the gray regions with a black outline, for the stochastic model switching probabilities are shown in green. **E** The state of the system during the signal is identified by simulating the deterministic model with the signal applied for the duration of the simulations. The dynamics is classified into three states: symmetric (blue), oscillatory (orange) and polarized (yellow).

to phosphorylated FrzX [127]). We assume the total amount X_t of X to have a step-like pulse form (Fig. 2.1C), parameterized by an amplitude X_{max} and duration τ. While

step-like pulses are a reasonable assumption, given that signals change via (rapid) protein modifications rather than (slow) changes in protein levels, we will also study the effect of more gradual changes further below. In the model of [127], cytoplasmic X is recruited to the poles by the antagonist B with rate k_X and spontaneously unbinds with rate k_x, such that its polar abundances change according to

$$\frac{dX_i}{dt} = k_X(X_t - X_1 - X_2)B_i - k_x X_i \ . \tag{2.3}$$

In order to systematically explore the possible mechanisms by which polar X may interact with the core polarity system, we allowed X to regulate each one of the 11 parameters in Eqs. 2.2. We allowed for both positive and negative regulation, thus obtaining 22 different candidate models for a switchable polarity system. In each case, one parameter, denoted k_j, depends on X_i while the others are not affected (the index j in k_j specifies which of the 11 parameters in Eqs. 2.2 is regulated). For a positive regulation, we have

$$k_j(X_i) = k_j(1 + X_i) \ , \tag{2.4}$$

and for a negative

$$k_j(X_i) = k_j(1 - X_i) \ . \tag{2.5}$$

Hence, a candidate signaling scenario is parameterized by (i) which parameter k_j is regulated by X, (ii) whether the regulation is enhancing or repressive, and (iii) the amplitude and duration of the pulse, as illustrated in Fig. 2.2A.

2.2.2 Identifying functional switching scenarios

To test a candidate signaling scenario for its ability to induce polarity switching, we simulate the dynamics (both deterministic and stochastic) of the model. The output of a simulation is a set of time-dependent abundances of the four proteins A, B, R, and X at the two poles (Fig. 2.2B). Each simulation run has three phases. First, we simulate the polarity model, Eq. 2.2, in the absence of signaling input ($X_t = 0$). In this condition, the system reaches a stable polarized configuration. At $t = 0$, we then switch to $X_t = X_{\max}$ for a duration τ, after which the simulation is continued with X_t set to zero again. We then compare the polarization of the cell at the time when the signal is initiated ($t = 0$) with a time point after the removal of the signal ($t_{end} = 30$ was chosen to allow for the system to fully relax back to a polarized steady state). The candidate signaling scenario is considered to generate a successful switch if the signs of $\omega_A(0)$ and $\omega_A(t_{end})$ were different (i.e., the initial and final polarity states were different), and unsuccessful otherwise (Fig. 2.2C). For the stochastic dynamics, we estimated the switching probability from 100 simulation runs (Fig. 2.2B,C). We repeated this procedure for each signaling scenario with a range of X_{max} and τ values, generating deterministic and stochastic phase diagrams delineating the functional regimes in (τ, X_{max})-space (Fig. 2.2D).

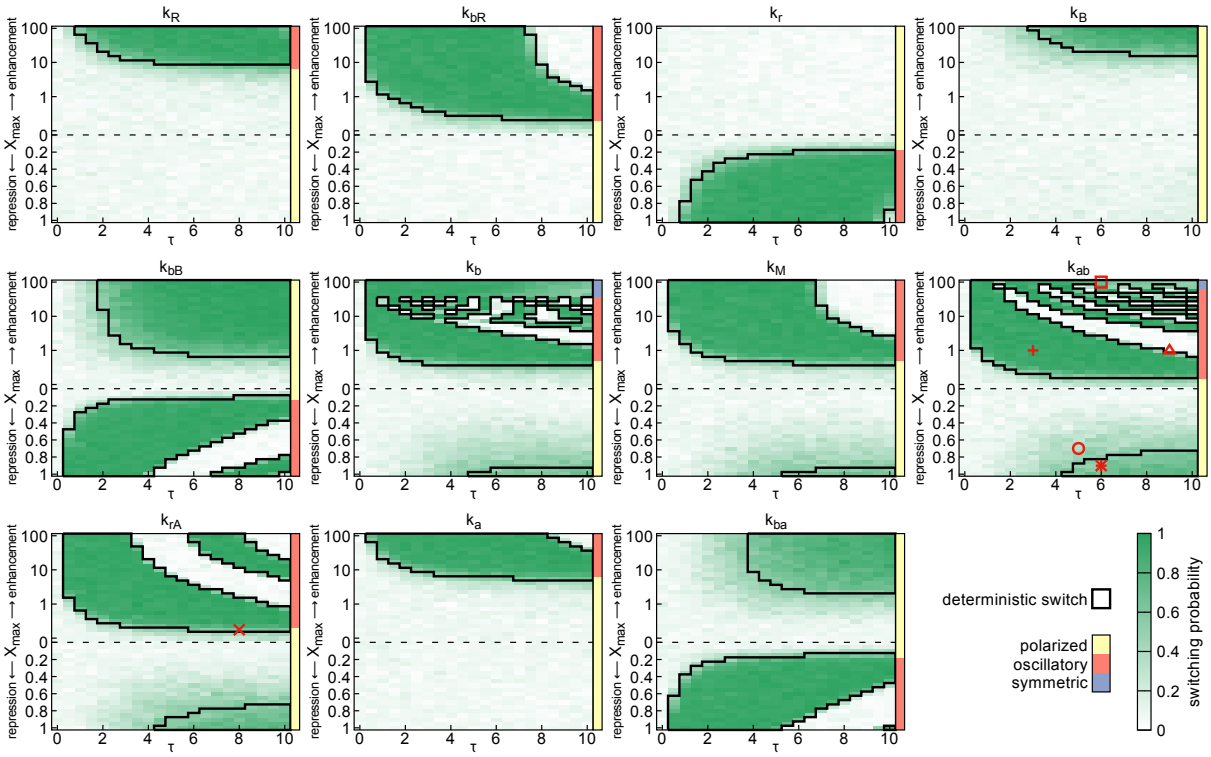

Figure 2.3 | Switching regimes for each of the model parameters. Regions in which the deterministic model shows switches are indicated by thick black outlines. The green shading shows the switching probability of the stochastic model with $N = 10^{3.75}$. The upper half of the phase diagram shows results for a signal that enhances the reaction rate, and the lower half for a repression of the rate. The colored bars to the right of each panel indicate the class of dynamics when the corresponding amplitude of signal is applied, with yellow for polarized, orange for oscillatory and blue for symmetric polar distribution of A. The red symbols indicate the signal amplitude and duration of the trajectories shown in Fig. 2.4

.

2.2.3 Characterizing functional switching scenarios

Fig. 2.3 shows the resulting phase diagrams, each representing regulation via one of the 11 model parameters and including both enhancing and repressive regulatory effects. Here, the deterministic regimes of successful polarity reversals (solid black lines) are superimposed with the stochastic switching probabilities (green shading). We identified at least one range of signal parameters with successful polarity reversals in each of the phase diagrams. That is, it is possible for X to induce reversals by regulating any of the interactions of the polarity proteins, provided that the profile of the signal pulse X_t is chosen appropriately. Surprisingly, in most cases reversals can be observed when X acts either positively *or*

negatively. For example, reversals can be induced by X either enhancing or repressing the strength of B self-recruitment via the parameter k_{bB}.

Polarity is highly sensitive to regulation of some parameters (e.g. k_{bB}, k_{ba}), with switching occurring for most signal profiles. These parameters tend to be those involved in the key interactions of Fig. 2.1B, including the nonlinear feedbacks in B recruitment, A recruitment by R, and A-B mutual antagonism, which together are crucial for the establishment and maintenance of polarity. For parameters that are more peripheral to the interaction network, in particular the spontaneous binding and dissociation rates (e.g. k_R, k_B), switching occurs only in small regions of high-amplitude signals.

Fig. 2.3 reveals two qualitatively different patterns in the signaling regimes generating switching: solid regions, in which switching is insensitive to X_{max} and τ provided these exceed a threshold; and alternating bands of successful and unsuccessful switching regions, in which the system remains sensitive to the values of X_{max} and τ. These qualitative patterns remain when the values of the basal parameters k_j are varied (Figs. 2.10 and 2.11). Intuitively, alternating bands would be expected to occur, if the system dynamics become oscillatory in presence of the signal, since Fig. 2.3 only compares the initial and final state, such that for instance it does not discriminate between trajectories in which polarity is never reversed, and those in which polarity reverses twice.

To investigate the switching mechanism in the successful parameter regimes, we examined trajectories of the system for different signals. For a trajectory within a banded region (plus symbol in Fig. 2.3), we see that once the signal is applied, A rapidly relocates to the opposite pole, followed by B and on a slower timescale R (Fig. 2.4A, solid lines). If a signal with the same amplitude X_{max} is applied for a longer time (open triangle in Fig. 2.3), a second switch takes place (Fig. 2.4A, dashed lines). Hence the width of the bands is determined by the timescale of R reorientation. This particular case, where X enhances k_{ab}, is precisely the relaxation oscillator dynamics reported in [127].

For a trajectory in the non-band signal regime (star symbol in Fig. 2.3), the system rapidly reaches a new steady state (with the same polarity) when the signal is applied (Fig. 2.4B). The polarity reversal occurs after, and appears to be initiated by, the removal of the signal. To confirm that there are no longer-period oscillations during the signal period, we examined the dynamics with a signal of the same amplitude for a long duration ($\tau = 100$). The system remained stably polarized throughout this duration. Thus, this switching mechanism is qualitatively different from the relaxation oscillator reported previously. Switching is insensitive to the signal duration τ, provided that it is above a threshold value. We interpret this threshold as meaning that the signal must be present for long enough to prime the system to switch, and refer to this mechanism as a "prime-release" switch.

We then examined trajectories over the entire signal space and determined the order in which the polarity of A, B and R reversed, defined by the times at which their asymmetry ω becomes zero. For almost all regimes with reversals the same order was observed (Fig. 2.12): first A, then B, and finally R. This suggests that the underlying dynamics of the trajectory

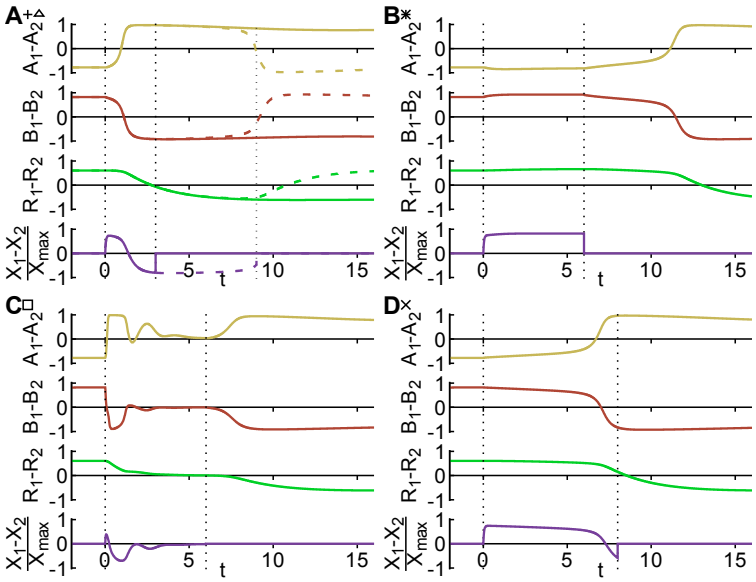

Figure 2.4 | Trajectories of the model during switches, classified as four different switching classes. Signal parameters X_{max} and τ and the parameter modified are indicated by the corresponding symbols in Fig. 2.3. Vertical dashed lines indicate the period during which the signal is present. **A** Relaxation oscillator. For a short signal (plus-symbol), the polarity switches during the applied signal as shown by the solid lines. For a longer signal (open triangle), the system switches a second time as shown by the dashed lines. **B** Prime-release switch. During the signal the polarity is unchanged, but switches after the signal is released. **C** Reset switch. During the signal, the system relaxes to a symmetric distribution of the polarity marker and establishes a reversed polarity after the signal is removed. **D** Push switch. The system switches while the signal is applied and does not switch back when the signal is applied longer.

between the two polarity states is similar in different switching regimes. In some limited regimes, for particularly high-amplitude signals, reversal of first B and then A was observed. However, these reversals were almost simultaneous. In some regimes reversals of A and B but not R occurred. In these cases, the polarity oscillations of A and B were so fast that a second reversal was initiated before the much slower dynamics of R could catch up to the new polarity state.

2.2.4 Classification of switching mechanisms

We next examined the dynamics during persistent signals for all regulations and signal amplitudes (Fig. 2.2E). We identified three classes of behavior (Fig. 2.13), reflecting qualitatively different topologies of the model's state space as shown in Fig. 2.5. These are (i) static asymmetrically polarized protein distributions, corresponding to bistable state space with the two stable states representing the two possible orientations of polarization;

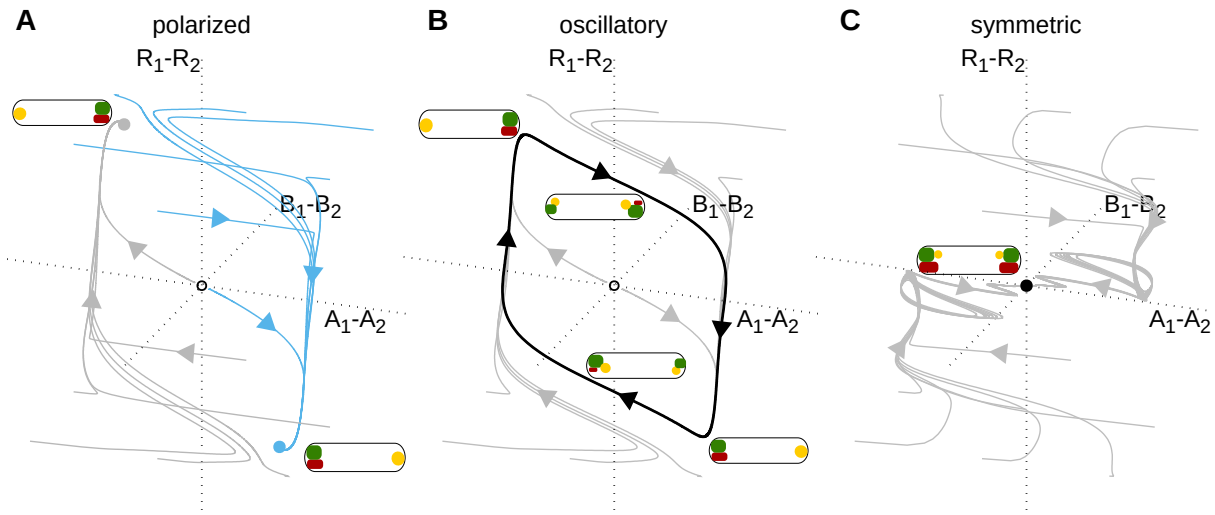

Figure 2.5 | In the presence of the signal, the polarity system can display three qualitatively different phase space topologies, here denoted as 'polarized', 'oscillatory', and 'symmetric'. For each case, the dynamics of the system is shown in the three-dimensional space $(A_1 - A_2, B_1 - B_2, R_1 - R_2)$, in which the origin corresponds to a completely symmetric protein distribution. **A** In a polarized state, the system is bistable, with two stable fixed points, marked grey and blue, which correspond to the two polarities of the cell. Depending on the initial condition, the system approaches one or the other stable fixed point, as illustrated by the shown trajectories. **B** In an oscillatory state, all trajectories of the system run into a stable limit cycle, marked in black. **C** In a symmetric state, the system is monostable, with a single stable fixed point at the origin, corresponding to an unpolarized cell.

(ii) oscillatory protein dynamics, corresponding to a stable limit cycle in state space; and (iii) symmetric protein distributions, corresponding to a single stable fixed point in state space. The extent of these different regimes are indicated by the colored bars adjacent to each panel in Fig. 2.3.

This analysis confirmed that band structures in Fig. 2.3 correspond largely to oscillatory dynamics in the presence of the X signal, while solid regions correspond to regimes where the system remains bistable when the signal is applied. However, we also identified regimes presenting two additional types of switches.

For large-amplitude signals, the system can transition from an oscillatory to a monostable regime. In this scenario, while the signal is applied the system gradually relaxes towards a symmetric configuration (Fig. 2.4C). Once the signal is removed, the system once again becomes polarized, but settles in the opposite polarization state from that in which it was initially. Effectively, the initial state of the system is erased and a new polarity state is chosen when the signal is removed. We therefore refer to this mechanism as a "reset" switch.

Finally, we found that as the oscillatory regime is approached, the onset of switching does not always coincide with the onset of oscillations. In the intervening region, the system still remains bistable. Examining the system trajectories, we observed qualitatively different behavior from Fig. 2.4B. Instead of switching once the signal is removed, the system begins to switch immediately when the signal is applied, and subsequently remains stably polarized in the opposite orientation (Fig. 2.4D). We refer to this mechanism as a "push" switch.

We have thus identified four distinct classes of switching dynamics, corresponding to four qualitatively different trajectories (Fig. 2.4). To understand these different mechanisms from a more general nonlinear dynamics perspective, we next ask how the topology of the phase space changes in each case. Prior to the application of the signal, the system is in a bistable configuration with two stable fixed points corresponding to the two possible polarity orientations (Fig. 2.5A). The subsequent behavior differs for each mechanism, as shown in Fig. 2.6 and described in the following.

2.3 Results

2.3.1 Transient oscillator switch

In this class of switching, the system becomes oscillatory when the signal is applied, following the prescribed path of the limit cycle in state space. Upon removal of the signal, the phase space reverts to being bistable. The system then relaxes to one of the polarized fixed points. Which fixed point is chosen depends on the state at the end of the signal period, and in particular on which side of the separatrix (the division between the basins of attraction of the two fixed points) the state lies, as shown in Fig. 2.6A. The duration of the signal relative to the oscillation period determines the phase at the time of signal removal and hence the final polarity state. How sensitive an oscillatory switch is to the signal duration varies dramatically between different regulations in our model, being relatively high for k_b and k_{ab}, but low for k_{bR} and k_r among others.

2.3.2 Reset switch

Instead of following a limit cycle during the signal period, the reset switch gradually relaxes (usually along a spiraling trajectory) towards a single stable fixed point (Fig. 2.6B). Once again, the choice of polarity state upon removal of the signal depends only on which side of the separatrix the system is once the signal is removed. In the deterministic model, the choice of final polarity state is reliable even with a small remnant of asymmetry at the time of signal removal. However, this mechanism will be susceptible to noise in the protein dynamics that can overwhelm memory of the previous state (see below).

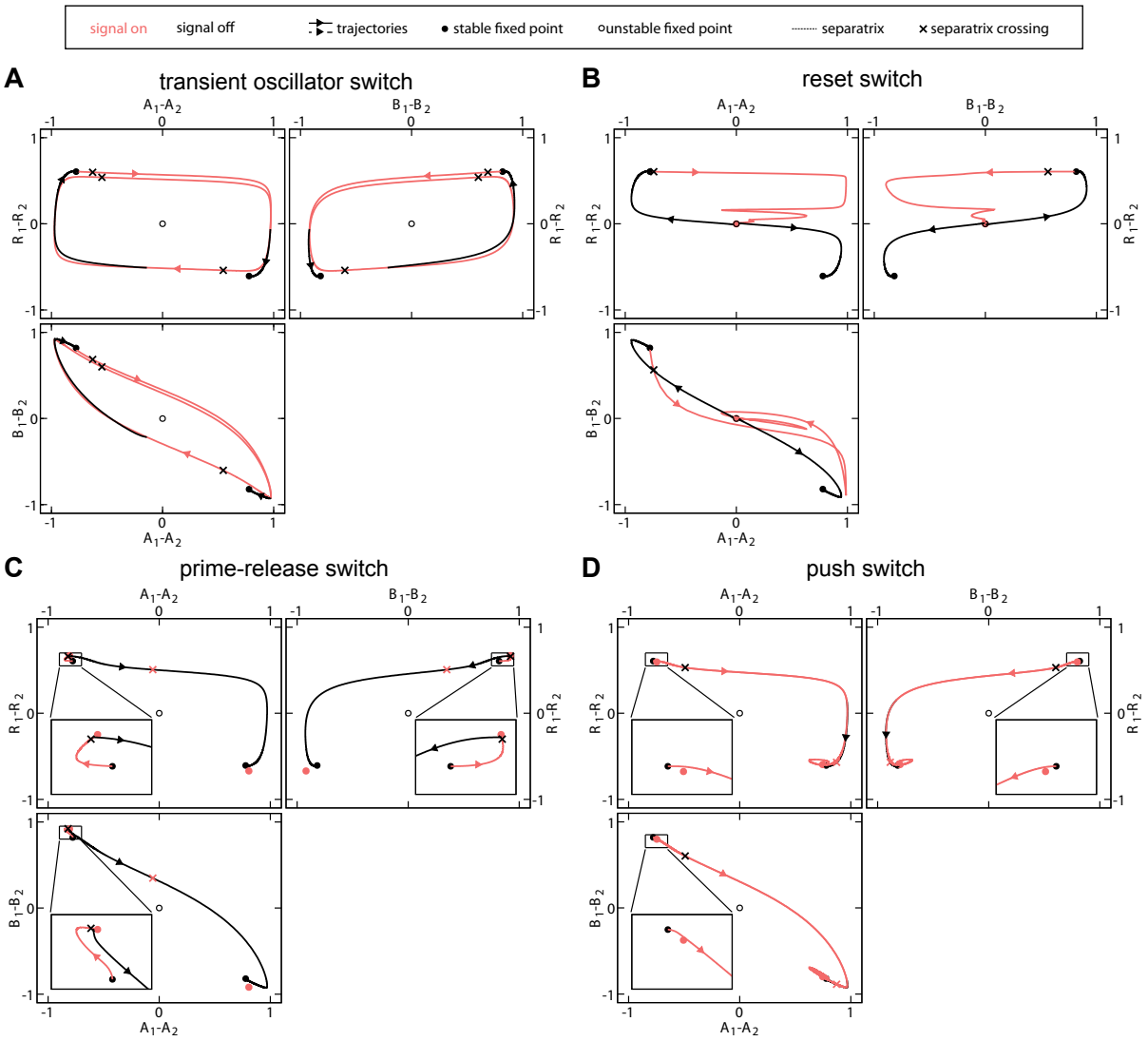

Figure 2.6 | Nonlinear dynamical behavior of the four different mechanisms of signal-induced polarity switching. In each case, the system dynamics are shown both during (red) and after (black) a signal pulse, with projections onto the (A_1-A_2, R_1-R_2)-plane, the (B_1-B_2, R_1-R_2)-plane, and the (A_1-A_2, B_1-B_2)-plane. **A** Transient oscillator switch. **B** Reset switch. **C** Prime-release switch. **D** Push switch.

2.3.3 Prime-release switch

This type of switch occurs when the model remains bistable even in the presence of the signal, and for parameter changes opposite to those that induce oscillations. The application of the signal does not cause a change in the topology of the state space, but does change the position of the fixed points and separatrix. If the signal is sufficiently strong, it may be that the new fixed points lie on the opposite side of the previous separatrix (Fig. 2.6C).

However, since the current state remains on the same side of the new separatrix, the system simply relaxes to the new fixed point with the same polarity orientation (the "prime" phase). Only upon removal of the signal (the "release" phase) does the system find itself in the basin of attraction of the opposite polarity state.

This picture allows us to rationalize various observations about this switching mechanism. The amplitude of the signal must be sufficiently large that the new fixed point lies on the opposite side of the old separatrix, leading to a threshold in X_{max}. The duration of the signal must be sufficiently long for the state of the system to move across the old separatrix, leading to a threshold in τ. Once these criteria are met, switching is insensitive to the signal amplitude and duration since the system can remain at the new polarized fixed point indefinitely.

2.3.4 Push switch

The mechanism of the push switch is similar to that of the prime-release switch, but effectively with the order of events reversed. The application of the signal ("push") again leads to a shift in the positions of the bistable fixed points and separatrix, but in the opposite direction (Fig. 2.6D). The system in its initial polarized state now finds itself on the opposite side of the new separatrix, from where it relaxes to the oppositely polarized fixed point. Upon removal of the signal, the system relaxes to the new slightly shifted fixed point but retains the same polarization. This mechanism is again largely robust to changes in the signal duration (after a threshold time needed for the initial relaxation phase), but occurs only for very small ranges of signal amplitudes in our model.

2.3.5 Signals with slow edges

Both the prime-release and push switches described above rely on the fact that the signal appears and disappears very quickly, which causes a correspondingly fast change in the phase space. We expected that if the onset and removal of the signal were slower than the relaxation of the system, then the state of the system would be able to track the fixed points as they move gradually from their old to their new positions and no switching would occur. To test this prediction we computed the dynamics with the X signal increasing and decreasing gradually according to $X_t(t) = X_{max}(1 - e^{-\lambda t})$ for $0 \leq t < \tau$ and $X_t(t) = X_{\mathrm{max}}(1 - e^{-\lambda\tau})e^{-\lambda(t-\tau)}$ for $t \geq \tau$ (Fig. 2.14). We saw that for large $\lambda \gg 1$, the dynamics was similar to a step signal and switching continued to occur (Fig. 2.15). However for slow signals with $\lambda \lesssim 1$, switching in bistable regimes was abolished (Figs. 2.16 and 2.17). This was specific to the prime-release and push mechanisms since switching in oscillatory regimes continued to occur, with slight shifts to band boundaries reflecting the effects of the gradual signal on the oscillation phase (Fig. 2.18, Fig. 2.19 and Fig. 2.20).

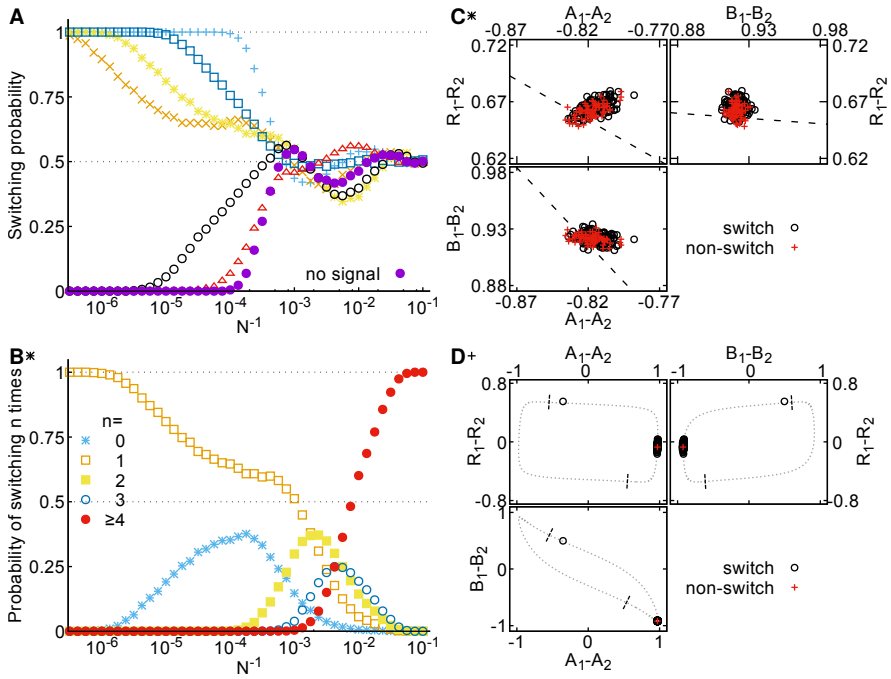

Figure 2.7 | Behavior of the model at different noise levels. **A** Switching probability as a function of noise strength for different switching mechanisms. Signal parameters are indicated by the corresponding symbols in Figs. 2.3 and 2.4. Each data point represents the results of 10^4 stochastic realizations. **B** Probability of different numbers n of switching events at different noise levels for the prime-release switch. Signal parameters are as for Fig. 2.4B. **C** States of 200 stochastic realizations ($N = 10^4$) of the prime-release switch at $t = \tau$. Dashed line shows an estimate of the position of the separatrix in the absence of the signal (see Materials and Methods). **D** States of 200 realizations of the relaxation oscillator at $t = \tau$ ($N = 10^4$). Dotted line shows the deterministic limit cycle of the system during the signal, dashed lines indicate where the limit cycle intersects with the separatrix in the absence of signal. The three different panels in **C** and **D** show different two-dimensional projections of the nine dimensional phase space. Point type and color indicate whether the system switches polarity (red) or not (black).

2.3.6 Stochastic effects

As seen in Fig. 2.3, the switching probability of the stochastic model for low to intermediate noise levels tends to closely follow the boundaries of regions in which the deterministic model switches (see also Figs. 2.21 and 2.22). However, switching can also occur for signal parameters X_{max} and τ for which the deterministic system does not switch. In particular, the regimes in which switching can occur are greatly expanded by noise for prime-release and push switches, while the transition boundaries between switching and non-switching regimes of relaxation oscillators appear much sharper. For reset switches, switching remains relatively robust with short signals, which are cut off before the system has fully relaxed

to a symmetric state. For longer signals the switching probability approaches 0.5, as the new polarity state is chosen randomly once the signal is removed.

Fig. 2.7A shows the switching probability for the signal parameters indicated in Fig. 2.3 for increasing noise level. Each mechanism displays a different noise threshold at which the switching probability departs from the deterministic result (either 0 or 1 depending on the signal parameters). This threshold is highest for the transient oscillator ($+$, $\triangle$), and lowest for the push ($\times$) and prime-release switches ($*$). Around $N \approx 10^{3.5}$ the switching probability converges to approximately 0.5 for all mechanisms. For higher noise levels (smaller N), all the mechanisms show qualitatively similar damped oscillations around 0.5. Similar behavior is observed in stochastic trajectories in the absence of any signal, indicating that these features are primarily the result of the dynamics during the period that the signal is not present ($\tau \leq t \leq t_{end}$). For this reason we first focus on the regime $N \gtrsim 10^4$, in which the switching behavior remains influenced by the signal, and return to the high-noise behavior later.

2.3.7 Noise-induced switching errors

The switching probability, comparing only the states of the system before and after the signal is applied, cannot distinguish between cases in which noise prevents a switch from occurring and cases in which noise causes an extra switch to occur. We therefore examined the number of polarity switching events, defined as times at which $A_1 = A_2$, in stochastic trajectories. The distributions of such events are plotted for the prime-release switch in Fig. 2.7B (see Fig. 2.23 for the other cases). We observe that the initial decrease in switching probability around $N \approx 10^6$ corresponds to the appearance of a sub-population of realizations that do not switch. A flattening out of the switching probability around $N = 10^4$, coincides with the appearance of trajectories exhibiting an extra second switch, due largely to stochastic switches during the period when no signal is present.

In the prime-release mechanism, switching is triggered by the removal of the signal. In the presence of noise, the system fluctuates around the fixed point of the dynamics, rather than resting exactly at the fixed point. The range of these fluctuations, visualized by sampling the states of different stochastic realizations at the end of the signal (prime) phase (Fig. 2.7C), expands with increasing noise strength. Importantly, when the signal is removed the states of the system are clustered close to the new separatrix of the system, allowing them to be forced from the basin of one fixed point to the other by noise. The same mechanism accounts for the expansion of the range of signals for which switching can be induced in the presence of noise beyond that in which the deterministic model will switch (Figs. 2.3 and 2.7A, $\circ$). The signal is not sufficiently strong for the deterministic fixed point with the signal applied to cross the original separatrix. However, some fraction of the distribution of states around this fixed point will lie close enough to the separatrix to undergo a switch when the signal is removed. Similar behavior can also be observed for the push signal with respect to the distribution of states at the onset of the signal period.

For the transient oscillator the initial deviation from the deterministic results is due to noise-induced extra switches once the signal has been removed. Noise in the dynamics during the signal predominantly leads to phase variability, as different realizations spread out around the limit cycle. However, the state of the system at the removal of the signal is typically far from the separatrix (Fig. 2.7D) in the slow phase of the dynamics where R reacts to the new polarity of A and B. Under these conditions, extremely high noise levels are required for the system to cross into the opposite basin of attraction. Hence, oscillatory switching appears extremely robust to noise.

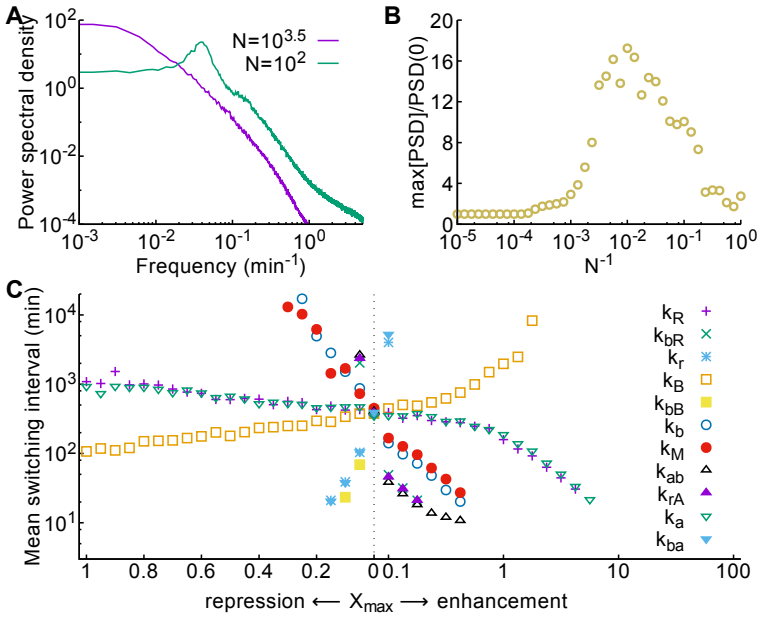

Figure 2.8 | Stochastic switching. **A** Power spectral density of $A_1(t) - A_2(t)$ in the absence of any X signal for different noise strengths. A peak in the power spectrum at high noise indicates stochastic coherence. **B** The maximal power density relative to the power at zero frequency shows a non-monotonic dependence on the noise strength. **C** The mean time between switching events, defined as points when $A_1 = A_2$, varies as different signals are applied, at a noise level $N = 10^{3.75}$. Signals that generate deterministic oscillations have been excluded. Times between switches were extracted from stochastic trajectories with the signal applied continuously for 50000 min.

2.3.8 Coherence resonance

Returning to the high-noise regime ($N \lesssim 10^{3.5}$), where switching in the absence of any signal dominates, we observe that the switching probability oscillates before it saturates at 0.5 for very high noise (Fig. 2.7A). These oscillations are reminiscent of a so-called "coherence resonance" [129]. A coherence resonance occurs when the activation timescale for noise to drive the system across the separatrix of a bistable system becomes shorter than the relaxation timescale to reach the vicinity of the opposite fixed point. The trajectory of

such a stochastic system has a largely oscillatory character. Indeed, the power spectrum of the dynamics changes from monotonically decreasing at small noise to peaked at a finite frequency for larger noise (Fig. 2.8A), indicating the appearance of oscillations. Additionally, the height of this peak shows a maximum at a finite noise level (Fig. 2.8B), confirming the coherence resonance behavior. Thus at high noise levels, noise can drive the system between the two polarity states with a largely oscillatory dynamics, even in the absence of any X signal (Fig. 2.24).

2.3.9 Signal-induced stochastic switching

The application of a signal could also influence the stochastic switching rate during the period that the signal is active. For example, a signal could lower the height of the separatrix barrier between two fixed points, thereby increasing the chance of a stochastic switch. To study which signals could give rise to such an increase of stochastic switching, we analyzed long trajectories where signals with different amplitudes were applied continuously. Fig. 2.8C shows the resulting mean times between switching events. We observe that indeed the mean time between switches is affected by the choice of signal. Interestingly, the mean interval between switches decreases as the signal approaches the regime of oscillations, consistent with a reduction in the height of the separatrix barrier as the bifurcation point is approached. Conversely, switches become rarer when the signal varies in the opposite direction, into the prime-release regime. In general, however, the frequency of switching is extremely low such that the expected number of switches during one signal period approaches zero. We therefore conclude that the effects of stochastic switching during the signal will be negligible and dominated by the responses of the system to the transient phases of the signal.

2.4 Discussion

In this work we developed a classification of signal-induced polarity switching mechanisms. Our classification of switching mechanisms is not based on the molecular interactions, but on the qualitative dynamic behavior. Interestingly, one can obtain different switching mechanisms already with the same signaling and regulation network, by changing only the signal amplitude and duration, or the sign of the regulatory effect of the signal (Fig. 2.3). Overall, we found four qualitatively different switching mechanisms: (i) the transient oscillator switch, (ii) the reset switch, (iii) the prime-release switch, and (iv) the push switch. The working principles underlying these four mechanisms can be understood already within a schematic, two-dimensional respresentation of the signal-dependent phase space structure of the system (Fig. 2.9).

In the absence of the signal input that triggers polarity switching, the phase space structure must be that of a bistable system, with two stable fixed points corresponding to the two

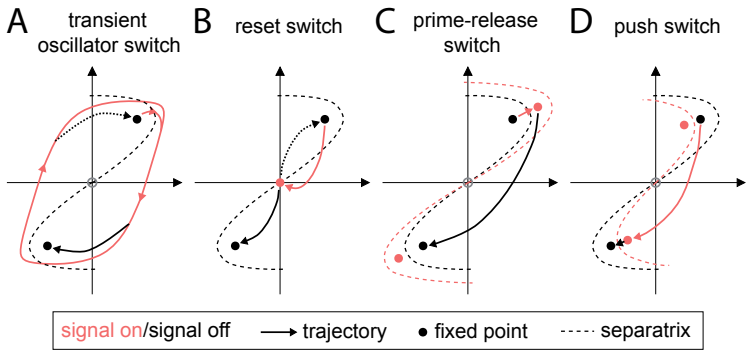

Figure 2.9 | Illustration of the working principles underlying the four classes of switching mechanisms. The different nonlinear dynamical behaviors are schematically represented in a two-dimensional phase space. Red/black symbols indicate the state space and dynamics when the signal is present/absent. **A** Transient oscillator switch. **B** Reset switch. **C** Prime-release switch. **D** Push switch.

polarity states. The basins of attraction of these fixed points are separated by a boundary (separatrix). Before the signal is applied, the system is at one of the stable fixed points (black filled circles in Fig. 2.9). When the signaling system is activated, it interferes with the polarity system. This temporarily deforms the structure of the phase space, and causes the state of the system to move within the phase space. The movement begins during the application of the signal (red trajectories in Fig. 2.9), but continues after the signal has disappeared and the structure of the phase space has returned to its original state (black trajectories in Fig. 2.9).

We found three types of phase space structure in the presence of the signal: monostable, bistable, and oscillatory (Fig. 2.5). With these three structures, our analysis revealed four types of polarity switches. All four have in common that the temporary deformation of the phase space structure leaves the system on the other side of the separatrix when the original bistable phase space structure is restored. The transient oscillator switch achieves this by moving the system along a limit cycle during the signal (Fig. 2.9A), while the reset switch moves it towards a single stable fixed point along a curved trajectory (Fig. 2.9B). When the system is bistable in the presence of the signal, there are two distinct types of switches: Either the signal moves the fixed point through the original separatrix (prime-release switch, Fig. 2.9C), or the signal pushes the separatrix through the original fixed point (push switch, Fig. 2.9D).

The actual phase space of the system is higher-dimensional, but the qualitative behavior is the same as that shown in Fig. 2.9. In principle, there could be polarity networks for which the signaling system induces more complex types of phase space structure, e.g. higher-order multistable or chaotic, albeit the functional benefits would be unclear. Assuming that the phase space structure is either monostable, bistable, or oscillatory in the presence of the signal, the four switching mechanisms of Fig. 2.9 appear to exhaust the spectrum of possible behaviors. We therefore do not expect additional classes of signal-induced polarity

switches to arise in other models of polarity systems with the above-mentioned properties. It is somewhat surprising that the interaction scheme of the Guzzo et al [127] model for *M. xanthus* polarity, which we took as the starting point for our analysis, is capable of producing all four types of switches. It remains to be seen whether the capacity for such diverse switching phenomenology is common to other models of prokaryotic and eukaryotic cell polarity, and which features of such models enable different switching modes. Some models, in particular those with fewer components, are likely not able to produce all four types of switches, e.g. because they cannot generate oscillations.

We also showed how the different switching mechanisms respond to signal variability and internal molecular noise. For instance, while the transient oscillator switch is most sensitive to signal variability it is least sensitive to molecular noise. By contrast, the prime-release switch is least sensitive to signal variability, but very sensitive to molecular noise. These differences in behavior will be useful as signatures to identify the actual switching mechanisms in biological systems. In addition, these properties will be relevant for the design of synthetic systems.

Currently, the *M. xanthus* system is perhaps the best studied system for polarity switching, but even there the question of the mechanism is not resolved. Guzzo et al [127] showed that the transient oscillator switch is a possible mechanism for the observed polarity switching, but other possible mechanisms are currently not excluded. Furthermore, important new components of this system continue to be found [130] and the precise interactions between the known components continue to be investigated [131]. The situation is even less clear for other experimentally studied examples of polarity switching such as neutrophils [120]. Given this state of research, it is of practical significance to know which types of mechanisms are in principle available, and what the properties of these mechanisms are.

To clearly distinguish between these mechanisms, it would be particularly useful to have experimental control over the input signal that triggers polarity switching. For the prime-release switch, the polarity reversal can only occur after the signal is removed. Hence, if the reversal is observed while the signal is still present, the prime-release switch can be excluded. The reset switch displays a loss of polarity during a long signal, which constitutes a unique signature of this mechanism. The transient oscillator switch is best detected by varying the duration of the signal. Finally, the push switch should switch only once during a long signal. Note, however, that such experiments will give insight only into the type of switch and not into the detailed interaction between the signaling protein and the polarity proteins, since the same qualitative dynamics can be generated by different modes of action of the signal. Our analysis of the systems' dynamics also revealed that, while the timing with respect to the input signal is different for the different mechanisms, the order in which the proteins of the core polarity system switch poles is almost always the same. This indicates that we cannot infer the interaction of the signaling protein X from looking at the order in which the polarity proteins switch poles, but that the order of switching is rather a characteristic of the interactions between different polarity proteins.

By analogy with the paradigmatic genetic toggle switch [132], the functionality analyzed here can be regarded as a 'spatial toggle switch'. The core of the genetic toggle switch is a circuit of two mutually repressing genes, conceptually similar to the mutual inhibition between the polarity marker A and its antagonist B. Some of the behavior is also analogous, e.g. molecular noise can cause the genetic toggle switch to flip spontaneously [133], just as it does for the polarity system. However, while the genetic toggle switch is a well-mixed bistable system, the core polarity system is a spatially extended bistable system that forms asymmetric patterns. The spatial extension of the polarity system allows a global signal (X_t) to be converted into a local signal (differential activity of X at the two poles), in a way that would be impossible in a well-mixed system. This permits the polarity system to function as a true toggle switch, i.e. the same signal causes switching in both directions, in contrast to the original genetic toggle switch, where different signals "set" and "reset" the switch [132]. The true toggle (or "push-on push-off") functionality in genetic switches requires more elaborate regulatory circuitry that manipulates the bistable system as a function of input signals to achieve control of the system [134–137].

In comparison with genetic systems, the control of pattern forming systems is only beginning to be explored, opening interesting directions for future research. Here, we used a simplified treatment for the pattern formation process, with the cell divided into only three regions, the two poles and the cytoplasm. The underlying assumption is time-scale separation between the diffusive transport and the relevant biochemical processes. Given typical cell lengths, e.g. $L \sim 6\,\mu$m for *M. xanthus*, and diffusion coefficients $D \sim 10\,\mu\text{m}^2/\text{s}$ for small cytoplasmic proteins [138], the mixing timescale $L^2/(2D)$ over which cytoplasmic proteins explore the bulk of the cell is less than 2 seconds. In contrast, the observed timescale of the actual switching process, during which the abundances of the polarity system proteins decrease at one pole and increase at the opposite pole, is on the order of 30 seconds for *M. xanthus* [127], suggesting that the assumption is reasonable. However, it will be interesting to explore the dynamics also under conditions where this assumption does not hold, using full spatial models.

Appendices

2.A Material and Methods

Deterministic dynamics

Reaction rates k_j were chosen as in [127], with the rate $k_{ab} = 15\ \text{min}^{-1}$. The deterministic dynamics was computed with Mathematica (Wolfram Research Inc.) using the function NDSolve separately in each domain (before, during and after the signal), with initial conditions set according to the protein abundances at the end of the previous segment.

Stochastic model

For the stochastic version of the model we used a Langevin extension of Eqs. 2.2, adding a noise term to each equation,

$$\begin{aligned}
\frac{dA_i}{dt} &= k_{rA}(1-A_1-A_2)R_i - k_a A_i - k_{ba}A_i B_i^2 + f_{A,i}(\mathbf{x})^{1/2}\eta_{A,i}(t) \\
\frac{dR_i}{dt} &= (1-R_1-R_2)(k_R + k_{bR}B_i) - k_r R_i + f_{R,i}(\mathbf{x})^{1/2}\eta_{R,i}(t) \\
\frac{dB_i}{dt} &= (1-B_1-B_2)(k_B + k_{bB}B_i) - k_b\frac{k_M}{B_i+k_M}B_i \\
&\quad - k_{ab}A_i B_i^2 + f_{B,i}(\mathbf{x})^{1/2}\eta_{B,i}(t) \\
\frac{dX_i}{dt} &= k_X(X_t - X_1 - X_2)B_i - k_x X_i + f_{X,i}(\mathbf{x})^{1/2}\eta_{X,i}(t)
\end{aligned} \tag{2.6}$$

where $\mathbf{x} = (A_1, A_2, R_1, \ldots, X_2)$ is the state vector, and the $\eta_{\cdot,i}$ are independent Gaussian random variables, $\langle \eta_{\cdot,i}(t)\rangle = 0$ and $\langle \eta_{p,i}(t)\eta_{q,j}(t')\rangle = N^{-1}\delta_{p,q}\delta_{i,j}\delta(t-t')$. We have introduced N as a parameter to tune the magnitude of the noise, with the deterministic model being recovered as $N \to \infty$. We chose to make the noise multiplicative by having the strengths $f_{\cdot,i}(\mathbf{x})$ depend on the current state of the system, $\mathbf{x}$. Specifically,

$$\begin{aligned}
f_{A,i}(\mathbf{x}) &= k_{rA}(1-A_1-A_2)R_i + k_a A_i + k_{ba}A_i B_i^2 \\
f_{R,i}(\mathbf{x}) &= (1-R_1-R_2)(k_R + k_{bR}B_i) + k_r R_i \\
f_{B,i}(\mathbf{x}) &= (1-B_1-B_2)(k_B + k_{bB}B_i) + k_b\frac{k_M}{B_i+k_M}B_i \\
&\quad + k_{ab}A_i B_i^2 \\
f_{X,i}(\mathbf{x}) &= k_X(X_t - X_1 - X_2)B_i + k_x X_i
\end{aligned} \tag{2.7}$$

We emphasize here that these noise terms were chosen simply as one plausible generalization of Eqs. 2.2. While they resemble those that might be obtained from a system-size expansion of a full Master equation for the reactions underlying Eqs. 2.2 [139, 140], we note that since the original model is defined only in terms of the rate equations and not in terms of the underlying molecular reactions, no such systematic derivation of the noise is possible. We verified that the particular choice of the form of the noise did not affect our conclusions, and found qualitatively similar results when white noise was used (implemented by fixing $\mathbf{x} = (1/3, 1/3, \ldots, 1/3, X_t/3, X_t/3)$ in Eq. 2.7), see Figs. 2.25 and 2.26.

Simulations of the stochastic model were performed by directly integrating Eqs. 2.6 using an update rule of the form

$$\mathbf{x}(t+dt) = \mathbf{x}(t) + dt\ \mathbf{d}(\mathbf{x}) + \sqrt{\frac{dt}{N}\mathbf{f}(\mathbf{x})}\ \xi, \tag{2.8}$$

where $\mathbf{d}(\mathbf{x})$ represents the deterministic part of Eqs. 2.6, $\mathbf{f}(\mathbf{x}) = (f_{A,1}, f_{A,2}, f_{R,1}, \ldots, f_{X,2})$ is a vector of noise strengths, $\boldsymbol{\xi}$ is a vector of independent samples from a normal distribution,

and multiplication of $\mathbf{f}^{1/2}$ and $\boldsymbol{\xi}$ is performed elementwise. A time step $dt = 10^{-4}$min was used throughout. After each update step, all protein abundances were corrected such that none were negative or exceeded the total protein numbers (i.e. ensuring $A_1 + A_2 \leq 1$, and similarly for each other protein). The simulation code (implemented in C++) is available at github.com/gerland-group/langevin_switching.

Estimation of separatrices

The separatrix lines in Fig. 2.7C,D were estimated as follows. For the prime-release switch (Fig. 2.7C), we first estimated the state space around the fixed point in the presence of the signal by simulating 10000 stochastic trajectories with $N = 10^3$ until $t = \tau$. For each of these points, we determined on which side of the separatrix they fell in the absence of signal, by taking these as the initial conditions for deterministic simulations over the period $\tau \leq t < t_{end}$. The projections of the separatrix in the planes shown were then estimated by using a linear discriminant classifier to determine, for each of the two-dimensional projections of the data in turn, the decision boundary between the sets of states that belong to each of the basins of attraction. This analysis was performed using the 'LinearDiscriminantAnalysis' class from scikit-learn [141] with default parameters. For the relaxation oscillator (Fig. 2.7D), we identified the path of the limit cycle from the trajectory of the deterministic model. The intersection points with the separatrix were then estimated by initializing simulations with the signal removed at different points along the limit cycle.

Power spectra

Power spectral densities were estimated from trajectories sampled every 0.01 min for 50000 min by Welch's method of averaged periodograms from overlapping segments of the trajectory [142] using the MATLAB (Mathworks) function pwelch with segments of length 2^{16} samples.

2.B Supplementary figures

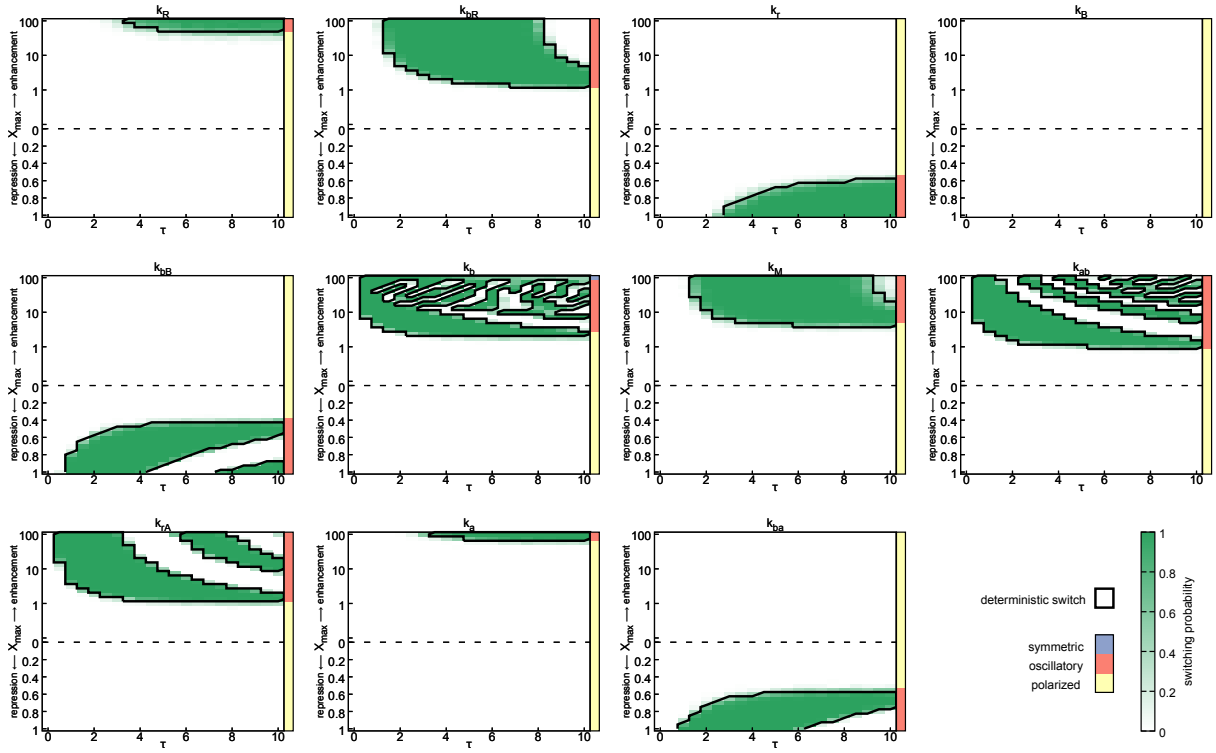

Figure 2.10 | Switching regimes, with the signal acting on each of the model parameters as in Fig. 2.3 of the main text, but with a different basal parameter set that was randomly chosen (by multiplying each of the original basal parameter values by a random number between 0.5 and 1.5). In the shown example, these values were $k_{rA} = 400{\cdot}1.01$, $k_a = 2{\cdot}1.38$, $k_{ba} = 400{\cdot}0.95$, $k_B = 2{\cdot}1.15$, $k_{bB} = 30{\cdot}0.54$, $k_b = 2.8{\cdot}0.96$, $k_M = 0.3 \cdot 1.36$, $k_{ab} = 0.5 \cdot 30 \cdot 0.59$, $k_R = 0.1 \cdot 1.49$, $k_{bR} = 1.5 \cdot 0.75$, $k_r = 0.4 \cdot 0.98$, $k_X = 20 \cdot 1.16$, and $k_x = 3 \cdot 0.61$. Here, the deterministic switching regimes shift only slightly in the space of signal amplitude and duration, but the sensitivity to noise becomes significantly stronger. However, the qualitative behavior remains the same as in Fig. 2.3 of the main text, with alternating bands and solid regions that show robust deterministic switching as long as the signal amplitude and duration exceed a threshold.

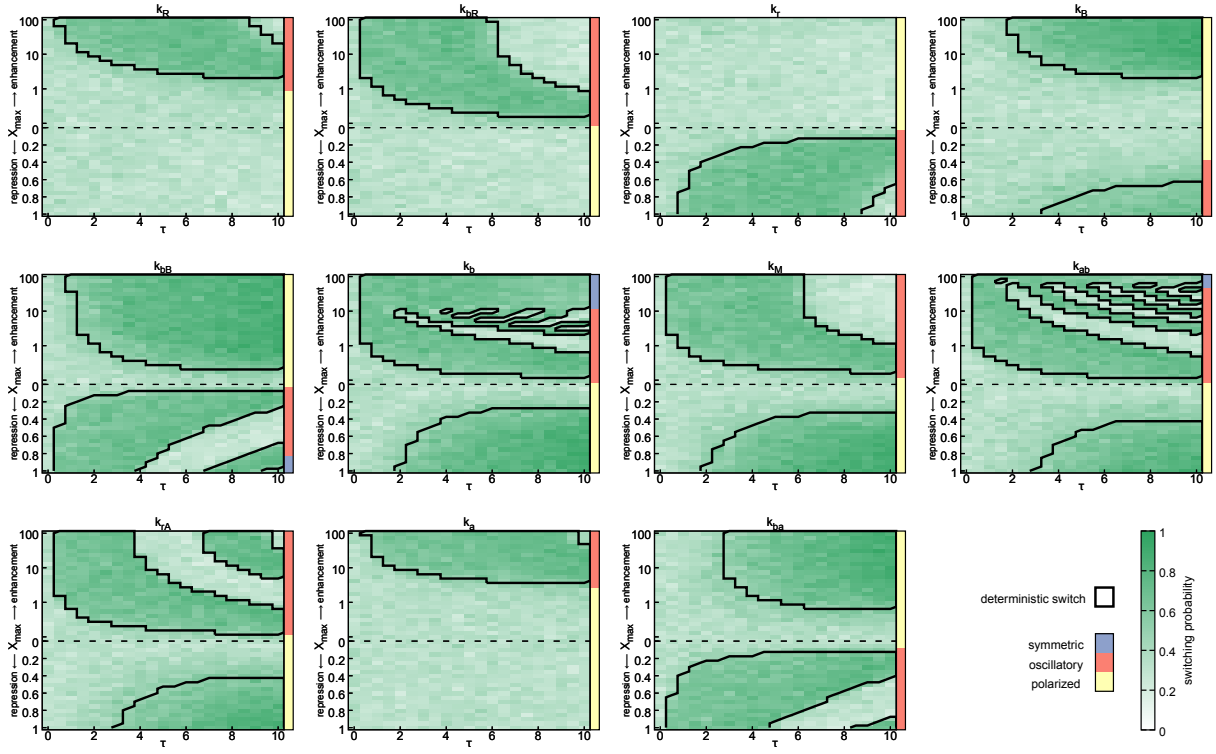

Figure 2.11 | Switching regimes, with the signal acting on each of the model parameters as in Fig. 2.3 of the main text, but with a different basal parameter set that was randomly chosen (by multiplying each of the original basal parameter values by a random number between 0.5 and 1.5). In the shown example, these values were $k_{rA} = 400 \cdot 1.1$, $k_a = 2 \cdot 0.58$, $k_{ba} = 400 \cdot 1.38$, $k_B = 2 \cdot 0.81$, $k_{bB} = 30 \cdot 1.31$, $k_b = 2.8 \cdot 0.69$, $k_M = 0.3 \cdot 1.02$, $k_{ab} = 0.5 \cdot 30 \cdot 1.04$, $k_R = 0.1 \cdot 1.37$, $k_{bR} = 1.5 \cdot 1.05$, $k_r = 0.4 \cdot 1.46$, $k_X = 20 \cdot 1.08$, and $k_x = 3 \cdot 1.35$. Here, the deterministic switching regimes shift significantly in the space of signal amplitude and duration, and the sensitivity to noise becomes significantly weaker. However, the qualitative behavior remains the same as in Fig. 2.3 of the main text, with alternating bands and solid regions that show robust deterministic switching as long as the signal amplitude and duration exceed a threshold.

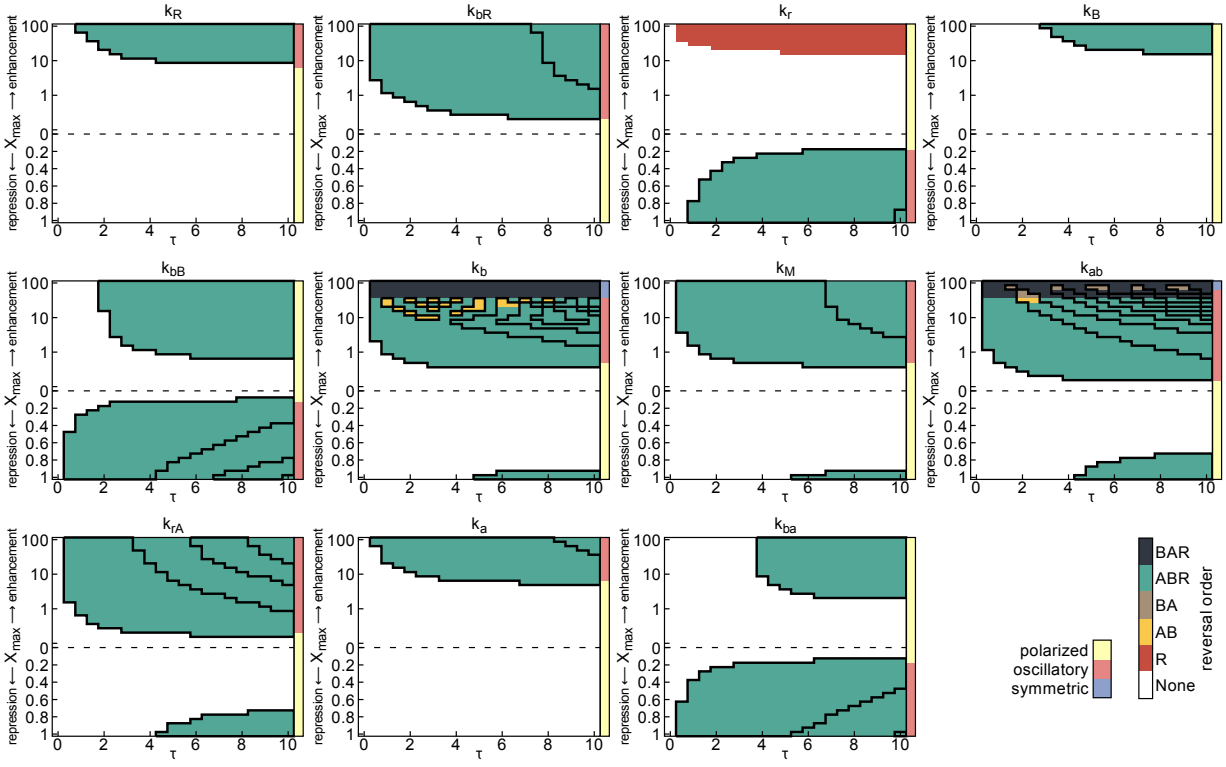

Figure 2.12 | Order of switching. Switching trajectories are obtained from the deterministic model. Black solid lines in the phase diagrams show switching regimes as in Fig. 2.3. The colors indicate in which order A, B and R switch polarity. In the regimes where the system switches polarity multiple times (due to the transient oscillator switch), the switching order represents the order of the first switch.

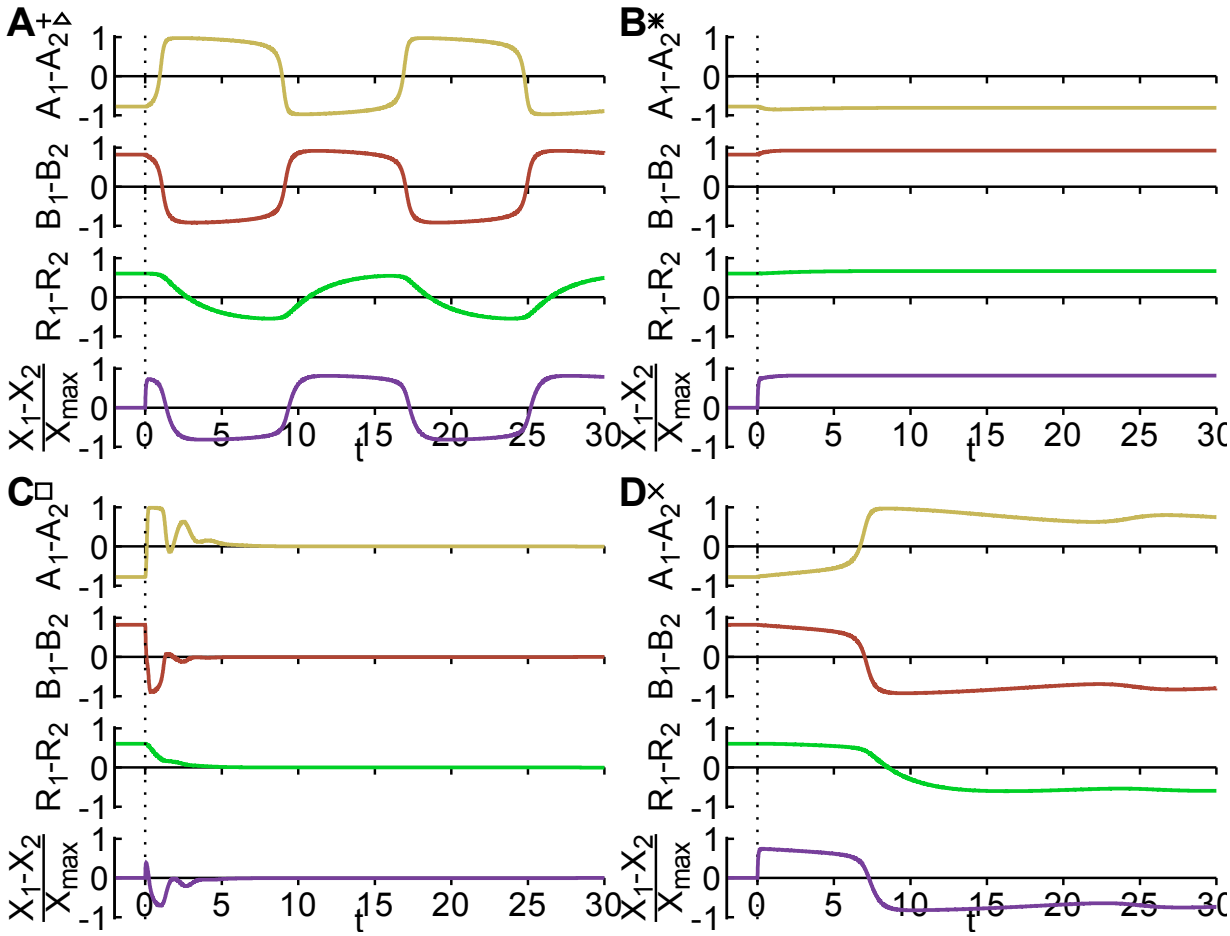

Figure 2.13 | Trajectories of the system during the signal for **A** the transient oscillator switch, **B** the prime-release switch, **C** the Reset switch and **D** the push switch. The symbols next to the panel labels indicate the signal parameter $X_{\max}$ as indicated in Fig. 2.3. The signal is applied for the duration of the simulation. During the transient oscillator switch (**A**) the polarity of the system oscillates, while during the reset switch (**C**) there is no polarity, i.e. the distribution of the proteins at pole 1 and pole 2 is symmetric. During the prime-release and push switch (**B** and **D**) the system is polarized during the switch.

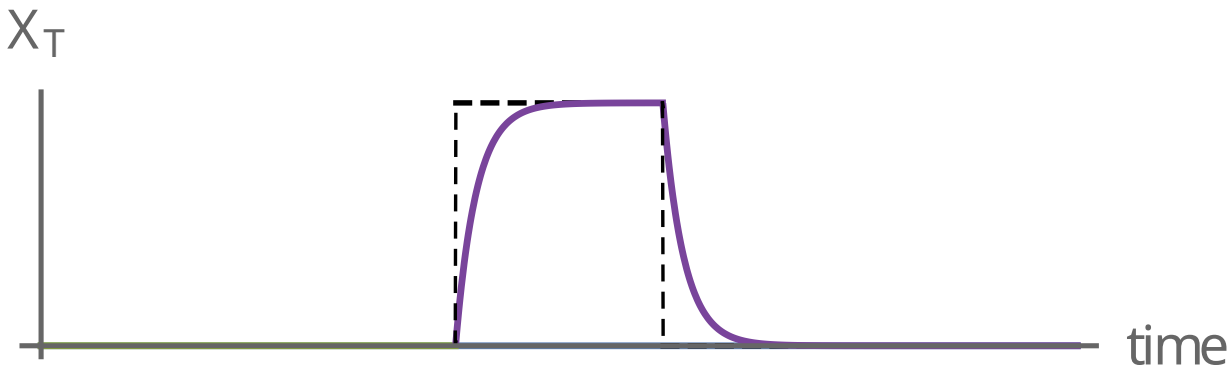

Figure 2.14 | Example of a gradually increasing and decreasing signal. The total amount of X, X_t, increases according to $X_t(t) = X_{\max}(1 - e^{-\lambda t})$ for $0 < t < \tau$ and decreases according to $X_t(t) = X_{\max}(1 - e^{-\lambda\tau})e^{-\lambda(t-\tau)}$ for $t > \tau$. The dashed line indicates the step-like signal.

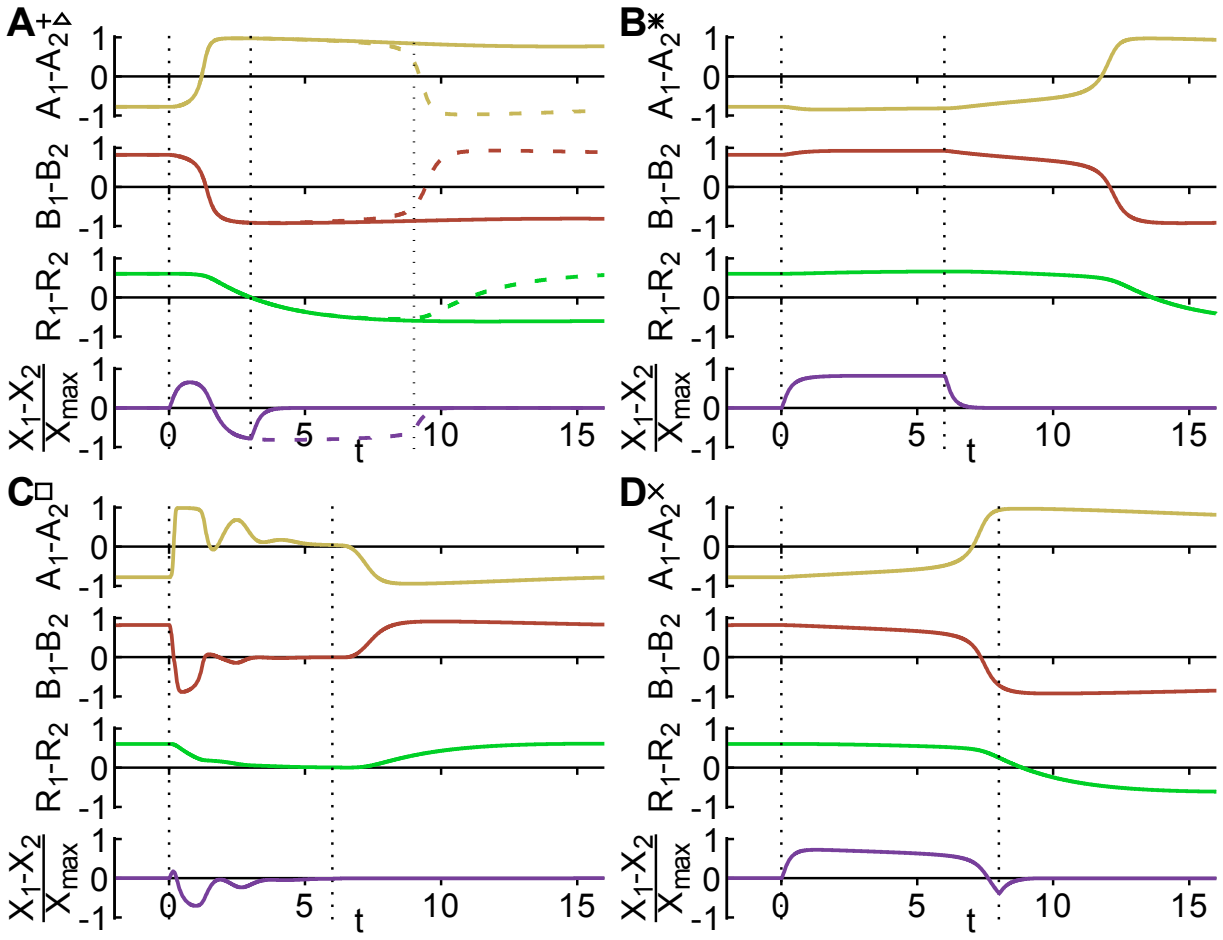

Figure 2.15 | Trajectories for a gradually increasing and decreasing signal with $\lambda = 4$. Signal amplitude $X_{\max}$ and duration τ are chosen the same as in Fig. 2.4, where in **A** the solid line corresponds to the short signal (plus-symbol) and the dashed line to the long signal (open triangle). The system shows qualitatively the same behavior as for the step-like signal.

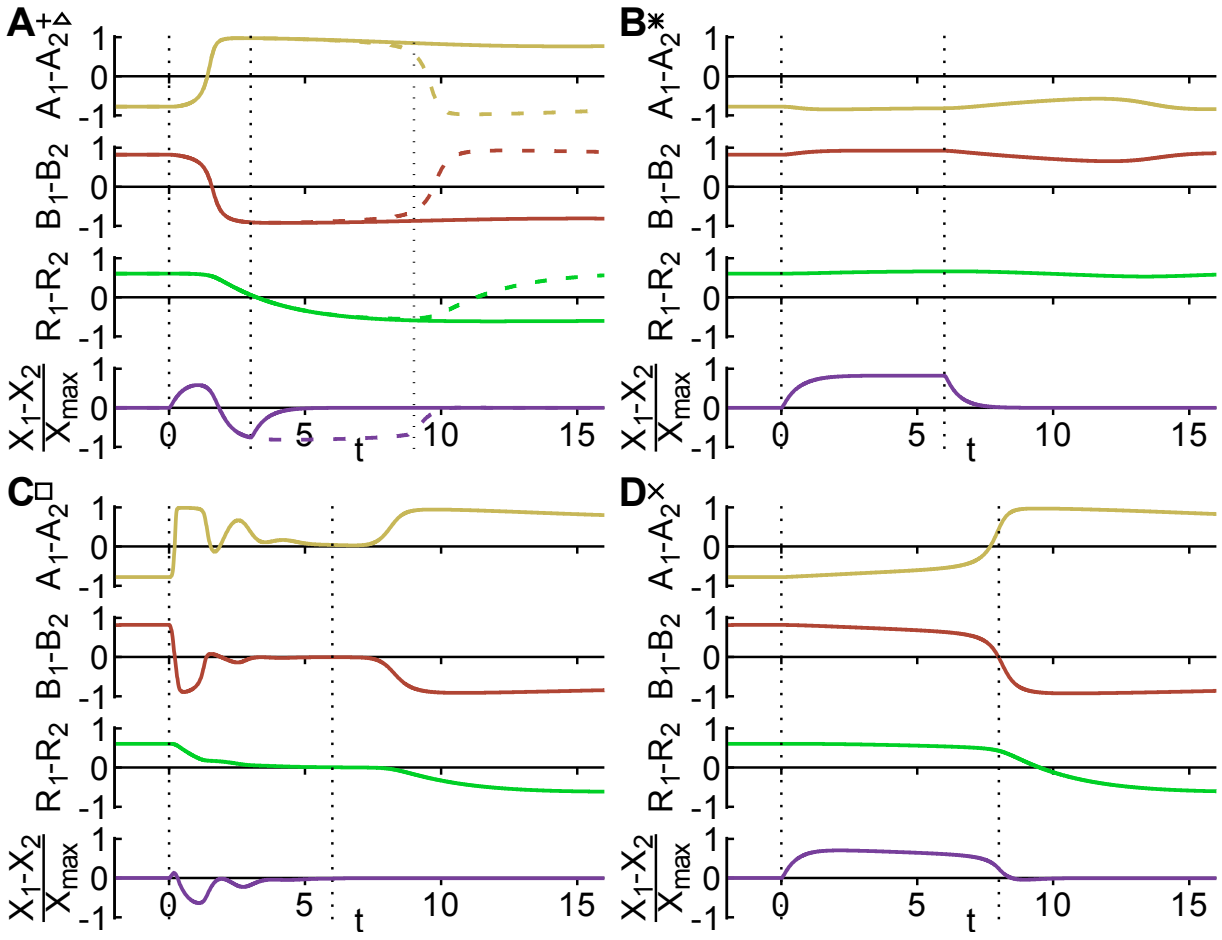

Figure 2.16 | Trajectories for a gradually increasing and decreasing signal with $\lambda = 2$. Signal amplitude $X_{\max}$ and duration τ are chosen the same as in Fig. 2.4, where in **A** the solid line corresponds to the short signal (plus-symbol) and the dashed line to the long signal (open triangle). For these gradual signals, the transient oscillator switch (**A**), the reset switch (**C**) and the push switch (**D**) switch qualitatively the same as for a step-like signal, while the prime-release switch (**B**) does not respond to the gradual signal.

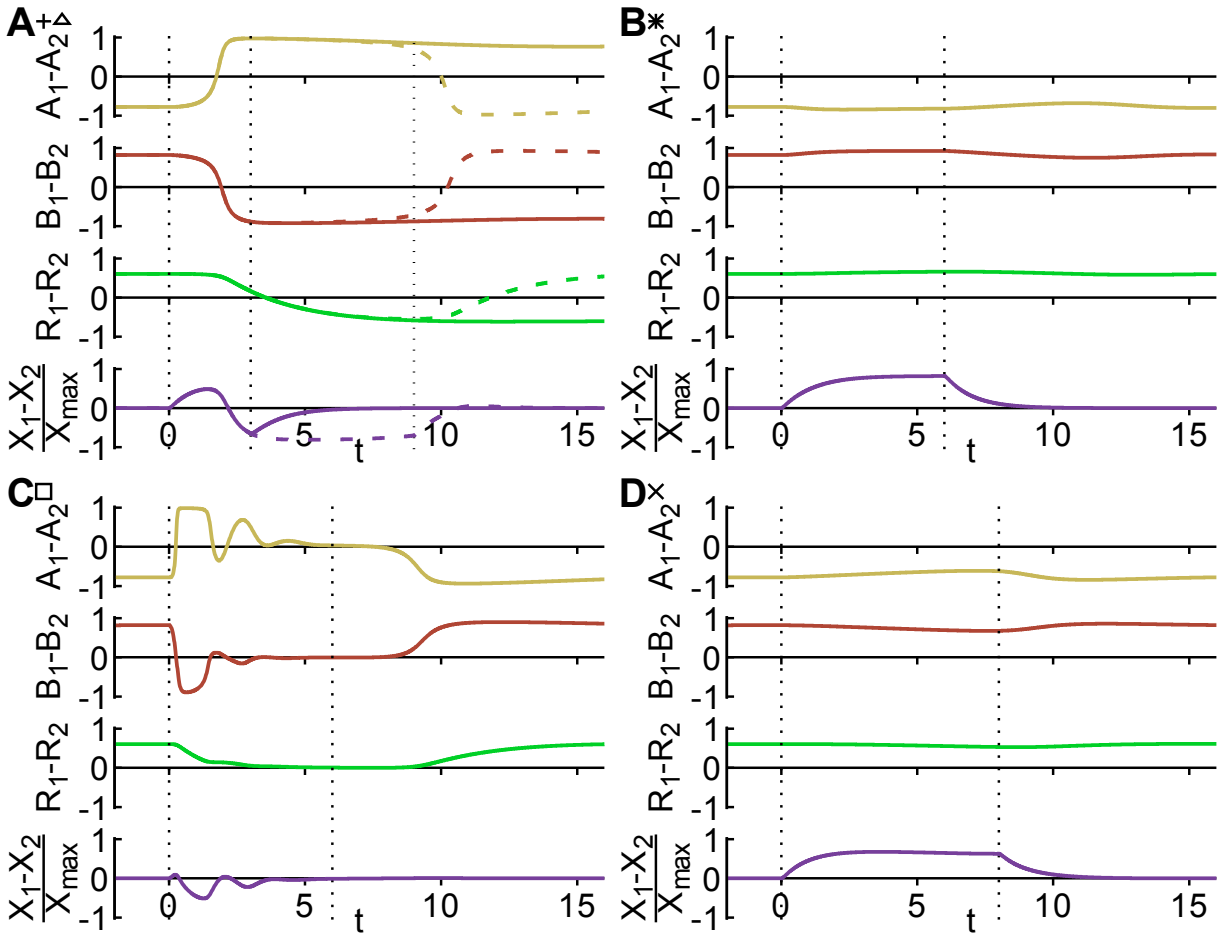

Figure 2.17 | Trajectories for a gradually increasing and decreasing signal with $\lambda = 1$. For these gradual signals, the prime-release (**B**) and push switch (**D**) do not respond to the signal, while the transient oscillator (**A**) and reset switch (**C**) do.

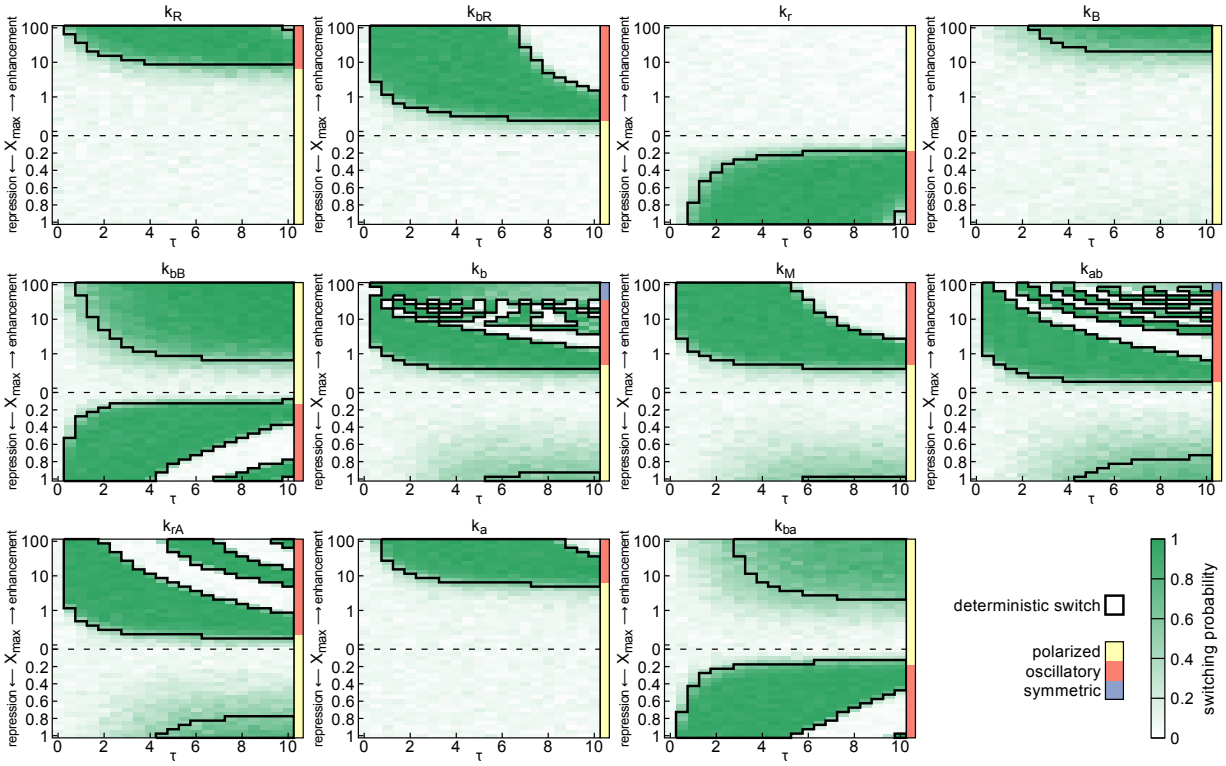

Figure 2.18 | Switching regimes for a gradually increasing and decreasing signal with $\lambda = 4$. Regions in which the deterministic model shows switches are indicated by thick black outlines. The green shading shows the switching probability of the stochastic model with $N = 10^3.75$. The upper half of the phase diagram shows results for a signal that enhances the reaction rate, and the lower half for a repression of the rate. The colored bars to the right of each panel indicate the class of dynamics when the corresponding amplitude of signal is applied, with yellow for polarized, orange for oscillatory and blue for symmetric polar distribution of A, for a gradually increasing and decreasing signal. The switching regimes are similar to the regimes for a step-like signal as shown in Fig. 2.3.

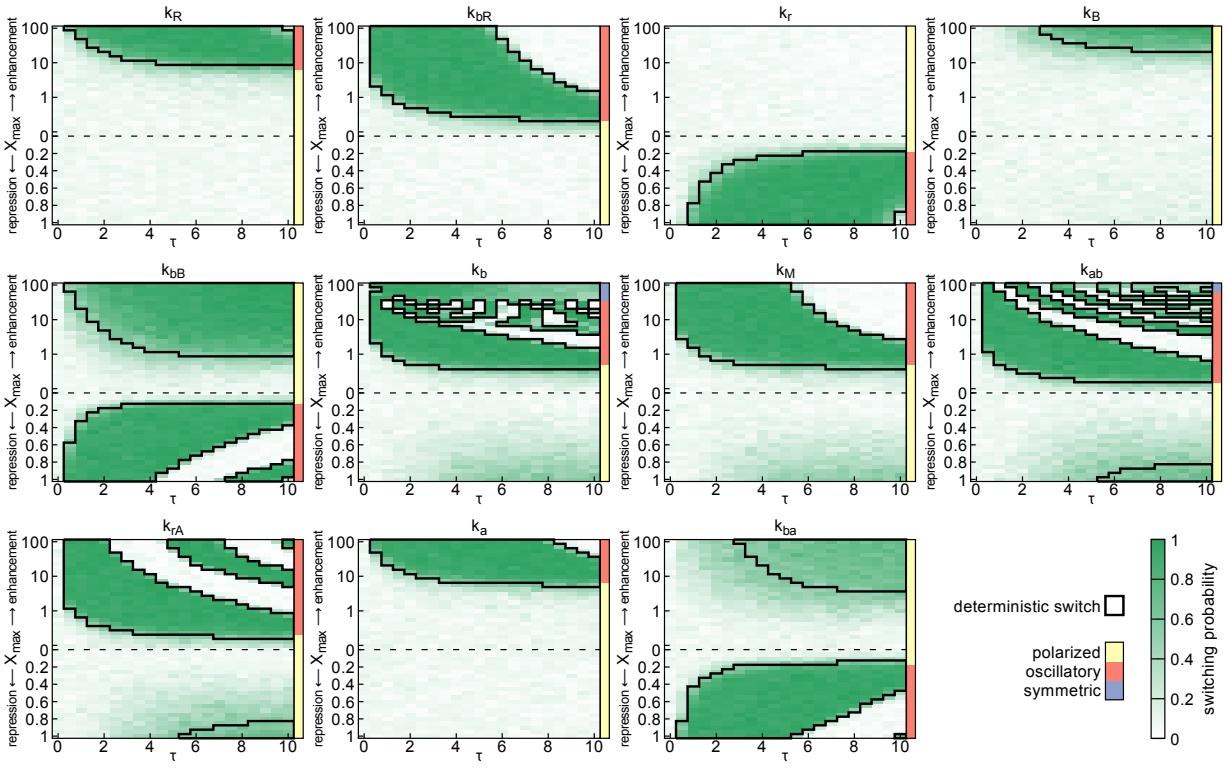

Figure 2.19 | Switching regimes for each of the model parameters for a gradually increasing and decreasing signal with $\lambda = 2$. The regimes where the prime-release switch acts to switch the polarity, for example via repression of the parameter k_{ab} or k_{rA}, have become smaller.

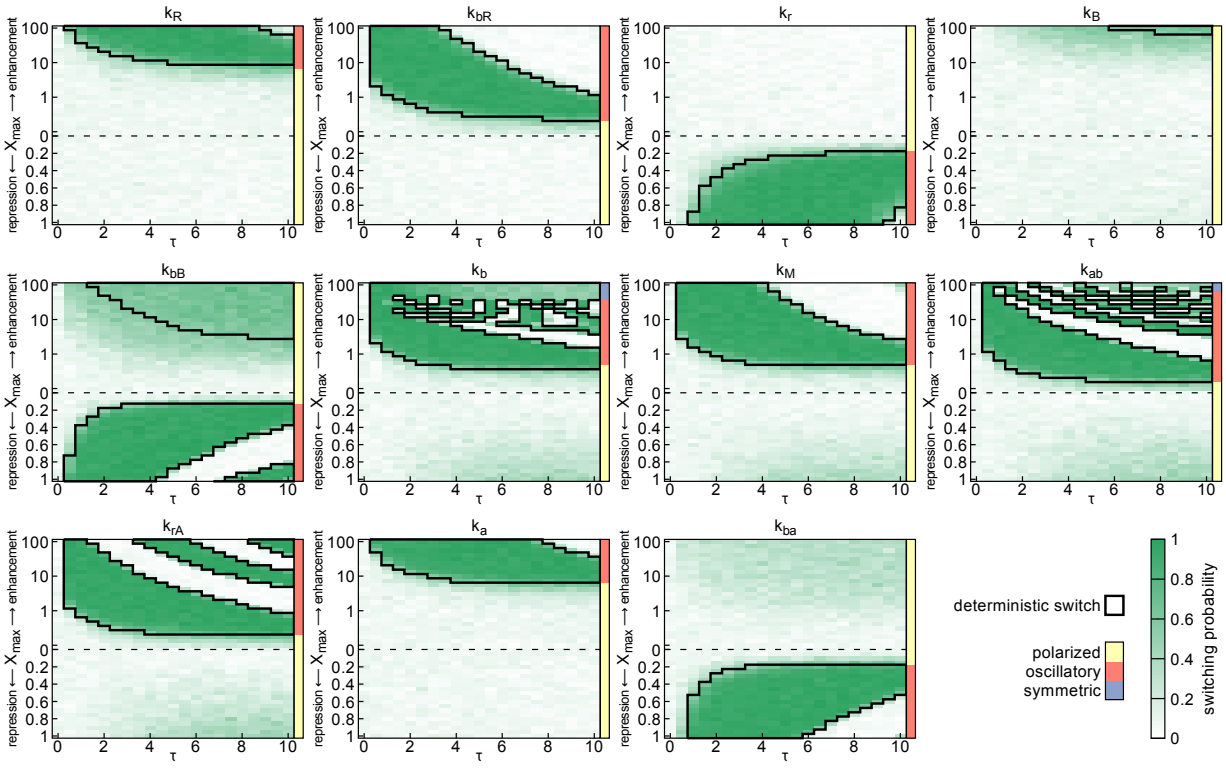

Figure 2.20 | Switching regimes for each of the model parameters for a gradually increasing and decreasing signal with $\lambda = 1$. The regimes where the prime-release switch acts to switch the polarity becomes smaller, for example by enhancing k_B, or completely vanishes, for example via repression of the parameters k_{ab} or k_{rA}. In addition, the regimes where the push switch acts vanishes, for example via a slight enhancement of the parameter k_{rA}.

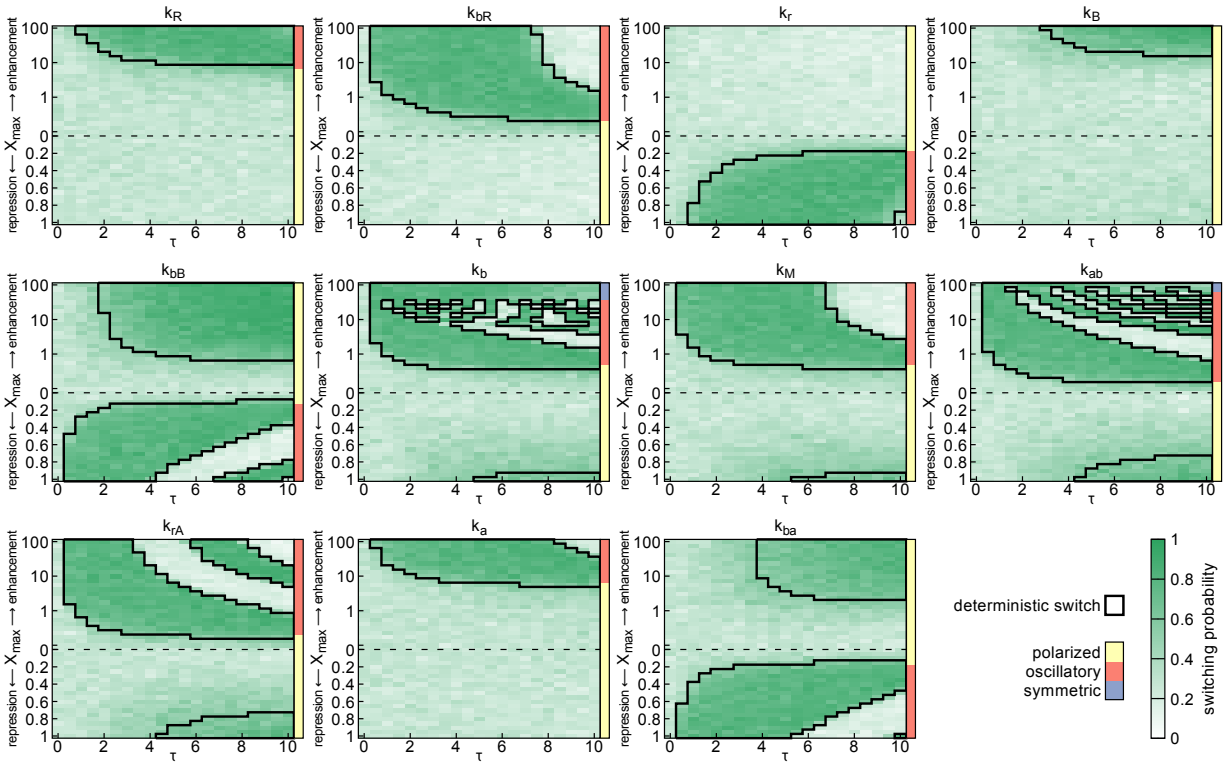

Figure 2.21 | Switching regimes for each of the model parameters with a step-like increasing and decreasing signal. The green shading shows the switching probability of the stochastic model with $N = 10^{3.5}$. The stochastic switching probability, outside of the deterministic switching regimes (solid black lines), is higher as compared to a noise level of $N = 10^{3.75}$ as shown in Fig. 2.3, while the switching probability in the deterministic regimes is smaller.

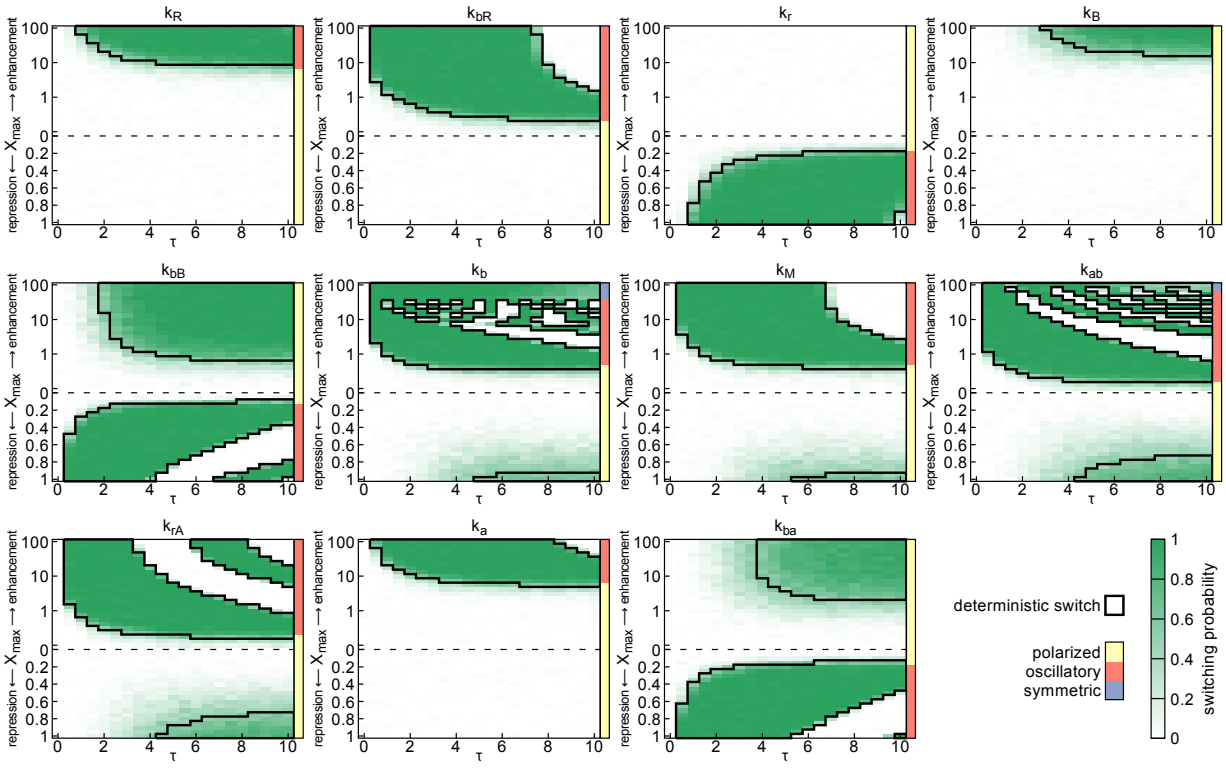

Figure 2.22 | Switching regimes for each of the model parameters with a step-like increasing and decreasing signal. The green shading shows the switching probability of the stochastic model with $N = 10^4$. The stochastic switching probability, outside of the deterministic switching regimes (solid black lines), is smaller as compared to a noise level of $N = 10^{3.75}$ as shown in Fig. 2.3, while the switching probability in the deterministic regimes is higher.

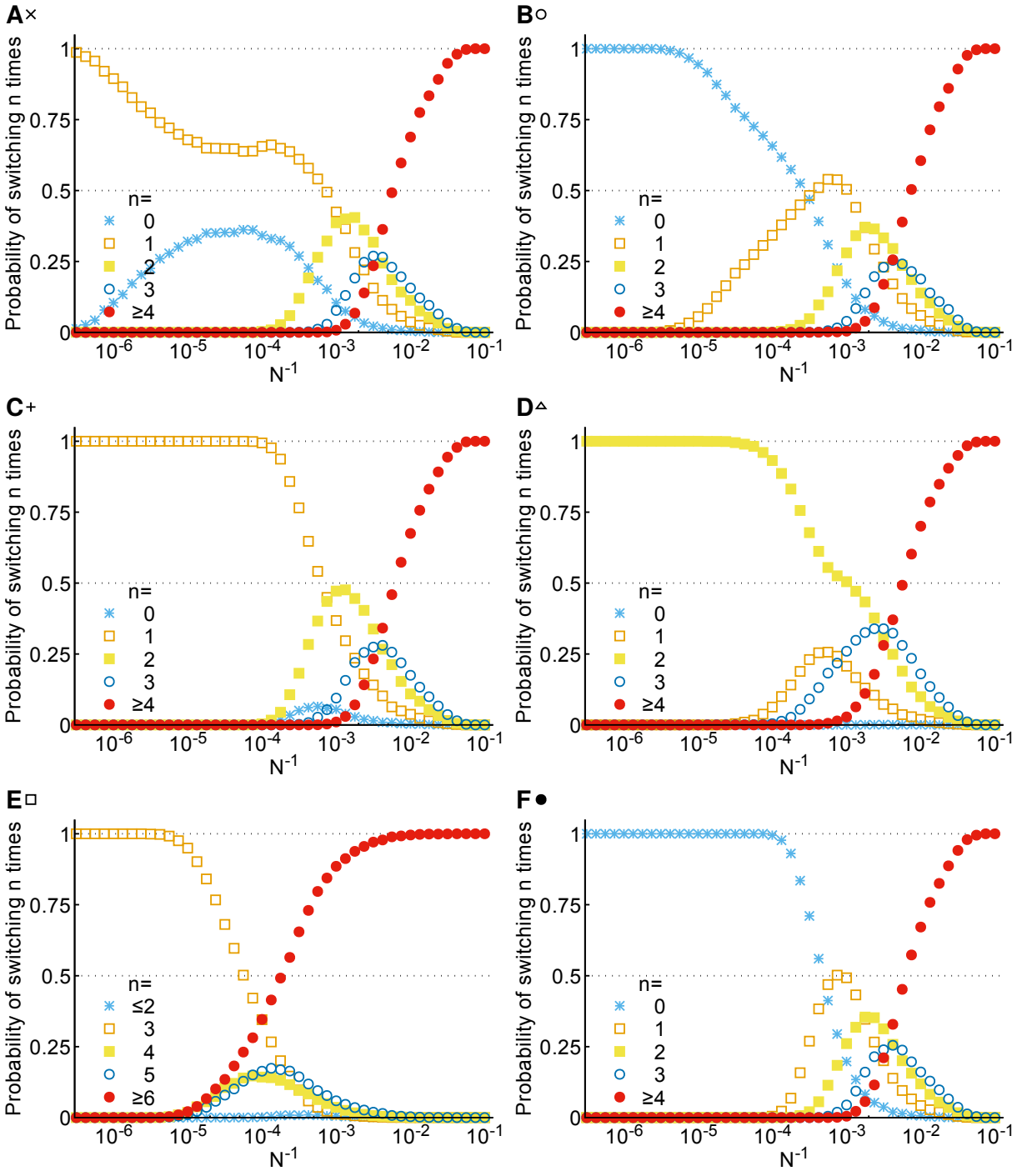

Figure 2.23 | Probability of different numbers of switching for different noise levels. Symbols next to the panel labels **A-E** correspond to the signal amplitude and duration as shown in Fig. 2.3. **F** shown the probability of different numbers of switches without a signal.

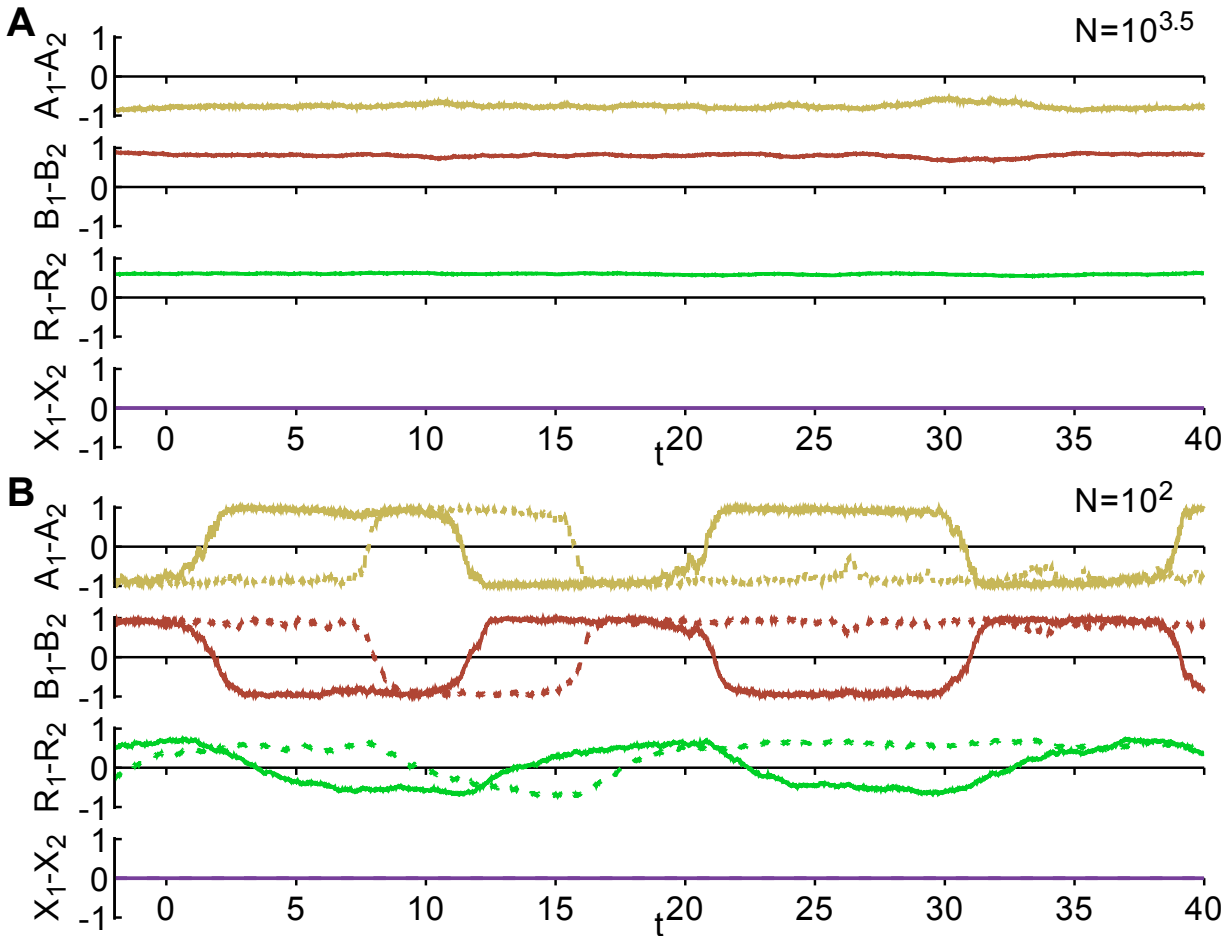

Figure 2.24 | Polarity switching of the stochastic model without a signal. **A** for low noise levels ($N = 10^{3.5}$) the system does not switch for the duration of the simulation. **B** for high noise levels ($N = 10^2$) the polarity switches several times without applying a signal.

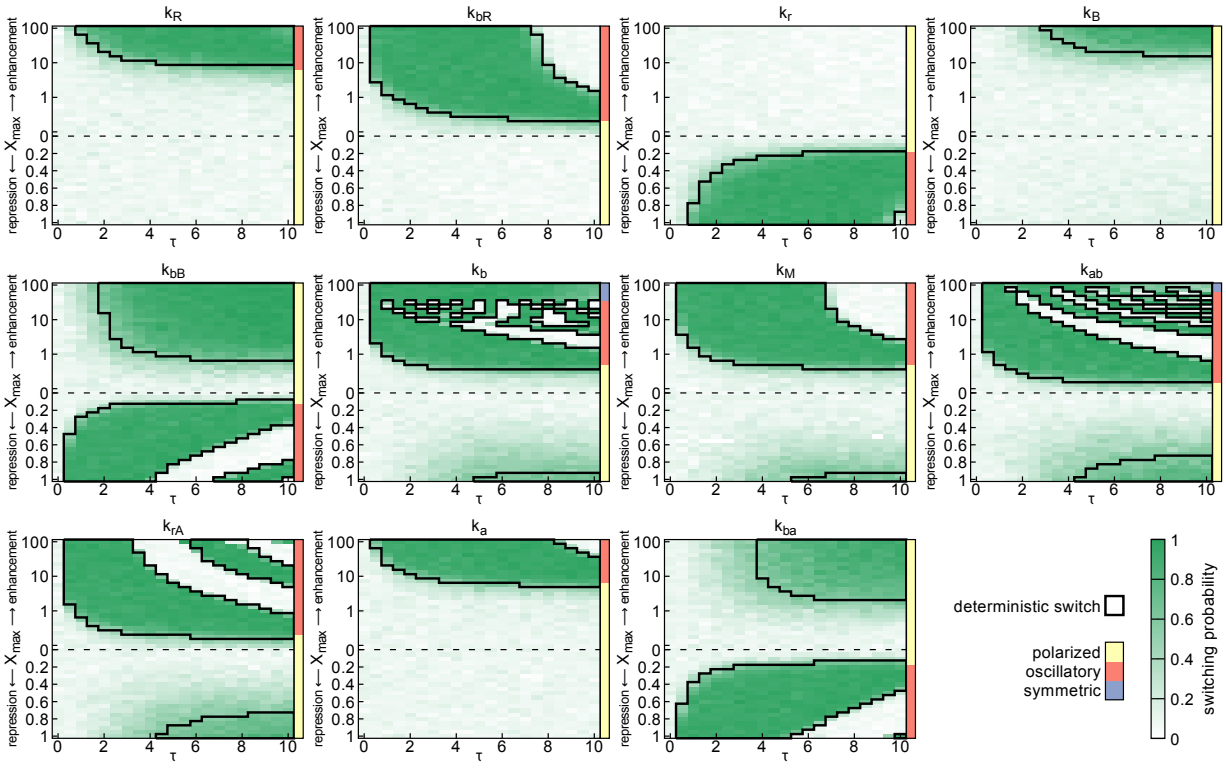

Figure 2.25 | Switching regimes for each of the model parameters with a step-like increasing and decreasing signal. The green shading shows the switching probability of the stochastic model with white noise and with $N = 10^4$. The switching regimes are qualitatively similar to the switching regimes in Fig. 2.3.

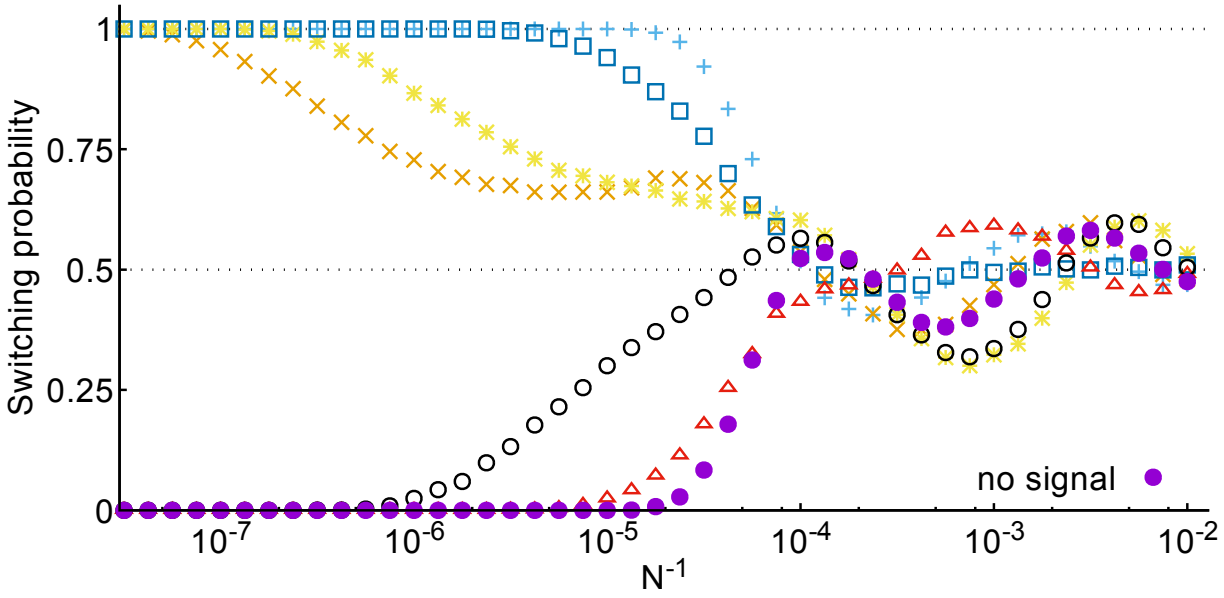

Figure 2.26 | Switching probability of the stochastic model with white noise. The signal parameters are indicated by the corresponding symbols in Figs. 2.3 and 2.4. Results are qualitatively similar to the results presented in Fig. 2.7A.

3 Finding a threshold in a shallow gradient

"You don't need fancy sneakers
to run fast."
– Jon Bon Jovi

Living cells rely on the precise interplay of several biological tasks, such as cell growth, cell motility, DNA segregation, and cell division. These processes are regulated in space and time by the precise spatiotemporal distribution of proteins that can transmit signals, direct cell motility and exert forces. To transmit spatiotemporal signals, such protein pattern acts as computational units that convert one protein pattern into another. In this chapter we demonstrate a mechanism by which a protein can measure a threshold concentration in a shallow concentration gradient.

This chapter is based on Section 3 in the Supplementary Information of our paper "A hierarchy of protein patterns robustly decodes cell shape information", which has been published in Nature Physics [143]. This work has been performed together with Tzer Han Tan, Fridtjof Brauns, Jinghui Liu, S. Zachary Swartz, Erwin Frey, and Nikta Fakhri

So far we have discussed how a temporal signal can be processed by polarity proteins. Next, we will focus on how proteins process spatial information. In this chapter we demonstrate how a protein can measure a threshold concentration in a shallow concentration gradient of another protein. We explain this mechanism using the propagating Ect2 front in starfish oocytes as a model system.

In starfish oocytes, it has been observed that a cytosolic gradient of the cell cycle regulator Cdk1, that is set up during meiosis and degraded during anaphase I, guides the propagation of a Rho pulse, thereby inducing a surface contraction wave (SCW) (Fig. 6.1a-c and 6.1l) [144]. We show in chapter 6 that the RhoGEF Ect2 forms a front-like pattern, that follows a threshold value of the Cdk1 concentration and localizes the Rho pulse to the front edge. In this chapter, we first recap the literature to motivate why Ect2 is a good candidate link between Cdk1 and Rho and review the interactions between Cdk1 and Ect2. Next, in Sec. 3.2, we motivate an effective reaction–diffusion model based on these interactions that exhibits bistability and therefore propagating fronts. In Sec. 3.3 we discuss how an Ect2 front can be initiated in the starfish oocyte. Finally, in Sec. 3.4, we discuss how the Cdk1 gradient guides the propagation of the Ect2 front as the gradient degrades.

3.1 Review of Ect2 reaction kinetics

It has been observed that Cdk1 inhibition induces Ect2-mediated Rho excitability on starfish oocyte membrane [145], suggesting that Ect2 is the protein that connects cell cycle regulation to Rho signaling. In fact, Ect2 is a RhoGEF that plays an important role in the formation of the cytokinetic ring by recruiting and activating Rho [146]. This activation step requires both Ect2 membrane binding as well as its catalytic activity [147]. Like most RhoGEFs, Ect2 has a DBL homology (DH) domain that is responsible for the guanine nucleotide exchange catalytic activity and a pleckstrin homology (PH) domain that is responsible for membrane binding activity [147, 148]. The binding and catalytic activities are regulated through multiple phosphorylation sites and different phosphorylation sites have different effects. For instance, in human cell lines, Ect2 phosphorylation by Cdk1 has been suggested to inhibit its membrane association ability [149]. This is consistent with the observation that Cdk1 inhibits Ect2-mediated excitability in starfish oocytes. Other phosphorylation sites, such as T412, are responsible for catalytic activity of Ect2 [150]. Although this would suggest that Cdk1 would be a very likely candidate to promote Ect2 activity, we note that other GEFs could be involved in the Cdk1-Rho interactions. For instance, another RhoGEF, GEF-H1, has been shown to have its catalytic activity inhibited by Cdk1 phosphorylation [151], which potentially could also play a role in the starfish oocyte.

In general, regulatory proteins of phosphorylation dynamics could feedback on one another and form a complex interaction network. While not much is known about the relevant

phosphatases that dephosphorylate Ect2, some common feedback motifs in the regulation of cell cycle kinases and phosphatases can give rise to bistable switches [124].

3.2 Model Description

To elucidate the mechanism by which the Ect2 front is guided by the Cdk1 gradient we aim to find a minimal model that integrates the available biochemical information and exhibits propagating fronts. We propose a model in which Ect2 can diffuse on the surface of a three-dimensional ellipsoidal, triangular or star geometry, representing the membrane and the cytosol close to the membrane. We assume that Ect2 cycles between an inactive phosphorylated (concentration $u_{Ep}(\vec{r},t)$) and an active non-phosphorylated state ($u_E(\vec{r},t)$) in the cytosol, and that the active non-phosphorylated state of Ect2 can bind to and detach from the membrane ($u_e(\vec{r},t)$). To describe the dynamics of Ect2, we use a reaction–diffusion model

$$\partial_t u_{\mathrm{E}} = D_{\mathrm{c}}\nabla^2 u_{\mathrm{E}} + f_{\mathrm{E}}(u_{\mathrm{E}}, u_{\mathrm{Ep}}, u_{\mathrm{e}}), \tag{3.1}$$
$$\partial_t u_{\mathrm{Ep}} = D_{\mathrm{c}}\nabla^2 u_{\mathrm{Ep}} + f_{\mathrm{Ep}}(u_{\mathrm{E}}, u_{\mathrm{Ep}}, u_{\mathrm{e}}), \tag{3.2}$$
$$\partial_t u_{\mathrm{e}} = D_{\mathrm{m}}\nabla^2 u_{\mathrm{e}} + f_{\mathrm{e}}(u_{\mathrm{E}}, u_{\mathrm{Ep}}, u_{\mathrm{e}}). \tag{3.3}$$

The diffusion constants are chosen such that the cytosolic components diffuse much faster than the membrane component ($D_c \gg D_m$). Motivated by the observation that Ect2 forms a front pattern on the membrane (Fig. 6.2d), we propose a model that exhibits bistability with the following reaction kinetics, as illustrated in Fig. 3.1:

$$f_{\mathrm{E}} = -\frac{k_{[\mathrm{Cdk1}]}u_{\mathrm{E}}}{K_{\mathrm{p}} + u_{\mathrm{E}}} + (k_{\mathrm{dp}} + k_{\mathrm{fb}}u_{\mathrm{E}})u_{\mathrm{Ep}}, \tag{3.4}$$
$$f_{\mathrm{Ep}} = \frac{k_{[\mathrm{Cdk1}]}u_{\mathrm{E}}}{K_{\mathrm{p}} + u_{\mathrm{E}}} - (k_{\mathrm{dp}} + k_{\mathrm{fb}}u_{\mathrm{E}})u_{\mathrm{Ep}}, \tag{3.5}$$
$$f_{\mathrm{e}} = k_{\mathrm{on}}u_{\mathrm{E}} - k_{\mathrm{off}}u_{\mathrm{e}}. \tag{3.6}$$

These reaction kinetics conserve total protein mass, such that $\int_0^L d\vec{r}\, u_{\mathrm{E}} + u_{\mathrm{Ep}} + u_{\mathrm{e}} = n_{\mathrm{E}}$ remains constant. The active Ect2 conformation can attach to and detach from the membrane with the rates k_{on} and k_{off}, respectively, as shown in Fig. 3.1. In the cytosol, Ect2 can get phosphorylated enzymatically with a rate $k_{[\mathrm{Cdk1}]}$, which we describe by Michaelis-Menten kinetics with a Michaelis-Menten constant K_{p}. Furthermore, Ect2 can get dephosphorylated with a rate k_{dp}. As bistability typically arises from feedback loops in the reaction kinetics, we include a feedback loop such that active Ect2 enhances its own activation with a rate k_{fb}.

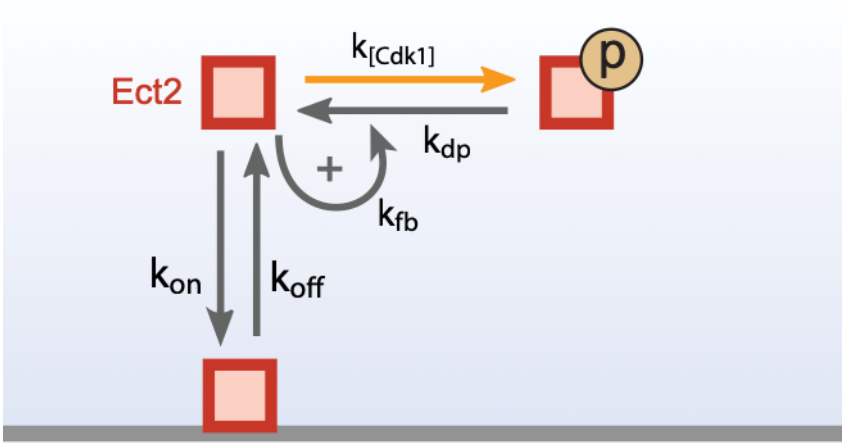

Figure 3.1 | Model schematic of the reaction kinetics for Ect2. Ect2 can bind and detach from the membrane with rates k_{on} and k_{off}, respectively. Cytosolic Ect2 can get phosphorylated with the Cdk1-dependent phosphorylation rate $k_{[\text{Cdk1}]}$, which prevents Ect2 from binding to the membrane. Furthermore, Ect2 can get dephosphorylated with a rate k_{dp}, and enhances its own dephosphorylation (activation) with a rate k_{fb}.

In the starfish oocytes, the surface contraction waves are triggered after nuclear envelope breakdown (NEBD). Upon NEBD, Cdk1 gets released from the nucleus and forms a gradient in the cytosol that gets degraded by APC/C [144]. Thus, initially the Cdk1 concentration is high and slowly decreases while maintaining a spatially non-uniform concentration profile [144, 152]. We assume that the phosphorylation rate of Ect2, $k_{[\text{Cdk1}]}$, depends on the Cdk1 concentration [149], such that the rate depends on space and time. For simplicity, we emulate this spatiotemporally varying phosphorylation rate using a decaying linear gradient

$$k_{[\text{Cdk1}]}(|\vec{r}|, t) = (c_0 - a|\vec{r}|)(1 - t/(\gamma + t)). \tag{3.7}$$

Here, γ is the Cdk1 half-life and c_0 and a are the maximum and slope of the gradient, respectively.

In order to find parameters for which the model exhibits bistability, we first only analyze the reaction kinetics of the model. This means that we consider the system to be well-mixed, with a uniform phosphorylation rate $k_{[\text{Cdk1}]}$ and numerically solve for the steady states. Indeed, we find that the model exhibits bistability for a broad parameter regime, with a stable steady state with a high Ect2 concentration on the membrane and a stable steady state with a low Ect2 concentration on the membrane (solid black dots in the purple shaded area in Fig. 3.2). By varying the Cdk1-dependent phosphorylation rate, we find that

Parameter	Value	Unit	Description
k_{on}	0.5	s^{-1}	Ect2 membrane attachment
k_{off}	5	s^{-1}	Ect2 membrane detachment
$k_{[\text{Cdk1}]}$	0-150	$\mu m^{-2} s^{-1}$	Phosphorylation rate
k_{dp}	2.5	s^{-1}	Dephosphorylation rate
k_{fb}	0.5	$\mu m^2/s$	Autocatalytic dephosphorylation rate
K_{p}	0.1	μm^{-2}	Phosphorylation saturation constant
n_{Ect2}	14.67	μm^{-2}	Ect2 total concentration
D_{c}	10	$\mu m^2/s$	Diffusion constant in cytosol
D_{m}	0.5	$\mu m^2/s$	Diffusion constant membrane
γ	100	s	Cdk1 half-life
c_0	750	μm^{-3}	Maximum Cdk1 concentration
a	3.6	μm^{-4}	Initial Cdk1 slope

Table 3.1 | Parameters Ect2 model. Parameters are chosen such that the model exhibits bistability for a range of phosphorylation rates (Cdk1 concentrations), and such that the front speed matches the experimentally observed wave speed.

the system transitions from a bistable regime (low phosphorylation rate) to a monostable regime (high phosphorylation rate) (purple and green shaded areas in Fig. 3.2).

3.3 Initial front formation

Traveling front-like concentration profiles are a generic phenomenon in bistable media [153]. The front corresponds to an interface connecting spatial regions where the concentrations are in either of the two (locally) stable steady states (fixed points), respectively. For propagating fronts to arise from a spatially homogeneous steady state, a strong enough stimulus is needed.

Consider a system with a spatially homogeneous distribution of Cdk1 (middle panel Fig. 3.3A), with a concentration that lies within the bistable regime (upper panel Fig. 3.3A). In addition, we consider that the initial Ect2 concentration is also spatially homogeneous (say at the low-Ect2 fixed point). For the front to form there needs to be a sufficiently strong local perturbation such that locally the Ect2 concentration relaxes toward the high-Ect2 fixed point (lower panel Fig. 3.3A), i.e. locally the Ect2 concentration enters the basin of attraction of the high-Ect2 fixed point. In the absence of such a perturbation the system remains in the respective spatially homogeneous steady state.

How does this picture change for a starfish oocyte where Cdk1 forms a cytosolic gradient (middle panel Fig. 3.3B)? Then, the phosphorylation rate is different at each position along the membrane (upper panel Fig. 3.3B). Thus, at each position in space the number, value, and nature of fixed points for the Ect2 concentration on the membrane can differ. Consider

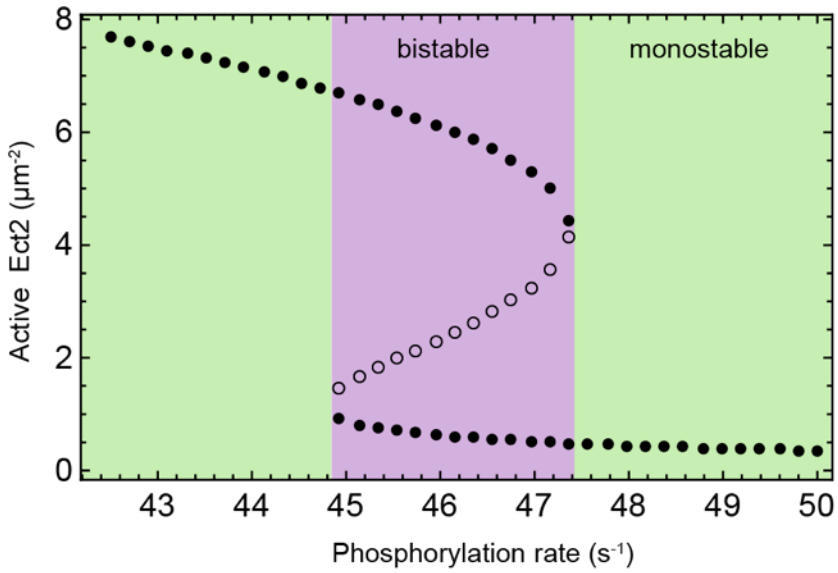

Figure 3.2 | Bifurcation diagram for increasing (Cdk1-dependent) phosphorylation rate. Solid black dots illustrate the stable steady states, open circles illustrate unstable steady states of the reaction kinetics. For an increasing phosphorylation rate, the system transitions from a monostable (green area) regime to a bistable (purple area) to a monostable (green area) regime. The parameters used are specified in Table 3.1.

a Cdk1 gradient for which the concentration range lies within the monostable regime (high Cdk1-dependent phosphorylation rates) (Fig. 3.2). As the Cdk1 gradient decays, the part of the system with the lowest Cdk1 concentration will become bistable first (upper panel Fig. 3.3B; see also Fig. 3.2). Such a gradient gives rise to a (nearly) uniform Ect2 concentration profile with a low Ect2 concentration on the membrane (lower panel Fig. 3.3B). However, to form a traveling front the system would need a large perturbation to get into the basin of attraction of the high-Ect2 fixed point. As the Cdk1 gradient further decays, the region where the Cdk1 concentration is lowest reaches a monostable regime with a fixed point with high active Ect2 concentration (upper and middle panel Fig. 3.3C). Consequently, the active Ect2 concentration in this region will relax to the high-concentration fixed point in the monostable regime, creating a front between the high- and low-Ect2 steady states (lower panel Fig. 3.3C). Thus, we expect the Ect2 front to start at the position where the Cdk1 concentration is lowest, which is consistent with our simulations in different geometries (movies S15-S17), and with the experimental observations (Fig. 6.1j-o, and Ref. [144]).

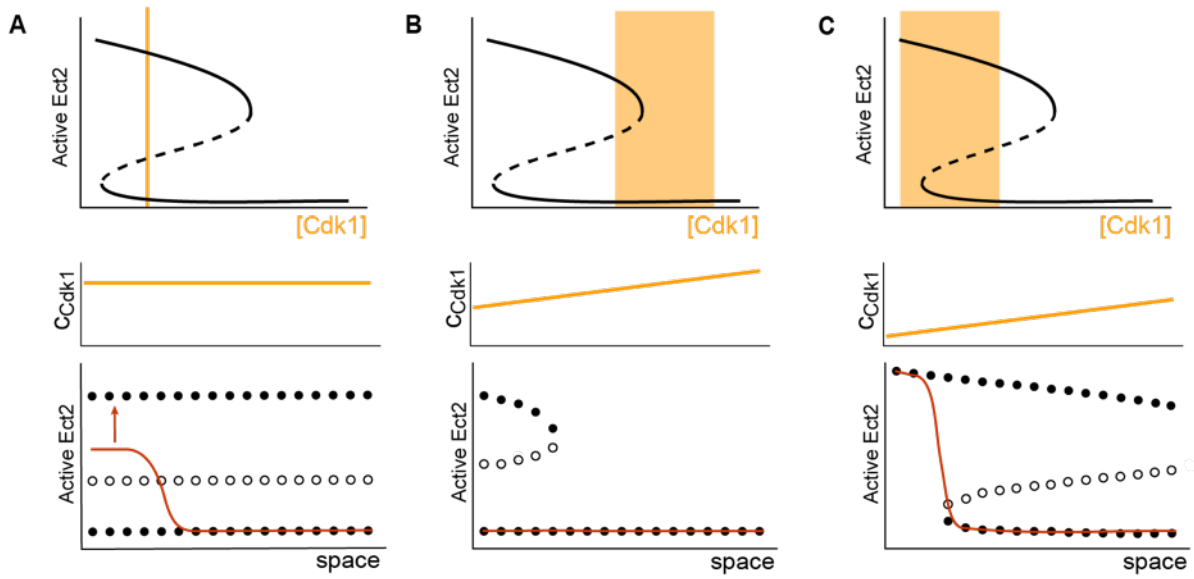

Figure 3.3 | Schematic of front initialization. Upper panels show a schematic of the bifurcation diagram. yellow area illustrates the Cdk1 concentration range. Solid lines indicate stable steady states, dashed lines illustrate unstable steady states. Middle panels show the Cdk1 distribution in space. Lower panels show the Ect2 concentration on the membrane. Red lines indicate the Ect2 concentration on the membrane. Solid black circles indicate the locally stable fixed points, open circles illustrate the locally unstable fixed points. **(A)** homogeneous Cdk1 concentration profile. The front starts due to a local perturbation. **(B)** Cdk1 gradient leads to different (number of) fixed points at different positions in space. **(C)** Cdk1 gradient with a lower concentration range. For lower Cdk1 concentrations the system is monostable, which leads to the formation of an Ect2 front.

3.4 Front propagation

Fronts in bistable media generically have a finite propagation velocity. The sign and magnitude of this velocity depend on the form of the reaction kinetics; see e.g. Refs. [153, 154]. Heuristically, a bistable front propagates because one of the steady states is 'more attractive', also called the dominant state [154], and invades the 'less attractive' steady state. Which steady state is more attractive depends on the reaction rates of the system. The speed at which the front propagates is given by the balance of the attraction strength of the two steady states [153].

In our case, the magnitude and sign of the front velocity therefore depends on the concentration of Cdk1. As a consequence, there is a threshold value $[\text{Cdk1}]^*$, for which the

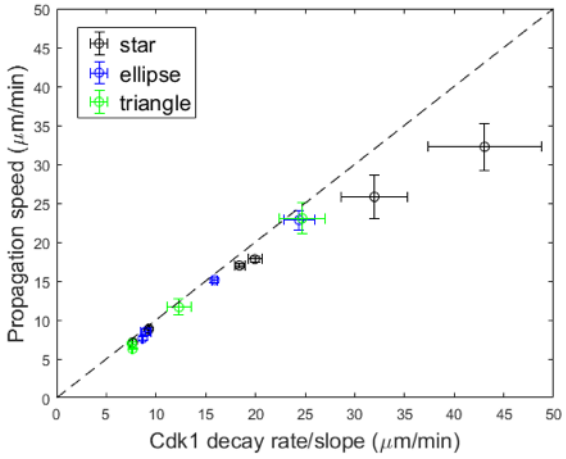

Figure 3.4 | Ect2 front follows the Cdk1 threshold value. Ect2 front speed, Cdk1 decay rate and Cdk1 slope at the Ect2 front is measured at various positions along the circumference of a cross section of the ellipsoidal, triangular and star shaped geometries.

front velocity is zero[1]. Hence, when the Cdk1 concentration in the cell is non-uniform, the relative dominance of the two states varies in different parts of the cell, and thereby also the velocity of the bistable front. If the Cdk1 gradient includes the threshold value $[\text{Cdk1}]^*$, the front will travel in the cell until it reaches that value and then stall there [91, 157], we call this position the pinning position. As the Cdk1 gradient decays, this threshold concentration moves in space, leading to subsequent Ect2 front propagation up to the new pinning position (Fig. 6.4). Thus, we expect that Ect2 follows the Cdk1 threshold concentration, as long as the Cdk1 gradient decays slower than the Ect2 front speed. To test this, we performed 3D simulations in ellipsoidal (movie S15), triangular (movie S16) and star-shaped (movie S17) geometries and measured the propagation of the Cdk1 threshold value from the decay rate and Cdk1 slope at the Ect2 front. Indeed, we find a positive correlation between and the Ect2 front propagation speed and the ratio of the Cdk1 decay rate to the Cdk1 slope (Fig. 3.4). In the model, we choose a Cdk1 half-life γ and gradient slope such that the speed of the Cdk1 threshold value corresponds to the observed speed of the surface contraction wave. In movies S15-S17, we initialize the system with all Ect2 starts in the phosphorylated conformation such that $u_{\text{E}} = u_{\text{e}} = 0$ and $u_{\text{Ep}} = n_{\text{Ect2}}$.

[1]Note that Cdk1 plays a similar role as curvature in modulating the front propagation speed [155, 156], such that the threshold Cdk1 concentration can depend on curvature.

4 Temporal derivative

"Hoed u voor de mensen die iets zeker weten.
Ze zijn gevaarlijk."
– Jan Terlouw

Cells constantly process signals from the external environment or internal cellular processes. In this chapter we present a mechanism by which the activity of a protein exhibits a pulse response after a signal is turned on. This is reminiscent of a temporal derivative. As an example, our discussion is based on the dynamics of the enzyme Rho. We first introduce a model for Rho which is based on the available biochemical information for Rho. We analyze the parameter regimes of the model using a phase portrait analysis and show that Rho exhibits oscillatory dynamics. We then show that the Rho dynamics is reminiscent of a temporal derivative when the reaction rates are excitable and close to the oscillatory regime. We will later show in Chapter 6 that the Rho activity on the membrane of starfish oocytes takes such a temporal derivative of a propagating Ect2 front on the membrane, which in turn leads to a band of Rho activity that localizes at the interface of the Ect2 front.

This chapter is based on Section 2 in the Supplementary Information of our manuscript "A hierarchy of protein patterns robustly decodes cell shape information", which has been published in Nature Physics [143]. This work has been performed together with Tzer Han Tan, Fridtjof Brauns, Jinghui Liu, S. Zachary Swartz, Erwin Frey, and Nikta Fakhri

4.1 Introduction

In this chapter we show how a protein concentration exhibits a pulse response after a signal is turned on. Such a response is reminiscent of a temporal derivative. We explain this mechanism using the dynamics of the cell shape regulator Rho in starfish oocytes as a model system. We first recap the literature to outline the biochemical interactions of the different conformational states of Rho with other proteins (see Sec. 4.2). Next, in section 4.3 we motivate a model based on the available biochemical information to describe the dynamics of Rho in the cell. We will analyze this model using a phase portrait analysis (Sec. 4.5), which we introduce in Sec. 4.4. Finally, we discuss how the Rho regulator Ect2 serves as an input to the Rho dynamics (Sec. 4.6) and how Rho, in turn, can take a temporal derivative of the Ect2 concentration (Sec. 4.7).

4.2 Review of the Rho GTPase reaction kinetics

The canonical view of the Rho GTPase cycle [148, 158] is that there are two major pools of Rho: (i) GDP-bound, inactive Rho that is usually cytosolic and (ii) GTP-bound, active Rho that is usually on the membrane. Three main classes of proteins that regulate the Rho GTPase cycling between the active and inactive form are: (i) the guanine nucleotide exchange factors (GEFs) which promotes exchange of GDP for GTP to activate Rho; (ii) the GTPase activating proteins (GAPs) which promotes hydrolysis of GTP to GDP to inactivate Rho; and (iii) the guanide nucleotide dissociation inhibitors (GDIs) which sequester Rho-GDP in the cytosol.

In starfish oocyte, at least three different RhoGEFs are present in the transcriptome: Ect2, GEF-H1 and MyoGEF (Fig. 4.1A-i) [152]. Ect2 has been implicated in the regulation of Rho, both during the surface contraction wave (where Ect2 over-expression is known to induce spiral wave dynamics [145]) and during contractile ring formation during polar body extrusion [152]. RhoGAPs have not been directly identified in the starfish oocyte, but their effects have been characterized to some extent. Experiments have shown that Rok (a Rho kinase) inhibition alters the Rho-GTP pulse dynamics to step like behavior (Fig. 4.1A-ii) [152], suggesting the existence of a Rok-associate GAP. In addition, filamentous actin has been shown to have an inhibitory role on Rho, potentially through the action of a GAP (Fig. 4.1A-iii) [145].

Important aspects of Rho dynamics and regulation has been shown in other organisms. For instance, in HeLa cells, GEF-H1 and Ect2 have been shown to play distinct roles in Rho regulation during cytokinetic furrow formation, where Ect2 localizes Rho to cleavage site while GEF-H1 is required for GTP loading on Rho (Fig. 4.1B-1) [151]. Recent work in mammalian U2OS cells suggests that in GEF-H1 mediated Rho excitable dynamics, membrane-bound Rho-GTP can recruit more GEF-H1, indicating that in addition to their catalytic activity, GEFs could additionally recruit more Rho to the membrane (Fig. 4.1B-2)

[159], forming a positive feedback loop. In terms of the role GDIs play in regulation of Rho, the textbook view is that GDI acts passively by binding to soluble Rho-GDP and sequester it in the cytosol. However, a recent study in *Xenopus* egg and supported lipid bilayer challenges this view by showing that GDI can actively extract both Rho-GDP and Rho-GTP from the membrane (Fig. 4.1B-3) [160].

In addition to having multiple variants, the regulatory proteins often have distinct domains that can interact with multiple protein partners, creating complex feedback between the different regulatory proteins. In the 'GTPase flux model', GEFs and GAPs are thought to act simultaneously to promote fast cycling of Rho (Fig. 4.1B-iv) [161]. Two different studies suggest that GAP may play an activating role: the MgcRacGAP is proposed to transiently anchor active Rho (Fig. 4.1B-v) [162] and Cyk4 is known to relieve GEF Ect2 auto-inhibition, thereby activating GEF (Fig. 4.1B-vi) [147]. Additionally, Rho itself can interact with other membrane proteins. A recent study demonstrated the role of anillin in increasing the dwell time of active Rho on the membrane through PIP2 accumulation [163].

4.3 Model description

We consider a three-component model based on the Rho GTPase cycle. The canonical view of the Rho GTPase cycle [148, 158] is that there are two major pools of Rho: (i) GDP-bound, inactive Rho that is usually cytosolic and (ii) GTP-bound, active Rho that is usually on the membrane. Three main classes of proteins regulate the Rho GTPase cycling between the active and inactive form are: (i) the guanine nucleotide exchange factors (GEFs) which promotes exchange of GDP for GTP to activate Rho; (ii) the GTPase activating proteins (GAPs) which promotes hydrolysis of GTP to GDP to inactivate Rho; and (iii) the guanide nucleotide dissociation inhibitors (GDIs) which sequester Rho-GDP in the cytosol.

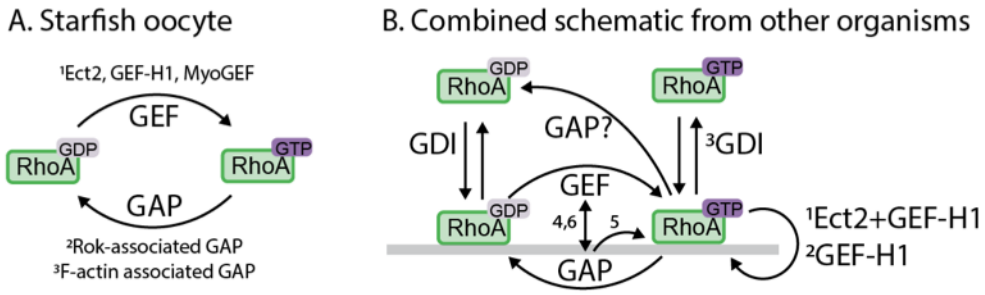

Figure 4.1 | Graphical summary of the literature of Rho reaction kinetics in (A) starfish and (B) other organisms.

Thus, we consider a model in which Rho can cycle between three conformations: (1) an inactive (GDP-bound) cytosolic conformation (concentration $u_{\mathrm{R}}(\vec{r},t)$), (2) an inactive state on the membrane (concentration $u_{\mathrm{rd}}(\vec{r},t)$) and (3) an active (GTP-bound) conformation on the membrane (concentration $u_{\mathrm{rt}}(\vec{r},t)$). The transitions between the different biochemical conformations of Rho are regulated by a complex network of Rho regulatory proteins, including several GEFs, GAPs and GDIs [148, 158]. We do not explicitly include these regulatory proteins in the model but instead consider an effective reaction–diffusion model

$$\partial_t u_{\mathrm{R}} = D_{\mathrm{R}}\nabla^2 u_{\mathrm{R}} + f_{\mathrm{R}}(u_{\mathrm{R}}, u_{\mathrm{rt}}, u_{\mathrm{rt}}), \tag{4.1}$$
$$\partial_t u_{\mathrm{rd}} = D_{\mathrm{rd}}\nabla^2 u_{\mathrm{rd}} + f_{\mathrm{rd}}(u_{\mathrm{R}}, u_{\mathrm{rd}}, u_{\mathrm{rt}}), \tag{4.2}$$
$$\partial_t u_{\mathrm{rt}} = D_{\mathrm{rt}}\nabla^2 u_{\mathrm{rt}} + f_{\mathrm{rt}}(u_{\mathrm{R}}, u_{\mathrm{rd}}, u_{\mathrm{rt}}), \tag{4.3}$$

where Rho in the cytosolic state diffuses with a diffusion constant D_{R}, which is much higher than the diffusion constant of the membrane-bound states, D_{rd} and D_{rt}. We consider both the membrane and the cytosol as a two-dimensional spherical shell. For the reaction kinetics, we assume a generic GTPase reaction cycle, with the reaction terms

$$f_{\mathrm{R}} = k_{\mathrm{off}}u_{\mathrm{rd}} - k_{\mathrm{on}}u_{\mathrm{R}} + k_{\mathrm{gap}}u_{\mathrm{rt}}, \tag{4.4}$$
$$f_{\mathrm{rd}} = k_{\mathrm{on}}u_{\mathrm{R}} - k_{\mathrm{off}}u_{\mathrm{rd}} - (k_{\mathrm{r}} + k_{\mathrm{dt}}u_{\mathrm{rt}}^2)u_{\mathrm{rd}}, \tag{4.5}$$
$$f_{\mathrm{rt}} = (k_{\mathrm{r}} + k_{\mathrm{dt}}u_{\mathrm{rt}}^2)u_{\mathrm{rd}} - k_{\mathrm{gap}}u_{\mathrm{rt}}, \tag{4.6}$$

as illustrated in Fig. 4.2. These reaction kinetics conserve total protein mass, such that $\int_\Omega d\vec{r}(u_{\mathrm{R}} + u_{\mathrm{rd}} + u_{\mathrm{rt}}) = n_{\mathrm{R}}$, where Ω denotes the surface of a 3D volume. We don't include protein production and degradation of Rho, as these processes are typically much slower (∼hours) than the Rho oscillation period (∼minutes). The inactive Rho conformation can attach to and detach from the membrane with rates k_{on} and k_{off}, respectively. On the membrane, the inactive conformation can get activated with the basal activation rate k_{r} and the autocatalytic activation rate k_{dt}. The autocatalytic activation rate effectively represents a mutual interaction between Rho and potentially multiple GEFs, in which Rho that has been activated by GEFs, recruits more GEFs. The action of the RhoGEFs is modeled implicitly through the choice of nonlinearity [145, 164, 165]. For example, the term $u_{\mathrm{rt}}^2 u_{\mathrm{rd}}$ arises when two GEFs (e.g. GEF-H1 and Ect2) are required for Rho activation, such that Rho activation scales as $[\text{GEF-H1}](u_{\mathrm{rt}}) \times [\text{Ect2}](u_{\mathrm{rt}}) \times u_{\mathrm{rd}} \sim u_{\mathrm{rt}}^2 u_{\mathrm{rd}}$ following [99]. Such a dependence on both GEF-H1 and Ect2 has indeed been suggested in HeLa cells [151]. In the active state, Rho can undergo hydrolysis, mediated by a RhoGAP. We do not consider the RhoGAP as a separate species in the model, but model the action of the RhoGAP implicitly via hydrolysis rate k_{gap}. We assume that Rho-GTP immediately detaches from the membrane after it is hydrolyzed [95, 166].

The reaction rates in the model are effective rates and depend on the concentrations of the regulatory proteins. For example, the nucleotide exchange rates will depend on the

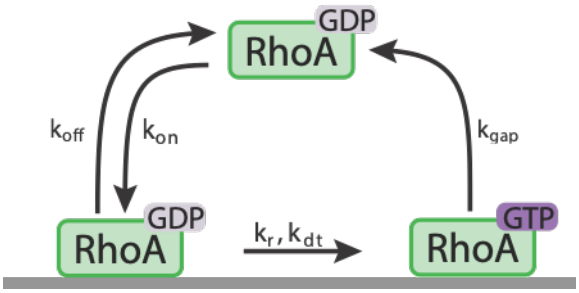

Figure 4.2 | Schematic of the reaction kinetics of the Rho model. Inactive Rho-GDP can bind to and detach from the membrane with a rate k_{on} and k_{off} respectively. On the membrane, Rho-GTP gets activated with a rate k_{r} and can autocatalytically enhance its own activation with a rate k_{dt}. When Rho-GTP is hydrolyzed with a rate k_{gap} it detaches from the membrane.

concentration of (potentially multiple) RhoGEFs, including Ect2. The hydrolysis rate depends on the concentration of RhoGAPs and the attachment and detachment rates depend on the concentration of RhoGDIs. Note that most regulatory proteins also interact among each other, such that variations in the concentration of one regulatory protein can indirectly results in a change of potentially multiple rates in the model. For example, it has been proposed that the RhoGEF Ect2 binds to the RhoGAP MgcRacGAP [162] or is involved in the localization of Rho to the membrane [151], such that an increase in the Ect2 concentration might lead to an increase in both the nucleotide exchange rate and the hydrolysis rate or attachment rates respectively. Furthermore, it has been suggested that the RhoGAPs are recruited by F-actin [145] and interact with the Rho kinase Rok [152], such that variations in the concentration of F-actin and Rok could indirectly affect the hydrolysis rate.

The oscillatory and excitable dynamics in this model depends on the mass conservation of Rho, as the local depletion of the cytosol in the vicinity of the membrane effectively leads to a negative feedback for Rho attachment. Oscillatory and excitable dynamics can also arise via delayed negative feedback from another protein, such as F-actin or a GAP [167–169]. A model based on the Rho GTPase cycle that explicitly accounts for such negative feedback has been used before to describe the Rho spirals [145]. In that model, specific interactions between Rho and Ect2 and Rho and F-actin were assumed, such that F-actin acts as an inhibitory protein to induce oscillations. Here, we instead model all regulatory interactions implicitly. This enables us to identify the key processes of the Rho GTPase cycle that give rise to the experimentally observed phenomena with minimal model assumptions. Furthermore, this minimal model facilitates an intuitive understanding of the reaction kinetics of the Rho conformations in a phase-portrait analysis. The insights gained from this analysis might help to develop a more detailed molecular model for the regulation of the Rho GTPase cycle in the future.

Parameter	Value	Unit	Description
k_{on}	1.5×10^{-4}	s^{-1}	Rho-GDP membrane attachment
k_{off}	1.5×10^{-5}	s^{-1}	Rho-GDP membrane detachment
k_{r}	$1.5 \times 10^{-4}\xi_{\text{Ect2}}$	s^{-1}	Nucleotide exchange rate/activation rate
k_{dt}	$9.45 \times 10^{-3}\xi_{\text{Ect2}}$	$\mu m^4 s^{-1}$	Autocatalytic activation rate
k_{gap}	1.5×10^{-2}	$\mu m^2/s$	Rho-GTP membrane detachment
n_{R}	10	μm^{-2}	Rho total concentration
D_{R}	10	$\mu m^2/s$	Diffusion constant Rho-GDP in the cytosol
D_{rd}	0.1	$\mu m^2/s$	Diffusion constant Rho-GDP on the membrane
D_{rt}	0.05	$\mu m^2/s$	Diffusion constant Rho-GTP on the membrane
V_{Ect2}	0.2	$\mu m/s$	Ect2 propagation speed
ϵ	1	μm	Width of Ect2 front interface
ξ_{Ect2}	[0.01, 1]	μm^{-2}	Ect2 front parameter in low and high Ect2 domain (movies S14 and S18)
ξ_{Ect2}	$u_{\text{e}} + u_{\text{E}}$	μm^{-2}	Ect2 front parameter to couple Rho and Ect2 module (movies S15- S17)

Table 4.1 | Model parameters for the Rho dynamics. Parameters are chosen such that the model exhibits oscillatory dynamics.

4.4 Phase portrait analysis of local reactions

In order to gain an intuitive understanding of the spatiotemporal dynamics of Rho, we first analyze the Rho reaction dynamics. Motivated by local equilibria theory [49, 56, 105], we consider a compartment along the membrane, small enough to be considered well-mixed. We picture this compartment isolated from the rest of the system, such that there is no diffusive mass transport in and out of the compartment. This is equivalent to analyzing a well-mixed system. We perform a phase portrait analysis for the local compartments, providing an intuitive understanding of the Rho reaction dynamics at a particular position in the cell.

To perform the phase space analysis, consider a position x with total density $n_{\text{R}}(\vec{r})$. Since the Rho reaction kinetics conserves total protein mass, the reactive flow of the system is restricted to the simplex $u_{\text{R}} + u_{\text{rd}} + u_{\text{rt}} = n_{\text{R}}(\vec{r})$, where $n_{\text{R}}(\vec{r})$ is the average protein density within the compartment. Thus, the local dynamics within each compartment can be characterized in the two-dimensional phase space of the reaction kinetics on this simplex. This allows us to eliminate one of the three components in the reactive dynamics at an isolated membrane position,

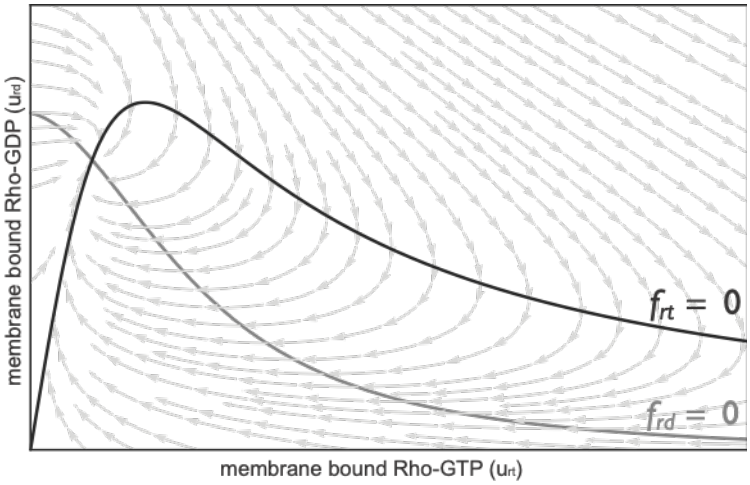

Figure 4.3 | The $(u_{\mathbf{rd}}, u_{\mathbf{rt}})$-phase portrait. The f_{rt} - and f_{rd}-nullcline are represented as black and gray lines respectively. The intersection of the two nullclines defines the steady state. The light gray arrows indicate the direction of the reactive flow towards the steady state.

$$\partial_t u_{\mathrm{rd}} = \tilde{f}_{\mathrm{rd}}(u_{\mathrm{rd}}, u_{\mathrm{rt}}) = f_{\mathrm{rd}}(n_{\mathrm{R}}(\vec{r}) - u_{\mathrm{rd}} - u_{\mathrm{rt}}, u_{\mathrm{rd}}, u_{\mathrm{rt}}), \tag{4.7}$$

$$\partial_t u_{\mathrm{rt}} = \tilde{f}_{\mathrm{rt}}(u_{\mathrm{rd}}, u_{\mathrm{rt}}) = f_{\mathrm{rt}}(n_{\mathrm{R}}(\vec{r}) - u_{\mathrm{rd}} - u_{\mathrm{rt}}, u_{\mathrm{rd}}, u_{\mathrm{rt}}), \tag{4.8}$$

such that we can visualize the reaction dynamics in the two-dimensional $(u_{\mathrm{rd}}, u_{\mathrm{rt}})$-phase plane, as shown in Fig. 4.3. The reactive flow at the isolated membrane position is then characterized by $\tilde{f}_{\mathrm{rd}}$ and $\tilde{f}_{\mathrm{rt}}$, indicated by the light-gray arrows in Fig. 4.3. The nullclines, $\tilde{f}_{\mathrm{rd}} = 0$ and $\tilde{f}_{\mathrm{rt}} = 0$ indicate the positions in phase space at which the reactive flow of u_{rd} and u_{rt} change sign respectively (gray and black solid lines respectively in Fig. 4.3). In the $(u_{\mathrm{rd}}, u_{\mathrm{rt}})$-phase plane, these nullclines are given by

$$u_{\mathrm{rd}} = \frac{k_{\mathrm{on}}(n_{\mathrm{R}} - u_{\mathrm{rt}})}{k_{\mathrm{off}} + k_{\mathrm{on}} + k_{\mathrm{r}} + k_{\mathrm{dt}} u_{\mathrm{rt}}^2}, \tag{4.9}$$

$$u_{\mathrm{rd}} = \frac{k_{\mathrm{gap}} u_{\mathrm{rt}}}{k_{\mathrm{r}} + k_{\mathrm{dt}} u_{\mathrm{rt}}^2}, \tag{4.10}$$

which we will call the f_{rt}- and f_{rd}-nullcline respectively. The intersection of the two nullclines defines the steady state. Thus, the shape of the nullclines reveals information about the reaction dynamics of Rho and the stability of the steady states.

In the following, we use the phase portrait analysis to explain the mechanism how the Rho pulse localizes to the Ect2 front in wild type oocytes and how Ect2 overexpression leads to a front of Rho spirals. First, in Sec. 4.5, we use the phase portrait to characterize

different parameter regimes of the model and discuss how variations of the reaction rates lead to transitions between the different parameters regimes. We then argue, in Sec. 4.6, how the front-like concentration profile in Ect2 affects the reaction rates of the model and explain, in Sec. 4.7, how the Rho dynamics at a single membrane position responds as the front-like concentration profile of Ect2 travels along the membrane (Fig. 6.3b). Using the intuition gained from the analysis of the local dynamics, we then explain, in Sec. 6.B, why the experimentally observed Rho pulse follows the travelling Ect2 front in the spatially extended system and how the width of the pulse depends on the speed of the front. Using a similar approach, in Sec. 6.C, we explain how overexpression of Ect2 can lead to spiral dynamics in the domain where the Ect2 concentration is high.

4.5 Parameter regimes

By exploring the parameter space of the model, we find four qualitatively different parameters regimes, which we characterize based on the intersection of the two nullclines:

1. A monostable regime where the nullclines intersect before the maximum of the f_{rt}-nullcline. In this parameter regime, the dynamics is monostable. The stable steady state (fixed point) is at low Rho-GTP concentration (Fig. 4.4A). The flow field, indicated by the gray arrows (cf. Eq. **??** and 4.10), shows how the concentration of Rho-GTP and Rho-GDP on the membrane transitions to the steady state. Importantly, in phase space, this is not always a direct path to the steady state but can be a large excursion as indicated by the green line in Fig. 4.4A. This excursion in phase space leads to a transient increase in the Rho-GTP concentration before it relaxes to the steady state.
2. A monostable regime where the nullclines intersect at the tail of the f_{rt}-nullcline. The fixed point is at high Rho-GTP concentration (Fig. 4.4B). Similar as in parameter regime 1, the dynamics towards the steady state can initially lead to a transient increase in the Rho-GTP concentration before relaxing to the steady state, as indicated by the green line in Fig. 4.4B.
3. An intermediate regime where the nullclines intersect right after the maximum of the f_{rt}-nullcline. In this regime, the system relaxes to a limit cycle, rather than a stable steady state (green line in Fig. 4.4C, lower panel). This means that the concentration of the Rho-states oscillates (Fig. 4.4C, upper panel).
4. A bistable parameter regime where the nullclines intersect three times such that there are two stable steady states with a low and high Rho-GTP concentration respectively and an unstable steady state (Fig. 4.4D). In this regime, it depends on the initial condition whether the Rho-GTP concentration if low or high in the steady state.

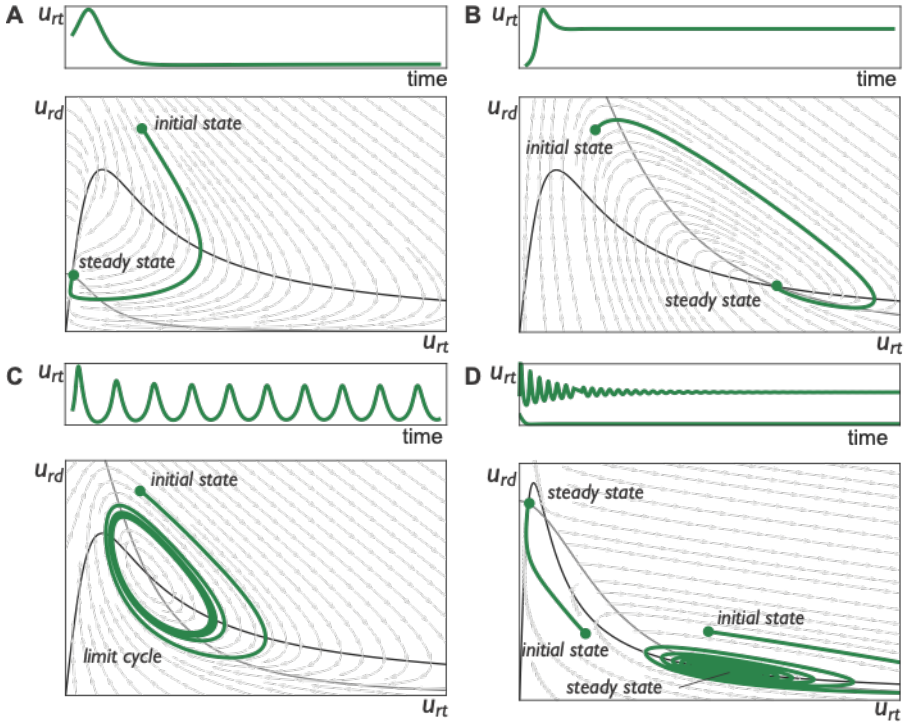

Figure 4.4 | Sketches of phase portraits for qualitatively different parameter regimes (lower panels) and a typical trajectory within that regime (upper panel). The f_{rt}- and f_{rd}-nullclines are shows as black and gray lines, respectively. Light gray arrows show the reactive flow towards the steady states. A typical trajectory (cf. Eq. **??** and 4.10) is shown as a green line. The intersections of the nullclines identify four qualitatively different parameters regimes: **(A)** monostable with low Rho-GTP concentration, **(B)** monostable with high Rho-GTP concentration, **(C)** limit cycle oscillations and **(D)** bistability.

In the following we discuss how the parameters of the model change the nullcline shape such that the system can transition between the qualitatively different regimes. We restrict our discussion to the regimes 1-3 and illustrate the change of the nullcline shape for varying a parameter in Fig. 4.5.

Attachment and detachment – The attachment and detachment rate only change the shape of the f_{rd}-nullcline. In particular, it changes the shape such that the maximum of the f_{rd}-nullcline shifts up, for increasing attachment rate (k_{on}) or decreasing detachments rate (k_{off}). The maximum cannot be larger than the total Rho concentration n_{R}. Thus, when the maximum of the f_{rt}-nullcline is low enough, an increase of the attachment rate or a decrease of detachment rate, can lead to a transition from the low Rho-GTP concentration (regime 1) to oscillations (regime 3) to a high stable Rho-GTP concentration (regime 2).

Hydrolysis – The hydrolysis rate (k_{gap}) only changes the shape of the f_{rt}-nullcline. In particular, it stretches the f_{rt}-nullcline along the u_{rd}-axis. Decreasing the hydrolysis rate

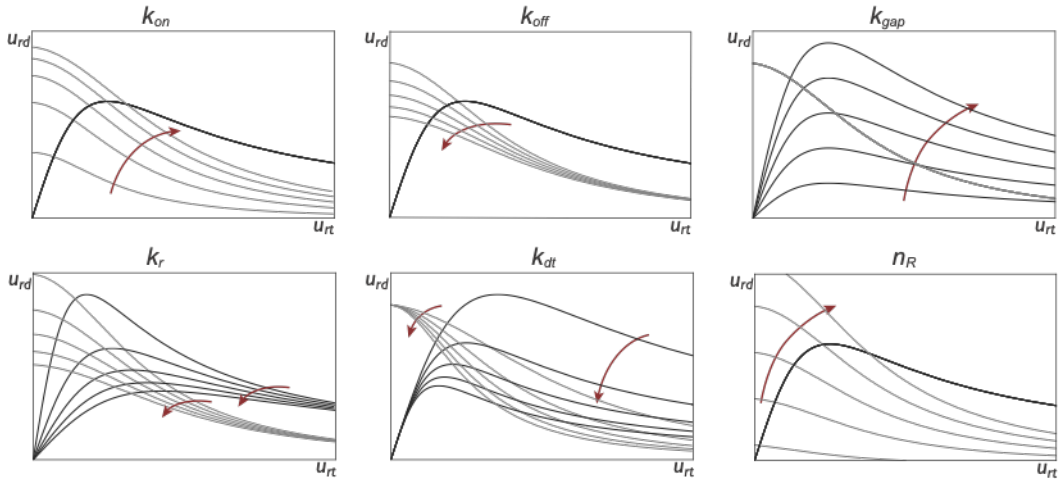

Figure 4.5 | Parameter sweeps For an increase of the reaction rate, the nullcline moves into the direction indicated by the red arrows. The increase of the reaction rate can lead to a transition between parameter regimes as classified illustrated in Fig. 4.4.

therefore leads to a transition from the low Rho-GTP concentration (regime 1) to oscillations (regime 3) to a high stable Rho-GTP concentration (regime 2).

Nucleotide exchange – The nucleotide exchange rates change the shape of both nullclines. The linear rate k_r has the same effect on the f_rd-nullcline as the detachment rate. In addition, k_r decreases the slope of the f_rt-nullcline for small Rho-GTP concentration. Thus, an increase in k_r shifts the system towards low Rho-GTP concentration (regime 1). The autocatalytic rate k_dt changes the slope of the f_rd-nullcline and the position of the maximum of the f_rt-nullcline. This typically leads to a transition from the low Rho-GTP concentration (regime 1) to oscillations (regime 3).

Total Rho concentration – In a spatially extended systems, the total concentration of Rho is generically inhomogeneous. Attachment and detachment of Rho to and from the membrane will induce gradients in the cytoplasmic Rho concentration. These gradients lead to mass transport due to fast diffusion in the cytoplasm. We therefore ask how the Rho dynamics depends on the total density of Rho. In regime 1, the change of the Rho-GTP concentration is proportional to the linear nucleotide exchange rate k_r until the system transitions to limit cycle oscillations (regime 3). In the oscillatory regime (regime 3), the increasing Rho concentration changes the amplitude of the limit cycle and therefore the amplitude of the oscillations (Fig. 4.6). Furthermore, a large enough increase could lead to a transition from oscillations to a stable steady state with high Rho-GTP concentration (regime 2) (Fig. 4.6).

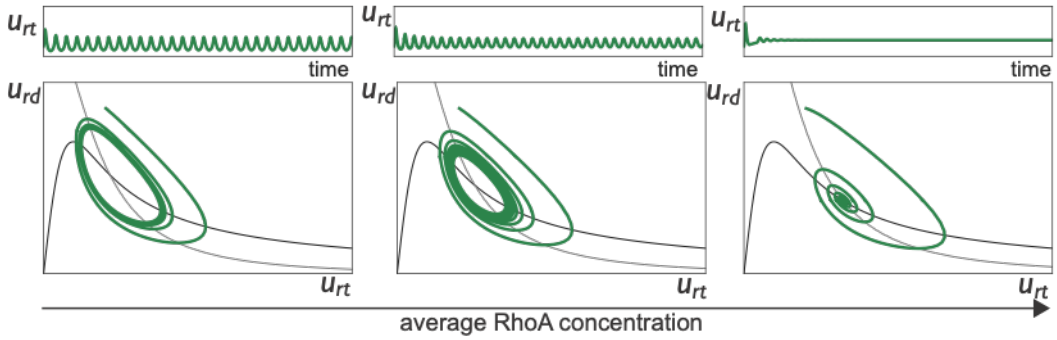

Figure 4.6 | Varying total concentration. Increase in total Rho concentration decreases the amplitude of the limit cycle oscillations. Upper panels show the Rho-GTP concentration over time, lowel panels show the $(u_{\mathrm{rd}}, u_{\mathrm{rt}})$-phase portrait.

4.6 The Ect2 front serves as a spatial template for Rho reaction kinetics

In Fig. 6.2d, we will show that Ect2 forms a front pattern on the membrane, with a high Ect2 concentration in the VP domain and a low concentration in the AP domain. Furthermore, we will show that this front pattern colocalizes to the Rho pulse (Fig. 6.2b). How can a front-like profile of the Ect2 concentration localize a Rho pulse? As Ect2 is a RhoGEF it must affect the reaction kinetics of the Rho GTPase cycle. However, it is not a priori evident how. At first sight, one would expect that an increase in the Ect2 concentration increases the nucleotide exchange rate of Rho. However, other scenarios are possible as well. For example, it has been suggested that apart from its GEF activity, Ect2 is also involved in recruiting Rho to the membrane [151], such that an increase in the Ect2 concentration might also lead to an increase of Rho's attachment rate. Furthermore, Ect2 could also indirectly affect processes of the GTPase cycle via interactions of Ect2 with other Rho regulatory proteins [148, 158]. Hence, an increase of the Ect2 concentration in the VP domain could also lead to an increase of other regulatory processes apart from the increase of the nucleotide exchange rate, for example via interactions with a RhoGAP [162] or microtubules [149]. Indeed, we showed that the microtubules also form a front pattern similar to the Ect2 front (movie S20). We therefore first ask to which qualitative parameter regimes (as outlined in Sec. 4.5) the two Ect2 levels correspond and then argue which parameter in our model could lead to such a transition, integrating the available biochemical information.

In the main text we discussed that, viewed from a position on the membrane, the Ect2 concentration suddenly increases as the Ect2 front passes along the membrane (Fig. 6.3b). In the phase portrait, the increase of the Ect2 concentration is represented as a change of the nullclines and therefore of the position of the fixed point. Hence there are two possible, qualitatively different, scenarios: (i) The change of the Ect2 concentration can change

the fixed point within the same parameter regime, leading to transient dynamics as the concentration transitions from the old fixed point to the new fixed point. (ii) The change in the Ect2 concentration can result in a transition between different parameter regimes, leading to a qualitatively different Rho behavior, in the VP and AP domain.

In the following, we will argue how the concentration of Rho-GTP at a position on the membrane responds to a change of the Ect2 concentration, in both the wild type (Sec. 4.7) and for Ect2 over expression (Sec. 6.B). As the Ect2 front travels along the membrane, such a response happens at each position in space, giving rise to a spatial template for the Rho dynamics.

4.7 Rho senses the temporal derivative of the Ect2 template

Here, we analyze how the Rho dynamics responds to the moving Ect2 front. To this end, we first consider the local Rho dynamics at a single position on the membrane. We argue how the Rho dynamics will play out in a diffusively coupled system and confirm this intuition in finite element simulations (implemented in COMSOL Multiphysics 5.4).

Local reaction dynamics – Before the Rho wave starts, the Rho-GTP concentration in the starfish oocyte is homogeneous with only little Rho-GTP on the membrane (Fig. 6.1d). This suggests that the reaction kinetics of Rho in the AP domain lies within regime 1 cf. Sec. 4.5. Viewed from a single position on the membrane, the concentration of Rho-GTP increases only transiently as the SCW travels along the membrane (Fig. 6.1d). Interestingly, after the Ect2 front has passed a single position on the membrane, the Ect2 concentration is still high, but Rho-GTP has returned to a low concentration, such that also the reaction kinetics in the VP domain must be in regime 1. This suggests that the transient increase of the Rho-GTP concentration arises from the dynamics of Rho-GTP as it transitions from the steady state in the AP domain to the new steady state in the VP domain. Thus, we seek parameters for the model such that the steady states in both the AP and VP domain have a low Rho-GTP concentration (regime 1) and are laterally stable, as the Rho-GTP concentration is homogeneous before and after the SCW. Furthermore, the difference between the AP- and VP-steady state must be such that a transition from the AP- to the VP-steady state leads to a large excursion in phase space, corresponding to an increase in the Rho-GTP concentration. Such excursions typically occur in parameter regimes close to oscillatory regimes [170].

How does Ect2 affect the Rho GTPase cycle? As Ect2 is a RhoGEF, the intuitive choice is that the increased Ect2 concentration in the VP domain increases the nucleotide exchange rates in this domain. As discussed in Sec. 4.5, an increase in the linear nucleotide exchange rate decreases the initial slope of the f_{rt}-nullcline and also decreases the intercept of the f_{rd}-nullcline, such that the fixed point moves towards a lower Rho-GDP concentration

on the membrane (Fig. 4.7A). A change in the autocatalytic nucleotide exchange rates only slightly changes the fixed point to a position with lower Rho-GDP concentration on the membrane (Fig. 4.7B). However, increasing k_{dt} mainly changes the reactive flow towards the steady state (gray arrows Fig. 4.7B). The reactive flow towards this fixes point (cf. Eq. 3, and gray arrows in Fig. 4.7B) indicates that starting from a low Rho-GTP concentration, Rho-GTP first increases before it relaxes to the fixed point. Indeed, our simulation (cf. Eq. 1, and green line in Fig. 4.7B) shows that a sudden increase in the nucleotide exchange rates leads to an excursion in phase space and therefore to a transient increase in the Rho-GTP concentration. In particular, the reactive flow shows that the increase in Rho-GTP concentration is larger for a larger autocatalytic activation rate. We therefore model the Ect2 front as a step-like increase of both the basal and the autocatalytic activation rates to describe the Rho pulse. This means that k_{r} and k_{dt} are multiplied by $\xi_{\mathrm{Ect2}} = 0.01 + 0.99\Theta(|\vec{r}| - (|\vec{r}_0| - V_{\mathrm{Ect2}}t))$, with $|\vec{r}_0|$ the initial front position and V_{Ect2} the front speed. Note that one can also use $\xi_{\mathrm{Ect2}} = u_{\mathrm{e}}(\vec{r}, t) + u_{\mathrm{E}}(\vec{r}, t)$ to couple the Ect2 module of the model to the Rho module.

How fast the Ect2 concentration increases at a position on the membrane depends on the speed of the front and the width of the front passing that position. For a slowly propagating front, or a large front width, the Ect2 concentration at a membrane position increases slowly. For a sufficiently slow rate of change in the local Ect2 concentration (dark red line in Fig. 4.8A) the Rho concentration will gradually transition from the old to the new steady state (dark green line in Fig. 4.8B). In phase space, this represented by a trajectory that stays slaved to fixed points as the system changes from the old to the new steady state (dark green line in Fig. 4.8C). However, when Ect2 increases faster than the relaxation of Rho the moving fixed point, the Rho-GTP concentration first increases before it relaxes to the new steady state, as illustrated by the brighter trajectories in Fig. 4.8. Thus, a Rho pulse only exist when the Ect2 concentration at a membrane position increases sufficiently fast to induce a large excursion of the Rho dynamics in phase space.

As the Ect2 front moves along the membrane, it continuously triggers such local excursions, resulting in a Rho pulse that follows the Ect2 front (Fig. 6.3f). Hence, the Rho pulse relies on the movement of the Ect2 front. Thus, the model predicts that a stationary Ect2 front would not localize a Rho pulse to its interface. Furthermore, in a system without diffusive coupling, the width of the pulse is given by the product of the excursion time and the Ect2 front speed. Indeed, our simulations in ellipsoidal, triangular and star geometry (Fig. 4.9) and experiments (Fig. 6.3g) show that the width of the Rho pulse is positively correlated with the wave speed.

Spatially (diffusively) coupled systems – In the spatially extended system with diffusive coupling, the local increase of Rho-GTP on the membrane results in a local decrease of the cytosolic Rho-GDP concentration. This leads to gradients in the cytoplasm, which in turn leads to diffusive transport of Rho-GDP in the cytosol. Thus, in a diffusively coupled system, each position on the membrane has a slightly different total density $n_{\mathrm{R}}(x)$. In Sec. 4.5 we showed that the total Rho density also changes the shape of the nullclines

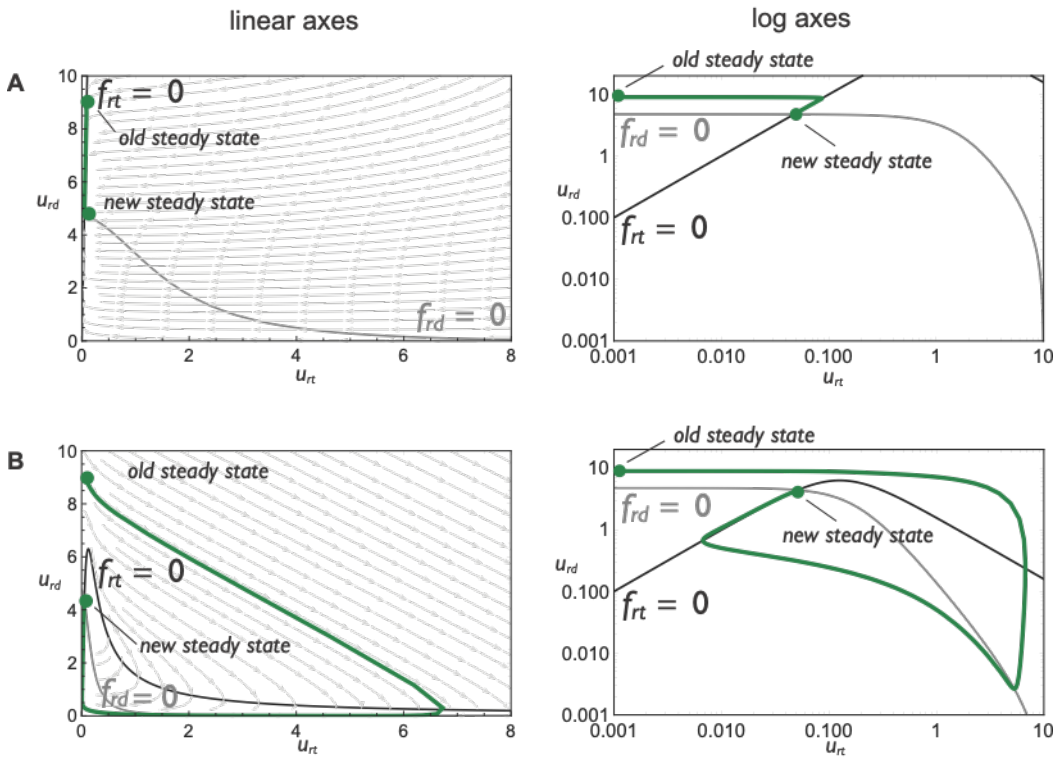

Figure 4.7 | Transition from the old to the new steady state leads to a large excursion in phase space. **(A)** increasing the linear nucleotide exchange rates, moves the fixed point to a position in phase space with a lower concentration for Rho-GDP and a slightly higher concentration of Rho-GTP. **(B)** An additional increase of the autocatalytic nucleotide exchange rate mainly changes the reactive flow towards the new steady state such that the Rho-GTP concentration first increases before it relaxes to the new steady state, as indicated by the larger excursion in phase space. Parameters are specified in Table 4.1.

describing the local Rho dynamics (cf. Eq. 4). However, as the Rho pulse is a robustly observed phenomenon in all wild type oocytes, we conclude that the local variations of the total Rho density should not qualitatively change the Rho dynamics. We therefore choose parameters such that variations in the total density only change the steady state concentrations, but not the qualitative dynamics of Rho (see Table 4.1 for parameters).

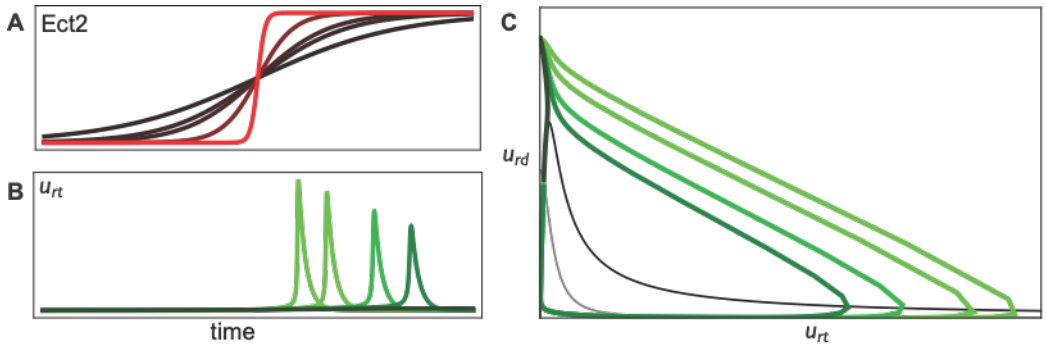

Figure 4.8 | Trajectories for varying widths of the Ect2 increase. **(A)** The change in Ect2 concentration viewed from a position on the membrane ranging from a gradual increase (dark) to a sudden increase (bright). **(B)** The transient dynamics of the Rho-GTP concentration on the membrane, and **(C)** the corresponding trajectory in the phase space. The faster the Ect2 concentration increases, the larger the excursion in phase space and the more pronounced the Rho-GTP increase.

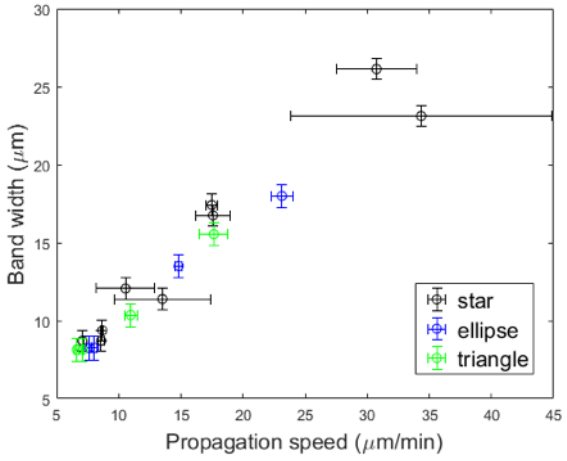

Figure 4.9 | Rho band width versus wave speed. The width of the Rho band is positively correlated with the propagation speed. The Rho band width and propagation speed are measured at various positions along the circumference of a cross section of the simulations in ellipsoidal (movie S15), triangular (movie S16) and star geometry (movie S17)

5 Spatial derivative

"I am as proud of what we don't do
as I am proud of what we do"
– Steve Jobs

The formation of protein patterns inside cells is generically described by reaction–diffusion models. The study of such systems goes back to Turing, who showed how patterns can emerge from a homogenous steady state when two reactive components have different diffusivities (e.g. membrane-bound and cytosolic states). However, in nature, systems typically develop in a heterogeneous environment, where upstream protein patterns affect the formation of protein patterns downstream. Examples for this are the polarization of Cdc42 adjacent to the previous bud-site in budding yeast, and the formation of an actin-recruiter ring that forms around a PIP3 domain in macropinocytosis. This suggests that previously established protein patterns can serve as a template for downstream proteins and that these downstream proteins can 'sense' the edge of the template. A mechanism for how this edge sensing may work remains elusive.

Here we demonstrate and analyze a generic and robust edge-sensing mechanism, based on a two-component mass-conserving reaction-diffusion (McRD) model. Our analysis is rooted in a recently developed theoretical framework for McRD systems, termed local equilibria theory. We extend this framework to capture the spatially heterogeneous reaction kinetics due to the template. This enables us to graphically construct the stationary patterns in the phase space of the reaction kinetics. Furthermore, we show that the protein template can trigger a regional mass-redistribution instability near the template edge, leading to the accumulation of protein mass, which eventually results in a stationary peak at the template edge. We show that simple geometric criteria on the reactive nullcline's shape predict when this edge-sensing mechanism is operational. Thus, our results provide guidance for future studies of biological systems, and for the design of synthetic pattern forming systems.

This chapter is based on our publication "Pattern localization to a domain edge', which has been published in Physical Review E [105]. This work has been performed together with Fridtjof Brauns, Tobias Hermann and Erwin Frey.

5.1 Introduction

5.1.1 Background and motivation

Many cellular processes, such as cell division and cell motility, rely crucially on the localization of proteins in space and time. Strikingly, these protein localization patterns can emerge from the collective coordination of transport and local molecular interactions of proteins. Diffusion in the cytosol is a simple means of protein transport that accounts for many self-organization processes [106]. To analyze how the interplay of diffusive protein transport and protein-protein interactions on a nanometer scale influences the protein patterns on the cellular scale, mass-conserving reaction–diffusion models have proven useful [53, 89–104]. The study of reaction–diffusion systems in general goes back to Turing [171], who showed how patterns can emerge from a homogenous steady state when two reactive components have different diffusivities. In cells, differential diffusivities are generic because many proteins have membrane-bound and cytosolic states, where diffusion on the membrane is orders of magnitude slower than in the cytoplasm. Turing's pioneering work [171] has led to vast advances in the field on how protein patterns arise from homogeneous (initial) steady states on spatially homogeneous domains. However, as Turing already pointed out [171], "most of an organism, most of the time, is developing from one pattern into another, rather than from homogeneity into a pattern."

For example, previously formed protein patterns can control pattern formation of proteins downstream by affecting their local interactions, such that the upstream pattern acts as a *spatial template* for the downstream proteins. A biological system where such "templating" has been suggested is macropinocytosis [24]. Here, a high density domain of PIP3 (a charged phospholipid) and a Ras-GTPase[1] have been suggested to serve as a template for a ring of actin recruiters (SCAR complex, Arp2/3), that forms around the PIP3 domain edge [22]. Recruitment of an actomyosin ring, controlled by GTPases, is also key for single-cell wound healing. Following the rupture of the cell wall, two GTPases– Abr and Cdc42 –are recruited to the wound edge, where they organize into two concentric rings of high protein concentration [19]. Cdc42 in turn recruits actomyosin which contracts to close the wound and repair the underlying cytoskeleton. Mutations of Abr, which forms the inner ring, leads to a loss of the outside Cdc42 ring, suggesting hierarchical interaction between Abr and Cdc42 [19]. Thus, the inner Abr-ring may be pictured as a template for the outer Cdc42-ring. Yet another example where protein patterns act as a spatial template, can be found during cell division in budding yeast. Here, landmark proteins direct the polarization of the GTPase Cdc42, such that the Cdc42 cluster emerges either adjacent to the previous bud-site, or at the opposite cell pole, depending on the cell-type [17]. Various mutations or deletions of individual landmark proteins lead to Cdc42 clusters right on top of the previous bud-site or at a random position [18, 20, 23]. Hence, the landmark proteins

[1] GTPases are hydrolase enzymes that can bind and hydrolyze guanosine triphosphate (GTP). Ras is a subfamily of small GTPases.

may be pictured as a template that controls Cdc42 pattern formation. Common to all the above examples is that the downstream proteins localize at the edge of some template. Both the specific (molecular) mechanisms, and the general principles underlying this 'edge sensing' remain elusive.

Here, we present a pattern-forming mechanism capable of robust edge sensing and provide criteria for its operation based on simple geometric relations in the phase space of the reaction kinetics. To find these criteria, we use a recently developed framework, termed *local equilibria theory* which enables us to gain insight into the dynamics of *mass-conserving reaction–diffusion* (McRD) systems [49, 56]. We introduce a step-like template that imposes heterogeneity in the reaction kinetics, and generalize the framework to study the dynamics of such systems. This enables us to explain why and under which conditions a density peak forms at the edge of the template. Thus, our results may provide guidance for the design of patterns in synthetic systems and may help to identify molecular mechanisms underlying edge-sensing in biological systems.

5.1.2 Pattern formation with a step-like template

A common feature of the biological examples we discussed in Section 5.1.1 is that the templates have a sharp edge, and that a downstream protein pattern localizes to this edge. To obtain a conceptual understanding of how such an edge-sensing mechanism might work, we study how an idealized step-like template affects the pattern formation of the two-component McRD model as a paradigmatic example.

We consider a step-like template profile $\theta(x)$ with a sharp edge at x_{E}

$$\theta(x) := \begin{cases} \theta_{\mathrm{A}} & x \leq x_{\mathrm{E}} \\ \theta_{\mathrm{B}} & x > x_{\mathrm{E}} \end{cases}, \tag{5.1}$$

as illustrated in Fig. 5.1(a). Such a template defines two spatial subdomains (labelled A and B). Here, we consider a template that couples to the downstream pattern forming system via the local reactions $f(m, c; \theta(x)$, such that different reactive dynamics

$$f_{\mathrm{A,B}}(m, c) := f(m, c; \theta_{\mathrm{A,B}}), \tag{5.2}$$

govern the system in the two subdomains (see Fig. 5.1(b)).

Pattern forming systems with a step-like (also called "jump-type") heterogeneity have a rich history in the mathematical literature (see e.g. [172–181]) where, they have been studied in the context of front-pinning [179], pulse localization [180], and wavenumber selection [181], to name a few recent examples. These studies predominantly focussed on excitable media and the models studied are not mass-conserving. Furthermore, the prevalent methods employed in these studies are singular perturbation theory (Refs. [182, 183] may serve as general introductions) and normal form theory (see e.g. Ref. [184]). The former method

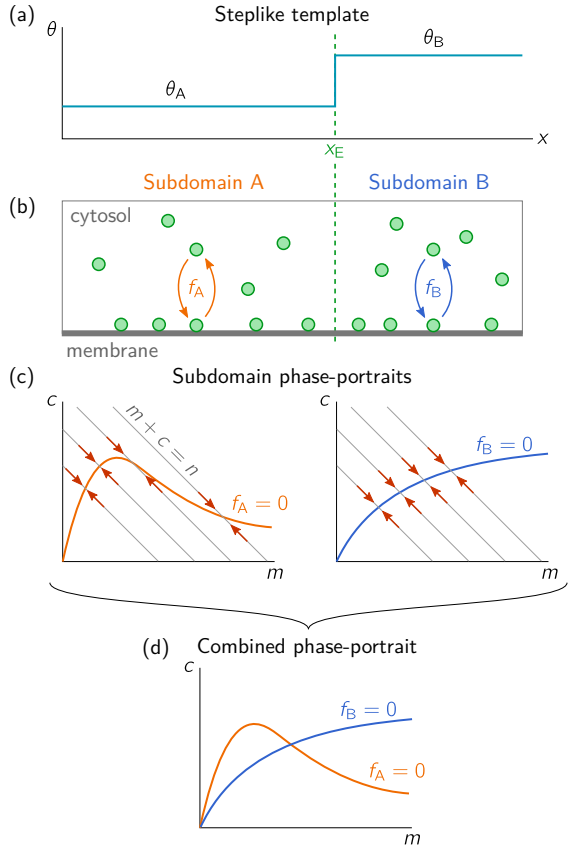

Figure 5.1 | Illustration of a step-like template (a) that acts on the reaction kinetics defines two subdomains, labelled A and B, with respective reaction kinetics f_A and f_B. (b) We consider a two-component system describing, for example, a single protein species that cycles between a membrane bound and a cytosolic state. (c) The reactive flow due to the reaction kinetics can be visualized in the (m, c)-phase space of concentrations. Due to mass-conservation, the flow points along the reactive phase spaces $m + c = n$ (indicated by gray lines). Along the nullclines $f_{\mathrm{A,B}}$, the flow vanishes. Therefore, the reactive flow in each subdomain is qualitatively captured by the shape of the respective nullcline. (d) With the reactive flow encoded by the nullclines, the phase portraits of the two subdomains can be combined ('overlaid') into a single phase space. This combined phase space will be used for the construction of stationary states.

uses matched asymptotics and is based on a separation of spatial scales; the latter applies in the vicinity of a bifurcation.

Here, we choose a conceptually different approach building on the recently developed local equilibria theory [49, 56], specifically the phase-portrait analysis outlined in Sec. 1.4.2 and introduced in detail in [56]. Our starting point is to use the reactive nullclines of the two subdomains as proxies for the respective reactive flows (Fig. 5.1(c)). For this purpose, we combine the phase portraits of the subdomains into a single phase portrait as shown in Fig. 5.1(d). This 'overlaying' of the phase portraits facilitates a geometric analysis of the system with a step-like template based on the approach presented previously for the two-component system on a homogeneous domain [56] (see recap in Sec. 1.4.2). Throughout the paper we will use nullcline shapes as illustrated in Fig. 5.1(d) (see Appendix 5.A for the specific equations and parameters). A different nullcline 'arrangement', and the general role of the nullcline shapes are discussed in Appendix 5.B.

The remainder of the paper is structured as follows. In Sec. 5.2.1, we first analyze steady states with a monotonic density profile and show how these states can be determined via a flux-balance construction in the (m, c)-phase portrait. In Sec. 5.2.2, we extend the flux-balance construction to also obtain the non-monotonic steady states of the system. In Sec. 5.2.3, we introduce the concept of *regional instability* to understand the transition from monotonic to non-monotonic steady states. Finally, in Sec. 5.3, we analyze how the peak responds to a moving template edge and show that this can lead to depinning or suppression of the peak when the template edge moves sufficiently fast.

5.2 Construction of steady states and their bifurcations

The goal of this section is to characterize the steady states of the two-component McRD system with a step-like template. These systems generically don't exhibit spatially homogenous states. Non-homogeneous steady states can be categorized based on the monotonicity of their density profiles. We first briefly summarize the main results of this section. In Sec. 5.2.1, we characterize the monotonic steady states, which consist of two plateaus connected by a monotonic interface at the template edge x_{E}, as shown in Fig. 5.2(a). We call these monotonic steady states the *(spatially) heterogenous base-states*. We will show that these base states only exist for low or high total mass. Starting from the low-mass base state and increasing the total mass $\bar{n}$, we find that the base state disappears through a saddle node bifurcation. In the subsequent intermediate-mass regime, the steady states are non-monotonic which are the self-organized patterns of the system. In Sec. 5.2.2 we show that the stable *stationary patterns* (i.e. non-monotonic steady states) exhibit a single density peak either at the system boundary or at the template edge. The transition between the monotonic base states to the non-monotonic patterns arises from a lateral instability localized at the template edge, which we call a *regional instability*. Via numerical simulations we show that from this instability a peak at the template edge emerges ('edge

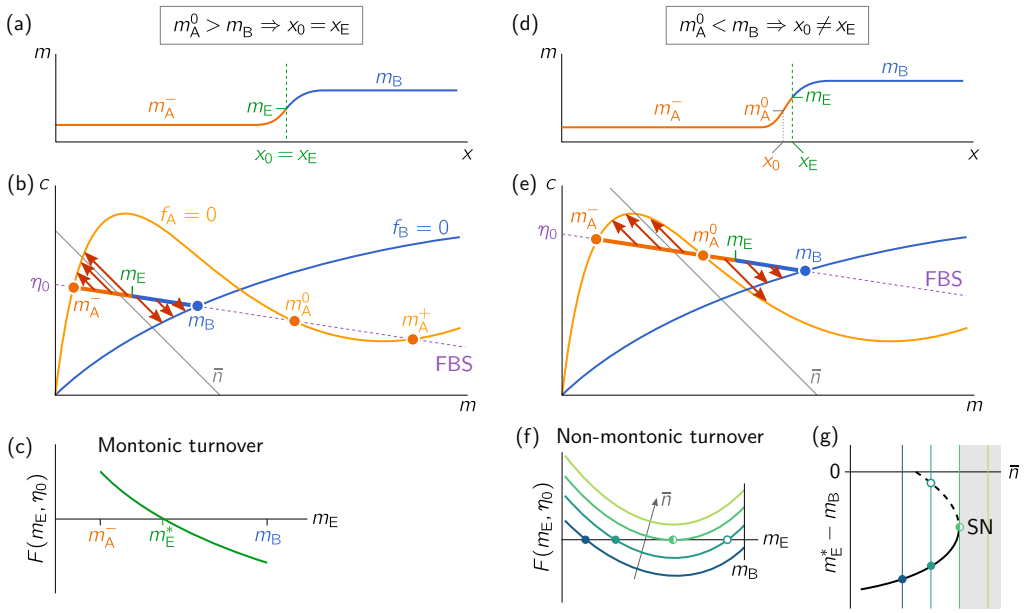

Figure 5.2 | Illustration of the construction of monotonic steady states (*heterogeneous base states*) in (m, c)-phase space. (a) Density profile with the inflection point at the template edge x_E. (b) Phase space including the reactive nullclines of subdomain A (orange) and B (blue) with the corresponding density distribution (thick orange and blue line). (c) Total turnover as a function of the membrane density at the template edge m_E. Total turnover balance determines the steady state value m_E^*. (d) Density profile for a case where the inflection point of the profile, x_0, lies within subdomain A, that is, when $m_A^0 > m_B$ as illustrated in the corresponding phase space representation (e). (f) In this case, the total turnover becomes a non-monotonic function of m_E, such that total turnover balance may have multiple solutions, or no solution at all. These different cases are sketched here for different average global total densities $\bar{n}$. (g) Bifurcation diagram of the base state, showing the saddle-node bifurcation due to breakdown of total-turnover balance. In the region beyond the saddle-node bifurcation (shaded in gray) no monotonic base state exists. Note that monotonicity enforces $m_E^* - m_B < 0$ here.

sensing'). Importantly, we find a simple geometric criterion for edge sensing: The reactive nullclines of the two subdomains have to intersect at a point where only one of them has negative slope, as illustrated in Fig. 5.1(d). Note that we restrict our construction to the nullcline shapes shown in Fig. 5.1(d) here. Generalizations to other arrangements follow the same principles and can be worked out analogously.

5.2.1 Monotonic steady states (base states)

In steady state, the net diffusive flux that redistributes mass must vanish and reactive flows in m and c must be balanced. This balance is encoded in the constraint that a stationary pattern's phase space distribution must be embedded in a flux-balance subspace (cf. Eq. (1.8)). This constraint is independent of the local reactions, and, hence, also holds when the local reaction are heterogeneous due to a template (purple dotted line in Fig. 5.2(b)).

Analogously to the construction of mesa patterns in Sec. 1.4.2, we can graphically construct the steady-state density profile in real space, as illustrated in Fig. 5.2(b, e). To that end, we approximate the density profile at the plateaus—where diffusive fluxes cancel everywhere—by the concentration at the FBS-NC intersections, such that the concentration at the plateaus is fully determined by the FBS-offset, η_0. Let us denote the membrane concentration at the FBS-NC intersections as $m_{\mathrm{A}}^{-}(\eta_0)$, $m_{\mathrm{A}}^{0}(\eta_0)$ and $m_{\mathrm{A}}^{+}(\eta_0)$ for subdomain A (orange nullcline) and as $m_{\mathrm{B}}(\eta_0)$ for subdomain B (blue nullcline). For specificity, we consider in the following a base state that approaches the plateaus m_{A}^{-} and m_{B} far away from the template edge. An analogous construction can be made for a monotonic state that connects m_{A}^{+} and m_{B}.[2]

The conservation of average total density $\bar{n}$ enforces a constraint on the construction of the base state. This constraint can be used to estimate η_0 from the average total density $\bar{n}$. For a domain much larger than the profile interface, the interface region can be neglected and the average total density can be approximated by the weighted average of the plateau densities in the two subdomains

$$\bar{n} \approx x_{\mathrm{E}}\, n_{\mathrm{A}}^{-}(\eta_0) + (L - x_{\mathrm{E}})\, n_{\mathrm{B}}(\eta_0), \tag{5.3}$$

with n_{A}^{-} and n_{B} the total density at the plateaus in subsystem A and B respectively. This determines an implicit, approximate relation between the control parameter $\bar{n}$ and the FBS-offset η_0.

Upon changing $\bar{n}$, the plateau concentrations of the density profile must change, and hence, η_0 must shift (cf. Eq. (5.3)). For the laterally stable plateaus, the nullcline slope at the corresponding FBS-NC intersections (m_{A}^{-} and m_{B}) is larger than the FBS-slope ($\partial_n \eta_{\mathrm{A,B}}^{*}(n) > 0$, cf. NC-slope criterion Eq. (1.11)). Hence, the relationship $\eta_0(\bar{n})$ must be monotonically increasing for stable base states, as one sees by taking the derivative of Eq. (5.3) w.r.t η_0, and using that monotonicity of a function implies monotonicity of its inverse.

Note that, even though the base state looks similar to a mesa pattern in a system on a homogeneous domain, the relationship between η_0 and $\bar{n}$ makes a key difference between the

[2] Furthermore, note that we ignore potential intersection points of FBS and B-nullcline at higher masses. In this regime, subdomain B will also exhibit lateral instability. Here, we restrict ourselves to the regime where only subdomain A becomes laterally unstable.

two cases. As we discussed in the introduction (Sec. 5.1B), in a system on a homogeneous domain, changing $\bar{n}$ does not affect η_0 in a system much larger than the interface width, but instead shifts the pattern interface (cf. Eq. (1.10)). In contrast, the interface position of a heterogeneous base state is determined by the position of the template edge x_E. Hence, to accommodate a given average mass $\bar{n}$ the plateau concentrations $n_\mathrm{A}^-(\eta_0)$ and $n_\mathrm{B}(\eta_0)$, determined by FBS-NC intersection points, must adapt (cf. Eq. (5.3)). Thus, η_0 of a heterogeneous base state depends directly on $\bar{n}$.

So far we have estimated the concentration at the two plateaus of the monotonic steady state profile. To determine how these two plateaus are connected at the template edge position x_E, we use the condition that in steady state the total reactive turnover in the system must vanish. In the vicinity of the template edge at x_E, the concentrations deviate from the local equilibria, such that there are reactive flows (illustrated by red arrows in Fig. 5.2(b)). Since the template introduces two subdomains with different reaction kinetics, the total reactive turnover in a system with a template is given by the sum over the turnover in the two subdomains,

$$\begin{aligned} F(m_\mathrm{E};\eta_0) &= F_\mathrm{A}(m_\mathrm{E};\eta_0) + F_\mathrm{B}(m_\mathrm{E};\eta_0) \\ &= \int_{m_\mathrm{A}^-}^{m_\mathrm{E}} dm\, f_\mathrm{A}(m, \eta_0 - \frac{D_m}{D_c} m) \\ &+ \int_{m_\mathrm{E}}^{m_\mathrm{B}} dm\, f_\mathrm{B}(m, \eta_0 - \frac{D_m}{D_c} m), \end{aligned} \tag{5.4}$$

where m_E is the membrane concentration at the template edge. In steady state, the total turnover $F(m_\mathrm{E};\eta_0)$ must vanish such that all reactive flows in the system balance. Thus, the solution of $F(m_\mathrm{E}^*;\eta_0) = 0$ (see Fig. 5.2(c)) determines the steady state concentration at the template edge $\widetilde{m}(x_\mathrm{E}) = m_\mathrm{E}^*$. Note that, due to monotonicity, η_0 and m_E^* uniquely identify a base state of a given system.

For small enough $\bar{n}$, the second FBS-NC intersection m_A^0 for the A-nullcline is larger than the FBS-NC intersection for the B-nullcline m_B as illustrated in Fig. 5.2(b). In this case, both summands of Eq. (5.4) are monotonic in $m_\mathrm{E} \in [m_\mathrm{A}^-, m_\mathrm{B}]$ because the reactive flow does not change sign within either subdomain, i.e. the inflection point of the profile coincides with the template edge. Hence, there is only a single solution m_E^* that fulfills total turnover balance. For larger $\bar{n}$ (and thus η_0, cf. Eq. (5.3)), m_A^0 can become smaller than m_B, as illustrated in the sketch in Fig. 5.2(d,e). This entails that the position where the reactive flows change sign (i.e. inflection point) lies in subdomain A (see Fig. 5.2(d,e)). Thus, $F_\mathrm{A}(m_\mathrm{E};\eta_0)$, and thereby also the total turnover F as a function of m_E becomes non-monotonic and may thus have multiple roots. Indeed, for increasing $\bar{n}$, our flux-balance construction predicts three different regimes: (i) A regime where there is one solution in the interval $[m_\mathrm{A}^-, m_\mathrm{B}]$, (ii) a regime with two solutions, and (iii) a regime with no solution (as illustrated in the sketch in Fig. 5.2(f)). In the last regime, total turnover balance becomes impossible for a *monotonic* steady state (base state). In Sec. 5.2.2, we will see how total turnover balance can be reached in this regime by a *non-monotonic* steady state.

The roots of F correspond to different base states which we characterize by the amplitude of the density profile in Subdomain B, $m_{\mathrm{E}}^* - m_{\mathrm{B}}$; see Fig. 5.2(g). For monotonic states (i.e. base states), $m_{\mathrm{E}}^* - m_{\mathrm{B}}$ is negative[3]. At the transition from regime (ii) to (iii), the base state undergoes a saddle-node bifurcation at $\bar{n}_{\mathrm{SN}}$. From the flux-balance construction and total turnover balance, we can estimate the position of this bifurcation. At the saddle-node bifurcation point, the minimum of F coincides with the root of F. From Eq. (5.4) it follows that F reaches its minimum at $f_{\mathrm{A}}(m_{\min}, \eta) = f_{\mathrm{B}}(m_{\min}, \eta)$. Thus, this condition, together with $F(m_{\min}; \eta_{\mathrm{SN}}) = 0$ implicitly determines the value of η_{SN} at the saddle-node bifurcation. From this we can then estimate $\bar{n}_{\mathrm{SN}}$ via (5.3).

To test this approximate construction of steady states, we use specific reaction terms f_{A} and f_{B} as specified in Appendix 5.A and compare the steady state profiles obtained from the flux-construction to the profiles obtained from numerical continuation (see Appendix 5.E for a short description of numerical continuation and the comparison of steady states. A more detailed explanation of continuation methods can be found in Ref. [185]). We find that the flux-balance construction gives a estimate of the steady states profiles for sufficiently large system sizes (see Appendix 5.E).

As we noted above, there is also a family of base states which connects a plateau at m_A^+ (instead of m_A^-) in subdomain A to m_{B} in subdomain B. These base states have a high average mass, and we will refer to them as 'high-mass' base states. Following the same arguments as above, we find that these base states undergo a saddle-node bifurcation when the average total mass is decreased below a critical average mass, analogously to the saddle-node bifurcation of 'low-mass' base states discussed in this section.

In summary, we have shown how to find monotonic steady states (base states) with a flux-balance construction. Notably, we found that for a range of total mass $\bar{n}$, this flux-balance construction has no solution, and hence, there exist no monotonic steady states. In this regime, the steady states must be non-monotonic. We next study these non-monontonic steady states, which we refer to as *patterns*.

5.2.2 Non-monotonic steady states (patterns)

To gain some intuition about the structure of the stationary patterns, we first calculate them numerically as a function of the average total density $\bar{n}$ using numerical continuation[4] for a specific choice of the reaction term $f(m, c; \theta)$ specified in Appendix 5.A. The resulting one-parameter bifurcation structure shows that the system exhibits two stable patterns, one with a peak (high density region) at the template edge and one with a peak at the system boundary, respectively (see Fig. 5.3(a)). In the bifurcation structure, the

[3]Note that for high-mass base states, monotonicity enforces $m_{\mathrm{E}}^* - m_{\mathrm{B}} > 0$, in the case of a nullcline arrangement as shown in Fig. 5.1.

[4]See Appendix 5.E for a brief description of the core idea behind numerical continuation. An excellent overview is provided in Ref. [185].

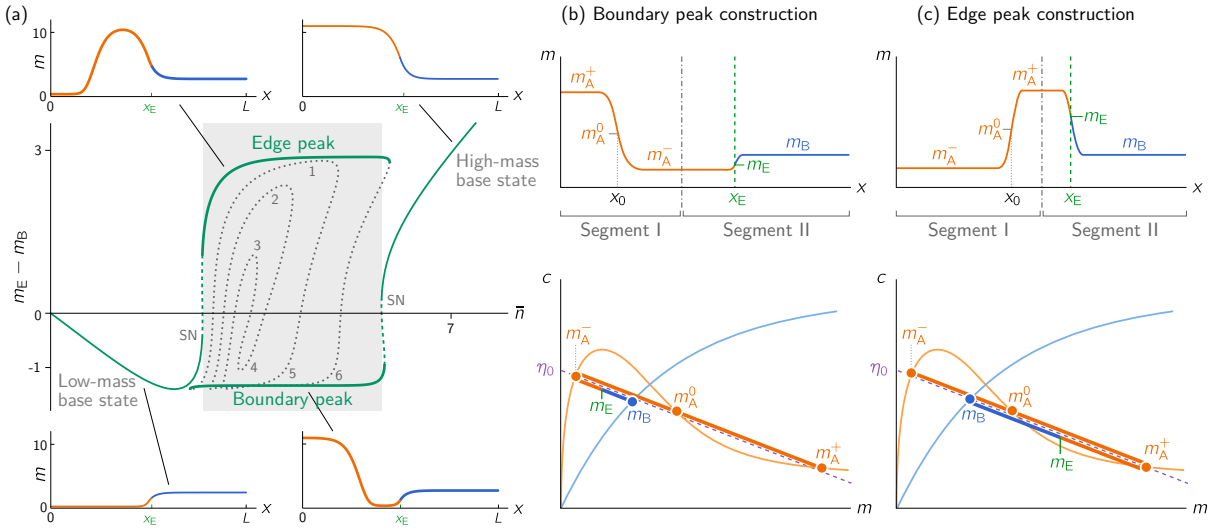

Figure 5.3 | Bifurcation structure and phase space construction of stationary patterns. (a) Bifurcation structure of stationary states for the average mass, $\bar{n}$, obtained by numerical continuation, together with spatial profiles for the stable steady states (montonic base states and non-monotonic patterns). In the area shaded in gray, no monotonic base states exist. Solid (dashed) lines indicate stable (unstable) branches. The unstable branches in the central region, marked by numbers 1–6 correspond to unstable patterns with multiple inflection points in subdomain A (see Fig. 5.12 in Appendix 5.E). The instability of these patterns is related to coarsening, which is generically exhibited by two-component McRD systems on a homogeneous domain ([93, 94, 108, 109]). (b,c) Sketches of stable, non-monotonic, stationary patterns together with the corresponding phase space constructions. At the density profile's extremum, marked by the dash dotted vertical line, there are no gradients ($\partial_x \widetilde{m} = 0 = \partial_x \widetilde{c}$), such that a notional no-flux boundary can be introduced. Thus, the resulting two segments (labelled I and II), can now be studied separately. In the phase portraits, the density distributions of the two segments connect at the extremal concentrations m_{A}^- and m_{A}^+, in (a) and (b) respectively. They are shown slightly offset from the FBS (dashed purple line) for visual clarity. The true density distribution must of course be embedded in a single FBS to fulfill diffusive flux-balance.
Parameters for the bifurcation diagram: $D_m = 0.01$, $D_c = 0.5$, $\hat{k}_{\mathrm{fb}} = 0.25$, $\hat{k}_{\mathrm{off}} = 4$, $\theta_{\mathrm{B}} = 20$, $\theta_{\mathrm{A}} = 2$, $L = 10$, $x_{\mathrm{E}} = 5$.

branches of stable patterns are connected to the base states via an unstable steady states (green dashed branches in the bifurcation structure in Fig. 5.3(a), see also Fig. 5.11 in Appendix 5.E). Between the two branches of stable patterns, there is a cascade of unstable patterns (numbered 1–6 in Fig. 5.3(a); see Fig. 5.12 in Appendix 5.E for representative density profiles). The instability of these patterns that have multiple interfaces within subdomain A can heuristically be understood as a coarsening process due to a competition for total density, similarly as in a system on a homogeneous domain [93, 94, 108, 109]. Some more technical aspects of this bifurcation structure are discussed in Appendix 5.E.

Can we use the flux-balance construction to construct non-monotonic steady states as well? At the extrema of any stationary pattern in a two-component McRD system, the gradients (and hence diffusive flux) in *both* membrane and cytosol concentration vanish simultaneously (cf. diffusive flux-balance Eq. (1.8)). This allows us to place notional reflective boundaries at extrema, effectively splitting the non-monotonic profile into monotonic segments. Thus, we can use the flux-balance construction as described in Sec. 5.2.1 to construct the steady states in the two segments separately, with the additional constraint of continuity at the boundaries connecting the segments.

The stable patterns in the two-component McRD system with a step-like template have only a single peak, and hence only a single extremum within the domain that splits the system into two segments (labelled I and II; see Fig. 5.3(b,c)). Segment I is fully embedded in subdomain A, i.e. it is a system on a homogeneous (sub)domain. Hence, for sufficiently large domain size, its steady state is a mesa pattern[5] as introduced in Sec. 1.4.2. The orientation of the mesa pattern in segment I determines whether the density peak is located at the left domain boundary or at the template edge. segment II contains the template edge, such that the steady state in segment II is a heterogeneous base state.

By continuity, the FBS-offset η_0 must be identical in both segments. Recall that for a mesa pattern, η_0 is determined by total turnover balance, and independent of the average mass and domain size in the large domain size limit (see Sec. 1.4.2 and Ref. [56]). We can thus find η_0 solely by total-turnover balance in segment I, without specifying the position of the boundary between the segments, and without specifying the average masses in the two segments respectively. Instead, given η_0, we find the average mass in segment II, $\bar{n}_{\mathrm{II}}$, via Eq. (5.3), which depends on the choice for the orientation of the mesa pattern in segment I. In segment II, subdomain B plays the role of a mass-reservoir that absorbs a fraction of the total average mass and thus reduces the mass available to the mesa pattern in segment I, $\bar{n}_{\mathrm{I}} = \bar{n} - \bar{n}_{\mathrm{II}}$. Finally, $\bar{n}_{\mathrm{I}}$ determines the position of the mesa pattern's interface in segment I via Eq. (1.10). Similarly, we can construct the (unstable) patterns with multiple peaks by splitting the system into more than two segments.

[5] In the vicinity of the saddle-node bifurcations of these patterns, segment I exhibits a peak pattern instead of a mesa pattern. To obtain an approximation for this case, one would need to generalize the peak approximation as discussed in Ref. [56].

We conclude that the flux-balance construction fully characterizes the stationary patterns of the system with a step-like template. These steady states exhibit density peaks similar to a system on a homogeneous domain, however, the position of the density peak depends on the template edge position.

We next ask which of the two stable patterns emerges as the base state ceases to exist. To that end, we use finite element simulations and adiabatically increase the total average density in a system such that it passes through the base-state bifurcation (Supplementary Movie 1). The system evolves into a pattern with a peak at the template edge (corresponding to the upper branch in Fig. 5.3(a)). Upon further increase of $\bar{n}$ the peak widens and eventually transitions into a mesa pattern at the template edge. The right hand interface of the mesa patter remains localized at the template edge while the left hand interface moves into subdomain A to accommodate the additional mass (cf. Eq. 1.10). Eventually for even larger $\bar{n}$, the mesa pattern ceases to exist as its interface hits the left boundary of the domain. The system then transitions to the 'high-mass' base state which connects the FBS-NC intersection points m_{A}^{+} and m_{B}. Going backwards by adiabatically decreasing $\bar{n}$, the system passes through the 'high-mass' base state's saddle-node bifurcation. The corresponding regional instability leads to the formation of a trough, rather than a peak, at the template edge. The resulting stationary pattern has a minimum at the template edge and a maximum at the left boundary (corresponding to the lower branch in Fig. 5.3(a)) (Supplementary Movie 2). Upon further decrease of $\bar{n}$, the interface of this pattern will reach the left boundary of the domain such that the system transitions back into the low-mass base state.

These transitions also take place when the average mass is changed non-adiabatically but still so slow that mass-transport across the system by cytosolic diffusion ($\sim L^2/D_c$) is faster than the rate at which mass is added or removed. Interestingly, when we increase the mass on a non-adiabatic timescale we observe multiple transient patterns, which we characterize in Appendix 5.D. Furthermore, we show that we can get similar transitions between the base state and the patterns if, instead of increasing the average mass, the local reactions $f_{\mathrm{A,B}}$ in the two subdomains are varied over time (Appendix 5.C).

Taken together, we have shown that the flux-balance construction can be used to construct non-monotonic steady states by splitting the density profile into monotonic segments. This is possible because, the stationary pattern profile can be split at extrema, where all diffusive fluxes vanish. We found that the system can exhibit two patterns, with a density peak either at the system boundary or at the template edge. The peak at the template edge only exists when the two nullclines intersect at a point where only one of them has negative slope. Furthermore, our finite element simulations show that increasing the mass, starting from the low-mass base state, leads to a peak at the template edge. Vice versa, decreasing mass, starting from the high-mass base state leads to a peak at the system boundary. In the next Section we provide a heuristic argument to understand under which conditions the peak emerges at the template edge.

5.2.3 Template-induced regional instability

We next want to understand the mechanism of pattern selection as the system goes through the saddle-node bifurcation(s) where the base state ceases to exist. We first show that a (numerical) linear stability analysis explains why either a peak or a trough pattern grows at the template edge, as the system goes through the bifurcation. We then provide a heuristic argument to explain this edge-sensing mechanism, and formulate a geometric criterion under which this mechanism works, based on the shape of the nullclines.

To study how the base state develops into a pattern, as the system goes through the saddle-node bifurcation, we consider a base state $(\widetilde{m}(x), \widetilde{c}(x))$ in the vicinity of the bifurcation point and analyze the dynamics of a small perturbation $(\delta m(x,t), \delta c(x,t))$. The dynamics of the perturbed state, up to linear order is given by:

$$\partial_t \delta m(x,t) = D_m \partial_x^2 \delta m + \tilde{f}_m(x)\delta m + \tilde{f}_c(x)\delta c\,, \tag{5.5a}$$

$$\partial_t \delta c(x,t) = \; D_c \partial_x^2 \delta c \; - \tilde{f}_m(x)\delta m - \tilde{f}_c(x)\delta c\,. \tag{5.5b}$$

The linearized reaction coefficients

$$\tilde{f}_{m,c}(x) = \partial_{m,c} f\big|_{(\widetilde{m}(x),\widetilde{c}(x))} \tag{5.6}$$

are not homogeneous in space and hence Eq. (5.5) is a set of linear PDEs with nonconstant coefficients. We seek solutions of the form $\delta m(x,t) = \Phi_m(x)e^{\sigma t}$, $\delta c(x,t) = \Phi_c(x)e^{\sigma t}$. With this ansatz, Eq. (5.5) turns into the Sturm–Liouville eigenvalue problem

$$\sigma\Phi_m(x) = D_m \partial_x^2 \Phi_m + \tilde{f}_m(x)\Phi_m + \tilde{f}_c(x)\Phi_c\,, \tag{5.7a}$$

$$\sigma\Phi_c(x) = \; D_c \partial_x^2 \Phi_c \; - \tilde{f}_m(x)\Phi_m - \tilde{f}_c(x)\Phi_c\,, \tag{5.7b}$$

for the eigenvalues σ and the associated eigenfunctions $(\Phi_m, \Phi_c)(x)$.

The defining feature of a a saddle-node bifurcation is that one eigenvalue vanishes exactly at the bifurcation point. The associated eigenfunction reveals the flow structure of the dynamics on the slowest timescale close to the bifurcation point (center manifold, see e.g. Ref. [184]). From this we can gain intuition about the fate of the system upon passing through the bifurcation.

At the base-state saddle-node bifurcation (marked SN in Fig. 5.3(a)), the numerically calculated[6] eigenfunction is peaked in the vicinity of the template edge (see Fig. 5.4(a)). This localized eigenfunction indicates that the density profile will change most in the vicinity of the template edge, giving rise to either a peak or a trough as the system goes through the saddle-node bifurcation.

[6] The Sturm–Liouville eigenvalue problem at the numerically calculated base-state saddle-node bifurcation is solved by discretizing the spatial derivatives (Laplace operator) and solving the resulting eigenvalue problem numerically in Mathematica. For further details see e.g. Ref. [186].

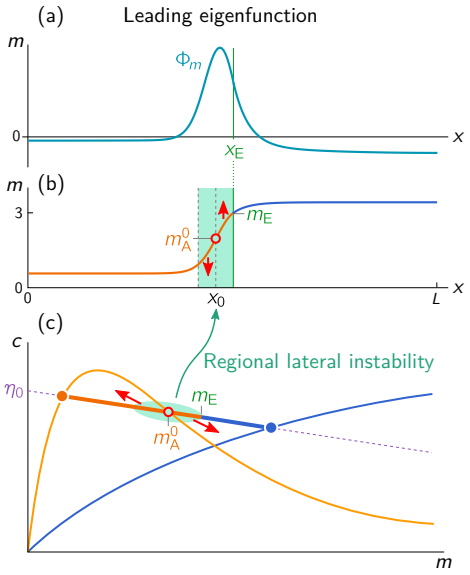

Figure 5.4 | Regional lateral instability at the base state's saddle-node bifurcation. (a) The numerically calculated eigenfunction, Φ_m, associated to the vanishing eigenvalue at the saddle-node bifurcation is localized at the template edge. (Parameters as in Fig. 5.3 at the saddle-node bifurcation $\bar{n} \approx 2.65541$). (b) The concentration profile $\widetilde{m}(x)$ of the base state at the saddle-node bifurcation. A spatial region that is fully contained in subdomain A and centered around the profile's inflection point x_0 is marked in green. (c) This spatial region corresponds to a phase space region where the dynamics is guided by a section of the nullcline with a negative slope, i.e. where the system is laterally unstable. (The phase space is shown as a sketch for visual clarity. See Fig. 5.7(a) in Appendix 5.B for a plot from numerical simulation.)

An intuition why the neutral eigenfunction at the base-state saddle-node bifurcation is peaked at the template edge can be gained from the phase portrait as sketched in Fig. 5.4(c)). Recall, that the inflection point of the base state's density profile $m_\mathrm{A}^0 = \widetilde{m}(x_0)$ lies within subdomain A (cf. Fig. 5.2(d,e)). Consider a region centered around x_0, fully contained within subdomain A, as indicated in green in Fig. 5.4(b). In phase space this point lies on a section of the A-nullcline with a slope steeper than the FBS. Suppose for a moment that this region is isolated from the rest of the system. Then, as the slope of the nullcline at m_A^0 is steeper than the slope of the FBS, the homogeneous equilibrium in this region will be unstable due to a mass-redistribution instability. This instability will set in when the region is large enough to contain the shortest growing mode[7]. We call this a *regional (mass-redistribution) instability*.

A necessary condition to trigger a regional instability at the template edge is that the nullclines of the two subdomains cross at a point where the the A-nullcline fulfills the

[7]More precisely, the size of the region centered around the inflection point, $2(x_\mathrm{E} - x_0)$, must be larger than the wavelength of the shortest growing mode $\pi/q_{\min}(n_0)$.

nullcline-slope criterion for lateral instability, Eq. (1.11) (see Fig. 5.5(a)). When this edge-sensing criterion is not fulfilled, as shown in Fig. 5.5(b), the regional instability sets in at the system boundary first, giving rise to a peak at the system boundary and not at the template edge (as illustrated in Fig. 5.7(b) in Appendix 5.B). Because the shapes of the nullclines in the two subdomains relative to each other depend on how the template affects the reaction kinetics, the edge-sensing criterion constrains models that can exhibit edge sensing. In Appendix 5.F we demonstrate that the edge-sensing criterion precisely predicts the regime of edge sensing for a phenomenological model of Cdc42. We furthermore show that edge sensing only works if the template increases both the attachment and detachment rate of Cdc42 in one of the subdomains. This may help to identify the relevant molecular players in biological systems.

The concept of regional instability was already discussed in Ref. [56] in the context of excitability ("nucleation and growth") for a homogeneous domain. There, a stable homogeneous steady state is perturbed by moving mass from the system into small region. When this region contains sufficient mass, it can become laterally unstable and thus formation of a peak pattern is "nucleated." With that, the regional instability at the template edge can also be understood in terms of lateral excitability. From the perspective of subdomain A, the differing reaction kinetics in subdomain B induces a perturbation at the subdomain interface, that is, the template edge (orange line in Fig. 5.4(b)). In that sense, the base state is a perturbed homogeneous steady state in each subdomain. If in subdomain A, this perturbation becomes large enough to cross the nullcline in a section of negative slope (Fig. 5.4(c)), it triggers a lateral instability and thus the formation of density peak at the template edge. This relationship to excitability highlights that it is the spatial *gradient* of

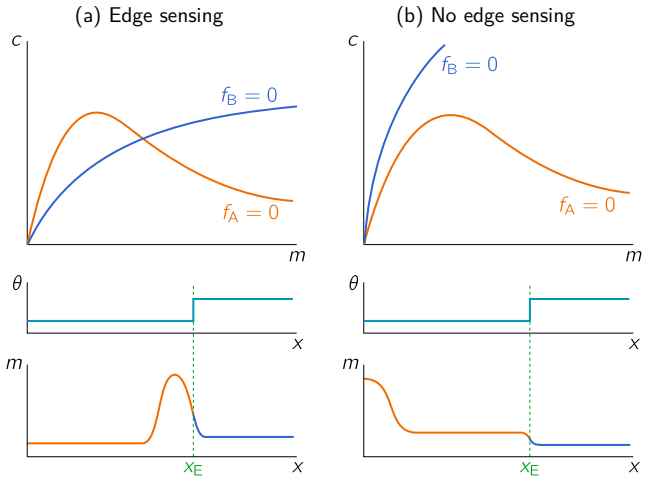

Figure 5.5 | Nullcline criterion for edge sensing, i.e. the emergence of a stable density peak at the template edge. Edge sensing is possible is the nullclines intersect in a point where one of them has negative slope (a). If they don't intersect (b) or intersect in a point where they have both positive (or both negative) slope, stable peaks only exist at a system boundary, and hence, edge sensing is not possible.

the reaction kinetics due to the template that localizes the instability. Heuristically this can be pictured as sensing the spatial derivative of the template. Here we focussed on a sharp template edge. For future work, it will be interesting to study also a smooth template edge. Intuitively, if the template gradient is too shallow, it will not induce a laterally unstable region, because the induced deviation from the local equilibria that effectively acts as the perturbation in the analogy to excitability will be too small.

In conclusion, we showed in this section that the template localizes the patterns and determines the position of the instability from which they emerge. Importantly, this instability determines which of the two stable stationary patterns forms when the system passes through a bifurcation of the base state. Finally, we presented a simple geometric criterion, shown in Fig. 5.5, that determines when the regional instability is localized at the template edge.

5.3 Moving template edge

Until now we considered pattern formation with a fixed template edge position x_E. We next ask what happens when x_E moves after a peak at the template edge has been established (Fig. 5.6).

When the template edge moves, the peak must adapt to the new template edge position. In order to reach the new stationary state, mass must be transported from one side of the peak to the other. Thus, we expect that the peak follows the template edge position as long as the mass is transported faster than the velocity v_E at which the template edge moves, i.e. for $v_\mathrm{E} \ll D_c/w$, where w is the width of the peak. To test the intuition for this adiabatic case, and study what happens in the non-adiabatic case of a fast-moving template edge, we turn to numerical simulations. To probe a range of template velocities v_E, we quadratically increase the template edge velocity during the simulation. At a distance $0.3\,L$ from the system boundary, the template movement is stopped. Furthermore, we move the interface either to the right, away from the peak Fig. 5.6(a,c) or to the left, towards the peak Fig. 5.6(b,d). In the adiabatic case, we find—in agreement with our expectation—that the peak remains pinned to the template edge position (see Fig. 5.6(a,b) and SI Movies 3 and 4).

In the non-adiabatic case, when the template edge moves faster than the peak can follow by diffusive mass transfer, the peak position will shift relative to the template edge. We find that, when the template moves away from the peak ('pulling'), the peak depins at a critical velocity and stops following the template edge (see Fig. 5.6(c) and SI Movie 5). Because peaks in the interior of subdomain A are unstable (cf. Figs. 5.3(a) and 5.12, the depinned peak will move very slowly either to the domain boundary or to the template edge (given that the movement of the template edge has stopped). There it reaches the respective stable steady state, a "boundary peak" or an "edge peak" (cf. Figs. 5.3(a)).

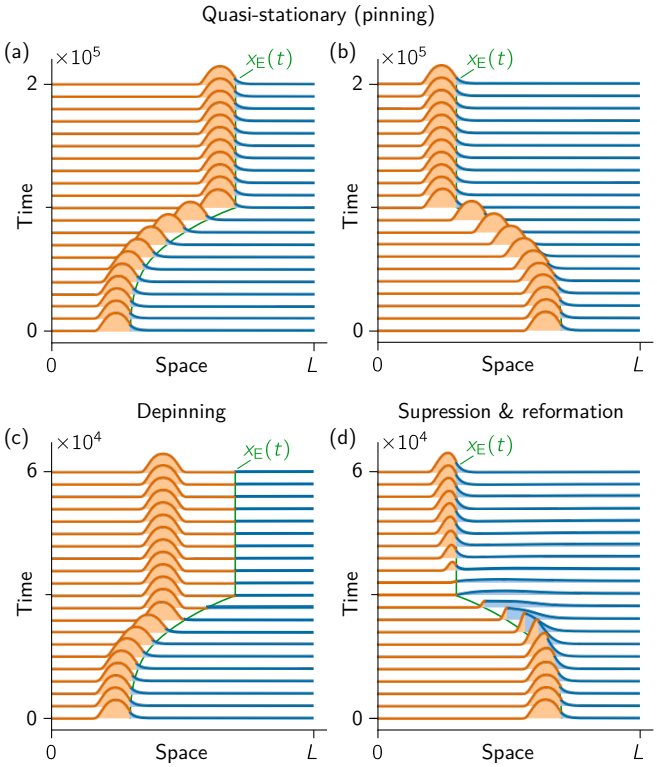

Figure 5.6 | Time evolution of m-profile due to dynamic template interface position. The supplementary material contains a movie for each of the four scenarios. (a) Slow pull (the template edge moves away from the peak): This results in pinning of the peak to the template edge (see SI Movie 3). (b) Slow push (the template edge moves towards the peak): This results in pinning of the peak to the template edge (see SI Movie 4). (c) Fast pull: This results in depinning as the peak cannot follow the template edge. However, the peak stays where it depins as it is quasi-stable in region A on the observed timescale (see SI Movie 5). (d) Fast push: This results in suppression as the peak is not stable in region B. As the peak dissipates the average mass at the new edge position slowly increases and potentially (if there is enough total mass in the system) leads to to a re-entrance of the peak (see SI Movie 6).
Parameters: $D_m = 0.01$, $D_c = 10$, $k_{\mathrm{on}} = 1$, $\hat{k}_{\mathrm{fb}} = 1$, $k_{\mathrm{off}} = 2$, $\hat{K}_{\mathrm{d}} = 1$, $\bar{n} = 5$, $\theta_{\mathrm{B}} = 20$, $\theta_{\mathrm{A}} = 0.5$, $L = 20$, $x_{\mathrm{E}} = 3/5\,L$, $v_{\mathrm{E}}(t) = \pm 2.4 \times 10^{-14}\,t^2$ in (a) and (b), $v_{\mathrm{E}}(t) = \pm 8.9 \times 10^{-13}\,t^2$ in (c) and (d).

When the template moves towards the peak ('pushing'), the peak is suppressed at some critical edge-velocity (see Fig. 5.6(d) and SI Movie 6). Interestingly, the critical velocity for depinning while pulling is much lower than the critical velocity for suppression while pushing.

To heuristically understand this difference of critical velocities, we take a closer look at how the peak adapts to a shifted template position. Suppose for a moment that we keep the peak profile frozen while shifting the template edge x_E by a small amount δx_E. This will change the local reactions in the vicinity of the template edge. When the peak profile is now "released", these reactions will lead to changes in the concentrations m and c, and hence in the mass-redistribution potential $\eta(x,t)$ between the original and shifted edge positions x_E and $x_\mathrm{E} + \delta x_\mathrm{E}$. The resulting η gradient leads to mass transport (Eqs. (1.6)), which in turn causes a movement of the peak.[8] The difference between pulling and pushing, i.e. moving the template edge away from the peak or towards it, is the amplitude of the η gradient that builds up as the template edge is shifted. In the case of pulling, the template edge moves into the flat tail of the peak, such that the η gradient decreases with increasing distance between peak and template edge. In contrast, while pushing, the template edge moves into the steep interface of the peak, leading to an continually increasing η gradient. Only when the template edge has shifted beyond the maximum of the peak, the induced η gradient starts decreasing again.

This effect qualitatively explains the different critical velocities for depinning (while pulling) and suppression (while pushing). In the former case the induced gradients in η, and hence, the rate of mass transport that shift the peak towards the moving template edge are small and decreasing with peak-to-edge distance. Therefore, depinning is self-enhancing. In the case of pushing, the η gradient keeps increasing as the peak-to-edge distance decreases. This in turn, increases the speed of the peak due to faster mass transport. Only when the template edge has crossed the peak maximum, the peak will be suppressed because it then lies mostly within the laterally stable subdomain B that does not support a stable peak.

In summary, we showed that in the case of an adiabatically slow template motion, the peak stays pinned at template edge. In the non-adiabatic case we found a qualitatively and quantitatively different behavior between pushing and pulling. Pulling leads to depinning, while pushing eventually leads to suppression. Furthermore, we heuristically explained why critical velocity for pulling (depinning) is lower than the critical velocity for pushing (suppresion). Going forward, it would be interesting to study this behavior more systematically, both in numerical simulations and on an analytic level. For example, concepts like response functions [187], projection onto slow manifolds [176] and singular perturbation theory [179, 180] may help to estimate the critical velocities for depinning and suppression.

[8] A geometric analysis in phase space, similar to the one presented in Figs. 5.2 and 5.3, shows that the η gradient is always such that the peak moves in the direction that the template edge was shifted, until it reaches it's new stationary (pinned) position at the shifted edge position.

5.4 Discussion

We showed how protein pattern formation can be controlled by a spatial template (e.g. an upstream protein pattern), which acts on the proteins interaction kinetics. In particular, we demonstrated for two-component McRD systems how a step-like template—which defines two subdomains with different reaction kinetics—can localize the formation of a peak pattern to the template edge. We explained this edge-sensing mechanism by a regional (mass-redistribution) instability that emerges at the template edge position. This is in contrast to pattern formation on a homogeneous domain, where the instability is generically "delocalized" (Fourier modes, cf. Fig. 1.1(d)), such that noisy initial conditions have a strong impact on pattern formation process.

Our analysis is based on a recently developed theoretical framework [49, 56], termed local equilibria theory. This theory proposes to analyze McRD systems as dissected into diffusively coupled compartments, so small that each of the compartments can be considered as well-mixed. For the paradigmatic (minimal) case of two-component systems, this framework enables one to to perform phase-portrait analysis of the interplay between local reactions and diffusive transport in the phase space of the reaction kinetics. Here, we have extended this phase-portrait analysis to incorporate the effect of a step-like heterogeneity of the reaction kinetics in the spatial domain. We were able to construct the bifurcation diagram for the average mass $\bar{n}$, which is a natural control parameter as it can be controlled by production or degradation/sequestration of proteins in cells (e.g. in a cell cycle dependent manner). We found that, at a critical average mass, the system's base state undergoes a saddle-node bifurcation, such that the system transitions to a stationary pattern, with either a peak at the template edge or at the system boundary. The peak forms at the template edge if the template triggers a regional (mass-redistribution) instability at the template edge. The phase-portrait analysis enables us to formulate a geometric criterion for this edge-sensing mechanism. In particular, we show that the step-like template can trigger a regional instability at the template edge, if the nullclines of the reaction kinetics in the two subdomains intersect at a point where one of them has a negative slope (more precisely, a slope steeper than the negative ratio of the diffusion constants, $-D_m/D_c$), as illustrated in Fig. 5.5. Finally, we showed that the edge-localized peak is stable when the template edge is slowly moved and demonstrated that qualitatively different processes—depinning vs. suppression—lead to the loss of the edge-localized peak when the template is shifted too rapidly away from the peak ('pulling') or towards it ('pushing').

We speculate that the edge-sensing mechanism studied here might underly formation of the actomysin ring during macropinocytosis and cellular wound healing, as well as the direction of Cdc42 polarization in budding yeast adjacent to the previous bud-site. In macropinocytosis a high density PIP3 domain has been suggested to act as a template for a ring of actin nucleators that localize to its periphery [22]. Similarly, during cellular wound healing, the inside Abr could act as a template for the outside Cdc42 ring which then drives recruitment of actin via formins [19]. Finally, in budding yeast, landmark pro-

teins that localize to the previous bud-site can be pictured as a template that suppresses Cdc42 accumulation at the previous bud-site and simultaneously localizes Cdc42 cluster to its vicinity [17, 18, 20, 23]. Furthermore, the spatio-temporal organization of intracellular membranes, like the Golgi apparatus, endosomes, and the endoplasmatic reticulum, involves cascades of coupled GTPases [188–190]. Hence, we speculate that this organization may rely on similar domain-edge sensing mechanisms.

The edge-sensing criterion (cf. Fig. 5.5) based on the shape of the nullcline, may provide guidance for the mathematical modeling of these systems and thereby help to identify the key bio-molecular players and processes. The nullcline shapes of a given model constrain the ability of this model for edge-sensing. As an example, we showed for an phenomenological two-component model for Cdc42 pattern formation [91] that edge sensing requires a template which increases both the attachment and detachment rate of Cdc42 in one subdomain. Indeed in single-cell wound healing, the protein Abr could provide such a template for Cdc42 since it is both a guanine exchange factor (GEF) and a GTPase-activation protein (GAP) for Cdc42 [19].

Beyond the understanding of living systems, our results may also advance the field of synthetic biology. Previous studies have explored mechanisms by which a gradient can position a sharp front pattern via a bistable reaction-diffusion system [157, 191]. The edge-sensing mechanism, presented in this paper, is a candidate for a further building block to design spatial protein patterns.

In future studies, it would be interesting to generalize our results beyond the paradigmatic case of a single, stationary, step-like template in one spatial dimension. Templates with multiple steps may be dissected into segments with single steps that can then be studied separately. Furthermore, it has been shown that the geometry of a cell indirectly affect the attachment–detachment kinetics via the ratio of bulk-volume to surface-area [6, 192], and curvature sensing proteins [10]. Another promising direction is to incorporate the dynamics of the template itself as a self-organized pattern-forming system, and include a feedback from the downstream pattern to the template. Such feedback may give rise to complex spatio-temporal behavior like oscillatory patterns and traveling waves that can then be characterized by building on the phase-portrait analysis presented here. Our results on the moving template (Sec. 5.3) and non-adiabatic upregulation of average mass (Appendix 5.D) indicate that the edge sensing works beyond the adiabatic regime.

Finally, even for the elementary case studied here, many important questions remain open. We showed that a moving template will lead to a loss of the edge-localized peak due to depinning (while pulling) or suppression (while pushing) at different critical edge-velocities. In future work, these transitions should be studied in more detail both numerically and analytically, e.g. using a response function formalism [187]. Furthermore, an analytic approach employing asymptotic methods like singular perturbation theory [176, 179, 180, 183] may help to cast our heuristic explanation of the localized eigenfunction, based on the concept of regional instability, into a more rigorous argument. Similarly, such an approach may elucidate the transition from edge-localized peaks to boundary-localized peaks for too

fast mass upregulation (cf. Appendix 5.D, Fig. 5.10). In general, we expect that combining mathematical tools like singular perturbation theory with the local equilibria framework will be a fruitful approach to systematically study complex pattern-forming systems.

Appendices

5.A Reaction kinetics and template definition

Throughout this paper we use a two-component McRD model on a one-dimensional domain with one protein species (cf. Eq. (1.4a) and (1.4b)). The proteins cycle between a cytosolic state (concentration $c(x,t)$) and membrane bound state (concentration $m(x,t)$) as specified by the reaction term $f(m,c)$. Importantly, our results are based on the shape of the reactive nullclines and, hence, don't depend on the specific choice for $f(m,c)$. To illustrate our findings, we use biochemically motivated reaction kinetics, comprising attachment, $a(m)$, and detachment, $d(m)$, reactions

$$f(m,c) := a(m)c - d(m)m \ . \tag{5.8}$$

Specifically we use

$$a(m) := (k_{\mathrm{on}} + k_{\mathrm{fb}}\, m)\,, \tag{5.9a}$$

$$d(m) := \frac{k_{\mathrm{off}}}{K_{\mathrm{d}} + m}, \tag{5.9b}$$

as introduced before in Ref. [56]. These reaction kinetics describe a protein species that can attach from the cytosol to the membrane with a rate k_{on} and get recruited from the cytosol to the membrane by membrane bound proteins with a rate k_{fb}. Membrane bound proteins detach from the membrane via an enzymatic process described by first order Michaelis-Menten kinetics, parameterized by the rate k_{off} and the dissociation constant K_{d}.

We consider systems were the reaction rates are different in subdomains A and B. This externally imposed heterogeneity was introduced as a step-like template in Sec. 5.1.2 (cf. Eq. (5.1)). For specificity, we choose a template that affects the reaction rates, such that the reactive nullcline in subdomain B is stretched along the m-axis with respect to the reactive nullcline in subdomain A. To that end, we rescale the feedback rate and the dissociation constant scale with the template value, such that these rates become space dependent

$$k_{\mathrm{fb}}(x) := \hat{k}_{\mathrm{fb}}/\theta(x), \tag{5.10a}$$

$$K_{\mathrm{d}}(x) := \hat{K}_{\mathrm{d}}\,\theta(x). \tag{5.10b}$$

The reaction term then becomes

$$f(m,c;\theta) = \left(k_{\text{on}} + \hat{k}_{\text{fb}}\,\frac{m}{\theta(x)}\right)\,c - \frac{k_{\text{off}}\,\frac{m}{\theta(x)}}{\hat{K}_{\text{d}} + \frac{m}{\theta(x)}}\ . \tag{5.11}$$

For convenience, we do not specify units of length and time. In an intracellular context a typical size would be $L \sim 10\ \mu$m, and typical diffusion constants are $D_m \sim 0.01{-}0.1\ \mu\text{m}^2\text{s}^{-1}$ on the membrane and $D_c \sim 10\ \mu\text{m}^2\text{s}^{-1}$ in the cytosol. Rescaling to different spatial dimensions is straightforward. To fix a timescale, the kinetic rates can be rescaled with respect to the attachment rate k_{on}. In an intracellular context, typical attachment timescales are on the order of seconds, i.e. $k_{\text{on}} \sim \text{s}^{-1}$.

5.B Nullclines without edge-sensing

In Sec. 5.2.3 in the main text, we analyzed the edge-sensing mechanism based on the reactive nullclines in phase space. In this analysis, the effect of the heterogeneous reaction kinetics, i.e. the template, is captured by the shapes of the reactive nullclines. From our analysis, we found a criterion for the edge-sensing mechanism, as illustrated in Fig. 5.4. The nullclines need to intersect at a point where only one nullcline is steeper than FBS (cf. Eq. (1.11)).

In this appendix, we discuss a case where the criterion for edge sensing is not fulfilled, such that a localization of the regional instability to the edge is not possible, and a peak at the template edge does not exist (cf. Fig. 5.5(b)). As an example, we consider a template, affecting the reaction kinetics such that the nullcline is stretched along the c-axes instead of the m-axis, as shown in Fig. 5.7(b).

For the specific attachment–detachment reaction kinetics (Eq. (5.9)), the nullclines is stretched along the c-axis via the off-rate while keeping all other rates constant:

$$k_{\text{off}}(x) := \hat{k}_{\text{off}}\,\theta(x). \tag{5.12}$$

The resulting reaction term then reads

$$f(m,c;\theta) = (k_{\text{on}} + k_{\text{fb}}\,m)\ c - \theta(x)\frac{\hat{k}_{\text{off}}\,m}{K_{\text{d}} + m}. \tag{5.13}$$

Following the same arguments as presented in Sec. 5.2.1,we can construct the base states (monotonic steady state). Starting from the low-mass base state, illustrated in Fig. 5.7(a), and increasing the average mass $\bar{n}$ results in an upwards shift of the FBS by the same argument as presented in Sec. 5.2.1. When the mass is further increased the FBS moves to the level where the two FBS-NC intersection points on the A-nullcline, m_A^- and m_A^0, annihilate in a saddle-node bifurcation, as shown in Fig. 5.7(b). If η_0 increases beyond that point, the base state vanishes. Note that the origin of the saddle-node bifurcation

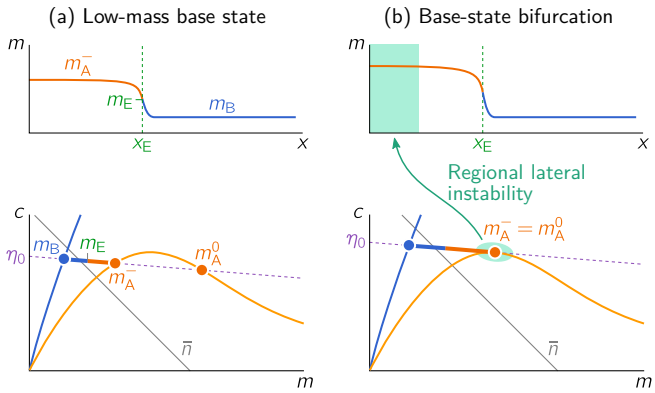

Figure 5.7 | Base states for nullclines shapes that do not facilitate edge-sensing. (a) The low-mass base state with a high-concentration plateau in subdomain A and a low-concentration plateau in subdomain B. (b) At a critical average mass, the base state undergoes a saddle-node bifurcation. The bifurcation arises from the 'annihilation' of the FBS-NC intersection point m_A^- and m_A^0, and not from the break down of turnover balance as discussed in Sec. 5.2.3 the main text. In this case, a regional instability is triggered at the system boundary. An adiabatic sweep of $\bar{n}$ through the saddle-node bifurcation of the FBS-NC intersection points is shown in Supplementary Movie 7.

lies in the annihilation of the two FBS-NC intersection points. This is different from the saddle-node bifurcation that occurs for the nullclines we analyzed in Sec. 5.2.1 in the main text. There, the base state vanishes due to a breakdown of total turnover balance which becomes apparent by the 'annihilation' of the two solutions for m_E of Eq. (5.4); cf. Fig. 5.2.

To study the dynamics in the vicinity of the base state bifurcation, we use the concept of regional instability (cf. Sec. 5.2.3). The part of the density distribution that enters the laterally unstable region in phase space corresponds to the concentration at the left hand system boundary ($x = 0$) (Fig. 5.7(b)). Hence, upon crossing the base state's saddle-node bifurcation, a regional instability emerges at this system boundary, and a peak forms there.

Moreover, for nullclines shown in Fig. 5.7, there is only one way to construct a stationary pattern with a single interface (inflection point) within subdomain A (in addition to the interface imposed by the template step). This pattern always has a density peak at the system boundary ($x = 0$) and decreases monotonically in space towards $x = L$. A stable peak localized to the template edge does not exist in this case.

5.C Temporal variation of the template

In Sec. 5.2 in the main text, we considered upregulation of average mass $\bar{n}$ while the spatial template was kept constant. One can perform a similar analysis for a varying template, while keeping the average mass constant. In this scenario, not $\bar{n}$ but the parametrization

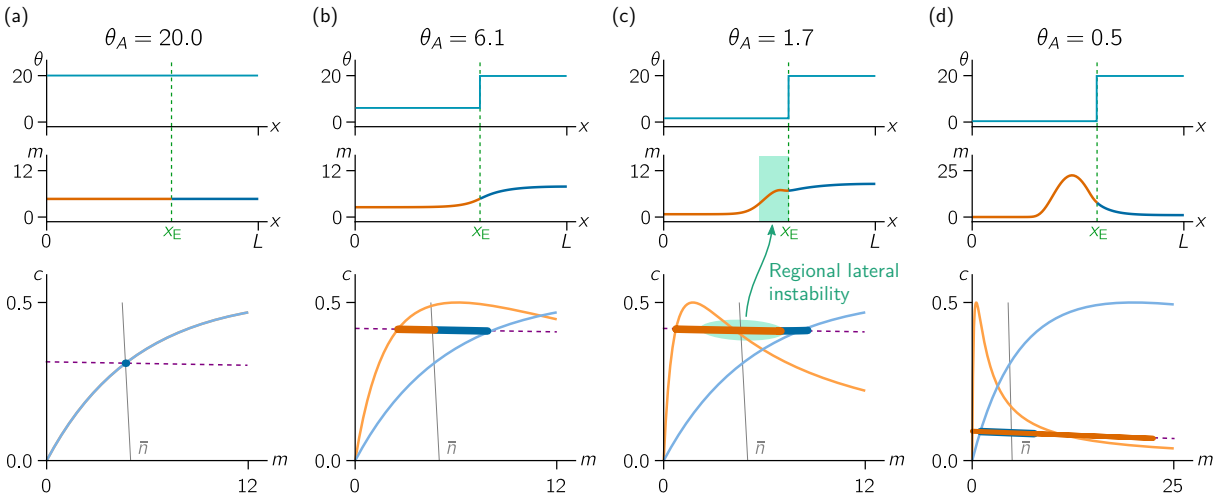

Figure 5.8 | An adiabatically changing template triggers peak formation at the template edge. See also Supplementary Movie 8.
(a) Initial state with a homogeneous template profile $\theta_\mathrm{A} = \theta_\mathrm{B}$. (b) Base state analogous to Fig. 5.2. (c) Base state right before the saddle-node bifurcation. The region that becomes laterally unstable in the bifurcation is highlighted in light green in the spatial profile and in phase space (cf. Fig. 5.4). (d) Peak pattern state after the system transitioned through the bifurcation. This state is qualitatively the same as sketched in Fig. 5.3(c).
Parameters as in Fig. 5.6 but with $L = 5$, $\theta_\mathrm{B} = 20$, and $\theta_\mathrm{A}^\mathrm{f} = 0.5$.

of the template (e.g. θ_A) serves as a bifurcation parameter. In the biological context, this corresponds to a dynamically varying upstream protein pattern.

To demonstrate that varying the template induces equivalent bifurcations as variation of the average mass, we use the template as in the main text (cf. Eq. (5.11)) and perform a numeric simulation where we let the template $\theta(x,t)$ slowly vary with time (for simplicity only in subdomain A):

$$\theta(x,t) = \begin{cases} \theta_\mathrm{A}(t) & x \leq x_\mathrm{E}, \\ \theta_\mathrm{B} & x > x_\mathrm{E}. \end{cases} \tag{5.14}$$

We initialize the template value in subdomain A at $\theta_A(0) = \theta_B$ and let it change via a sinusoidal ramp to its final value $\theta_A(t_\mathrm{f}) = \theta_A^\mathrm{f}$.

An exemplary simulation is shown in Fig. 5.8 and Supplementary Movie 8. At the start of the simulation, the reaction rates, and thus the reactive nullclines, are the same in subdomain A and subdomain B, which is illustrated by the overlapping nullclines in Fig. 5.8(a). The template is homogeneous, and the corresponding steady state is a homogeneous density profile for sufficiently low average mass. Upon decreasing θ_A, the reaction rates in subdomain A change, leading to a change in the shape of the reactive nullcline (Fig. 5.8(b)).

The resulting base state is equivalent to the low-mass base state, similar to the case for mass upregulation analyzed in Sec. 5.2.1. When θ_{A} is further decreased, the density profile becomes regionally unstable at the template edge(Fig. 5.8(c)), which triggers a peak at the template edge (Fig. 5.8(d)). This shows that the pattern formation process as discussed in the main text can also be realized with a dynamic template.

5.D Non-adiabatic mass upregulation

In Sec. 5.2 in the main text, we analyzed the steady states as a function of average mass and found that the system undergoes a transition from base states to patterns through a saddle-node bifurcation. To analyze how the patterns emerge as the system goes through this bifurcation, we performed numerical simulations where we adiabatically increased the average mass by a global cytosolic source with rate κ_{s}

$$\partial_t c = D_c\, \partial_x^2 c - f(m, c) + \kappa_{\mathrm{s}}, \tag{5.15}$$

which entails $\partial_t \bar{n} = \kappa_{\mathrm{s}}$. In this appendix, we explore the emergence of patterns when the average mass is non-adiabatically increased beyond the base-state bifurcation. We initialize the system at zero mass and increase mass up to a value $\bar{n}_{\mathrm{f}}$ within the regime where no base state exists. Varying the rate of mass inflow κ_{s}, we find six regimes with qualitatively different transient dynamics (see Supplementary Movies 9-14). Below, we briefly describe the observed dynamics of the density profile in real space in these regimes going from slow to fast κ_{s}. We then use the (m, c)-phase space and the concept of regional instability (cf. Sec. 5.2.3) to heuristically explain the observed dynamics.

1. *Template-edge peak.* For small κ_{s}, a density peak emerges at the template edge, even though the density profile does not relax to a quasi-steady state. This highlights that the edge-sensing mechanism is robust against rate of mass inflow. (Supplementary Movie 9)
2. *Transition regime.* Here, we observe two peaks emerging simultaneously, one at the outer boundary of subdomain A and one at the template edge. This is an intermediate regime between the boundary peak regime (3) and the template edge peak regime (1), as both peaks emerge simultaneously. (Supplementary Movie 10)
3. *System-boundary peak.* Here, we observe one peak forming at the system boundary at $x = 0$. (Supplementary Movie 11)
4. *Sequential peak formation.* First, a peak forms at the domain boundary of subdomain A, as in the system- boundary peak regime (3). Then, after the first peak already formed, another peak forms at the template edge as in regime (1).(Supplementary Movie 12)

5. *Multiple peaks.* Here, the pattern-formation process is very similar to the system-boundary peak regime (3). However, multiple peaks form at the outer boundary of subdomain A simultaneously. (Supplementary Movie 13)

6. *Quenched system.* Here the mass is upregulated almost instantaneously, $\kappa_s^{-1} \to 0$, which is equivalent to a system initialized with the complete mass in the cytosol. This results in a sequence of peaks forming in subdomain A, starting from the template edge in a process akin to front invasion into an unstable state [51, 193, 194]. (Supplementary Movie 14)

Note that all states with multiple peaks (corresponding to multiple inflection points of the pattern profile in subdomain A) are unstable due to coarsening. The final steady state is always a pattern with a peak either at the template edge or at the system boundary $x = 0$.

In Sec. 5.2.3 and Appendix 5.B, we showed that the formation of a density peak is determined by the position of a regional instability, when the system is in quasi-steady state. The position of the regional instability can be found from a phase portrait analysis, since the nullcline slope criterion (cf. Eq. (1.11)) determines which part of the density profile becomes unstable. To use the same heuristic for understanding the formation of these transient peaks, we analyze the density distribution in phase space obtained from numerical simulations in these non-adiabatic regimes. When mass is added to the system on a faster timescale than it can relax to its steady state, the density distribution in phase space is no longer embedded in a single FBS. Instead, the density distribution in phase space follows a 'zig-zag' shape, as illustrated in Fig. 5.9. This indicates that the density in the vicinity of the template edge is still embedded in a FBS, with offset η_{int}, but the density far away from the template edge deviates from this FBS. Instead, these 'quasi-plateaus' are slaved to the nullcline which indicates that they are locally close to reactive equilibrium, and that their relaxation is limited by diffusive mass transport. Accordingly, for faster inflow of mass, the zig-zag shape is more pronounced—that is, the quasi-plateaus deviate more from η_{int}. If inflow of mass is faster than diffusive transport across the quasi-plateaus, a region at the system boundary in subdomain A enters the lateral unstable region in phase space first, as illustrated in Fig. 5.9(b). This leads to the emergence of a peak at the system boundary in regime (3), and to more complex pattern formation in regimes (4)–(6). In the transition regime (2), mass inflow and mass transport roughly balance, such that a region at the system boundary and a region at the template edge enter the laterally unstable region in phase space at the same time.

The $(L^2/D_c, \kappa_s^{-1})$-phase diagram shown in Fig. 5.10 confirms the intuition that pattern emergence depends on the competition between the time scales of mass inflow, κ_s, and diffusive mass transport across the system $\sim L^2/D_c$. Indeed, the regime boundaries in the phase diagram are roughly straight lines emanating from the origin. In particular, the transition from a 'template-edge peak' to a 'system-boundary peak' corresponds to a line $\kappa_s^{-1} \approx L^2/D_c$. This confirms the intuition that edge sensing is only possible when the inflow of mass into the system is slower than the timescale of diffusive mass transport. For

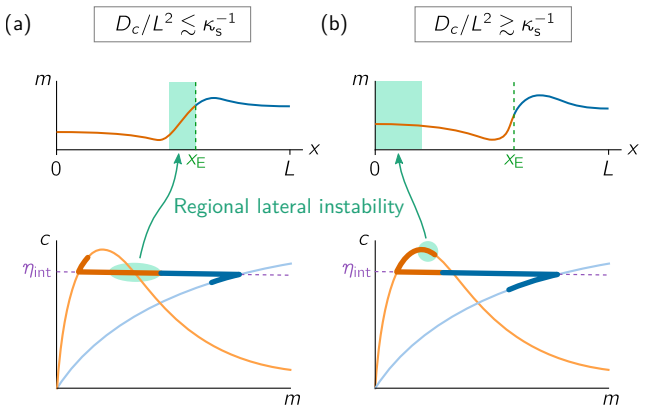

Figure 5.9 | Effect of non-adiabatic mass upregulation on the pattern formation dynamics. (a) Peak formation at the template edge: The density distribution is not embedded in a single FBS, leading to the 'zig-zag'-shaped density distribution in phase space. The regional instability is still triggered at the template edge, as highlighted by the (green) shaded region. (b) Peak formation at the system boundary: The faster mass-inflow leads to a more pronounced 'zig-zag'-shaped density distribution in phase space. The regional instability is now first triggered at the system boundary. This results in a peak forming at the system boundary as shown in Fig. 5.3(b).

comparison, in an intracellular context one has $L \approx 10$ μm and $D_c \approx 10$ $\mu\text{m}^2\text{s}^{-1}$, such that the timescale of mass transport across the cell is on the order of seconds. This is fast compared to changes in average protein concentrations (for instance, due to protein expression or release from the nucleus). Hence, the edge-sense mechanism is a realistic candidate for template guided intracellular pattern formation.

5.E Numerical continuation, steady state construction and bifurcation scenarios

Numerical continuation. — To numerically calculate steady state solutions of the two-component McRD system (Eq. (1.4)), we choose a finite-difference discretization of the PDEs. For steady states, this yields an algebraic system of equations that can be solved with an iterative Newton method. The basic idea of numerical continuation is to follow a solution branch through parameter space (see for instance, Ref. [185] for an excellent overview over continuation methods). This "path-following" is often performed by employing a predictor-âcorrector scheme: Starting from one solution, the next solution along the branch is predicted from the tangent space of the solution branch which can be obtained from the Jacobian.

Steady state construction and finite domain size effects. — In order to test the geometric constructions introduced in Sec. 5.2 we characterize the steady state of the system with

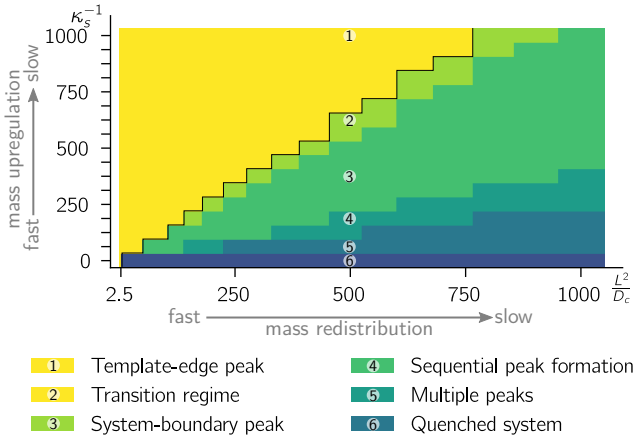

Figure 5.10 | Phase diagram for the timescale of mass upregulation (global cytosolic inflow κ_s^{-1}) against the timescale of mass-redistribution across the entire domain (L^2/D_c). Edge sensing, i.e. formation of a single density peak a the template edge, is operational in regime (1), see Supplementary Movie 9. In regimes (2)-(6) a peak at the system boundary ($x = 0$) or multiple peaks form, see Supplementary Movies 10-14. Parameters: $D_m = 0.01$, $D_c = 10$, $k_{\text{on}} = 1$, $\hat{k}_{\text{fb}} = 1$, $k_{\text{off}} = 2$, $\hat{K}_{\text{d}} = 1$, $\theta_{\text{A}} = 0.5$, $\theta_{\text{B}} = 20$, $x_E = 3/5\,L$, $\bar{n}_{\text{f}} = 5$.

the quantity $m_{\text{E}}^* - m_{\text{B}}$, which must be negative for low-mass base states (monotonic steady states in the low-mass regime, cf. Sec. 5.2.1) and positive for non-monotonic steady states (stationary peak pattern localized at the template edge, cf. Sec. 5.2.2). We perform numerical continuation and compare the results from the simulation (solid lines in Fig. 5.11) with the approximation from the geometric construction (red dots and dash-dotted line). The geometric construction serves as a good approximation for the steady for sufficiently large system sizes.

Also note that for small system sizes the base state smoothly transitions into the pattern state (purple line corresponding to $L = 5$ in Fig. 5.11).

Bifurcation scenario. — The bifurcation scenario connecting the base state and the patterns can be understood as a series of imperfect subcritical pitchfork bifurcations. The imperfection is caused by the template that breaks mirror symmetry of the system. On a homogeneous domain (i.e. without a template), the bifurcations from homogeneous steady state to patterns are subcritical pitchfork bifurcation that become supercritical for small system sizes / large wavenumbers [56]. A more detailed analysis of the bifurcation scenario induced by the step-like template is left for future work. One interesting starting point would be to analyze the two-parameter bifurcation diagram in the $(\bar{n}, \theta_{\text{A}})$-plane, where the line $\theta_{\text{A}} = \theta_{\text{B}}$ correspond to the homogeneous domain. Alternatively, one can investigate the bifurcation scenario in the template edge position (i.e. the $(\bar{n}, x_{\text{E}})$ parameter plane), where $x_{\text{E}} = 0$ and $x_{\text{E}} = L$ correspond to homogeneous domains.

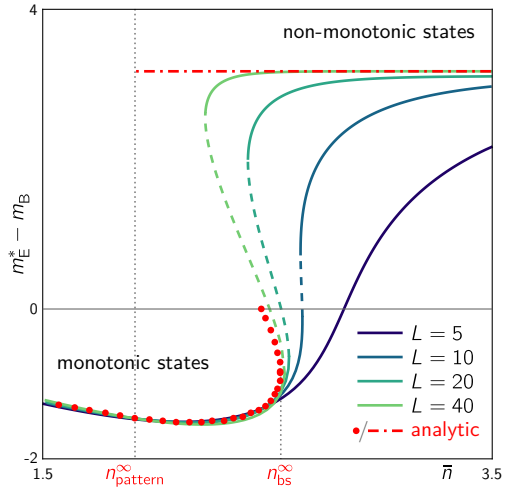

Figure 5.11 | One-parameter bifurcation structure in $\bar{n}$ (average mass) connecting the low-mass base state (monotonic, i.e. $m_E < m_B$ and the peak pattern at the template edge (non-monotonic, i.e. $m_E > m_B$). Solid (dashed) lines indicate stable (unstable) branches from numerical continuation for different domain sizes (increasing from dark to light lines). The corresponding steady state profiles are shown in Movies 15 and 16, for domain sizes $L = 10, 40$. Solutions from the analytic construction of base states in the large domain size limit ($L \to \infty$) are shown as red dots and (position of the saddle-node bifurcation denoted by n^∞_{bs}). Note that for small domain size ($L = 5$), the saddle-node bifurcations vanish and the base state smoothly transitions into a stable peak pattern upon increasing $\bar{n}$. The red, dash dotted line indicates the analytically constructed edge-localized pattern (limit $L \to \infty$). The lower bound in average mass for the existence of these patterns is denoted by $n^\infty_{\text{pattern}}$.
Fixed parameters as in Fig. 5.3(a).

Unstable multi-interface patterns. — The dotted branches in the bifurcation structure Fig. 5.3(a) correspond to patterns with multiple self-organized interfaces (i.e. more than two inflection points in the spatial profile, since the template edge enforces one inflection point at x_E). Figure 5.12 shows spatial profiles at the numbered points in Fig. 5.3(a) representative for the respective branches. The spiral structure of the bifurcation structure reflects an increasing number of of peaks from the outside to the center of the spiral. For the branches numbered 1-3 (4-6) the concentration difference $m_E^* - m_B$ is positive (negative), corresponding to a peak (trough) at the template edge.

All multi-interface patterns are unstable due to a competition for mass and decay into one of the two stable patterns, with a peak either at the system boundary or at the template edge, in a coarsening process.

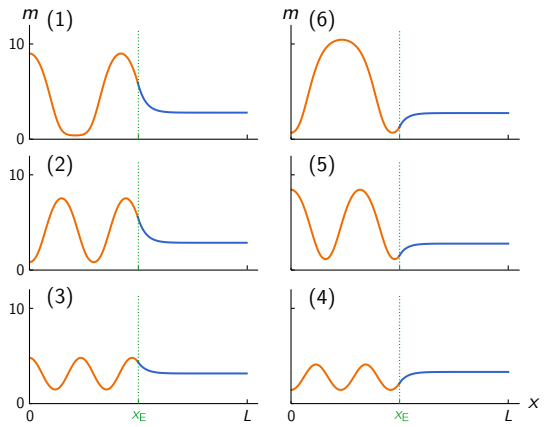

Figure 5.12 | Spatial profiles representative of the unstable branches numbered (1-6) in the $\bar{n}$-bifurcation diagram Fig. 5.3(a).

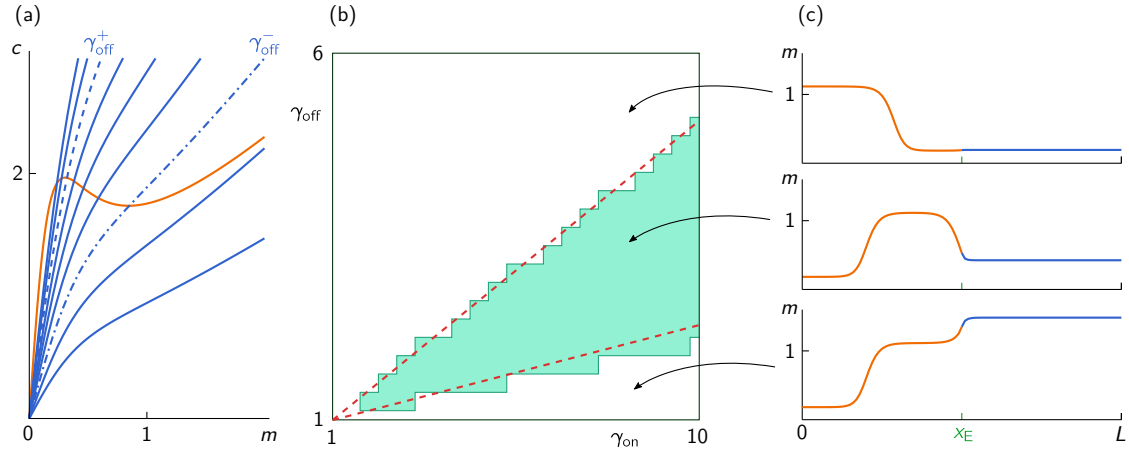

Figure 5.13 | Demonstration of the edge-sensing criterion for a phenomenological model for Cdc42 pattern formation. (a) Nullclines of the reaction kinetics Eq. (5.16) in subdomains A (orange) and B (blue), defined by the reaction rates in Eq. (5.19). Multiple B-nullclines are shown for off-rate factors $\gamma_{off} = 1, 1.5, \ldots, 5$ while the on-rate factor is fixed at $\gamma_{on} = 8$. The critical values $\gamma_{off}^{\pm}$ between which the A-nullcline is intersected at negative slope (i.e. the edge-sensing criterion is fulfilled) are shown as dashed and dash-dotted lines respectively. (b) Phase diagram of on- and off-rate factors $(\gamma_{on}, \gamma_{off})$. The shaded region shows the regime where edge-sensing is observed in numerical simulations with adiabatically increasing average mass (cf. Eq. (5.15)). Dashed red lines show the curves $\gamma_{off}^{\pm}(\gamma_{on})$, cf. Eq. (5.21), between which the edge-sensing criterion is fulfilled. (c) Quasi-stationary density profiles obtained from numerical simulations with adiabatically increasing average mass $\bar{n}$ illustrating the typical pattern emerging from the base-states's saddle-node bifurcation in the three regimes of the $(\gamma_{on}, \gamma_{off})$ phase diagram ($\gamma_{on} = 8$; top: $\gamma_{off} = 5.5, \bar{n} = 2.9$; $\gamma_{off} = 3, \bar{n} = 2.35$; bottom: $\gamma_{off} = 1.5, \bar{n} = 2.24$.). Fixed parameters: $k_{fb} = 1, k_{on} = 0.07, k_{off} = 1, D_m = 10^{-4}, D_c = 0.1, L = 1, x_E = 0.5, \kappa_s = 10^{-5}$.

5.F Demonstration of the edge-sensing criterion

To illustrate how the edge sensing criterion might help in modeling of biological systems we consider a concrete biological example. Cdc42 pattern formation is described by a phenomenological two-component model of the form Eq. (1.4) with the reaction kinetics [91]

$$f(m,c) = \left(k_{\mathrm{on}} + k_{\mathrm{fb}}\frac{m^2}{1+m^2}\right)c - k_{\mathrm{off}}m \tag{5.16}$$

The nullcline $c^*(m)$ determined by $f(m, c^*(m)) = 0$ has a section of negative slope for $k_{\mathrm{fb}} > 8k_{\mathrm{on}}$ in the interval $[m_{\mathrm{max}}, m_{\mathrm{min}}]$ given by

$$m_{\mathrm{min,max}} = \sqrt{\frac{1}{1+k_{\mathrm{on}}/k_{\mathrm{fb}}}\left(\frac{1\mp\nu}{2} - \frac{k_{\mathrm{on}}}{k_{\mathrm{fb}}}\right)} \tag{5.17}$$

with

$$\nu = \sqrt{1 - 8\frac{k_{\mathrm{on}}}{k_{\mathrm{fb}}}}. \tag{5.18}$$

Since cytosolic diffusion is multiple orders of magnitude faster than diffusion of membrane bound Cdc42, we consider the limit $D_c \gg D_m$ where the FBS-slope is zero. Then the criterium for lateral instability is that the nullcline slope be negative $\partial_m c^*(m) < 0$; and the edge-sensing criterion is that nullclines must intersect at a point where one of them has negative slope.

In cellular wound healing, Abr forms a ring of high concentration around the wound edge, followed by the formation of a Cdc42 ring around the Abr ring [19]. Cdc42 then activates the actomyosin machinery that drives the contraction of the cell membrane to close the wound. Protein mutation on Abr and Cdc42 studies suggest that the high density Abr ring acts as a template for Cdc42 [19]. Furthermore, it has been shown that Abr acts as both a nucleotide exchange factor (GEF) and a GTPase-activating protein (GAP) for Cdc42 [19]. We therefore model the effect of Abr on the Cdc42 kinetics as a factor increasing both the attachment rate k_{on} and the detachment rate k_{off}. The reaction terms in the two subdomains with low and high Abr density, are thus defined as $f_{\mathrm{A,B}}(m,c) = f(m,c;k_{\mathrm{on}}^{\mathrm{A,B}}, k_{\mathrm{off}}^{\mathrm{A,B}})$ with

$$k_{\mathrm{on}}^{\mathrm{A}} = k_{\mathrm{on}}, \qquad k_{\mathrm{on}}^{\mathrm{B}} = \gamma_{\mathrm{on}}k_{\mathrm{on}}, \tag{5.19}$$

$$k_{\mathrm{off}}^{\mathrm{A}} = k_{\mathrm{off}}, \qquad k_{\mathrm{off}}^{\mathrm{B}} = \gamma_{\mathrm{off}}k_{\mathrm{off}}, \tag{5.20}$$

where the factors $\gamma_{\mathrm{on}}, \gamma_{\mathrm{off}} > 1$ encode the relative enhancement of attachment and detachment rates in subdomain B compared to subdomain A.

The edge-sensing criterion (nullclines intersect at a point where the A-nullcline has negative slope) is fulfilled when the intersection point $(m_{\mathrm{i}}, c_{\mathrm{i}})$ of the two nullclines, defined by

$f_A(m_i, c_i) = 0$ & $f_B(m_i, c_i) = 0$, lies in the range $[m_{max}, m_{min}]$ (see Fig. 5.13(a)). Solving these equations for γ_{off}, we find that nullclines fulfill the edge-sensing criterion when γ_{off} lies in the range $[\gamma_{off}^-, \gamma_{off}^+]$ as a function of γ_{on}:

$$\gamma_{off}^{\pm}(\gamma_{on}) = \frac{1}{1 + k_{fb}/k_{on}} \left(\frac{k_{fb}}{k_{on}} + \frac{2}{\nu \mp 1} + \gamma_{on} \frac{\nu \mp 3}{\nu \mp 1} \right). \tag{5.21}$$

Note that $\gamma_{off}^{\pm}(1) = 1$ corresponds to the singular case where the template has no effect, i.e. the reaction kinetics in the two subdomains are identical. The dashed, red lines in Fig. 5.13(b) show the curves $\gamma_{off}^{\pm}(\gamma_{on})$ that delineate the regime where the edge-sensing criterion is fulfilled.

To test the criterion, we ran numerical simulations, for different combinations $(\gamma_{on}, \gamma_{off})$. In each simulation, the average mass is adiabatically increased at a rate $\kappa_s = 10^{-5}$, cf. Eq. (5.15).

We find three different types of patterns emerging from the base-states's saddle-node bifurcation. Examples of these are shown in Fig. 5.13(c). The regime where we find edge-localized peaks agrees well with the prediction from the geometric edge-sensing criterion (shown as dashed, red lines in (b)).

Interestingly, the $(\gamma_{on}, \gamma_{off})$-phase diagram shows that both attachment and detachment need to be enhanced in subdomain B. This implies that proteins, like Abr, that have both GEF- and GAP-catalytic domains may play a crucial role for edge sensing by GTPases.

6 Decoding cell shape information

"Simplicity is the final achievement.
After one has played a vast quantity of notes and more notes,
it is simplicity that emerges as the crowning reward of art."
– Frédéric Chopin

Many cellular processes rely on precise positioning of proteins on the membrane. Such protein patterns are susceptible to cell-shape changes, raising the question of how these patterns can robustly regulate cellular tasks including cell division. Here, we elucidate a shape-adaptation mechanism that robustly controls spatiotemporal protein dynamics on the membrane despite cell-shape deformations. By combining experiments on starfish oocytes with biophysical theory, we show how cell-shape information contained in a cytosolic gradient can be decoded by a bistable regulator of Rho. In turn, this bistable front precisely controls a mechanochemical response by locally triggering excitable dynamics of Rho. We posit that such a shape-adaptation mechanism based on a hierarchy of protein patterns may constitute a general physical principle for cell-shape sensing and control.

This chapter is based on our paper "A hierarchy of protein patterns robustly decodes cell shape information", which has been published in Nature Physics [143]. This work has been performed together with Tzer Han Tan, Fridtjof Brauns, Jinghui Liu, S. Zachary Swartz, Erwin Frey, and Nikta Fakhri

6.1 Shape adaptation mechanism

Cellular protein patterns emerge from a combination of protein interactions, transport, conformational state changes, and chemical reactions at the molecular level [106]. Recent experimental and theoretical work clearly demonstrates the role of geometry and flows – including membrane curvature [57, 195, 196], local cytosolic-to-membrane ratios [6, 197] and advective cortical flow – in modulating membrane protein patterns. Given that diverse biological processes, such as cell division [198–200], cell motility [201], wound healing [202] and tissue folding [203, 204], rely on precise spatiotemporal organization of regulatory proteins on the membrane, how can these patterns form robustly in the face of dynamic cell-shape changes during physiological processes?

Here, we uncover such a mechanism using the oocytes of the starfish Patiria miniata as a model system. In these oocytes, the cell shape is dynamically deformed by surface contraction waves (SCWs) that travel along the membrane from the vegetal pole (VP) to the animal pole (AP) during meiotic anaphase (Fig. 6.1a and b). While SCWs are observed in many species [205–209], their functional role is still under debate [28, 210]. SCWs are induced by the GTPase Rho, which, when GTP-bound, locally triggers actomyosin contractility, thus generating a zone of surface contraction that travels as a band across the membrane (Fig. 6.1c, movie S1) [144]. When the mechanical properties of the oocyte surface are altered by removing the extracellular jelly layer, the degree of deformation becomes larger and, remarkably, the SCW slows down (Fig. 6.1d). The same effect was previously observed when myosin contractility was increased to amplify shape deformations [152]. These observations establish the starfish oocyte as an ideal model system to unravel the dynamic interplay between cell shape and biochemical dynamics.

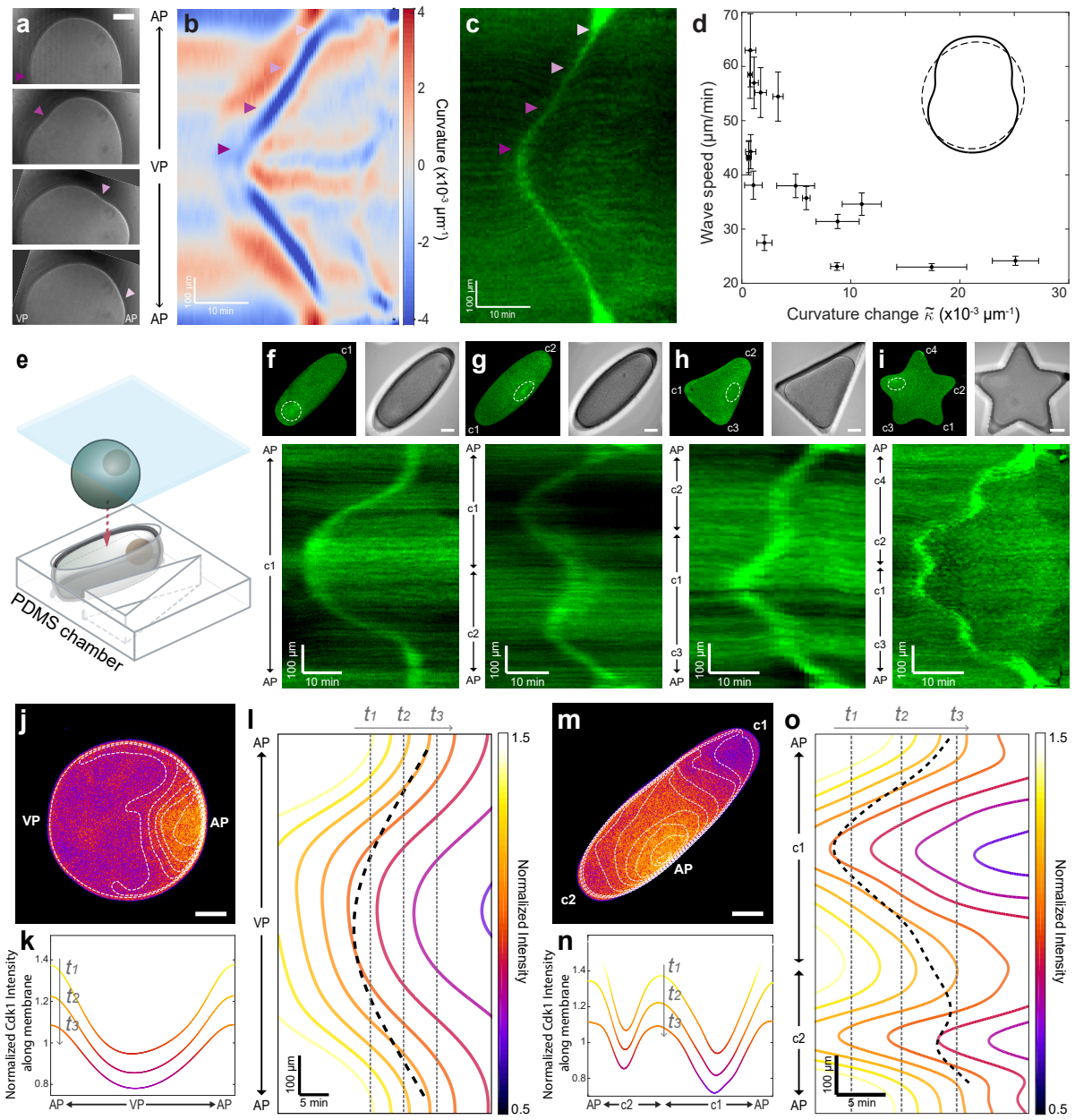
a
b
c
d
AP
VP
Curvature (x10-3 µm-1)
Wave speed (µm/min)
Curvature change (x10-3 µm-1)
10 min
100 µm
e
PDMS chamber
f
g
h
i
c1
c2
c3
c4
5 min
j
k
l
m
n
o
t1
t2
t3
Normalized Intensity
Normalized Cdk1 Intensity along membrane

Figure 6.1 ***(previous page)*** **| Contraction waves in starfish oocytes confined in compartments with different geometries. a**, Differential interference contrast (DIC) images of a surface contraction wave (SCW) traveling from the vegetal pole (VP) to the animal pole (AP) during meiotic anaphase I. **b**, Kymograph of the SCW tracing cell surface curvature. **c**, Kymograph showing the distribution of active Rho-GTP (labeled with rGBD-GFP) which coincides with the SCW (movie S1). **d**, Contraction wave speed plotted as a function of curvature change. Error bars indicate standard deviation (see Method). **e**, Schematic of the confinement experiments. **f-i**, Representative confocal cross-sections of Rho (top left) and DIC (top right) images, and membrane Rho kymographs of oocytes confined in different geometries. (**f**) Ellipse with AP at the tip (N=4). (**g**) Ellipse with AP on the long side (N=4). (**h**) Triangle (N=6). (**i**) Star (N=2) (movies S2 to S5). White dotted circles indicate positions of nucleus. **j-o**, Spatiotemporal gradient of Cdk1-cyclinB in wildtype (circular) and elliptical oocyte. (**j, m**) Confocal cross-sections of Cdk1-cyclinB distribution in wildtype oocyte (movie S6, N=3) and elliptical oocyte with AP on the long side (movie S7, N=2). (**k, n**) Cdk1 distribution along the membrane at three different time points. The times t1, t2, and t3 are 100s, 400s, and 700s after the first wave initiation. (**l, o**) Kymographs of the membrane Cdk1 gradient during passage of the SCW in wildtype and elliptical oocyte. The dotted line indicates the position of Rho-GTP band estimated from cell surface deformation (see Method). Cdk1-cyclinB intensity is normalized to the value at the initiation point of the first wave. All white scale bars represent 50 µm.

To investigate how the Rho dynamics is affected by cell shape, we confine the oocytes in microfabricated chambers of various shapes during anaphase (Fig. 6.1e). We find that shape affects both the initiation and the propagation speed of the Rho-GTP band. Specifically, we observe that the Rho-GTP band always initiates from regions of high curvature, which we refer to as corners (red arrowheads, Fig. 6.1, f to i, movies S2 to S5). Moreover, in elliptical (Fig. 6.1g) and triangular (Fig. 6.1h) geometries, multiple wave initiations occur, with the first starting from the corner furthest from the nucleus (red asterisks). In the star geometry, where two such corners are present, wave initiations occur simultaneously from both corners (red asterisks, Fig. 6.1i). Strikingly, these waves propagate with varying speeds on different sections of the membrane such that they always meet closest to the nucleus (AP). This suggests that wave initiations and propagation are globally coordinated.

Motivated by recent experimental evidence that the Rho-GTP band is guided by a temporally decaying cytosolic gradient of the kinase-active Cdk1-cyclinB complex [144], we hypothesize that Cdk1-cyclinB provides this global coordination, analogous to positional information in morphogenesis [211]. In unconfined oocyte, the Cdk1-cyclinB forms a cytosolic gradient that is high at the AP and low at the VP (Fig. 6.1j-l, movie S6). To test how cell shape modulates this gradient, we imaged the evolution of the Cdk1-cyclinB concentration gradient (in short: cytosolic Cdk1 gradient) in different cell shapes (Fig. 6.1m , movies S7 to S9). In all cell shapes tested, this gradient extends radially from the AP into the cytoplasm (Fig. 6.1, j and m). Consequently, the gradient perceived along the mem-

brane (in short: membrane Cdk1 gradient) depends on the membrane orientation relative to the Cdk1 cytosolic gradient. In an elliptical geometry, the membrane Cdk1 gradient is shallow at the corners (C1 and C2) but steeper in the middle of the elliptically-shaped oocyte (Fig. 6.1m-o). These results demonstrate how the membrane Cdk1 gradient encodes information about cell shape.

In the different cell shapes, the Cdk1-cyclinB concentration is always lowest at corners, which precisely coincides with the wave initiation points (Fig. 6.1o). This is consistent with prior work indicating that the Rho-GTP band originates at the point of lowest Cdk1-cyclinB concentration in unconfined oocytes21. Furthermore, our experiments show that, as the Cdk1 gradient decays, the Rho-GTP band (as indicated by the SCW) follows an isocline of the Cdk1-cyclinB concentration, such that multiple waves arrive at the nucleus simultaneously. Hence, the Rho-GTP band on the membrane must follow a specific concentration of the decaying membrane Cdk1 gradient.

How can the Rho-GTP band be coupled to a particular level of Cdk1-cyclinB? A likely molecular link between the Cdk1 gradient and the Rho-GTP band is the Rho guanine nucleotide exchange factor (GEF) Ect2, which activates Rho (Fig. 6.2a). Cdk1-cyclinB phosphorylates Ect2, which has been suggested to decrease its membrane affinity [149]. Moreover, it has been reported that Ect2 over-expression induces a propagating front of Rho-GTP spirals instead of a Rho-GTP-band [145] (Fig. 6.2b-c, movie S10). When we imaged the fluorescently-tagged Ect2 , we observed that an Ect2 front coincides with the Rho-GTP band (Fig. 6.2d-e, movie S11). We hypothesize that the Ect2 front follows a threshold of Cdk1-cyclinB concentration and that the Ect2 front, in turn, regulates the downstream Rho dynamics. To test these hypotheses, we simultaneously imaged Ect2 and Rho. Indeed, we find that the domain of high Ect2 concentration coincides with the domain of Rho spirals (dashed line in Fig. 6.2f , movie S12). Furthermore, simultaneous imaging of Ect2 and Cdk1-cyclinB confirmed that the Ect2 front approximately follows a single Cdk1-cyclinB level (dashed line in Fig. 6.2g , movie S13).

Taken together, this suggests that the propagating Rho-GTP band is a result of the following hierarchy of protein localization patterns (Fig. 6.2h): Cdk1-cyclinB forms a cytosolic gradient in the cell, which serves as a spatial map to guide a front of Ect2 by localizing the front interface to a threshold Cdk1-cyclinB level. The Ect2 front demarcates a domain of high and a domain of low Ect2 concentration, providing a spatial cue for the Rho-GTP band on the membrane. This cue leads to a Rho-GTP band at the interface of the Ect2 front in the wild type, or Rho spirals in the high concentration domain when Ect2 is over-expressed. Since the position of the two Ect2 domains are determined by the Cdk1-cyclinB threshold concentration, the propagation of the Rho-GTP band is ultimately controlled by the degradation of Cdk1-cyclinB. To elucidate the underlying physical mechanism of this Cdk1-Ect2-Rho pattern hierarchy, we propose a reaction-diffusion model with two distinct modules. First, we demonstrate how the Ect2 front controls the downstream Rho-GTP band and spiral front dynamics. We then propose a mechanism for how the membrane Cdk1 gradient controls the position of the Ect2 front.

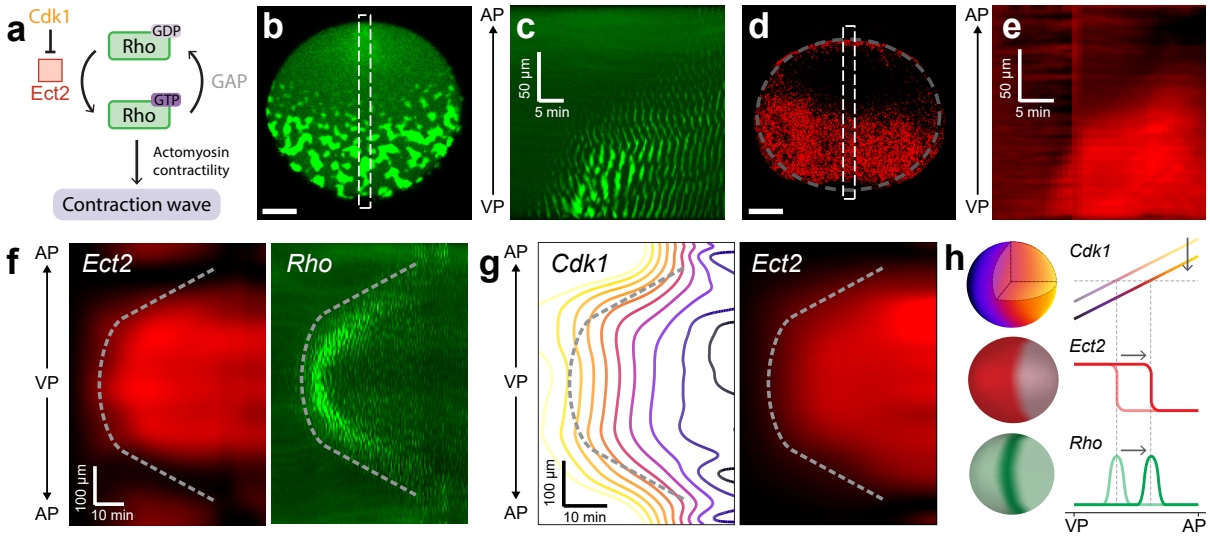

Figure 6.2 | The Cdk1-Ect2-Rho pattern hierarchy. **a**, Biochemical interaction network of the signaling molecules controlling SCW in starfish oocyte. **b-e**, Snapshots of the Rho spiral front (**b**) and the cumulative intensity difference of the Ect2 front (**d**) on the membrane during SCW propagation in an Ect2-overexpressing oocyte (movie S10-S11). The kymographs show the Rho signal (**c**) and the cumulative intensity difference of Ect2 (**e**) within a narrow region around the AP-VP axis during SCW propagation (white dashed boxes in (**b**) and (**d**) respectively). Grey dashed line in (**d**) marks the boundary of the cell. Scale bars in (**b**) and (**d**) represent 50 µm. **f**, Kymographs of Ect2 and Rho concentrations along the membrane of an oocyte expressing both rGBD-GFP and Ect2-mCherry during SCW propagation (movie S12). **g**, Kymographs of Cdk1-cyclinB and Ect2 concentration along the membrane of an oocyte expressing both cyclinB-GFP (a marker for Cdk1 activity) and Ect2-mCherry during SCW (movie S13). The Cdk1-cyclinB intensity is normalized the same way as in Fig. 6.1l. Grey dotted lines in (**f**) and (**g**) are guides for the eyes showing approximately the front positions. **h**, Schematic showing how the spatial distributions of Cdk1-cyclinB (top), Ect2 (middle) and Rho (bottom) proteins couple to each other during SCW propagation.

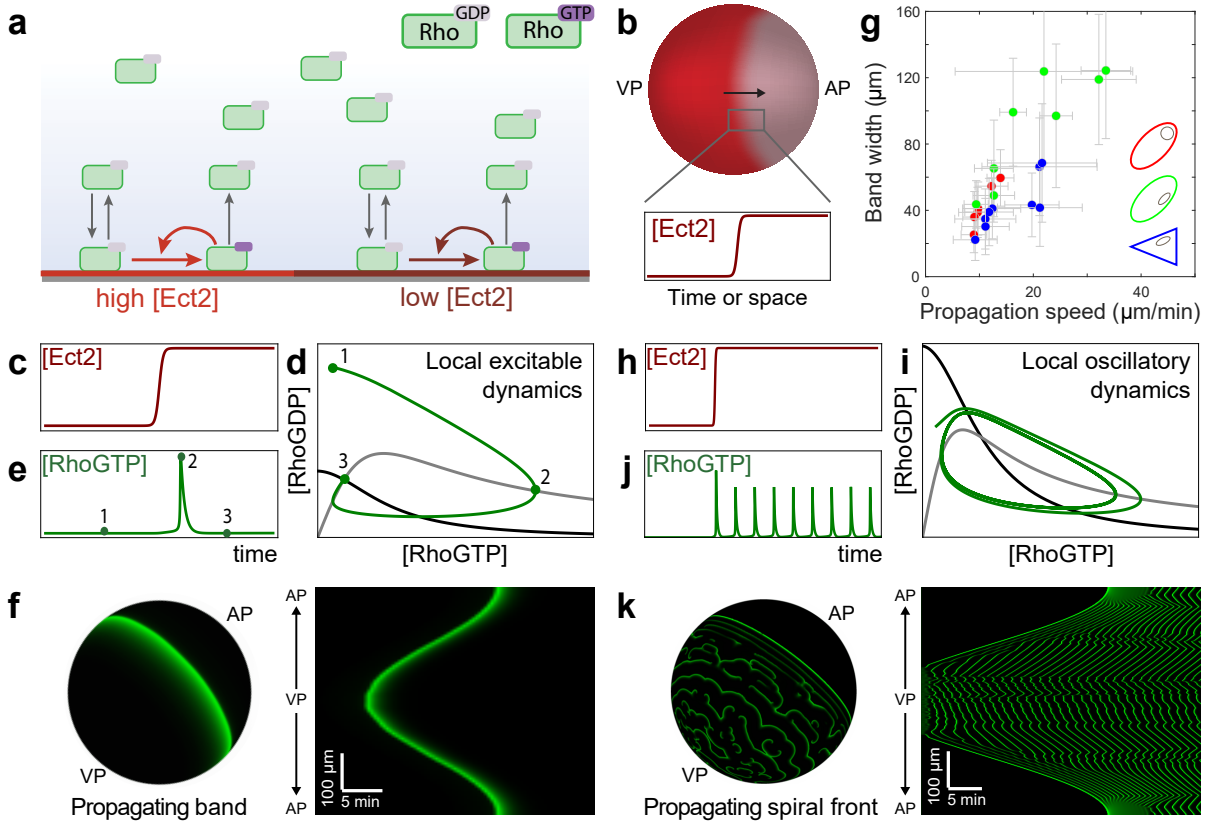

Figure 6.3 | Model of Rho dynamics. **a**, Schematic of the reaction-diffusion dynamics of Rho proteins in different Ect2 subdomains. **b**, The Ect2 front, serving as an input to the model, effectively increases the nucleotide exchange rates, thus activating Rho. Viewed from a single membrane position, the Ect2 concentration suddenly increases as the Ect2 front passes by. **c-e**, With local excitable dynamics, the sudden increase in Ect2 (**c**) leads to a large excursion of the dynamics in phase space (**d**), resulting in a transient increase in the Rho-GTP concentration on the membrane (**e**). **f**, Snapshot of a finite-element simulation of the Rho-GTP band traveling over the surface of a three-dimensional sphere (movie S14), with the accompanying kymograph of the traveling Rho-GTP band. **g**, Rho-GTP band width versus propagation speed in oocytes confined to three different geometries. The band width is calculated as the product of excitation time and propagation speed. Error bars indicate standard deviation. **h-j**, With local oscillatory dynamics, the increase in Ect2 (**h**) leads to oscillations along a limit cycle in phase space (**i**), resulting in oscillatory Rho dynamics (**j**). **k**, Snapshot of a finite-element simulation of the Rho spiral domain traveling over the surface of a three-dimensional sphere (movie S18), with the accompanying kymograph of Rho-GTP spirals. See Methods and Table S1 and S2 in the SI for the model equations and parameters used in (**f**) and (**k**).

The first module of our model captures key features of the Rho GTPase cycle [148, 158] (Fig. 6.3a, Figs. 4.1 and 4.2). In its inactive GDP-bound state, Rho can either be membrane-bound or cytosolic (GDI-bound). Once bound to the membrane, Rho-GDP can undergo nucleotide exchange which converts it into an active GTP-bound state, a process mediated by GEFs. When Rho-GTP is hydrolyzed by GTPase-activating proteins (GAPs), it detaches from the membrane. The GEF Ect2 front demarcates subdomains on the membrane with high and low nucleotide exchange rates (Fig. 6.3a, Figs. 4.5 and 4.7; see also Sec. 4.4-4.7). Thus, viewed from a position on the membrane, the passing Ect2 front induces a sudden increase in the nucleotide exchange rates (Fig. 6.3, b and c). Can such an increase lead to the observed Rho-GTP band? As the Ect2 increase shifts the steady-state concentration of Rho-GTP upwards, one might, at first glance, assume that this merely translates the Ect2 front into a Rho-GTP front. However, this focus on steady states assumes an instantaneous response and thus overlooks the transient dynamics, which can be qualitatively different when the increase in the Ect2 concentration occurs suddenly (Fig. 4.8). Consider an initially low Ect2 concentration, such that most Rho is in the inactive GDP-bound form (point 1, Fig. 6.3, d and e). A sudden increase in the Ect2 concentration then shifts the steady state towards a (slightly) increased Rho-GTP and decreased Rho-GDP concentration on the membrane (from point 1 to 3 in Fig. 6.3d). Owing to the positive feedback on Rho activation, the Rho concentrations do not relax directly into the new steady state, but transitions to it via a large excursion in phase space; in other words, the Rho dynamics is excitable (Figs. 4.3 and 4.4, and Sec. 4.4 and 4.5). The large excursion in phase space corresponds to a transient increase in the Rho-GTP concentration on the membrane (point 2 in Fig. 6.3, d and e). Thus, the time differential of the local Ect2 concentration, rather than the absolute Ect2 level, induces the large transient increase in Rho activation.

As the Ect2 front moves along the membrane, it continuously triggers such local excitations, resulting in a spatially localized band of Rho activity that follows the Ect2 front (Fig. 6.3f, movie S14). Consequently, this model predicts that the width of the Rho-GTP band is given by the product of the excitation time and the propagation speed. We confirm this numerically using finite element simulations of the system in different geometries (movies S15-S17). Indeed, we find that the band width is positively correlated with the propagation speed (Fig. 4.9). To test this prediction experimentally, we confine oocytes in three different geometries and also observe the predicted increase in band width with propagation speed (Fig. 6.3g).

In oocytes that overexpress Ect2, we observe a propagating front of Rho-GTP spirals (Fig. 6.2c). Viewed from a fixed position on the membrane, spirals correspond to oscillations in Rho-GTP concentration. In accordance with this experimental observation, our model exhibits limit-cycle oscillations over a broad parameter regime (Fig. 6.3h to i, Fig. 4.6; see also Sec. 4.5 and 6.B). Indeed, our simulations show that the resulting oscillatory medium can exhibit spiral waves (Fig. 6.3k, Fig. 6.7, movie S18). In fact, this is generic because excitability and limit-cycle oscillations are closely related nonlinear phenomena, and are often found in neighboring parameter regimes. Taken together, the model

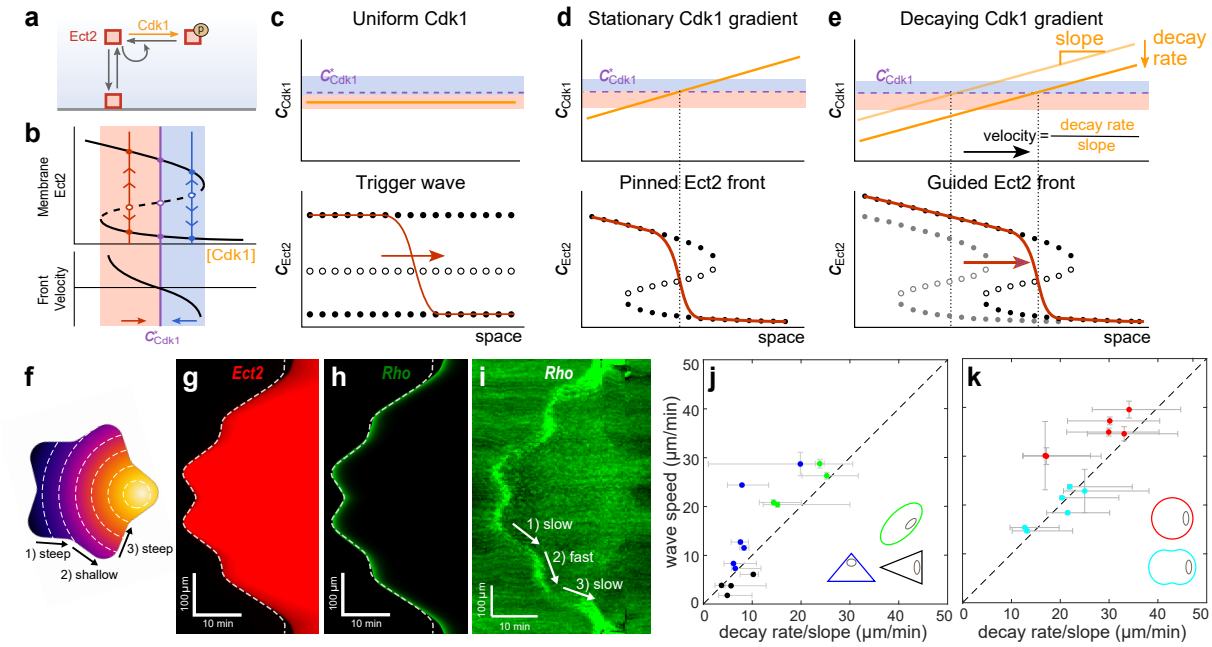

Figure 6.4 | Model of Ect2 front regulation by the Cdk1-cyclinB gradient. **a**, Schematic of the reaction-diffusion dynamics of Ect2. **b**, Schematic representation of the bistable regime of membrane-bound Ect2 when the Cdk1-cyclinB dependent phosphorylation rate is varied. **c**, A uniform Cdk1-cyclinB distribution induces an Ect2 trigger wave. d, A stationary Cdk1 gradient pins an Ect2 front at the c^*_{Cdk1} threshold level. **e**, A decaying Cdk1 gradient guides the propagation of the Ect2 front pinned to the c^*_{Cdk1} threshold level. **f**, Snapshot of the Cdk1 gradient in star geometry. **g-h**, Kymographs of simulated Ect2 front (**g**) and Rho band (**h**) in star geometry (movie S17). Grey dotted line shows an isocline of the membrane Cdk1 gradient. The model equations are defined in the Methods and parameters are as in Table 6.1 and 3.1, see also Sec. 4.3 and 3.2. **i**, Experimental kymograph of Rho-GTP band propagation in a star-shaped oocyte correlates with that of the Cdk1 gradient along the membrane. **j-k**, The Rho-GTP band speed in different static (**j**) and dynamic (**k**) geometries plotted against the quotient of decay rate and slope of the Cdk1 gradient. Error bars indicate maximum and minimum values measured at the start and end of each segment (see Sec. 6.A).

provides a mechanism that explains how different levels of Ect2 can account for both the Rho-GTP band and spiral wave dynamics in the starfish oocyte. In addition, it shows that the propagation of the Ect2 front fully determines the propagation of the Rho-GTP band, and therefore the SCW.

To elucidate how the propagating Rho-GTP band adapts to changes in cell shape, we ask how the propagating Ect2 front itself is controlled by the upstream Cdk1 gradient. Propagating fronts are a generic feature of bistable media. These fronts connect two plateaus, corresponding to the two stable steady states [153, 154], and propagate such

that the steady state with the stronger attraction (dominant steady state) invades the other steady state. While such a mechanism of front propagation does not depend on the precise origin of the underlying bistability, we hypothesize that a candidate for bistable dynamics in starfish oocytes is Ect2, potentially as part of an interaction network with other Rho regulators, where active (unphosphorylated) Ect2 autocatalytically enhances its own dephosphorylation (Fig. 6.4a and Fig. 3.1; see Sec. 3.2). Furthermore, we assume that Ect2 can be phosphorylated by cytosolic Cdk1-cyclinB24 and that Ect2 can only bind to or detach from the membrane in its active conformation. This reaction kinetics exhibits bistability for a range of Cdk1-cyclinB concentrations, with the two steady states corresponding to high and low Ect2 concentrations on the membrane (Fig. 6.4b and Fig. 4.9). To demonstrate the bistable nature of Ect2 dynamics, we developed a photo-recruitable GEF catalytic domain in starfish oocytes [212] (see Sec. 6.A). We showed that oocyte contractility exhibits an abrupt and switch-like response to membrane GEF recruitment (Fig. 6.5 and movie S19). This result, together with the observation that Ect2 forms a front, suggests that Ect2 activation dynamics is bistable.

In the model, the Cdk1-cyclinB concentration determines the relative dominance between the two steady states, and therefore the speed of the Ect2 front (Fig. 6.4c). For a critical Cdk1-cyclinB concentration, c^*_{Cdk1} (purple line, Fig. 6.4b and Fig. 3.2), the front is equally attracted to both steady states, resulting in a stalled front. Since Cdk1-cyclinB forms a gradient, the critical concentration c^*_{Cdk1} at which the front stalls, corresponds to a certain position on the membrane, and the Ect2 front will move towards this position, where it in turn stalls [157] (Fig. 6.4d). As the gradient decays, this stalling point will itself move in space, causing the Ect2 front to follow (Fig. 6.4e and Fig. 3.3). Hence, the speed at which the stalling point moves along the membrane is determined by the ratio of the decay rate (temporal variation of the concentration) to the slope (spatial variation of the concentration) of the Cdk1 gradient (Fig. 6.4e). This implies that the speed of the Ect2 front, and thus of the Rho-GTP band, is determined by the same ratio. Simulating the reaction-diffusion dynamics numerically, we indeed find that the Ect2 front propagates up to the stalling point and then follows this concentration as the gradient decays (movies S15-S17). Thus, propagation of the Ect2 front is strongly correlated with, and limited by, the speed of the stalling point.

In summary, we have identified a direct link between the speed of the Rho-GTP band and the decaying Cdk1 gradient. Based on this insight, we can now explain how the propagating Rho-GTP band adapts to the cell shape. A striking example that illustrates this adaptation is the propagation of the Rho-GTP band in a star geometry, where the different arms of the star exhibit membrane Cdk1 gradients of varying slope (Fig. 6.4f). As a consequence, the speed of the Ect2 front and the Rho-GTP band vary greatly from slow speed along arms with steep gradients to high speed along arms with shallow gradients. We verified this using finite element simulation (Fig. 6.4g-h), which agrees well with the experimental data (Fig. 6.4i). To further test this relationship between the speed of the Rho-GTP band and the decaying gradient quantitatively, we analyzed the Cdk1-cyclinB distribution in different cell shapes and measured both the average slope and average decay rate of the membrane

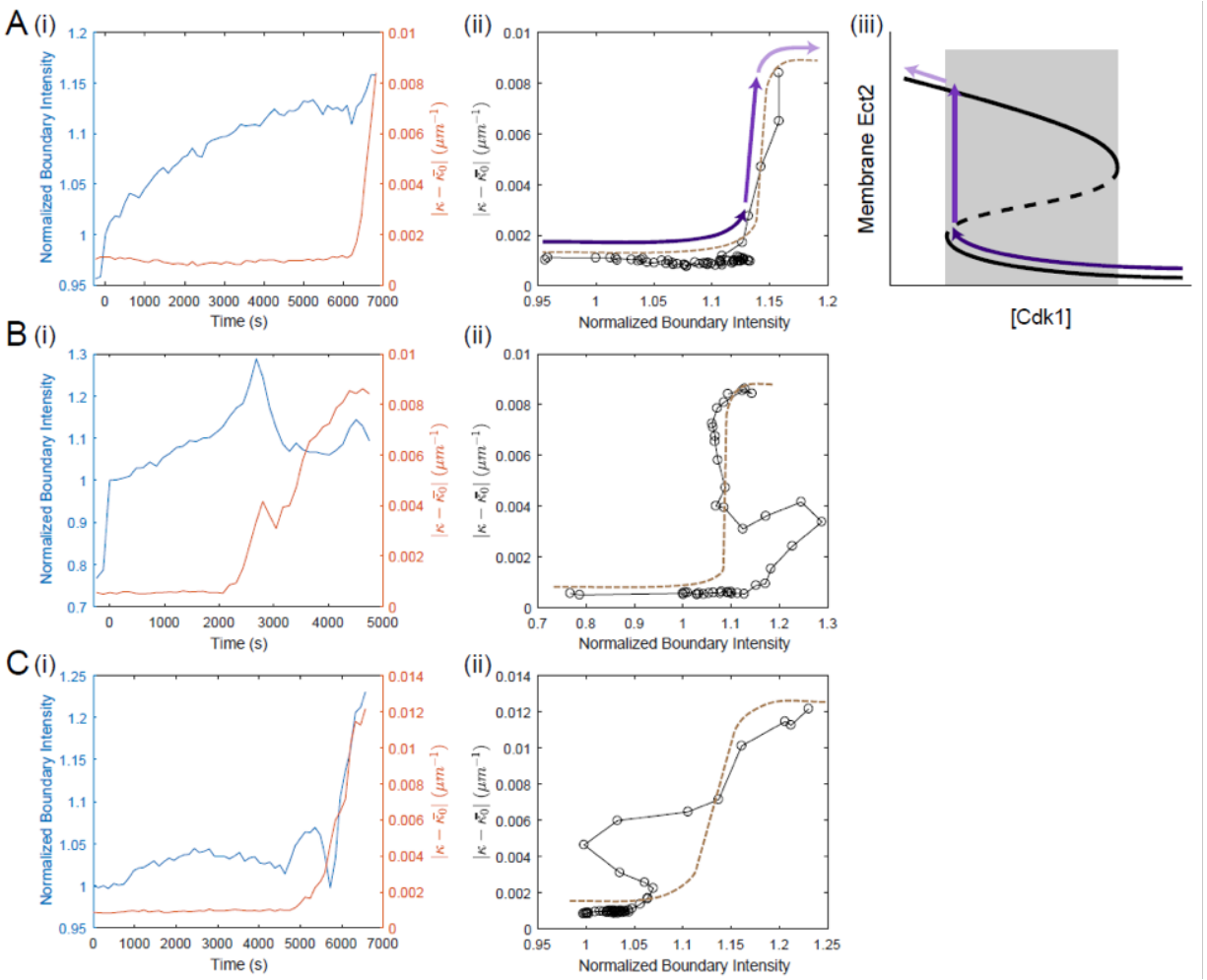

Figure 6.5 | Photo-activation experiments and Ect2 bistability. (**A-C**) Three replicates of photo-activation experiment. **(i)** 405 nm light is turned on at 0 min. The boundary intensity is obtained by integrating the fluorescence of YFP-tagged photo-activatable GEF along the oocyte periphery and normalized with the intensity at time 0 min (blue line). Oocyte contractility is quantified using the average curvature change $|\kappa - \bar{\kappa}_0|$, where $\bar{\kappa}_0$ is the mean curvature of the oocyte boundary at time 0 min. **(ii)** Average curvature change plotted against normalized boundary condition. Note that the intensity jumps in (**B (i)**) at around 2500s and in (**C (i)**) at around 5200s are experimental artifacts due to background auto-fluorescence. The brown dashed lines serve as guides for the eye. We can compare this observation with Ect2 bistability as follows. The increase in normalized boundary intensity is analogous to the increase in membrane-bound GEF through Cdk1 decay (dark purple arrows in A (ii)-(iii)). Beyond a certain threshold level, the oocyte contractility (a measure of total membrane bound, dephosphorylated GEF) abruptly increases (purple arrows in A (ii)-(iii)). Taken together, this result and the observation that Ect2 forms a front further supports the hypothesis that Ect2 activation is bistable in the starfish oocyte system.

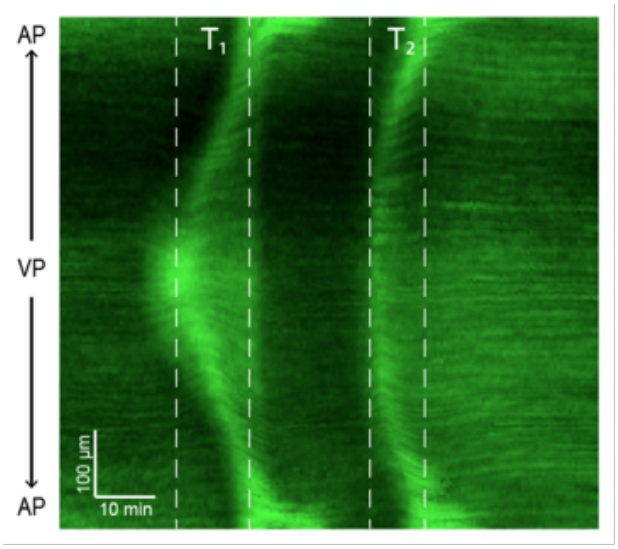

Figure 6.6 | Rho-GTP band in anaphase II is faster than anaphase I. Duration of first wave $T_1 \sim 10$ mins while duration of second wave $T_2 \sim 5$ mins.

Cdk1 gradient . We estimated the front speed from the membrane deformation induced by the SCW . Combining measurements of multiple SCWs from different cell shapes, we indeed find that the propagation speed is positively correlated with, and limited by, the ratio of the decay rate to the slope of the membrane Cdk1 gradient (Fig. 6.4j).

As a final test of our model, we ask whether the Cdk1-Ect2-Rho pattern hierarchy can explain the negative correlation between the speed of the Rho-GTP band and the magnitude of deformation during the contraction wave (Fig. 6.1d). We reason that the contraction wave must reorient the membrane with respect to the gradient, such that the Cdk1 gradient along the membrane becomes steeper, resulting in a slower front propagation. In agreement with this expectation, we find that for oocytes with a larger shape deformation, the ratio of the decay rate to the slope of Cdk1 gradient is reduced (Fig. 6.4k). Furthermore, our proposed mechanism predicts that the Cdk1 gradient during meiosis II should be shallower or should decay faster, resulting in a faster progression of the SCW during meiotic anaphase II (Fig. 6.6).

In summary, we have demonstrated a mechanism that confers robustness to protein self-organization against cell-shape changes. This mechanism integrates positional information encoded in gradients and self-organized patterns [213]. Here, the cell shape information is encoded in a cytosolic Cdk1 gradient. This is decoded by the propagating Ect2 front, which is consistent with Ect2 bistability. Finally, the moving Ect2 front triggers excitable dynamics of the shape regulator Rho. Thus, this hierarchical coupling of bistability and excitability processes cell shape information to induce a mechanochemical response. The excitable dynamics underlying the Rho-GTP band is reminiscent of the spiking dynamics in neural systems [170], suggesting that information processing on widely differing scales arises from similar organizing principles. In addition, this coupling elucidates how the

Rho-GTP band and spiral front propagation arise from the same underlying regulatory network, unifying the two phenomena that have been previously reported separately [144, 145, 214]. As Rho induces actomyosin contractility to change cell shape, this mechanism provides a mechanochemical feedback loop which could also facilitate cell-shape control, a process distinct from previously reported mechanochemical coupling mechanisms [215, 216]. Interestingly, the Cdk1-Ect2-Rho hierarchy shows striking similarities with surface contraction waves in Xenopus eggs [217], nuclear positioning [218] and cell cycle waves in Drosophila embryos [219, 220], and morphogenetic furrow formation during Drosophila eye development [221], suggesting that our results may underpin a wide range of cellular patterning processes. We hypothesize that this hierarchical coupling of protein patterns is a generic mechanism that facilitates robust spatiotemporal information processing on various scales, from single cells to tissues.

Appendices

6.A Methods

Experimental Methods

Starfish oocyte preparation. Starfish *Patiria Miniata* was procured from South Coast Bio-Marine LLC. The animals were kept in salt water fish tank maintained at 15 °C. The ovaries were extracted through a small incision made at the bottom of the starfish. The ovaries were carefully fragmented using a pair of scissors to release the oocytes. Extracted oocytes were washed twice with calcium free seawater to prevent maturation and incubated in filtered seawater (FSW) at 15 °C. Experiments were performed within three days of oocyte extraction. To induce large shape deformation, oocytes are incubated in 0.1 mg/mL actinase E for 30 mins.

Constructs. The following constructs used were described in previous studies: GFP-labeled rhotekin binding domain construct, EGFP-rGBD42 (Addgene plasmid #26732); 3XmCherry-labeled Ect2 [222] (gift from Kuan-Chung Su); EGFP-labeled cyclinB21 (gift from Peter Lenart). Additionally, the constitutively active Ect2 construct fluorescently labeled with mCherry, mCherry-Ect2-T808A, was a gift from George von Dassow.

To manipulate Rho activity with light, we adapted the TULIP optogenetic system30 to enable photo-recruitment of GEF to the membrane. The system consists of two components: (1) a membrane targeted photosensitive domain LOVpep, and (2) a nucleotide exchange factor (GEF) LARG fused with tandem PDZ tag that binds to LOVpep in a 405nm light dependent manner. To adapt this system in starfish oocyte, we cloned the Stargazin-GFP-LOVpep (Addgene plasmid #80406, using primers atggggctgtttgatcgagg and ttacacccaggtatccaccgc) and PR-GEF-YFP (2XPDZ-YFP-LARG-DH, Addgene plas-

mid #80408, using primers atggcaaaacaagagattcgagtga and ttagcgctgcttgttttctgcc) into pCS2+8 backbone constructs [223] (Addgene plasmid #34931). Stargazin-GFP-LOVpep and PR-GEF-YFP (2XPDZ-YFP-LARG DH) were gifts from Michael Glotzer and PCS2+8 was a gift from Amro Hamdoun.

in vitro synthesis of mRNA and microinjection. For in vitro synthesis of mRNA, we first amplified the constructs by bacterial growth overnight. The plasmids were then purified using Miniprep (Qiagen) and linearized using the appropriate restriction enzymes. EGFP-rGBD and 3XmCherry-Ect2 mRNA were synthesized using the SP6 mMessage mMachine transcription kits (Thermo Fisher Scientific). cyclinB-EGFP mRNA was synthesized using the T7 Ultra mMessage mMachine transcription kits (Thermo Fisher Scientific). To express the constructs, the synthesized mRNA was microinjected into the cytoplasm of the oocytes and incubated overnight at 15 °C.

PDMS (Polydimethylsiloxane) chamber. Microfabricated chambers were fabricated by casting PDMS onto patterned silicon wafers. The chamber shapes were designed with a height of 80 μm and surface area of around 27000 μm^2, to match typical volumes of the oocytes. The patterned silicon wafer was manufactured using photolithography (Microfactory SAS, France). The silicon wafer was silanized with Trichlorosilane (Sigma 448931). PDMS was made by mixing Dow SYLGARD™ 184 Silicone Elastomer Clear solution at a 10:1 base-to-curing agent ratio. After mixing thoroughly, the elastomer was poured over the silicon master mold, degassed in a vacuum chamber and cured at 60 °C in oven for an hour.

Confocal imaging. Fluorescence imaging was performed on either the Zeiss 700 or 710 laser scanning confocal system. The Zeiss 700 laser scanning confocal system consists of a Zeiss AxioObserver motorized inverted microscope stand, a LSM photomutiplier detector and a transmitted light detector. Images were acquired using 40x/NA 1.3 Oil Plan Apochromat objective with the appropriate laser line and emission filter. The system is operated using Zeiss Zen 2010 acquisition software.

The Zeiss 710 laser scanning confocal system consists of a Zeiss AxioObserver motorized inverted microscope stand with DIC optics, motorized XY stage and two LSM photomutiplier detector and a transmitted light detector. Images were acquired using 40x/NA 1.1 Water LD C-Plan Apochromat objective with the appropriate laser line and emission filter. The system is operated using Zeiss Zen Black 2012 acquisition software.

Image analysis and quantification

Space-time kymograph of Rho-GTP. The space time kymograph of GFP-labeled Rho-GTP $I_R(s,t)$ is computed by first extracting the boundary of the oocyte $\vec{r}(s) = (x(s), y(s))$ and then extracting the fluorescence intensity $I_R(s)$ along the boundary for all time frame t. Here, we used s to parameterize the arclength of the oocyte boundary. For each time frame t, we performed a Gaussian filtering step (with a standard deviation of 1.2 pixel) on the

confocal image of the oocyte cross-section before applying a thresholding step (threshold level set at 80% of the mean intensity of each frame) to make a binary image. The oocyte boundary $\vec{r}(s)$ is obtained by using the *bwboundaries* function in MATLAB on the binary image and then smoothed using the MATLAB function smoothing. The intensity $I_R(s)$ is obtained by first identifying a local window of size 12-by-12 pixels centered at $\vec{r}(s)$ and taking the mean intensity of the pixels in the top 50 percentile intensity within the local window. To construct the full kymograph $I_R(s,t)$, the intensity $I_R(s)$ at each time frame t is aligned such that the AP corresponds to the same arclength position and resampled at the appropriate arclength s.

Space-time kymograph of membrane curvature change. From the oocyte boundaries $\vec{r}(s) = (x(s), y(s))$ measured for all time points, the positions $x(s)$ and $y(s)$ are aligned to a common point (consistent with alignment done for $I_R(s)$) and resampled at appropriate arclength s to produce $\tilde{x}(s)$ and $\tilde{y}(s)$. The in-plane membrane curvature is computed using the resampled positions and according to the equation:

$$\kappa = \frac{|\tilde{x}'\tilde{y}'' - \tilde{y}'\tilde{x}''|}{(\tilde{x}'^2 + \tilde{y}'^2)^{3/2}}$$

where primes refer to derivative with respect to arclength s. The full curvature kymograph $\kappa(s,t)$ is obtained by repeating the calculation for all time points t. The kymograph of membrane curvature change $\tilde{\kappa}(s,t)$ is obtained by subtracting the rest state curvature $\kappa(s, t = 0)$ from the kymograph. The contraction wave appears as a band of negative values in the curvature change kymograph. The maximum curvature change plotted in Fig. 6.1D is the average of six curvature values sampled mid-wave (when curvature change is maximum). Error bar is the standard deviation of the six values. To minimize batch-to-batch variation, all experiments in Fig. 6.1D are performed using oocytes from the same batch.

Space-time kymograph and contour plot Cdk1. The Cdk1 concentration near the membrane $c(s)$ is obtained by averaging the intensity measurements within an annulus region beneath the membrane. A set of 4 progressively smaller perimeters sharing the same centroid are obtained from the oocyte boundary $\vec{r}(s) = (x(s), y(s))$ with dilation factors (0.95, 0.91, 0.87, 0.83). The intensity $I_{C_i}(s)$ along the ith perimeter $\vec{r}_i(s)$ is obtained by first identifying a local window of size 12-by-12 centered at $\vec{r}_i(s)$ and taking the mean intensity of the pixels in the top 50 percentile intensity within the local window. The concentration of cdk1 $I_C(s)$ is obtained by taking the average of the four intensities $I_{C_i}(s)$. To construct the full kymograph $I_C(s,t)$, the concentration $I_C(s)$ at each time frame t is aligned such that the AP corresponds to the same arclength position and resampled at the appropriate arclength s. The final kymograph is obtained by normalizing $I_C(s,t)$ with the concentration of Cdk1 at the point when the contraction wave first initiated, c_0. The contour plot is obtained from the kymograph using MATLAB function *contour*.

Space-time kymograph of Ect2. The Ect2 kymograph along cell boundary $I_E(s,t)$ is obtained using a similar method as the Cdk1 kymograph with one significant difference. In

addition to background fluorescence from cytosolic Ect2-mCherry, the cortex of starfish oocyte also contains granules with significant autofluorescence in the mCherry fluorescence window. To better separate signal from background, the fluorescence intensity of Ect2 $I_E(s)$ at each time point is first obtained from the oocyte boundary $\vec{r}(s)$ using the same approach as Cdk1 intensity $I_C(s)$, but with 3 dilation factors (0.95, 0.91, 0.87) instead of 4. To remove noise, a smoothing spline is fitted to $I_E(s)$ using Matlab smoothing spline function spaps, with tolerance value set at 10% of the range of $I_E(s)$ (that is, tol = [max$I_E(s)$ − min$I_E(s)$]/10). To remove background, the time difference of $I_E(s)$ at subsequent time point $\Delta I_E(s,t) = I_E(s,t) - I_E(s,t-1)$ is obtained. The final Ect2 kymograph $I_E(s,t)$ is taken to be the cumulative sum of the intensity difference $\Delta I_E(s,t)$, that is $I_E(s,t) = \sum_{\tau=1}^{t} \Delta I_E(s,)$. The Ect2 cumulative difference snapshot and kymograph in Fig. 6.2B is obtained using a similar procedure for background subtraction. Starting from the raw video $I_E(\vec{r},t)$ (Movie S10, left), we computed the temporal intensity difference at subsequent time point $\Delta I_E(\vec{r},t) = I_E(\vec{r},t) - I_E(\vec{r},t-1)$. The final cumulative difference snapshot is taken to be $I_E(\vec{r},t) = \sum_{\tau=1}^{t} \Delta I_E(\vec{r},\tau)$ (Movie S10, right). The kymograph in Fig. 6.2B is obtained by taking the average intensity of a thin section in the middle of membrane over the duration of the SCW.

Co-localization of Ect2 with Cdk1/Rho-GTP. To show that Ect2 front co-localize with Cdk/Rho-GTP, we co-expressed Ect2-mCherry with cyclinB-GFP/rGBD-GFP (Rho-GTP reporter) simultaneously and performed confocal imaging. We extracted the space-time kymograph of Ect2 together with Cdk1/Rho-GTP the same way as described above. We were unable to visualize co-localization of Ect2 with Rho pulse in wildtype condition, since we lack the tools to label the endogenous pool of Ect2 proteins. However, our Ect2/Rho-GTP two color imaging experiment clearly demonstrates that the Ect2 front co-localizes well with a Rho-GTP spiral front.

Cdk1 decay rate and slope calculation. To estimate the decay rate γ, the total cdk1 intensity over the entire oocyte boundary $I_{C_T}(t) = \sum_s I_C(t,s)$ is plotted as a function of time. The intensity curve is approximately linear over the time window of the wave. The decay rate γ is obtained by taking the slope of the linear line connecting $I_{C_T}(t_{\text{start}})$ and $I_{C_T}(t_{\text{end}})$. The spatial slope of cdk1 can be estimated from the spatial profile of Cdk1 at mid-wave $I_{C_{\text{mid}}}(s) = I_C(s,t_{\text{mid}})$. The slope for each wave segment is obtained by taking the slope of the linear line connecting $I_{C_{\text{mid}}}(s_{\text{start}})$ and $I_{C_{\text{mid}}}(s_{\text{end}})$, where s_{start} and s_{end} are the initiation and the annihilation position of each wave segment. The slopes similarly calculated from the spatial profiles of Cdk1 at the start and end of the wave $I_C(s,t_{\text{start}})$ and $I_C(s,t_{\text{end}})$ are used as upper and lower error bars.

Ect2 front speed calculation from oocyte shape deformation. Since the membrane deformation arises from the Rho peak, which in turn localizes at the Ect2 front, we use the deformation of the membrane as a proxy for the Ect2 front position. To estimate the Ect2 front speed, we track the point of maximal deformation of the membrane along the arclength. From the curvature kymograph $\kappa(s,t)$, the curvature difference $\Delta\kappa(s,t) = \kappa(s,t) - \kappa(s,t-1)$ is computed. For a particular arclength location s, we found that the

point at which curvature change $\Delta\kappa(t)$ passes zero is a good estimate of the Rho peak position. We verified this by performing Rho fluorescent imaging and showed that the Rho peak trajectory corresponds to point of maximal deformation identified from $\Delta\kappa(s,t)$. After identifying all the points of zero crossing in the curvature difference kymograph $\Delta\kappa(s,t)$, a straight line is fitted for each wave segment. The slope of the linear line gives the Ect2 front speed for the particular oocyte segment. Error bar is the 95% prediction interval.

Reaction-diffusion model for Rho and Ect2 module

In this section, we specify the model equations and parameters.

Reaction-diffusion equations for the Ect2 module.
We propose a model in which Ect2 cycles between an inactive phosphorylated (concentration $u_{Ep}(\vec{r},t)$) and an active non-phosphorylated state ($u_E(\vec{r},t)$). Furthermore, we assume that active Ect2 can bind to and detach from the membrane ($u_e(\vec{r},t)$). Ect2 can diffuse on the surface of a two-dimensional elliptical, triangular or star geometry, representing the focus plane in experiments of geometrically confined oocytes. To describe the dynamics of Ect2, we use a reaction–diffusion model

$$\partial_t u_E = D_c\nabla^2 u_E + f_E(u_E, u_{Ep}, u_e) \tag{6.1}$$
$$\partial_t u_{Ep} = D_c\nabla^2 u_{Ep} + f_{Ep}(u_E, u_{Ep}, u_e) \tag{6.2}$$
$$\partial_t u_e = D_m\nabla^2 u_e + f_e(u_E, u_{Ep}, u_e) \tag{6.3}$$

with

$$f_{\mathrm{E}} = k_{\mathrm{off}}u_{\mathrm{e}} - k_{\mathrm{on}}u_{\mathrm{E}} - \frac{k_{[\mathrm{Cdk1}]}u_{\mathrm{E}}}{K_{\mathrm{p}} + u_E} + (k_{\mathrm{dp}} + k_{\mathrm{fb}}u_{\mathrm{E}})u_{\mathrm{Ep}}, \tag{6.4}$$
$$f_{\mathrm{Ep}} = \frac{k_{[\mathrm{Cdk1}]}u_E}{K_p + u_E} - (k_{dp} + k_{fb}u_{\mathrm{E}})u_{\mathrm{Ep}}, \tag{6.5}$$
$$f_{\mathrm{e}} = k_{\mathrm{on}}u_{\mathrm{E}} - k_{\mathrm{off}}u_{\mathrm{e}} \tag{6.6}$$

These reaction kinetics conserve total protein mass, such that $\int_\Omega d\vec{r}\,(u_E + u_{\mathrm{Ep}} + u_e) = n_{\mathrm{E}}$ remains constant, where Ω denotes the computational domain.

Parameters for the Ect2 module.
The parameters of this model are specified in Table 3.1. The reaction rates represent effective rates which can depend on the concentration of other proteins. These rates are chosen such that the model exhibits a bistable window for a range for phosphorylation rates

(Cdk1 concentrations). The diffusion constants are chosen such that the diffusion constant in the cytosol is much larger than the diffusion constant on the membrane ($D_c \gg D_m$). The ratio of the Cdk1 decay rate to the Cdk1 slope can be estimated from the SCW propagation speed (10-35 μm/min).

To emulate the effect of the Cdk1 gradient, we assume that the Cdk1-dependent phosphorylation rate $k_{[\mathrm{Cdk1}]}(\vec{r},t)$ is a decaying linear gradient

$$k_{[\mathrm{Cdk1}]}(|\vec{r}|,t) = (c_0 - a|\vec{r}|)(1 - \frac{t}{\gamma + t}).$$

Here, γ is the Cdk1 concentration half-life and c_0 and a are the maximum and slope of the gradient, respectively. As an initial condition, we use that Ect2 is in the phosphorylated state such that $u_{\mathrm{Ep}} = n_{\mathrm{E}}$ and $u_{\mathrm{e}} = u_{\mathrm{E}} = 0$.

Reaction-diffusion equations for the Rho module. We consider a model in which the Rho GTPase diffuses on the surface of a three-dimensional volume and can cycle between three conformations: (1) an inactive (GDP-bound) cytosolic conformation close to the membrane (concentration $u_{\mathrm{R}}(\vec{r},t)$), (2) an inactive state on the membrane (concentration $u_{\mathrm{rd}}(\vec{r},t)$) and (3) an active (GTP-bound) conformation on the membrane (concentration $u_{\mathrm{rt}}(\vec{r},t)$). We only consider the cytosolic concentration close to the membrane, assuming the absence of cytosol gradients normal to the membrane. The corresponding reaction-diffusion equations are given by

$$\partial_t u_{\mathrm{R}} = D_{\mathrm{R}}\nabla^2 u_{\mathrm{R}} + f_{\mathrm{R}}(u_{\mathrm{R}}, u_{\mathrm{rd}}, u_{\mathrm{rt}}) \tag{6.7}$$
$$\partial_t u_{\mathrm{rd}} = D_{\mathrm{rd}}\nabla^2 u_{\mathrm{rd}} + f_{\mathrm{rd}}(u_{\mathrm{R}}, u_{\mathrm{rd}}, u_{\mathrm{rt}}) \tag{6.8}$$
$$\partial_t u_{\mathrm{rt}} = D_{\mathrm{rt}}\nabla^2 u_{\mathrm{rt}} + f_{\mathrm{rt}}(u_{\mathrm{R}}, u_{\mathrm{rd}}, u_{\mathrm{rt}}) \tag{6.9}$$
$$\tag{6.10}$$

with the reaction terms

$$f_{\mathrm{R}} = k_{\mathrm{off}}u_{\mathrm{rd}} - k_{\mathrm{on}}u_{\mathrm{R}} + k_{\mathrm{gap}}u_{\mathrm{rt}}, \tag{6.11}$$
$$f_{\mathrm{rd}} = k_{\mathrm{on}}u_{\mathrm{R}} - k_{\mathrm{off}}u_{\mathrm{rd}} - (k_r + k_{\mathrm{dt}}u_{\mathrm{rt}}^2)u_{\mathrm{rd}}, \tag{6.12}$$
$$f_{\mathrm{rt}} = (k_{\mathrm{r}} + k_{\mathrm{dt}}u_{\mathrm{rt}}^2)u_{\mathrm{rd}} - k_{\mathrm{gap}}u_{\mathrm{rt}}. \tag{6.13}$$
$$\tag{6.14}$$

These reaction kinetics conserve total protein mass, such that $\int_\Omega d\vec{r}\,(u_{\mathrm{R}} + u_{\mathrm{rd}} + u_{\mathrm{rt}}) = n_{\mathrm{R}}$, where Ω denotes the computational domain (here the surface of a 3D cytosolic volume).

Parameters for the Rho module.
The parameters of this model are specified in Table 6.1. Diffusion constants are chosen

such that diffusion in the cytosol is much faster than diffusion on the membrane ($D_R \gg D_{\mathrm{rd}}, D_{\mathrm{rt}}$). The reaction rates of this model represent effective rates and may depend on the concentration of other regulatory proteins that are not explicitly accounted for in our minimal model. To reproduce the experimental observations, we choose the rate constants such that the reaction kinetics are excitable. A detailed motivation for the parameter is presented in Sec. 4.7 and 6.B.

To emulate the concentration profile of the propagating Ect2 front we use a propagating front $\xi_{\mathrm{Ect2}} = 0.01 + 0.99\Theta(|\vec{r}| - (|\vec{r}_0| - V_{\mathrm{Ect2}}t))$, which we multiply with the activation rates k_{r} and k_{dt}. This was done for the simulations shown in Fig. 6.3f and 6.3k and movies S14 and S18. Note that one can also use $\xi_{\mathrm{Ect2}} = u_{\mathrm{e}}(\vec{r}, t) + u_{\mathrm{E}}(\vec{r}, t)$, which couples the concentration profile of active Ect2 of the Ect2 module to the Rho module of the model. The latter was used for the simulation in elliptical, triangular, and star geometry in movies S15-S17.

Simulation methods, geometry and domain size. The simulations presented in Fig. 6.3f, 6.3k, and Fig. 6.8C and in movies S14 and S18 are finite element simulations on the surface of a three-dimensional spherical volume, implemented in COMSOL Multiphysics version 5.4 and with parameters as in Table 6.1. The simulations presented in Fig. 6.4f-h and movie S15-S17 are finite element simulations on the surface of a three-dimensional ellipsoidal-, triangular- and star-shaped domain, with parameters as in Table 6.1 and 3.1. Here, the Rho and Ect2 dynamics are constrained to the surfaces of the static three-dimensional geometries, while the Cdk1 concentration is modelled as a linear gradient in the three-dimensional bulk which radially extends from the position of the nucleus into the cytoplasm.

6.B Ect2 overexpression leads to a transition to local oscillations

In the starfish oocyte, Ect2 overexpression leads to a front of Rho spirals, instead of a single concentration peak at the Ect2 front. Thus, viewed at a membrane position in the VP domain, the Rho-GTP concentration oscillates. This suggests that the Rho reaction kinetics in the VP domain lies within regime 3 instead of regime 1 cf. Sec. 4.5. Notably, the oscillation timescale is roughly 10 times faster than the excursion time for the Rho pulse (Fig. 6.1c and 6.2c). This suggest that Ect2 overexpression does not only lead to a transition to oscillations but also to an overall increase in the GTPase cycling rate. This implies that Ect2 overexpression effectively also increases the attachment rate and the hydrolysis-driven detachment rate of Rho, for example via interactions between Ect2 and other Rho regulatory proteins. Indeed, as discussed in Sec. 4.2, it has been suggested that Ect2 plays a role in the localization of Rho to the membrane [151] and that Ect2 can interact with a RhoGAP [162]. Furthermore, the hypothesis that Ect2 affects more than

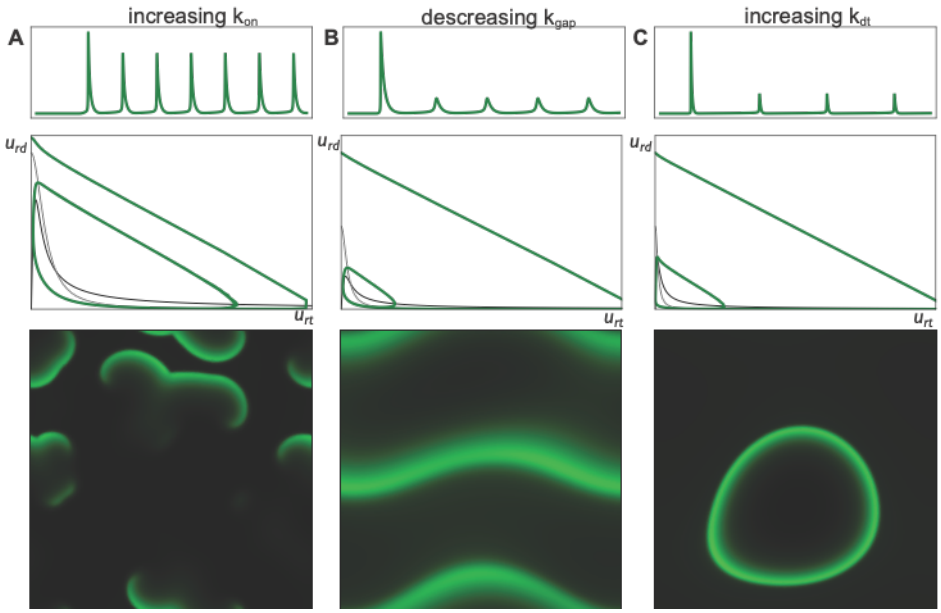

Figure 6.7 | Oscillatory media. A transition from the wild type parameters to local oscillations is obtained by **(A)** increasing the attachment rate k_{on}, **(B)** decreasing the hydrolysis rate k_{gap}, or **(C)** increasing the autocatalytic nucleotide exchange rate k_{dt}. In a spatially extended system, these oscillatory media show A) spirals, B) traveling waves and C) extending rings (target pattern).

the nucleotide exchange is also consistent with our model, as only increasing the nucleotide exchange rates in the VP domain does not lead to oscillations. Thus, this implies that upon Ect2 overexpression more than one process of the GTPase cycle is varied.

Which process of the Rho GTPase cycle drives the system into the oscillatory regime? As discussed in Sec. 4.5 a transition to oscillations can be realized by increasing the attachment rate k_{on}, decreasing the hydrolysis rate k_{gap}, or increasing the autocatalytic nucleotide exchange rate k_{dt} (keeping the linear nucleotide exchange rate small). Consistently, changing one of these three rates leads to a transition to oscillations (Fig. 6.7). We therefore reasoned that in oocytes where Ect2 is overexpressed, one of these processed must be enhanced with respect to the wild type. However, in all cases the oscillation timescale in the model is still similar to the excitation time of the Rho pulse, showing that such an additional change in the rates is sufficient to explain the experiments only qualitatively, but not quantitatively. To match the experimentally observed oscillation period quantitatively in our model, we choose to increase the global timescale of the Rho dynamics by multiplying all rates with a common factor τ.

Spatially (diffusively) coupled system – In a spatially coupled system, oscillatory dynamics typically results in traveling waves [170]. When these traveling waves develop phase defects, either due to a wave front instability or when they encounter obstacles, traveling waves typically form spirals. Indeed, using finite element simulations, we confirm that the

Parameter	Wild type	Ect2 over expression	Unit	Description
k_{on}	1.5×10^{-4}	$1.5 \times 10^{-3}\tau$	s^{-1}	Rho-GDP membrane attachment
k_{off}	1.5×10^{-5}	$1.5 \times 10^{-5}\tau$	s^{-1}	Rho-GDP membrane detachment
k_{r}	$1.5 \times 10^{-4}\xi_{\text{Ect2}}$	$1.5 \times 10^{-4}\tau\xi_{\text{Ect2}}$	s^{-1}	Nucleotide exchange rate/activation rate
k_{dt}	$9.45 \times 10^{-3}\xi_{\text{Ect2}}$	$9.45 \times 10^{-3}\tau\xi_{\text{Ect2}}$	$\mu m^4 s^{-1}$	Autocatalytic activation rate
k_{gap}	1.5×10^{-2}	$1.5 \times 10^{-2}\ \tau$	$\mu m^2/s$	Rho-GTP membrane detachment
n_{R}	10	10	μm^{-2}	Rho total concentration
D_{R}	10	10	$\mu m^2/s$	Diffusion constant Rho-GDP in the cytosol
D_{rd}	0.1	0.1	$\mu m^2/s$	Diffusion constant Rho-GDP on the membrane
D_{rt}	0.05	0.05	$\mu m^2/s$	Diffusion constant Rho-GTP on the membrane
V_{Ect2}	0.2	0.2	$\mu m/s$	Ect2 propagation speed
ϵ	1	1	μm	Width of Ect2 front interface
τ	1	40	–	Timescale scaling factor
ξ_{Ect2}	[0.01, 1]	[0.01, 1]	μm^{-2}	Ect2 front parameter in low and high Ect2 domain (movies S14 and S18)
ξ_{Ect2}	$u_{\text{e}} + u_{\text{E}}$	–	μm^{-2}	Ect2 front parameter to couple Rho and Ect2 module (movies S15- S17)

Table 6.1 | Model parameters for the Rho dynamics. Parameters are chosen such that the model exhibits oscillatory dynamics.

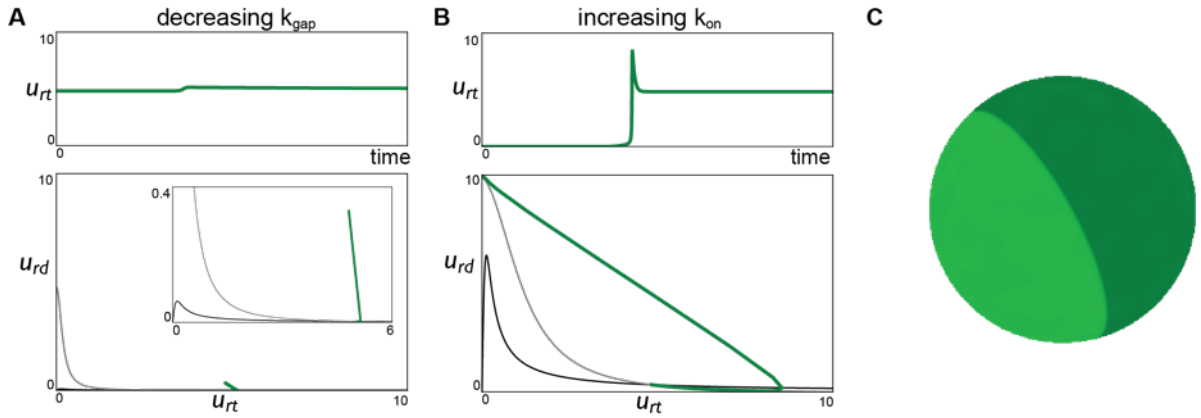

Figure 6.8 | Rho front. **(A)** A decrease in de hydrolysis rate k_{gap}, or **(B)** an increase in the attachment rate k_{on}, leads to a transition from regime 1 to regime 2 (cf. Sec. 4.5). **(C)** On the membrane, this leads to a propagating Rho front. (A) and (B) show simulations of the reduced model (Eqs. 4.8), (C) shows a snapshot of a simulation of the full model (Eqs. 6.7 and 6.11), performed on the surface of a spherical volume.

system exhibits traveling waves in the parameter regime where it exhibits local oscillations (Fig. 6.7). For an increased attachment rate, the system develops spiraling dynamics. For the change in the hydrolysis rate we find traveling waves, and for a change in the autocatalytic nucleotide exchange rate the traveling waves form rings. We therefore choose to increase the attachment rate to describe the front of Rho spirals.

6.C Propagating Rho front

So far, we have shown that as the Ect2 front travels along the membrane it leads to a transition from one steady state to another steady state. For the wild type, both steady states are in regime 1 cf. Sec. 4.5. For Ect2 over expressed oocytes, the Ect2 front leads to a transition from a steady state in regime 1 to regime 3, giving rise to a front of Rho spirals. What is the concentration profile of Rho-GTP on the membrane when the Ect2 front leads to a transition between regime 1 and 2? As discussed in Sec. 4.5, the steady state in regime 2 is monostable with a high Rho-GTP concentration on the membrane. A transition to regime 2 can be achieved for example by decreasing the hydrolysis rate (Fig. 6.8B) or increasing the attachment rate even more than for Ect2 OE (Fig. 6.8C). Thus, a sudden change from a steady state in regime 1 to a steady state in regime 2, would lead to an increase in the Rho-GTP concentration that stays high as the Ect2 front has passed. In a spatially extended system, this leads to a propagating Rho front rather than a propagating Rho pulse or front of Rho spirals (Fig. 6.8D). Interestingly, such Rho dynamics has been observed previously by using a Rok inhibitor [152].

6.D Movie captions

All movies are available on
https://www.dropbox.com/sh/yzyqjvm6erkv4vd/AACp5KzHZuMLChRynGG4DSH0a?dl=0

Movie S1: Surface contraction wave (SCW) of starfish oocyte during meiosis I. Rho-GTP is labeled fluorescently using rGBD-GFP reporter. Video taken with confocal microscopy at cross section (left) and bottom plane (right) of oocytes. Time in min:sec.

Movie S2-5: Rho-GTP wave (labeled with rGBD-GFP) of starfish oocyte during meiosis I when imaged in PDMS chamber of different geometries: ellipse with animal pole (AP) at one corner (movie S2), ellipse with AP at side (movie S3), triangle with AP in the midle (movie S4) and star shape with AP at one corner (movie S5). Video taken with confocal microscopy at cross section of oocyte. Time in min:sec.

Movie S6: Spatiotemporal dynamics of Cdk1-cyclinB cytosolic gradient during meiosis I in starfish oocyte. The Cdk1 complex is imaged with cyclinB-GFP fluorescent reporter. Video taken with confocal microscopy at cross section of oocyte. Time in min:sec.

Movie S7-9: Spatiotemporal dynamics of Cdk1-cyclinB cytosolic gradient during meiosis I in starfish oocyte in different geometries: ellipse with AP at the side (movie S7), triangle with AP at different sides (movie S8-9). Video taken with confocal microscopy at cross section of oocyte. Time in min:sec.

Movie S10: Dynamics of Rho-GTP spiral front at the oocyte membrane imaged using fluorescently labeled reporter rGBD-GFP. Time in min:sec.

Movie S11: Ect2-mCherry front dynamics at the membrane. Due to significant auto-fluorescent from cortex granules, we performed background subtraction by taking the cumulative sum of the fluorescent intensity difference (same procedure as Ect2 space-time kymograph). The left video shows the raw data. The right video shows the background subtracted video. Note that the intensity around the periphery of oocyte in background subtracted video is due to the oocyte motion during SCW. Time in min:sec.

Movie S12: Two color imaging of Ect2 (Ect2-mCherry fluorescent reporter) front and Rho-GTP (rGBD-GFP reporter) spiral front. Time in min:sec.

Movie S13: Two color imaging of Cdk1-cyclinB (cyclinB-GFP fluorescent reporter) gradient and Ect2 (Ect2-mCherry fluorescent reporter) front. Time in min:sec.

Movie S14: Simulation of the Rho model (cf. Eq. 6.7 and 6.11 in Section 6.A) on the surface of a spherical 3D volume using parameters for the wild type as specified in Table 6.1.

Movie S15-17: Simulations of the Rho and Ect2 module in ellipsoidal, triangular and star shaped 3D geometries. Left panel shows the Cdk1 concentration ($\log_{10}(k_{[\mathrm{Cdk1}]})$) in the cytoplasm and Rho-GTP (u_{rt}) on the membrane, middle and right panel show the active Ect2 concentration ($u_e + u_E$) and the Rho-GTP concentration (u_{rt}) on the surface of the 3D geometry.

Movie S18: Simulation of the Rho model (cf. Eq. 6.7 and 6.11 in Section 6.A) on the surface of a spherical 3D volume using parameters for Ect2 overexpression as specified in Table 6.1.

Movie S19: Photoactivation experiment. Global light illumination at 488nm begins at 0s. Increase in yellow fluorescence indicates the recruitment of PR_GEF_YFP (photo-recruitable GEF labeled with yellow fluorescent protein) to the membrane. Beyond a certain threshold level, the oocyte contractility abruptly increases.

Movie S20: Maximal intensity projection of microtubule front near oocyte membrane during SCW imaged using ensconsin-GFP. Time in min:sec.

7 Symmetry breaking in response to cytoplasmic flow

"You can't buy happiness
but you can buy a surfboard"
– Jibe City, Bonaire

Important cellular processes, such as cell motility and cell division, are coordinated by cell polarity, which is determined by the non-uniform distribution of certain proteins. Such protein patterns form via an interplay of protein reactions and protein transport. Since Turing's seminal work, the formation of protein patterns resulting from the interplay between reactions and diffusive transport has been widely studied. Over the last few years, increasing evidence shows that also advective transport, resulting from cytosolic and cortical flows, is present in many cells. However, it remains unclear how and whether these flows contribute to protein-pattern formation. To address this question, we use a minimal model that conserves the total protein mass to characterize the effects of cytosolic flow on pattern formation. Combining a linear stability analysis with numerical simulations, we find that membrane-bound protein patterns propagate *against* the direction of cytoplasmic flow with a speed that is maximal for intermediate flow speed. We show that the mechanism underlying this pattern propagation relies on a higher protein influx on the upstream side of the pattern compared to the downstream side. Furthermore, we find that cytosolic flow can change the membrane pattern qualitatively from a peak pattern to a mesa pattern. Finally, our study shows that a non-uniform flow profile can induce pattern formation by triggering a regional lateral instability.

This Chapter is based on our paper "Flow induced symmetry breaking in a conceptual polarity model", which has been published in Cells [224]. This work has been performed together with Fridtjof Brauns, Ching Yee Leung and Erwin Frey

7.1 Introduction

Many biological processes rely on the spatiotemporal organization of proteins. Arguably one of the most elementary forms of such organization is cell polarization — the formation of a "cap" or spot of high protein concentration that determines a direction. Such a polarity axis then coordinates downstream processes including motility [225, 226], cell division [227], and directional growth [40]. Cell polarization is an example for *symmetry breaking* [99], as the orientational symmetry of the initially homogeneous protein distribution is broken by the formation of the polar cap.

Intracellular protein patterns arise from the interplay between protein interactions (chemical reactions) and protein transport. Diffusion in the cytosol serves as the most elementary means of transport. Pattern formation resulting from the interplay of reactions and diffusion has been widely studied since Turing's seminal work [171]. In addition to diffusion, proteins can be transported by fluid flows in the cytoplasm [28, 228, 229] and along cytoskeletal structures (vesicle trafficking, cortical contractions) driven by molecular motors [230–232]. These processes lead to *advective* transport of proteins.

Recently, it has been shown experimentally that advective transport (caused by cortical flows) induces polarization of the PAR system in the *C. elegans* embryo [8, 13, 25]. Furthermore, *in vitro* studies with the MinDE system of *E. coli*, reconstituted in microfluidic chambers, have shown that the flow of the bulk fluid has a strong effect on the protein patterns that form on the membrane [233, 234]. Increasing evidence shows that cortical and cytosolic flows (also called "cytoplasmic streaming") are present in many cells [72, 235–239]. In addition, cortical contractions can drive cell-shape deformations [144], inducing flows in the incompressible cytosol [28, 240]. However, the role of flows for protein-pattern formation remains elusive. This motivates to study the role of advective flow from a conceptual perspective, with a minimal model. The insights thus gained will help to understand the basic, principal effects of advective flow on pattern formation and reveal the underlying elementary mechanisms.

The basis of our study is a paradigmatic class of models for cell polarization that describe a single protein species which has a membrane-bound state and a cytosolic state. Such two-component mass-conserving reaction–diffusion (2cMcRD) systems serve as conceptual models for cell polarization [56, 91, 96, 103, 118, 228, 241]. Specifically they have been used to model Cdc42 polarization in budding yeast [92] and PAR-protein polarity [97]. 2cMcRD systems generically exhibit both spontaneous and stimulus-induced polarization [56, 97, 99]. In the former case, a spatially uniform steady state is unstable against small spatial perturbations ("Turing instability" [171]). Adjacent to the parameter regime of this lateral instability, a sufficiently strong, localized stimulus (e.g. an external signal) can induce the formation of a pattern starting from a stable spatially uniform state. The steady state patterns that form in two-component McRD systems are generally stationary (there are no traveling or standing waves). Moreover, the final stationary pattern has no characteristic wavelength. Instead, the peaks that grow initially from the fastest growing mode ("most

unstable wavelength") compete for mass until only a single peak remains ("winner takes all") [93, 94, 103]. The location of this peak can be controlled by external stimuli (e.g. spatial gradients in the reaction rates) [94, 105].

Recently, a theoretical framework, termed *local equilibria theory*, has been developed to study these phenomena using a geometric analysis in the phase plane of the protein concentrations [56, 106]. With this framework one can gain insight into the mechanisms underlying the dynamics of McRD systems both in the linear and in the strongly nonlinear regime, thereby bridging the gap between these two regimes.

Here, we show that cytosolic flow in two-component systems always induces upstream propagation of the membrane-bound pattern. In other words, the peak moves against the cytosolic flow direction. This propagation is driven by a higher protein influx on the upstream side of the membrane-concentration peak compared to its downstream side. Using this insight, we are able to explain why the propagation speed becomes maximal at intermediate flow speeds and vanishes when the rate of advective transport becomes fast compared to the rate of diffusive transport or compared to the reaction rates. We first study a uniform flow profile using periodic boundaries. This effectively represents a circular flow, which is observed in plant cells (where this phenomenon is called cytoplasmic streaming or cyclosis) [242]. It also represents an *in vitro* system in a laterally large microfluidic chamber. We then study the effect of a spatially non-uniform flow profile in a system with reflective boundaries, as a minimal system for flows close to the membrane [8, 25, 228], e.g. in the actin cortex. We show that a non-uniform flow profile redistributes the protein mass, which can trigger a regional lateral instability and thereby induce pattern formation from a stable homogeneous steady state.

The remainder of the paper is structured as follows. We first introduce the model in Sec. 7.2. We then perform a linear stability analysis in Sec. 7.3 to show how spatially uniform cytosolic flow influences the dynamics close to a homogeneous steady state. In Sec. 7.4, we use numerical simulations to study the fully nonlinear long-term behavior of the system. Next, we show that upon increasing the cytosolic flow velocity, the pattern can qualitatively change from a mesa pattern to a peak pattern in Sec. 7.5. Finally, in Sec. 7.6, we study how a spatially non-uniform cytosolic flow can trigger a regional lateral instability and thus induce pattern formation. Implications of our findings and links to earlier literature are briefly discussed at the end of each section. We conclude with a brief outlook section.

7.2 Model

We consider a spatially one-dimensional system of length L. The proteins can cycle between a membrane-bound state (concentration $m(x,t)$) and a cytosolic state (concentration $c(x,t)$), and diffuse with diffusion constants D_m and D_c, respectively (Fig. 7.1). In cells, the diffusion constant on the membrane is typically much smaller than the diffusion con-

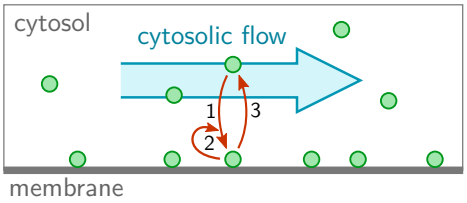

Figure 7.1 | One-dimensional two-component system with cytosolic flow into the positive x direction. The reaction kinetics include (1) attachment, (2) self-recruitment and (3) enzyme-driven detachment.

stant in the cytosol. In the cytosol, the proteins are assumed to be advected with a speed $v_\mathrm{f}(x)$, as indicated by the blue arrow in Fig. 7.1. Thus, the reaction-diffusion-advection equations for the cytosolic density and membrane density read

$$\partial_t c + \partial_x(v_\mathrm{f} c) = D_c \partial_x^2 c - f(m,c), \tag{7.1a}$$
$$\partial_t m = D_m \partial_x^2 m + f(m,c), \tag{7.1b}$$

with either periodic or reflective boundary conditions. The nonlinear function $f(m,c)$ describes the reaction kinetics of the system. Attachment–detachment kinetics can generically be written in the form

$$f(m,c) = a(m)c - d(m)m, \tag{7.2}$$

where $a(m) > 0$ and $d(m) > 0$ denote the rate of attachment from the cytosol to the membrane and detachment from the membrane to the cytosol, respectively. The dynamics given by Eq. (7.1) conserve the average total density

$$\bar{n} = \frac{1}{L}\int_0^L \mathrm{d}x\, n(x,t). \tag{7.3}$$

Here, we introduced the *local* total density $n(x,t) := m(x,t) + c(x,t)$.

For illustration purposes, we will use a specific realization of the reaction kinetics [56],

$$a(m) = k_\mathrm{on} + k_\mathrm{fb} m \quad \text{and} \quad d(m) = \frac{k_\mathrm{off}}{K_\mathrm{D} + m}, \tag{7.4}$$

describing attachment with a rate k_on, self-recruitment with a rate k_fb, and enzyme-driven detachment with a rate k_off and the Michaelis-Menten constant K_D, respectively. However, our results do not depend on the specific choice of the reaction kinetics. Unless stated otherwise, we use the parameters: $k_\mathrm{on} = 1s^{-1}, k_\mathrm{fb} = 1\mu m s^{-1}, k_\mathrm{off} = 2s^{-1}, K_\mathrm{D} = 1\mu m^{-1}, \bar{n} = 5\mu m^{-1}, D_m = 0.01\mu m^2/s, D_c = 10\mu m^2/s$.

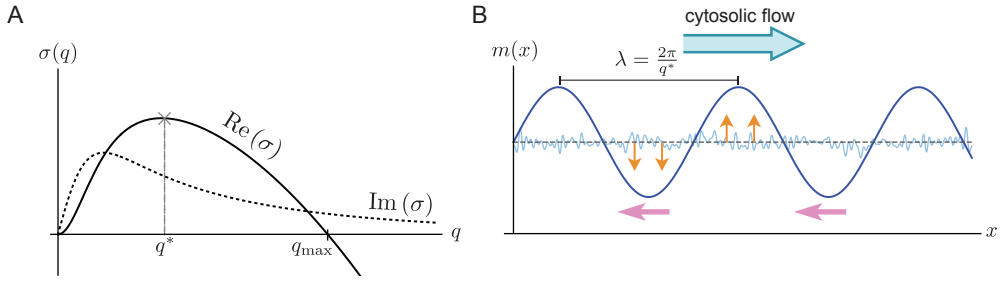

Figure 7.2 | (A) Sketch of real (solid) and imaginary (dotted) part of a typical dispersion relation with a band $[0, q_{\max}]$ of unstable modes. (B) The initial dynamics of a spatially homogeneous state with a small random perturbation (blue thin line). The direction of cytosolic flow is indicated by a blue arrow. The typical wavelength (λ) of the initial pattern is determined by the fastest growing mode q^* and the phase velocity is determined by the value of the imaginary part of dispersion relation at the fastest growing mode ($v_{\text{phase}} = -\mathrm{Im}\sigma(q^*)/q^*$). The growth of the pattern is indicated by orange arrows, while the travelling direction is indicated by pink arrows.

7.3 Linear stability analysis

7.3.1 Linearized dynamics and basic results

To study how cytosolic flow affects the formation of protein patterns, we first consider a spatially uniform flow profile (i.e. constant $v_{\mathrm{f}}(x) = v_{\mathrm{f}}$) and perform a linear stability analysis of a spatially homogeneous steady state $\mathbf{u}^* = (c^*, m^*)$:

$$f(m^*, c^*) = 0, \quad m^* + c^* = \bar{n}. \tag{7.5}$$

Following the standard procedure, we linearize the dynamics for small perturbations $\mathbf{u}(x,t) = (c(x,t), m(x,t)) = \mathbf{u}^* + \delta\mathbf{u}(x,t)$ around the homogeneous steady state. Expanding $\delta\mathbf{u}(x,t)$ in exponentially growing (or decaying) Fourier modes $\delta\mathbf{u} = \widehat{\mathbf{u}}_q\, e^{\sigma t} e^{iqx}$ leads to the eigenvalue problem

$$\mathcal{J}\widehat{\mathbf{u}}_q = \sigma\widehat{\mathbf{u}}_q, \tag{7.6}$$

with the Jacobian

$$\mathcal{J} = \begin{pmatrix} -D_c q^2 - i v_{\mathrm{f}} q - f_c & -f_m \\ f_c & -D_m q^2 + f_m \end{pmatrix},$$

where $f_c = \partial_c f|_{\mathbf{u}^*}$ and $f_m = \partial_m f|_{\mathbf{u}^*}$ encode the linearized reaction kinetics. Note that for reaction kinetics of the form Eq. (7.2), $f_c = a(m) > 0$ and we consider this case in the following.

For each mode with wavenumber q, there are two eigenvalues $\sigma_{1,2}(q)$. The case $q = 0$ corresponds to spatially homogeneous perturbations, where the two eigenvalues are given by $\sigma_1 = f_m - f_c$ and $\sigma_2 = 0$ [56]. Here, we restrict our analysis to homogeneously stable states ($\sigma_1 < 0$). The second eigenvalue ($\sigma_2 = 0$) corresponds to perturbations that change

the average mass $\bar{n}$ and therefore shift the homogeneous steady state $\mathbf{u}^*(\bar{n})$ along the nullcline $f = 0$. Because these perturbations break mass-conservation, they are not relevant for the stability of a closed system as considered here. The modes $q > 0$ determine the stability of the system against spatially inhomogeneous perturbations (*lateral stability*). The eigenvalue with the larger real part determines the stability and will be denoted by $\sigma(q)$, suppressing the index.

A typical dispersion relation with a band of unstable modes is shown in Fig. 7.2A. The real part (solid line), indicating the mode's growth rate, has a band of unstable modes $[0, q_{\max}]$ where $\operatorname{Re}\sigma(q) > 0$. The fastest growing mode q^* determines the wavelength λ of the pattern that initially grows, triggered by a small, random perturbation of the spatially homogeneous steady state. For $v_\mathrm{f} = 0$, the imaginary part of $\sigma(q)$ vanishes, for locally stable steady states ($\sigma(0) \leq 0$). [56]. However, in the presence of flow, the imaginary part of $\sigma(q)$ is non-zero (dashed line in Fig. 7.2A), which implies a propagation of each mode with the phase velocity $v_\mathrm{phase}(q) = -\operatorname{Im}\sigma(q)/q$. This means that a mode q not only grows over time (orange arrows in Fig. 7.2B), but also propagates as indicated by the pink arrows in Fig. 7.2B. Further below, in Sec. 7.3.4, we will show that $\operatorname{Im}\sigma(q)$ always has the same sign as the flow velocity v_f, such that all modes propagate *against* the flow direction.

To gain physical insight into the mechanisms underlying the growth and propagation of perturbations (modes) we will first give an intuitive explanation of a lateral instability in McRD systems, building on the concepts of local equilibria theory [56, 106]. We then provide a more detailed analysis in the limits of long wavelength as well as fast and slow flow.

7.3.2 Intuition for the flow-driven instability and upstream propagation of the unstable mode

Lateral instability in McRD systems can be understood as a *mass-redistribution instability* [56]. Let us briefly recap the mechanism underlying this instability for a system without flow. To this end, we first discuss the effect of reactions and diffusion separately, and explain how these effects together drive the mass-redistribution instability. We then explain how this instability is affected by cytosolic flow.

Consider a spatially homogeneous steady state, perturbed by a slight redistribution of the *local* total density $n(x,t)$. The dashed orange line in Figure 7.3A shows such a perturbation where the membrane concentration (Fig. 7.3A top) is slightly perturbed in a sinusoidal fashion. In phase space this is represented by a density distribution that slightly deviates from the spatially homogeneous steady state (marked by the orange dashed line). Here, the open star and open circle mark the minimum and maximum of the local total density, respectively. The local total density determines the local reactive equilibrium concentrations $m^*(n)$ and $c^*(n)$ (cf. Eq. (7.5), replacing the average mass $\bar{n}$ by the local mass $n(x,t)$). In phase space (Fig. 7.3A bottom) these local equilibria can be read off from the

intersections (marked by black circles) of the reactive subspaces $n(x,t) = m(x,t) + c(x,t)$ (gray solid lines) and the reactive nullcline (black solid lines). A slight redistribution of the local total density shifts the reactive equilibria, leading to reactive flows towards these shifted equilibria (red and green arrows in Fig. 7.3A). Thus, the reactive equilibria, and thereby the reactive flows, are encoded in the shape of the reactive nullcline in phase space. If the nullcline slope is negative, increasing the total density leads to a decreasing equilibrium cytosolic concentration and therefore to *attachment* (green arrows in Fig. 7.3A). Conversely, in regions of lower total density, the equilibrium cytosolic concentration increases via *detachment* (red arrows in Fig. 7.3A). Hence, regions of high total density become *self-organized attachment zones* and regions of low total density become *self-organized detachment zones* [106] (green and red areas in Fig. 7.3 top and middle).

These attachment and detachment zones act as sinks and sources for diffusive mass-transport on the membrane and in the cytosol: The attachment zone acts as a cytosolic sink and membrane source, and the detachment zone acts as a cytosolic source and a membrane sink (blue arrows in Fig. 7.3B). As diffusion in the cytosol is much faster than in the membrane, mass is transported faster in the cytosol than on the membrane, as indicated by the size of the blue arrows in Fig. 7.3B top and middle. This leads to net mass transport from the detachment zone to the attachment zone. As the local total density increases in the attachment zone, it facilitates further attachment and thereby the growth of the pattern on the membrane. In short, the mechanism underlying the mass-redistribution instability is a cascade of attachment–detachment kinetics (Fig. 7.3A) and net mass-transport towards attachment zones (Fig. 7.3B).

How does cytosolic fluid flow affect the mass-redistribution instability? Cytosolic flow transports proteins advectively. This advective transport shifts the cytosolic density profile downstream relative to the membrane density profile (dashed to solid orange line in Fig. 7.3C middle). This shift leads to an increase of the cytosolic density on the upstream (cyan) side of the membrane peak and a decrease on the downstream (magenta) side, in Fig. 7.3C (middle), respectively. In phase space, this asymmetry is reflected as a 'loop' shape of the phase space trajectory that corresponds to the real space pattern (Fig. 7.3C bottom). The higher cytosolic density on the upstream side increases attachment relative to the downstream side. This leads to a propagation of the membrane concentration profile in the upstream direction.

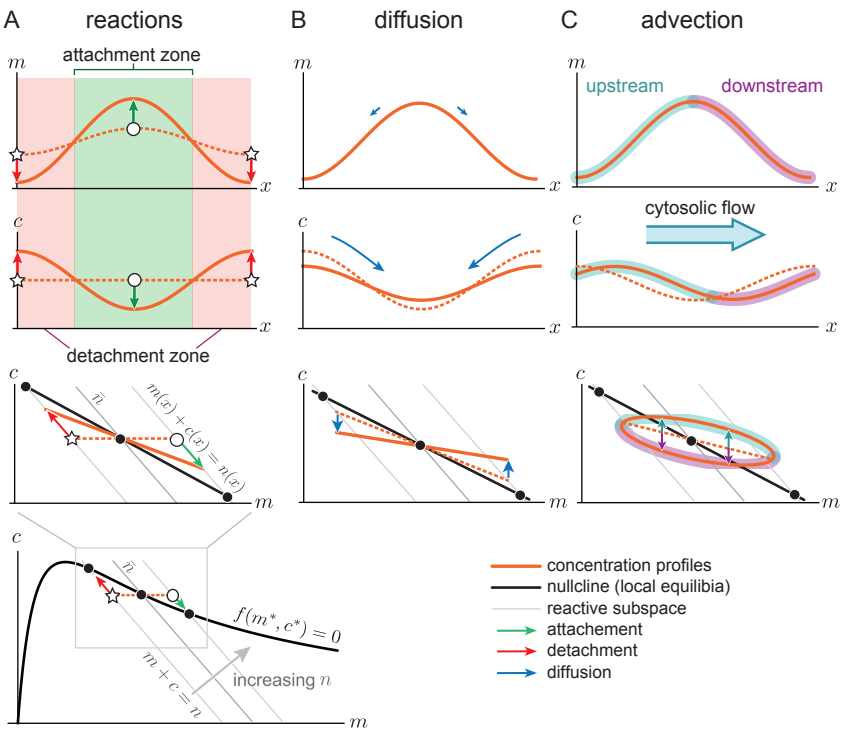

Figure 7.3 | Sketch of the initial dynamics of an laterally unstable spatially homogeneous steady state. The role of reactions (A), diffusion (B) and advection (C) for a mass-redistribution instability are presented for the membrane (top) and cytosolic (middle) concentration profiles and in phase space (bottom). (A) A small perturbation of the spatially homogeneous membrane concentration (orange dashed lines in top panel) leads to a spatially varying local total density $n(x)$, with a larger total density at the maximum of the membrane profile (open circle) and a smaller total density at the minimum (open star). These local variations in total density lead to attachment zones (green region) and detachment zones (red region). The reactive flow, indicated by the red and green arrows, points along the reactive subspace (gray lines) in phase space towards the shifted local equilibria (black circles). These reactive flows lead to the solid orange density profiles after a small amount of time. (B) Faster diffusion in the cytosol compared to the membrane (indicated by the large and small blue arrows in the middle and top panel, respectively), lead to net mass transport from the detachment zone to the attachment zone. Again, dashed and solid lines indicate the state before and after a short time interval of diffusive transport. (C) Cytosolic flow shifts the cytosolic concentration with respect to the membrane concentration (orange dashed to orange solid lines), increasing the cytosolic concentration on the upstream side of the pattern and decreasing the cytosolic concentration on the downstream side . In phase space, the trajectory of this density profile forms a 'loop'.

7.3.3 Long wavelength limit

To complement this intuitive picture we consider the long wavelength limit $q \to 0$.[1] In this limit, the dispersion relation expanded to second order in q reads

$$\sigma(q) \approx -\frac{1}{1+s_{\mathrm{nc}}}\left[is_{\mathrm{nc}}v_{\mathrm{f}}q + (D_m + s_{\mathrm{nc}}D_c)q^2 + \frac{s_{\mathrm{nc}}\, v_{\mathrm{f}}^2}{f_c(1+s_{\mathrm{nc}})^2}q^2\right], \tag{7.7}$$

where $s_{\mathrm{nc}} = -f_m/f_c$ is the slope of the reactive nullcline. The imaginary part $\mathrm{Im}\,\sigma(q)$ is linear in q to lowest order, implying a phase velocity $v_{\mathrm{phase}} = v_{\mathrm{f}}s_{\mathrm{nc}}/(1+s_{\mathrm{nc}})$ that is independent of the wavelength. The growth rate $\mathrm{Re}\,\sigma(q)$ is quadratic in q to lowest order. If this quadratic term is positive, there is a band of unstable modes.[2] Hence, the criterion for a mass-redistribution instability can be expressed in terms of the nullcline slope [56]

$$s_{\mathrm{nc}} < -\frac{D_m}{D_c}\left[1 + \frac{v_{\mathrm{f}}^2}{(1+s_{\mathrm{nc}})^2 D_c f_c}\right]^{-1}. \tag{7.8}$$

In the absence of flow, $v_{\mathrm{f}} = 0$, we recover the slope criterion $s_{\mathrm{nc}} < -D_m/D_c$ for a mass-redistribution instability driven by cytosolic diffusion [56]. We find that flow always increases the range of instability since the second term in the square brackets monotonically increases with flow speed $|v_{\mathrm{f}}|$. Furthermore, the instability criterion becomes independent of the diffusion constants in the limit of fast flow ($|v_{\mathrm{f}}| \gg \sqrt{D_c f_c}$). The criterion for the (flow-driven) mass-redistribution instability then simply becomes $s_{\mathrm{nc}} < 0$, independently of the ratio of the diffusion constants. This has the interesting consequence that, for sufficiently fast flow, a mass-redistribution instability can be driven solely via cytoplasmic flow, independent of diffusion.

7.3.4 Limits of slow and fast flow

To analyze the effect of flow for wavelengths away from the long wavelength limit it is instructive to consider the limit cases of slow and fast flow speed.

We first consider a limit where advective transport $(qv_{\mathrm{f}})^{-1}$ is slow compared either to the chemical reactions or to diffusive transport. To lowest order in v_{f}, the dispersion relation is given by (see Appendix 7.A)

$$\sigma(q) \approx \sigma^{(0)}(q) + i\frac{v_{\mathrm{f}}q}{2}A(q), \tag{7.9}$$

[1] In principle, the dispersion relation can be easily obtained in closed form using the formula for eigenvalues of 2×2 matrices: $\sigma_{1,2} = \frac{1}{2}\,\mathrm{tr}\,\mathcal{J} \mp \frac{1}{2}\sqrt{(\mathrm{tr}\,\mathcal{J})^2 - 4\det\mathcal{J}}$ where $\mathrm{tr}\,\mathcal{J}$ and $\det\mathcal{J}$ are the Jacobian's trace and determinant, respectively. Because the resulting expression is rather lengthy, we don't write it out it explicitly here.

[2] Homogeneous stability implies that the nullcline slope s_{nc} is larger than -1 [56], such that the prefactor $(1+s_{\mathrm{nc}})^{-1}$ is positive.

where the zeroth order term, $\sigma^{(0)}(q)$, is the dispersion relation in the absence of flow, which has no imaginary part [56] (cf. Eq. (7.11)). The function $A(q)$ is positive for all laterally unstable modes ($\mathrm{Re}\,\sigma(q) > 0$). Equation (7.9) shows that to lowest order (linear in v_f) the effect of cytosolic flow is to induce propagation of the modes with the phase velocity $v_\mathrm{phase}(q) = -\,\mathrm{Im}\,\sigma(q)/q \approx -v_\mathrm{f}A(q)$. Since $A(q) > 0$ for laterally unstable modes, all growing perturbations propagate against the direction of the flow (as illustrated in Fig. 7.2B).

In the limit of fast flow (compared either to reactions or to cytosolic transport) we find that the dispersion relation (given by the eigenvalue problem Eq. (7.6)) reduces to

$$\sigma(q) \approx f_m - D_m q^2 + i\frac{f_c f_m}{v_\mathrm{f} q} \tag{7.10}$$

for non-zero wavenumbers. The real part of the dispersion relation in this fast flow limit becomes identical to the dispersion relation in the limit of fast diffusion [56]. In both limits, cytosolic transport becomes (near) instantaneous. In particular, in the limit of fast flow, advective transport completely dominates over diffusive transport in the cytosol such that the dispersion relation becomes independent of the cytosol diffusion constant D_c.

From the imaginary part of $\sigma(q)$, we obtain the phase velocity $v_\mathrm{phase} = -f_c f_m/(v_\mathrm{f} q^2)$. In other words, an increase in cytosolic flow leads to a *decrease* of the phase velocity. This is opposite to the slow flow limit discussed above, where the phase velocity increased linearly with the flow speed.

To rationalize these findings, we recall the propagation mechanism as discussed above. There, we argued that a phase shift between the membrane and the cytosol pattern is responsible for the pattern propagation, as it leads to an asymmetry in the attachment–detachment balance upstream and downstream. This phase shift increases with the flow velocity and eventually saturates at $\pi/4$.[3] On the other hand, the cytosol concentration gradients become shallower the faster the flow. To understand why this is, imagine a small volume element in the cytosol being advected with the flow. The faster the flow, the less time it has to interact with each point on the membrane it passes. Therefore, for faster advective flow, the attachment–detachment flux at the membrane is effectively diluted over a larger cytosolic volume. This leads to a flattening of the cytosolic concentration profile (see Movie 2), and therefore a reduction in the upstream–downstream asymmetry of attachment. As a result, in the limit of fast flow, the pattern propagates *slower* the faster the flow, whereas, in the limit of slow flow, the pattern propagates *faster* the faster the flow. Thus, comparing these two limits, we learn that the phase velocity reaches a maximum at intermediate flow speeds.

[3] The phase shift can be read off from the real and imaginary parts of the eigenvectors in the linear stability analysis.

7.3.5 Summary and discussion of linear stability

Let us briefly summarize our main findings from linear stability analysis. We found that the leading order effect of cytosolic flow is to induce upstream propagation of patterns. This propagation is driven by the faster resupply of protein mass on the upstream side of the pattern compared to the downstream side. A similar effect was previously found for vegetation patterns which move uphill because nutrients are transported downhill by water flow [243]. Even though these systems are not strictly mass conserving, their pattern propagation underlies the same principle: The nutrient uptake in regions of high vegetation density creates a nutrient sink which is resupplied asymmetrically due to the downhill flow of water and nutrients.

Moreover, we used a phase-space analysis to explain how flow extends the range of parameters where patterns emerge spontaneously, i.e. where the homogeneous steady state is laterally unstable. This was previously shown mathematically for general two-component reaction–diffusion systems (not restricted to mass-conserving ones) [243, 244]. Our analysis in the long wavelength limit explains the physical mechanism of this instability for mass-conserving systems: The flow-driven instability is a mass-redistribution instability, driven by a self-amplifying cascade of (flow-driven) mass transport and the self-organized formation of attachment and detachment zones (shifting reactive equilibria). This shows that the instability mechanism is identical to the mass-redistribution instability that underlies pattern formation in systems without flow (i.e. where only diffusion drives mass transport) [56]. For these systems, the instability strictly requires $D_c > D_m$. In contrast, we find that for sufficiently fast flow, there can be a mass-redistribution instability even in the absence of cytosolic diffusion ($D_c = 0$). While the case $D_c = 0$ is not physiologically relevant in the context of intracellular pattern formation, it may be relevant for the formation of vegetation patterns on sloped terrain [245], where c and m are the soil-nutrient concentration and plant biomass density, respectively. In conclusion, advective flow can fully replace diffusion as the mass-transport mechanism driving the mass-redistribution instability.

7.4 Pattern propagation in the nonlinear regime

So far we have analyzed how cytosolic flow affects the dynamics of the system in the vicinity of a homogeneous steady state, using linear stability analysis. However, patterns generically don't saturate at small amplitudes but continue to grow into the strongly nonlinear regime [56] (see Movie 1 for an example in which a small perturbation of the homogeneous steady state evolves into a large amplitude pattern in the presence of flow).

To study the long time behavior (steady state) far away from the spatially homogeneous steady state, we performed finite element simulations in Mathematica [246]. To interpret

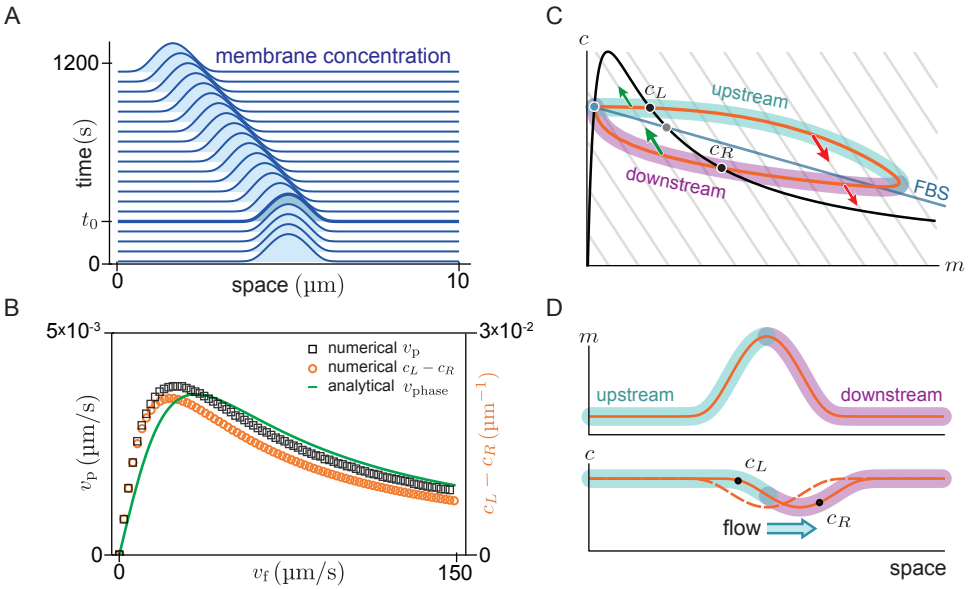

Figure 7.4 | Pattern dynamics far from the spatially homogeneous steady state. (A) Time evolution of the membrane-bound protein concentration. At time $t_0 = 240s$ a constant cytosolic flow with velocity $v_f = 20\mu m/s$ towards the right is switched on (cf. Movie 3). (B) Relation between the peak speed (v_p) and flow speed (v_f). Results from finite element simulations (black open squares) are compared to the phase velocity of the mode q_{max} obtained from linear stability analysis (green solid line) and to an approximation (orange open circles) of the area enclosed by the density distribution trajectory in phase space (area enclosed by the 'loop' in D). (The domain size, $L = 10\mu m$, is chosen large enough compared to the peak width such that boundary effects are negligible.) (C) A schematic of the phase portrait corresponding to the pattern in D. The density distribution in the absence of flow is embedded in the FBS (blue straight line). In the presence of flow, the density distribution trajectory forms a 'loop' in phase space. The upstream and downstream side of the pattern are highlighted in cyan and magenta, respectively. Red and green arrows indicate the direction of the reactive flow in the attachment and detachment zones, respectively. At intersection points of the density distribution with the nullcline (c_L and c_R) the system is at its local reactive equilibrium. (D) Sketch of the membrane (orange solid line, top) and cytosolic (orange dashed line, bottom) concentration profiles for a stationary pattern in the absence of cytosolic flow. Flow shifts the cytosol profile downstream (orange solid line, bottom).

the results of these numerical simulations, we will use *local equilibria theory*, building on the phase-space analysis introduced in Refs. [56, 106].

Figure 7.4A shows the space-time plot (kymograph) of a system where there is initially no flow ($t < t_0$), such that the system is in a stationary state with a single peak. For such a stationary steady state, diffusive fluxes on the membrane and in the cytosol have to balance exactly. This diffusive flux balance imposes the constraint that in the (m, c)-phase plane, the trajectory corresponding to the pattern lies on a straight line with slope $-D_m/D_c$, called '*flux-balance subspace*' (FBS) [56] (see light blue line in Fig. 7.4C). At the plateaus and inflection points of the pattern, the net diffusive flow vanishes and attachment and detachment are balanced, i.e. the system is locally in reactive equilibrium ($f = 0$). Hence, plateaus and inflection points of the spatial concentration profile correspond to intersection points between the reactive nullcline and the FBS in the (m, c)-phase plane (blue and green points in Fig. 7.4C). At the first intersection point (blue), the nullcline slope is larger than the FBS slope. Thus, by the slope criterion $s_{\mathrm{nc}} < -D_m/D_c$ for lateral instability, this point corresponds to a laterally *stable* state in the spatial domain—i.e. a plateau. Following a spatial perturbation, the concentrations will relax back towards the flat plateau.

At the second intersection point (green point in Fig. 7.4C), the nullcline slope is more negative than the FBS slope, indicating a laterally unstable state. This state corresponds to the inflection point of the pattern and the lateral instability there can be thought of as "spanning" the interfacial region of the pattern that connects the two plateaus. An in-depth analysis of stationary patterns based on these geometric relations in phase space can be found in Ref. [56]. Here we ask how the phase portrait changes in the presence of flow.

At time $t = t_0$, a constant cytosolic flow in the positive x-direction is switched on. Consistent with the expectation from linear stability analysis, we find that the peak propagates against the flow direction in the negative x-direction (solid lines in Fig. 7.4A). The diffusive fluxes no longer balance for this propagating steady state, such that the phase-space trajectory is no longer embedded in the FBS. Instead, as advective flow shifts the cytosol concentration profile relative to the membrane profile, the phase-space trajectory becomes a 'loop' (Fig. 7.4C). On the upstream side of the peak, the cytosolic density is increased, such that net attachment — which is proportional to the cytosolic density — is increased relative to net detachment. Conversely, the reactive balance is shifted towards detachment on the downstream side. Because the reactive flow is approximately proportional to the distance from the reactive nullcline in phase space, the asymmetry between net attachment and detachment on the upstream and downstream side of the peak can be estimated by the area enclosed by the loop-shaped trajectory in phase space.

To test whether the attachment–detachment asymmetry explains the propagation speed of the peak, we estimate the enclosed area in phase space by the difference in cytosolic concentrations at the points c_{L} and c_{R} (black dots in Fig. 7.4C and D) where the loop intersects the reactive nullcline ($f = 0$ black line Fig. 7.4C). At these points, the system is in a local reactive equilibrium. Indeed, we find that the propagation speed of the pattern

obtained from numerical simulations (black open squares in Fig. 7.4B) is well approximated by the difference in cytosolic density ($v_\mathrm{p} \propto c_\mathrm{L} - c_\mathrm{R}$) for all flow speeds (orange open circles in Fig. 7.4B). Furthermore, in the limit of slow and fast flow, the peak propagation speed is well approximated by the propagation speed of the unstable traveling mode with the longest wavelength, as obtained from linear stability analysis.[4] For small flow speeds, the pattern's propagation speed v_p increases linearly with v_f (cf. Eq. 7.7) and for large flow speeds the pattern speed is proportional to $1/v_\mathrm{f}$ (cf. Eq. 7.10).

In summary, we found that the peak propagation speed in the slow and fast flow limits is well described by the propagation speed of the linearly unstable mode with the longest wavelength (i.e. the right edge of the band of unstable modes q_max). Moreover, we approximated the asymmetry of protein attachment by the area enclosed by the density distribution in phase space, and found that this is proportional to the peak speed for all flow speeds.

7.5 Flow-induced transition from mesa to peak patterns

So far we have studied the propagation of patterns in response to cytosolic flow. Next, we will show how cytosolic flow can also drive the transition between qualitatively different pattern types. We distinguish two pattern types exhibited by McRD systems, peaks and mesas [56, 103]. Mesa patterns are composed of plateaus (low density and high density) connected by interfaces, while a peak can be pictured as two interfaces concatenated directly (cf. Fig. 7.5A). Mesa patterns form if protein attachment saturates in regions of high total density, forming a plateau there. As we argued above, the low- and high-density plateaus correspond to laterally *stable* steady states, marked—in the phase plane—by intersection points between the FBS and the reactive nullcline where the nullcline slope is larger than the FBS slope. Peaks form if the attachment rate does not saturate at high density, i.e. if the third intersection point between nullcline and FBS is not reached [56]. Thus, while the amplitude of mesa patterns is determined by the attachment–detachment balance in the two plateaus, the amplitude (maximum concentration) of a peak is determined by the total mass available in the system [56].

How does protein transport affect whether a peak or a mesa forms? As we argued above, a peak pattern forms if protein attachment in regions of high density does not saturate. In general, this will happen if attachment to the membrane depletes proteins from the cytosol slower than lateral transport can resupply proteins (see Fig. 7.5A). Let us first recap the situation without flow, where proteins are resupplied by diffusion from the detachment zone to the attachment zone across the pattern's interface with width ℓ_int. Thus, a peak

[4] The phase velocity depends on the mode's wavelength. The relevant length scale for the peak's propagation is its width, which is approximately given by $2\pi/q_\mathrm{max}$ at the pattern's inflection point [56]. Thus, we infer the peak propagation speed from $-\operatorname{Im}\sigma(q_\mathrm{max})/q_\mathrm{max}$ at the inflection point of the stationary peak.

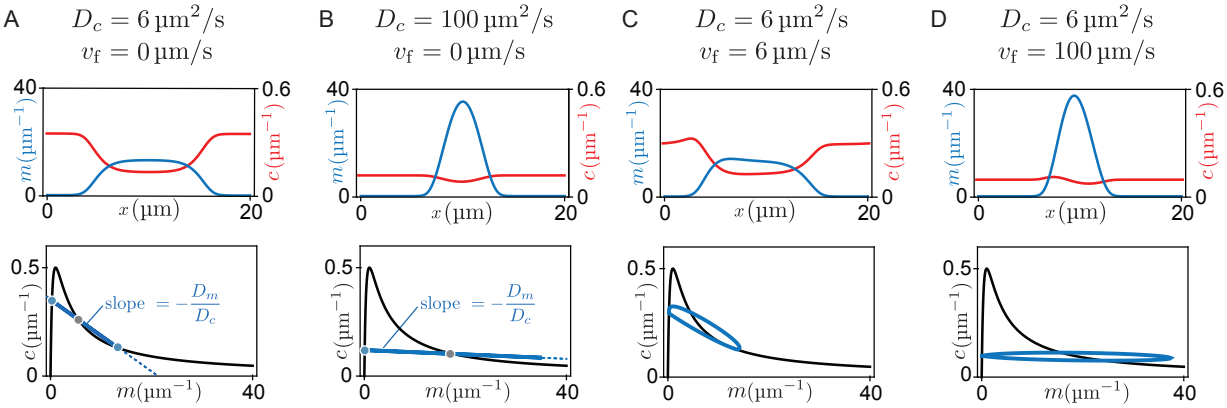

Figure 7.5 | Demonstration of the transition from a mesa pattern to a peak pattern. Each panel shows a snapshot from finite element simulations in steady state. Top concentration profiles in real space; bottom: corresponding trajectory (blue solid line) in phase space. (A) Mesa pattern in the case of slow cytosol diffusion and no flow. The two plateaus (blue dots) and the inflection point (gray dot) of the pattern correspond to the intersection points of the FBS (blue dashed line) with the reactive nullcline (black line). (B) For fast cytosol diffusion, the third intersection point between FBS and nullcline lies at much higher membrane concentration such that it no longer limits the pattern amplitude. Therefore, a peak forms whose amplitude is limited by the total protein mass in the system. (C) Slow flow only slightly deforms the mesa pattern, compare to (A). Fast cytosolic flow leads to formation of a peak pattern (D), similarly to fast diffusion. Parameters: $\bar{n} = 7\mu m^{-1}, D_m = 0.1\mu m^2/s$ and $L = 20\mu m$.

pattern forms if the rate of transport by cytosolic diffusion is faster than the attachment rate ($D_c/\ell_{\text{int}}^2 \gg \tau_{\text{react}}^{-1}$). Further using that the interface width is given by a balance of membrane diffusion and local reactions ($\ell_{\text{int}}^2 \sim \tau_{\text{react}} D_m$), we obtain the condition $D_c \gg D_m$ for the formation of peak patterns.

In terms of phase space geometry, this means that the slope $-D_m/D_c$ of the flux-balance subspace in phase space must be sufficiently shallow. For a steep slope $-D_m/D_c$ of the FBS, the membrane concentration saturates at the point where the FBS intersects with the reactive nullcline blue dots in Fig. 7.5A. There, attachment and detachment balance such that a mesa forms (Fig. 7.5A). For faster cytosol diffusion, the flux-balance subspace is shallower such that the third FBS-NC intersection point shifts to higher densities. Thus, for sufficiently fast cytosol diffusion a peak forms (Fig. 7.5B).

Adding slow cytosolic flow does not significantly contribute to the resupply of the cytosolic sink (i.e. attachment zone) and therefore does not alter the pattern type (Fig. 7.5C). In contrast, when cytosolic protein transport (by advection and/or diffusion) is fast compared to the reaction kinetics, the cytosolic sink gets resupplied quickly, leading to a flattening of the cytosolic concentration profile. Accordingly, the density distribution in phase space approaches a horizontal line, both for fast cytosolic diffusion (Fig. 7.5B) and for fast cytosolic flow (Fig. 7.5D). As a consequence, the point where the density distribution meets

the nullcline shifts towards larger membrane concentrations, resulting in an increasing amplitude of the mesa pattern. Eventually, when the amplitude of the pattern can not grow any further due to limiting total mass, a peak pattern forms (Fig. 7.5B,D). Hence, an increased flow velocity can cause a transition from a mesa pattern to a peak pattern (see Movie 4).

In summary, we found that cytosolic flow can qualitatively change the membrane-bound protein pattern from a small-amplitude, wide mesa pattern to a large-amplitude, narrow peak pattern. In cells, such flows could therefore promote the precise positioning of polarity patterns on the membrane. Furthermore, we hypothesize that flow can contribute to the selection of a single peak by accelerating the coarsening dynamics of the pattern via two distinct mechanisms. First, flow accelerates protein transport that drives coarsening. Second, as peak patterns coarsen faster than mesa patterns [52, 103], flow can accelerate coarsening via the flow-driven mesa-to-peak transition. Such fast coarsening may be important for the selection of a single polarity axis, e.g. a single budding site in *S. cerevisiae* [40], for axon formation in neurons [247], and to establish a distinct front and back in motile cells [226, 248].

7.6 Flow-induced pattern formation

So far we have studied how a uniform flow profile affects pattern formation on a domain with periodic boundary conditions, representing circular flows along the cell membrane and bulk flows in microfluidic *in vitro* setups. However, flows in the vicinity of the membrane can be non-uniform. For example, one (or more) components of the pattern forming system may be embedded in the cell cortex [8, 25, 249] which is a contractile medium driven by myosin-motor activity. Furthermore, the incompressible cytosol can flow in the direction normal to the membrane, such that the 3D flow field of the cytosol is perceived as a compressible flow along the membrane [229]. In this Section we will discuss how such non-uniform, uni-directional flows lead to pattern formation.

A non-uniform flow transports the proteins at different speeds along the membrane. Starting from a spatially homogeneous initial state, such a non-uniform flow leads to a redistribution of mass. It has been demonstrated in previous work that this non-uniform flow can induce pattern formation even if the homogeneous steady state is laterally stable (i.e. there is no spontaneous pattern formation) [8, 25, 228]. Based on numerical simulations, a transition from flow-guided to self-organized dynamics has been reported [8]. However, the physical mechanism underlying this transition, and what determines the transition point have remained unclear.

We address this question using the two-component model, which serves a conceptual model that mimics the qualitative behavior of the more complex PAR system [97]. While flow in the PAR system is governed by the myosin concentration, we assume a stationary

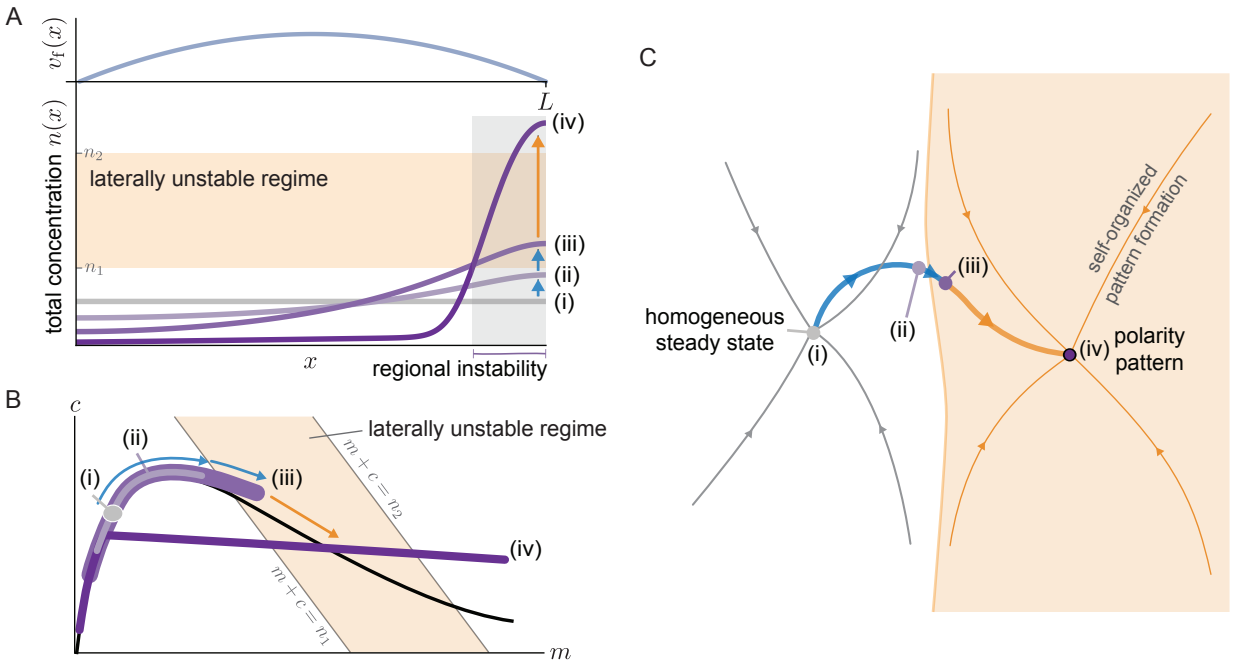

Figure 7.6 | Flow-driven protein mass accumulation can induce pattern formation by triggering a regional lateral instability. (A) Top: quadratic flow velocity profile: $v_f(x)/v_{\max} = 1 - 4\,(x/L - 1/2)^2$. Bottom: illustration of the total density profiles at different time points starting from a homogeneous steady state (i) to the final pattern (iv); see Movie 5. Mass redistribution due to the non-uniform flow velocity drives mass towards the right hand side of the system, as indicated by the blue arrows. The range of total densities shaded in orange indicates the laterally unstable regime determined by linear stability analysis. Once the total density reaches this regime locally, a regional lateral instability is triggered resulting in the self-organized formation of a peak (orange arrow). (B) Sketch of the phase space representation corresponding to the profiles shown in A. Note that the concentrations are slaved to the reactive nullcline (black line) until the regional lateral instability is triggered. (C) Schematic representation of the state space of concentration patterns in a case where both the homogeneous steady state and a stationary polarity pattern are stable. Thin trajectories indicate the dynamics in the absence of flow and the pattern's basin of attraction is shaded in orange. The thick trajectory connecting both steady states shows the flow-induced dynamics, corresponding to the sequence of states (i)–(iv) shown in A and B.

parabolic flow profile that vanishes at the system boundaries (Fig. 7.6A, top). We use a one-dimensional domain with no-flux boundary conditions that correspond to the symmetry axis of a rotationally symmetric flow profile. In the following, we describe the flow-induced dynamics starting from a spatially homogeneous steady state to the final polarity pattern observed in numerical simulations (see Movie 5). Figure 7.6 visualizes these dynamics in real space (A) and in the (m, c)-phase plane (B). To relate our findings to the previous study Ref. [8], we also visualize the dynamics in an abstract representation of the state space (comprising all concentration profiles) used in this previous study. In this state space, steady states are points and the time evolution of the system is a trajectory (thick blue/orange line in Fig. 7.6C).

Starting from the homogeneous steady state (*i*), the non-uniform advective flow redistributes mass in the cytosol (*ii*). Due to this redistribution of mass, the local reactive equilibria shift as we have seen repeatedly here and in earlier studies of mass-conserving systems [49, 56]. In fact, as long as the gradients of both the membrane and cytosol profiles are shallow, the concentrations remain close to the local equilibria, as evidenced by the density distribution in phase space spreading along the reactive nullcline (see profile (ii) in Fig. 7.6A,B). As long as there is no laterally unstable region, the mass accumulation is limited by the counteracting diffusive flow in the cytosol. Eventually, the region where mass accumulates (here the right edge of the domain) enters the laterally unstable regime (see profile *iii*). In this laterally unstable region, cytosol diffusion will enhance the accumulation of mass via the mass-redistribution instability, until it is limited by the much slower membrane diffusion. In the phase plane (Fig. 7.6B), the laterally unstable regime corresponds to the range of total densities $\bar{n}$ where the nullcline slope has a steeper negative value than the flux-balance subspace slope ($s_{\mathrm{nc}} < -D_m/D_c$)[5]. The mass-redistribution instability in this region, based on the self-organized formation of attachment and detachment zones (cf. Sec. 7.3.2) will lead to the formation of a polarity pattern there (*iv*). Thus, the onset of a *regional lateral instability* marks the transition from flow-guided dynamics to self-organized dynamics.

In the abstract state space visualization (Fig. 7.6C) the area shaded in orange indicates the polarity pattern's basin of attraction comprising all states (concentration profiles) where a spatial region in the system is laterally unstable. In the absence of flow, states that do not exhibit such a laterally unstable region return to the homogeneous steady state (thin gray lines). Non-uniform cytosolic flow induces mass-redistribution, that can drive an initially homogeneous system (i) into the polarity pattern's basin of attraction. From there on, self-organized pattern formation takes over, leading to the formation of a polarity pattern (iv), essentially independently of the advective flow (orange trajectory).

In future work, it would be interesting to make the abstract state space representation, Fig. 7.6C, more quantitative. For example, one could try to estimate the minimal flow velocity required to drive the system past the separatrix, i.e. into the basin of attraction

[5]More precisely, the size of the laterally unstable region must be larger than the shortest unstable mode (corresponding to the right edge of the band of unstable modes in the dispersion relation (Fig. 7.2A)).

of the polarity pattern. A promising approach is to use the fact that prior to the onset of regional lateral instability, the concentrations are slaved to the local equilibria that depend on the local total density. Thus, one can obtain an approximate, closed equation for the flow-driven evolution of the total density, similar to the "adiabatic scaffolding approximation" made in [56]. Solving this equation would provide a criterion for when the total density exceeds the critical density for lateral instability in some spatial region that initiates the self-organized formation of a polarity pattern there.

Similar pattern forming mechanisms based on a regional instability have previously been shown to also underlie stimulus-induced pattern formation following a sufficiently strong initial perturbation [56] and peak formation at a domain edge where the reaction kinetics abruptly change [105]. Thus, an overarching principle for stimulus-induced pattern formation emerges: To trigger (polarity) pattern formation, the stimulus, be it advective flow or heterogeneous reaction kinetics, has to redistribute protein mass in a way such that a regional (lateral) instability is triggered.

It remains to be discussed what happens once the cytoplasmic flow is switched off after the polarity pattern has formed. In general, the polarity pattern will persist (see Movie 5), since it is maintained by self-organized attachment and detachment zones, largely independent of the flow. However, as long as there is flow, the average mass on the right hand side of the system (downstream of the flow) is higher than on the left hand side. Hence, flow can maintain a polarity pattern even if the average mass in the system as a whole is too low to sustain polarity patterns in the absence of flow (see bifurcation analysis in Ref. [56]). If this is the case, the peak disappears once the flow is switched off (see Movie 6).

In summary, the redistribution of the protein mass is key to induce (polarity) pattern formation starting from a stable homogeneous state.

7.7 Conclusions and outlook

Inside cells, proteins are transported via diffusion and fluid flows, which, in combination with reactions, can lead to the formation of protein patterns on the cell membrane. To characterize the role fluid flows play in pattern formation, we studied the effect of flow on the formation of a polarity pattern, using a generic two-component model. We found that flow leads to propagation of the polarity pattern *against* the flow direction with a speed that is maximal for intermediate flow speeds, i.e. when the rate of advective transport is comparable to either the reaction rates or to the rate diffusive transport in the cytosol. Using a phase-space analysis, we showed that the propagation of the pattern is driven by an asymmetric influx of protein mass to a self-organized protein-attachment zone. As a consequence, attachment is stronger on the upstream side of the pattern compared to the downstream side, leading to upstream propagation of the membrane bound pattern. Furthermore, we have shown that flow can qualitatively change the pattern from

a wide mesa pattern (connecting two plateaus) to a narrow peak pattern. Finally, we have presented a phase-space analysis to elucidate the interplay between flow-guided dynamics and self-organized pattern formation. This interplay was previously studied numerically in the context of PAR-protein polarization [8, 25]. Our analysis reveals the underlying cause for the transition from flow-guided to self-organized dynamics: the regional onset of a mass-redistribution instability.

We discussed implications of our results and links to earlier literature at the end of each section. Here, we conclude with a brief outlook. We expect that the insights obtained from the minimal two-component model studied here generalize to systems with more components and multiple protein species. For example, *in vitro* studies of the reconstituted MinDE system of *E. coli* show that MinD and MinE spontaneously form dynamic membrane-bound patterns, including spiral waves [250] and quasi-stationary patterns [251]. These patterns emerge from the competition of MinD self-recruitment and MinE-mediated detachment of MinD [90, 95]. In the presence of a bulk flow, the traveling waves were found to propagate upstream [233]. Our analysis based on a simple conceptual model suggests that this upstream propagation is caused by a larger influx of the self-recruiting MinD on the upstream flanks compared to the downstream flanks of the travelling waves. However, the bulk flow also increases the resupply of MinE on the upstream flanks. As MinE mediates the detachment of MinD and therefore effectively antagonizes MinD's self-recruitment, this may drive the membrane-bound patterns to propagate downstream instead of upstream. Which one of the two processes dominates — MinD-induced upstream propagation or MinE-induced downstream propagation — likely depends on the details of their interactions. This interplay will be the subject of future work.

A different route of generalization is to consider advective flows that depend on the protein concentrations. In cells, such coupling arises, for instance, from myosin-driven cortex contractions [8, 218] and shape deformations [28, 240]. Myosin-motors, in turn, may be advected by the flow and their activity is controlled by signalling proteins such as GTPases and kinases [252]. This can give rise to feedback loops between flow and protein patterns. Previous studies show that such feedback loops can give rise to mechano-chemical instabilities [253], drive pulsatile (standing-wave) patterns [254, 255] or cause the breakup of traveling waves [256]. We expect that our analysis based on phase-space geometry can provide insight into the mechanisms underlying these phenomena.

Appendices

7.A Limit of slow flow and timescale comparison

The dispersion relation in the absence of flow ($v_\mathrm{f} = 0$) reads

$$\sigma^{(0)} = -\frac{1}{2}\left[(D_m + D_c)\, q^2 + f_c - f_m\right] + \frac{B(q)}{2A(q)}, \tag{7.11}$$

with $A(q) = \left[1 - 4f_c f_m / B(q)^2\right]^{-1/2} - 1$ and $B(q) = f_m + f_c + (D_c - D_m)q^2$. To find the effect of slow flow, we first need to identify the relevant timescales such that we can define a dimensionless small parameter to expand in. Because pattern formation is driven by transport in the cytosol (diffusive and advective) and attachment from the cytosol to the membrane, there are three relevant timescales: (*i*) The the rate of advective transport on length scale q^{-1} is given by qv_f; (*ii*) The rate of diffusive transport on that scale, given by $D_c q^2$; and (*iii*) the attachment rate $f_c = a(m)$ (cf. Eq. (7.2)). To compare these timescales, we form two dimensionless numbers: the Peclét number $\mathrm{Pe} = v_\mathrm{f}/(D_c q)$ and the Damköhler number $\mathrm{Da} = f_c/(v_\mathrm{f} q)$. Flow can either be slow compared to reactions ($\mathrm{Da} \gg 1$) or slow compared to diffusion ($\mathrm{Pe} \ll 1$). In both cases, expanding the the dispersion relation $\sigma(q)$ to first order yields

$$\sigma(q) = \sigma^{(0)}(q) + i\frac{v_\mathrm{f} q}{2} A(q) + \mathcal{O}(\varepsilon^2), \tag{7.12}$$

where $\varepsilon = \min(\mathrm{Pe}, \mathrm{Da}^{-1})$. By elementary algebra using the assumptions $D_c > D_m$ and $f_c > 0$ made above, it follows that $A(q)$ is positive when $s_\mathrm{nc} < 0$. As Eq. (7.8) in Sec. 7.3.3 shows, the condition $s_\mathrm{nc} < 0$ is necessary for a band of unstable modes to exist. Therefore, $A(q)$ is positive for all unstable modes.

8 Discussion and Outlook

" All ends with beginnings."
– Get Lucky, Daft Punk

In cells, many processes need to be coordinated in space and time to ensure functional cellular behavior. Such processes are coordinated by proteins, which can self-organize in spatial protein patterns. It has been studied extensively how such protein patterns arise spontaneously from a homogeneous steady state, due to a combination between protein transport and protein-protein interactions [59, 106, 107, 257]. In recent years, it has become increasingly clear that many protein patterns depend on the cells size, shape and biochemical interactions with other proteins [8, 16, 19, 21]. However, for many observations the underlying biophysical mechanisms remain unknown. In this thesis, we used reaction–diffusion models to study several mechanisms by which one protein pattern serves as a template for the formation and steady states of downstream protein patterns inside cells. In the following, we highlight three key implications of our work and make several suggestions for future research.

First, our work shows how a hierarchy of self-organized protein patterns integrates two main paradigms in the field of protein pattern formation: Turing's idea that proteins self-organize from a homogeneous state into patterns via reaction and diffusion [171], and Wolpert's idea that cells have a notion of positional information, which they use to form patterns [211]. The mechanisms presented in chapter 3 – 5 show that the positional information contained in a protein pattern can be used as an input for the reaction–diffusion dynamics of a downstream protein. Such mechanisms, that arise from an hierarchical sequence of self-organized protein patterns, are reminiscent of spatial computational operations to process spatial information inside cells. In chapter 6, we showed how a sequence of two such computational operations leads to a protein pattern that adapts to the shape of the cell. Thus, our work illustrates the importance of the self-organized formation of hierarchical patterns in understanding emergent biological functions, complementing genetic and molecular studies.

We believe that these mechanisms, based on the hierarchical coupling of self-organizing protein 'modules' can be generalized to a wide range of processes in which spatial information is processed, such as cell migration and cytokinesis. A major challenge in future research will be to identify the underlying mechanisms that enable such spatial information processing in living cells. To that end, it will be important to develop mechanistic and quantitative models to understand how one protein pattern affects the formation of

downstream protein patterns. In addition, as more quantitative data from single cell experiments becomes available, such models can help to interpret these experiments, ultimately leading to the characterization of general biophysical principles of information processing in living cells.

A second implication of our work follows from our results in chapter 6, that demonstrate a shape-adaptation mechanism, explaining how protein patterns can adapt to variations in the cell shape. The interplay between protein patterns and cell mechanics is central to a long-standing puzzle, first formulated by Alan Turing in his seminal paper on "The chemical basis of morphogenesis". There he notes that "the description of the state depends on two parts, the mechanical and chemical," and that "the interdependence of the chemical and mechanical data adds enormously to the difficulty." Thus, there are two distinct scenarios: the formation of functional protein patterns could either *rely* on the interplay with cell mechanics and cell geometry, or the formation of patterns has to *adapt* to such mechanical and geometrical influences in order to be robust. As reviewed in chapter 1, several mechanisms have been reported by which protein patterns are affected by cell size, shape and cell mechanics. Furthermore, it has been suggested that the formation of protein patterns can even rely on cell mechanics via changes in the cell shape and cortical flows [8, 16]. In contrast to these mechanisms, the results in chapter 6 demonstrate how the formation of protein patterns can adapt to be robust to cell shape. Future research on pattern formation mechanisms in living cells will demonstrate whether there are more examples where the formation of protein patterns adapts to be robust to the effects of cell mechanics and geometry.

Finally, the pattern hierarchy presented in chapter 6, establishes a mechano-chemical feedback loop, coupling shape information to a cell shape regulator. Thus, such a pattern hierarchy may also be important for how cells regulate cell-shape. Feedback-loops between protein patterns and cell mechanics have also been suggested to play a role in other biological model systems, such as during polarization of the *C. elegans* zygote [8, 13]. However, it remains unclear to what extent the functional polarity pattern relies on the interplay with cell mechanics [7]. To characterize the role of feedback-loops between protein patterns, cell mechanics and cell shape for the formation of functional protein patterns, it will be key to compare realistic three-dimensional models to experimental data. The properties of such mechano-chemical models that include both protein reaction–diffusion dynamics, as well as a dynamically varying three-dimensional cell shape, are challenging to study due to the computational complexity of simulating such models [12, 258–260]. In future research, it will be important to further develop such methods such that they can be compared to quantitative experimental data and contribute to the interpretation of experimental results in mechano-chemical model systems.

Bibliography

[1] K. E. Kasza et al. *The Cell as a Material*. In: **Current Opinion in Cell Biology** 19.1 (2007), pp. 101–107. DOI: 10.1016/j.ceb.2006.12.002 (cit. on p. 1).

[2] A. B. Verkhovsky. *The Mechanisms of Spatial and Temporal Patterning of Cell-Edge Dynamics*. In: **Current Opinion in Cell Biology** 36 (2015), pp. 113–121. DOI: 10.1016/j.ceb.2015.09.001 (cit. on p. 1).

[3] T. Lecuit and P.-F. Lenne. *Cell Surface Mechanics and the Control of Cell Shape, Tissue Patterns and Morphogenesis*. In: **Nature Reviews Molecular Cell Biology** 8.8 (2007), pp. 633–644. DOI: 10.1038/nrm2222 (cit. on p. 1).

[4] C. T. Mierke. *Cellular Mechanics and Biophysics, Structure and Function of Basic Cellular Components Regulating Cell Mechanics*. In: **Biological and Medical Physics, Biomedical Engineering** (2020). DOI: 10.1007/978-3-030-58532-7 (cit. on p. 1).

[5] C. Cadart et al. *The Physics of Cell-Size Regulation across Timescales*. In: **Nature Physics** 15.10 (2019), pp. 993–1004. DOI: 10.1038/s41567-019-0629-y (cit. on p. 1).

[6] D. Thalmeier, J. Halatek, and E. Frey. *Geometry-Induced Protein Pattern Formation*. In: **Proceedings of the National Academy of Sciences of the United States of America** 113.3 (2016), pp. 548–53. DOI: 10.1073/pnas.1515191113 (cit. on pp. 2, 5, 6, 8, 9, 102, 116).

[7] R. Geßele et al. *Geometric Cues Stabilise Long-Axis Polarisation of PAR Protein Patterns in C. Elegans*. In: **Nature Communications** 11.1 (2020), p. 539. DOI: 10.1038/s41467-020-14317-w (cit. on pp. 2, 8, 9, 162).

[8] P. Gross et al. *Guiding Self-Organized Pattern Formation in Cell Polarity Establishment*. In: **Nat Phys** 15.3 (2019), pp. 293–300 (cit. on pp. 2, 10, 20, 140, 141, 154, 156, 158, 161, 162).

[9] F. Wu et al. *Symmetry and Scale Orient Min Protein Patterns in Shaped Bacterial Sculptures*. In: **Nature Nanotechnology** 10.8 (2015), pp. 719–726. DOI: 10.1038/nnano.2015.126 (cit. on p. 2).

[10] A. Haupt and N. Minc. *How Cells Sense Their Own Shape – Mechanisms to Probe Cell Geometry and Their Implications in Cellular Organization and Function*. In: **Journal of Cell Science** 131.6 (Mar. 2018), jcs214015. DOI: 10.1242/jcs.214015 (cit. on pp. 2, 102).

[11] J.B. Moseley and P. Nurse. *Cell Division Intersects with Cell Geometry*. In: **Cell** 142.2 (2010), pp. 189–193. DOI: 10.1016/j.cell.2010.07.004 (cit. on p. 2).

[12] N. Tamemoto and H. Noguchi. *Pattern Formation in Reaction–Diffusion System on Membrane with Mechanochemical Feedback*. In: **Scientific Reports** 10.1 (2020), p. 19582. DOI: 10.1038/s41598-020-76695-x. eprint: 2007.10606 (cit. on pp. 2, 162).

[13] R. Illukkumbura, T. Bland, and N.W. Goehring. *Patterning and Polarization of Cells by Intracellular Flows*. In: **Current Opinion in Cell Biology** 62 (2020), pp. 123–134. DOI: 10.1016/j.ceb.2019.10.005 (cit. on pp. 2–4, 140, 162).

[14] A. Goychuk and E. Frey. *Protein Recruitment through Indirect Mechanochemical Interactions*. In: **Physical Review Letters** 123.17 (2019), p. 178101. DOI: 10.1103/physrevlett.123.178101. eprint: 1910.00977 (cit. on pp. 2, 8).

[15] M. Mishra et al. *Cylindrical Cellular Geometry Ensures Fidelity of Division Site Placement in Fission Yeast*. In: **Journal of Cell Science** 125.16 (2012), pp. 3850–3857. DOI: 10.1242/jcs.103788 (cit. on pp. 2, 7).

[16] L. Hubatsch et al. *A Cell-Size Threshold Limits Cell Polarity and Asymmetric Division Potential*. en. In: **Nature Physics** 15.10 (Oct. 2019), pp. 1078–1085. DOI: 10.1038/s41567-019-0601-x (cit. on pp. 2, 6, 161, 162).

[17] J. Chant and J.R. Pringle. *Patterns of Bud-Site Selection in the Yeast Saccharomyces Cerevisiae*. In: **The Journal of Cell Biology** 129.3 (May 1995), pp. 751–765. DOI: 10.1083/jcb.129.3.751 (cit. on pp. 2, 11, 84, 102).

[18] Z. Tong et al. *Adjacent Positioning of Cellular Structures Enabled by a Cdc42 GTPase-Activating Protein–Mediated Zone of Inhibition*. In: **The Journal of Cell Biology** 179.7 (Dec. 2007), pp. 1375–1384. DOI: 10.1083/jcb.200705160 (cit. on pp. 2, 11, 84, 102).

[19] E.M Vaughan et al. *Control of Local Rho GTPase Crosstalk by Abr*. en. In: **Current Biology** 21.4 (Feb. 2011), pp. 270–277. DOI: 10.1016/j.cub.2011.01.014 (cit. on pp. 2, 11, 84, 101, 102, 113, 161).

[20] W.-C. Lo et al. *Polarization of Diploid Daughter Cells Directed by Spatial Cues and GTP Hydrolysis of Cdc42 in Budding Yeast*. In: **PLoS ONE** 8.2 (Feb. 2013). Ed. by S. Harris, e56665. DOI: 10.1371/journal.pone.0056665 (cit. on pp. 2, 11, 84, 102).

[21] D. Kiekebusch and M. Thanbichler. *Spatiotemporal Organization of Microbial Cells by Protein Concentration Gradients*. en. In: **Trends in Microbiology** 22.2 (Feb. 2014), pp. 65–73. DOI: 10.1016/j.tim.2013.11.005 (cit. on pp. 2, 5, 11, 161).

[22] D.M Veltman et al. *A Plasma Membrane Template for Macropinocytic Cups*. In: **eLife** 5 (Dec. 2016). Ed. by J. Swanson, e20085. DOI: 10.7554/eLife.20085 (cit. on pp. 2, 11, 84, 101).

[23] K. E. Miller et al. *Fine-Tuning the Orientation of the Polarity Axis by Rga1, a Cdc42 GTPase-Activating Protein*. In: **Molecular Biology of the Cell** 28.26 (Dec. 2017). Ed. by R. Li, pp. 3773–3788. DOI: 10.1091/mbc.e17-01-0074 (cit. on pp. 2, 11, 84, 102).

[24] T. D. Williams, P. I. Paschke, and R. R. Kay. *Function of Small GTPases in Dictyostelium Macropinocytosis*. In: **Philosophical Transactions of the Royal Society B: Biological Sciences** 374.1765 (Feb. 2019), p. 20180150. DOI: 10.1098/rstb.2018.0150 (cit. on pp. 2, 11, 84).

[25] N. W. Goehring et al. *PAR Proteins Diffuse Freely across the Anterior–Posterior Boundary in Polarized C. Elegans Embryos*. In: **J Cell Biol** 193.3 (Apr. 2011), pp. 583–594 (cit. on pp. 2, 23, 140, 141, 154, 158).

[26] A. G. Gubieda et al. *Going with the Flow: Insights from Caenorhabditis Elegans Zygote Polarization*. In: **Philosophical Transactions of the Royal Society B: Biological Sciences** 375.1809 (2020), p. 20190555. DOI: 10.1098/rstb.2019.0555 (cit. on pp. 3, 4, 7, 9, 10).

[27] K. Klinkert et al. *Aurora A Depletion Reveals Centrosome-Independent Polarization Mechanism in Caenorhabditis Elegans*. In: **eLife** 8 (2019), e44552. DOI: 10.7554/elife.44552 (cit. on pp. 3, 7).

[28] N. Klughammer et al. *Cytoplasmic Flows in Starfish Oocytes Are Fully Determined by Cortical Contractions*. In: **PLoS computational biology** 14.11 (2018), e1006588. DOI: 10.1371/journal.pcbi.1006588 (cit. on pp. 3, 9, 116, 140, 158).

[29] J. Stricker et al. *Rapid Assembly Dynamics of the Escherichia Coli FtsZ-Ring Demonstrated by Fluorescence Recovery after Photobleaching*. In: **Proceedings of the National Academy of Sciences** 99.5 (2002), pp. 3171–3175. DOI: 10.1073/pnas.052595099 (cit. on p. 3).

[30] Y. Chen et al. *A Rapid Fluorescence Assay for FtsZ Assembly Indicates Cooperative Assembly with a Dimer Nucleus*. In: **Biophysical Journal** 88.1 (2005), pp. 505–514. DOI: 10.1529/biophysj.104.044149 (cit. on p. 3).

[31] M. Loose and T. J. Mitchison. *The Bacterial Cell Division Proteins FtsA and FtsZ Self-Organize into Dynamic Cytoskeletal Patterns*. In: **Nature Cell Biology** 16.1 (2014), pp. 38–46. DOI: 10.1038/ncb2885 (cit. on p. 3).

[32] M. Schliwa and G. Woehlke. *Molecular Motors*. In: **Nature** 422.6933 (2003), pp. 759–765. DOI: 10.1038/nature01601 (cit. on p. 3).

[33] N. Hirokawa. *Kinesin and Dynein Superfamily Proteins and the Mechanism of Organelle Transport*. In: **Science** 279.5350 (1998), pp. 519–526. DOI: 10.1126/science.279.5350.519 (cit. on p. 3).

[34] J. Mata and P. Nurse. *Tea1 and the Microtubular Cytoskeleton Are Important for Generating Global Spatial Order within the Fission Yeast Cell*. In: **Cell** 89.6 (1997), pp. 939–949. DOI: 10.1016/s0092-8674(00)80279-2 (cit. on p. 3).

[35] H. A. Snaith, I. Samejima, and K. E. Sawin. *Multistep and Multimode Cortical Anchoring of Tea1p at Cell Tips in Fission Yeast*. In: **The EMBO Journal** 24.21 (2005), pp. 3690–3699. DOI: 10.1038/sj.emboj.7600838 (cit. on p. 3).

[36] N. Minc et al. *Establishing New Sites of Polarization by Microtubules*. In: **Current Biology** 19.2 (2009), pp. 83–94. DOI: 10.1016/j.cub.2008.12.008 (cit. on p. 3).

[37] K. J. A. Vendel et al. *Minimal in Vitro Systems Shed Light on Cell Polarity*. In: **Journal of Cell Science** 132.4 (2019), jcs217554. DOI: 10.1242/jcs.217554 (cit. on p. 3).

[38] A. Gennerich and R. D. Vale. *Walking the Walk: How Kinesin and Dynein Coordinate Their Steps*. In: **Current Opinion in Cell Biology** 21.1 (2009), pp. 59–67. DOI: 10.1016/j.ceb.2008.12.002 (cit. on p. 3).

[39] G. M Langford. *Myosin-V, a Versatile Motor for Short-Range Vesicle Transport*. In: **Traffic** 3.12 (2002), pp. 859–865. DOI: 10.1034/j.1600-0854.2002.31202.x (cit. on p. 3).

[40] J.-g. Chiou, M. K. Balasubramanian, and D. J. Lew. *Cell Polarity in Yeast*. en. In: **Annual Review of Cell and Developmental Biology** 33.1 (Oct. 2017), pp. 77–101. DOI: 10.1146/annurev-cellbio-100616-060856 (cit. on pp. 3, 140, 154).

[41] S. M Huisman and D. Brunner. *Cell Polarity in Fission Yeast: A Matter of Confining, Positioning, and Switching Growth Zones*. In: **Seminars in Cell & Developmental Biology** 22.8 (2011), pp. 799–805. DOI: 10.1016/j.semcdb.2011.07.013 (cit. on p. 3).

[42] H. Tatebe et al. *Wsh3/Tea4 Is a Novel Cell-End Factor Essential for Bipolar Distribution of Tea1 and Protects Cell Polarity under Environmental Stress in s. Pombe*. In: **Current Biology** 15.11 (2005), pp. 1006–1015. DOI: 10.1016/j.cub.2005.04.061 (cit. on p. 3).

[43] F. Peglion, F. Llense, and S. Etienne-Manneville. *Adherens Junction Treadmilling during Collective Migration*. In: **Nature Cell Biology** 16.7 (2014), pp. 639–651. DOI: 10.1038/ncb2985 (cit. on p. 4).

[44] E. A. Marnik and D. L. Updike. *Membraneless Organelles: P Granules in Caenorhabditis Elegans*. In: **Traffic** 20.6 (2019), pp. 373–379. DOI: 10.1111/tra.12644 (cit. on p. 4).

[45] G. Seydoux. *The p Granules of c. Elegans: A Genetic Model for the Study of RNA-Protein Condensates*. In: **Journal of Molecular Biology** 430.23 (2018), pp. 4702–4710. DOI: 10.1016/j.jmb.2018.08.007 (cit. on p. 4).

[46] P. A. Chong and J. D. Forman-Kay. *Liquid–Liquid Phase Separation in Cellular Signaling Systems*. In: **Current Opinion in Structural Biology** 41 (2016), pp. 180–186. DOI: 10.1016/j.sbi.2016.08.001 (cit. on p. 4).

[47] Z. Liu et al. *Par Complex Cluster Formation Mediated by Phase Separation*. In: **Nature Communications** 11.1 (2020), p. 2266. DOI: 10.1038/s41467-020-16135-6 (cit. on p. 4).

[48] D. Kiekebusch et al. *Localized Dimerization and Nucleoid Binding Drive Gradient Formation by the Bacterial Cell Division Inhibitor MipZ*. In: **Molecular Cell** 46.3 (2012), pp. 245–259. DOI: 10.1016/j.molcel.2012.03.004 (cit. on p. 5).

[49] J. Halatek and E. Frey. *Rethinking Pattern Formation in Reaction–Diffusion Systems*. en. In: **Nature Physics** 14.5 (May 2018), pp. 507–514. DOI: 10.1038/s41567-017-0040-5 (cit. on pp. 5, 6, 13, 15, 72, 85, 87, 101, 156).

[50] F. Brauns, J. Halatek, and E. Frey. *Phase-Space Geometry of Mass-Conserving Reaction-Diffusion Dynamics*. en. In: **Physical Review X** 10.4 (Nov. 2020), p. 041036. DOI: 10.1103/PhysRevX.10.041036. eprint: 1812.08684 (cit. on p. 5).

[51] W. van Saarloos. *Front Propagation into Unstable States*. In: **Physics Reports** 386.2 (Nov. 2003), pp. 29–222. DOI: 10.1016/j.physrep.2003.08.001. eprint: cond-mat/0308540 (cit. on pp. 5, 108).

[52] F. Brauns et al. *Bulk-Surface Coupling Reconciles Min-Protein Pattern Formation in Vitro and in Vivo*. In: **bioRxiv** (2020), p. 2020.03.01.971952. DOI: 10.1101/2020.03.01.971952 (cit. on pp. 5, 6, 154).

[53] F. Wu et al. *Multistability and Dynamic Transitions of Intracellular Min Protein Patterns*. In: **Molecular systems biology** 12.6 (2016), p. 873. DOI: 10.15252/msb.20156724 (cit. on pp. 5, 7, 8, 12, 84).

[54] M. Loose et al. *Min Protein Patterns Emerge from Rapid Rebinding and Membrane Interaction of MinE*. In: **Nat Struct Mol Biol** 18.5 (2011), pp. 577–583 (cit. on pp. 5, 21).

[55] J.E. Ferrell, T.Y.-C. Tsai, and Q. Yang. *Modeling the Cell Cycle: Why Do Certain Circuits Oscillate?* In: **Cell** 144.6 (2011), pp. 874–885. DOI: 10.1016/j.cell.2011.03.006 (cit. on p. 5).

[56] F. Brauns et al. *Wavelength Selection by Interrupted Coarsening in Reaction-Diffusion Systems*. In: **arXiv** (2020). eprint: 2005.01495 (cit. on pp. 6, 12–17, 72, 85, 87, 93, 97, 101, 103, 110, 140–144, 147–149, 151, 152, 156, 157).

[57] B. Antonny. *Mechanisms of Membrane Curvature Sensing*. en. In: **Annual Review of Biochemistry** 80.1 (July 2011), pp. 101–123. DOI: 10.1146/annurev-biochem-052809-155121 (cit. on pp. 6, 7, 116).

[58] D.M Raskin and P.A.J. de Boer. *Rapid Pole-to-Pole Oscillation of a Protein Required for Directing Division to the Middle of Escherichia Coli*. In: **Proceedings of the National Academy of Sciences** 96.9 (1999), pp. 4971–4976. DOI: 10.1073/pnas.96.9.4971 (cit. on pp. 6, 7).

[59] E. Frey and F. Brauns. *Self-Organisation of Protein Patterns*. In: **arXiv** (2020). eprint: 2012.01797 (cit. on pp. 6, 161).

[60] B. J. Peter et al. *BAR Domains as Sensors of Membrane Curvature: The Amphiphysin BAR Structure*. In: **Science** 303.5657 (2004), pp. 495–499. DOI: 10.1126/science.1092586 (cit. on p. 7).

[61] I. Begemann et al. *Mechanochemical Self-Organization Determines Search Pattern in Migratory Cells*. en. In: **Nature Physics** 15.8 (Aug. 2019), pp. 848–857. DOI: 10.1038/s41567-019-0505-9 (cit. on p. 7).

[62] H. Feddersen et al. *Dynamics of the Bacillus Subtilis Min System*. In: **bioRxiv** (2020), p. 2020.04.29.068676. DOI: 10.1101/2020.04.29.068676 (cit. on p. 7).

[63] C. Mim and V. M Unger. *Membrane Curvature and Its Generation by BAR Proteins*. In: **Trends in Biochemical Sciences** 37.12 (2012), pp. 526–533. DOI: 10.1016/j.tibs.2012.09.001 (cit. on pp. 7, 8).

[64] M. Simunovic et al. *When Physics Takes over: BAR Proteins and Membrane Curvature*. In: **Trends in Cell Biology** 25.12 (2015), pp. 780–792. DOI: 10.1016/j.tcb.2015.09.005 (cit. on pp. 7, 8).

[65] H. T. McMahon and E. Boucrot. *Membrane Curvature at a Glance*. In: **Journal of Cell Science** 128.6 (2015), pp. 1065–1070. DOI: 10.1242/jcs.114454 (cit. on p. 7).

[66] K. Faelber et al. *Structural Insights into Dynamin-Mediated Membrane Fission*. In: **Structure** 20.10 (2012), pp. 1621–1628. DOI: 10.1016/j.str.2012.08.028 (cit. on pp. 7, 8).

[67] S. M Ferguson and P. D. Camilli. *Dynamin, a Membrane-Remodelling GTPase*. In: **Nature Reviews Molecular Cell Biology** 13.2 (2012), pp. 75–88. DOI: 10.1038/nrm3266 (cit. on p. 8).

[68] S. Morlot and A. Roux. *Mechanics of Dynamin-Mediated Membrane Fission*. In: **Biophysics** 42.1 (2013), pp. 629–649. DOI: 10.1146/annurev-biophys-050511-102247 (cit. on p. 8).

[69] A. Roux et al. *Membrane Curvature Controls Dynamin Polymerization*. In: **Proceedings of the National Academy of Sciences** 107.9 (2010), pp. 4141–4146. DOI: 10.1073/pnas.0913734107 (cit. on p. 8).

[70] J. L. Gallop and H. T. McMahon. *BAR Domains and Membrane Curvature: Bringing Your Curves to the BAR*. In: **Biochemical Society Symposia** 72.72 (2005), pp. 223–231. DOI: 10.1042/bss0720223 (cit. on p. 8).

[71] B. He et al. *Apical Constriction Drives Tissue-Scale Hydrodynamic Flow to Mediate Cell Elongation*. In: **Nature** 508.7496 (2014), pp. 392–396. DOI: 10.1038/nature13070 (cit. on p. 10).

[72] M. Mayer et al. *Anisotropies in Cortical Tension Reveal the Physical Basis of Polarizing Cortical Flows*. en. In: **Nature** 467.7315 (Sept. 2010), pp. 617–621. DOI: 10.1038/nature09376 (cit. on pp. 10, 140).

[73] W. O. Fenn. *A Quantitative Comparison between the Energy Liberated and the Work Performed by the Isolated Sartorius Muscle of the Frog*. In: **The Journal of Physiology** 58.2-3 (1923), pp. 175–203. DOI: 10.1113/jphysiol.1923.sp002115 (cit. on p. 10).

[74] A. F. Huxley and R. M Simmons. *Proposed Mechanism of Force Generation in Striated Muscle*. In: **Nature** 233.5321 (1971), pp. 533–538. DOI: 10.1038/233533a0 (cit. on p. 10).

[75] C. Veigel et al. *Load-Dependent Kinetics of Force Production by Smooth Muscle Myosin Measured with Optical Tweezers*. In: **Nature Cell Biology** 5.11 (2003), pp. 980–986. DOI: 10.1038/ncb1060 (cit. on p. 10).

[76] T. Luo et al. *Understanding the Cooperative Interaction between Myosin II and Actin Cross-Linkers Mediated by Actin Filaments during Mechanosensation*. In: **Biophysical Journal** 102.2 (2012), pp. 238–247. DOI: 10.1016/j.bpj.2011.12.020 (cit. on p. 10).

[77] K. Hayakawa, H. Tatsumi, and M. Sokabe. *Actin Filaments Function as a Tension Sensor by Tension-Dependent Binding of Cofilin to the Filament*. In: **The Journal of Cell Biology** 195.5 (2011), pp. 721–727. DOI: 10.1083/jcb.201102039 (cit. on p. 10).

[78] A. McGough et al. *Cofilin Changes the Twist of F-Actin: Implications for Actin Filament Dynamics and Cellular Function*. In: **The Journal of Cell Biology** 138.4 (1997), pp. 771–781. DOI: 10.1083/jcb.138.4.771 (cit. on p. 10).

[79] V. E. Galkin et al. *Actin Depolymerizing Factor Stabilizes an Existing State of F-Actin and Can Change the Tilt of f-Actin Subunits*. In: **The Journal of Cell Biology** 153.1 (2001), pp. 75–86. DOI: 10.1083/jcb.153.1.75 (cit. on p. 10).

[80] P. M McCall et al. *Cofilin Drives Rapid Turnover and Fluidization of Entangled F-Actin*. In: **Proceedings of the National Academy of Sciences** 116.26 (2019), pp. 12629–12637. DOI: 10.1073/pnas.1818808116 (cit. on p. 10).

[81] E. Egelman and D. DeRosier. *Image Analysis Shows That Variations in Actin Crossover Spacings Are Random, Not Compensatory*. In: **Biophysical Journal** 63.5 (1992), pp. 1299–1305. DOI: 10.1016/s0006-3495(92)81716-2 (cit. on p. 10).

[82] H. Huxley and W. Brown. *The Low-Angle X-Ray Diagram of Vertebrate Striated Muscle and Its Behaviour during Contraction and Rigor*. In: **Journal of Molecular Biology** 30.2 (1967), 383–IN16. DOI: 10.1016/s0022-2836(67)80046-9 (cit. on p. 10).

[83] S. Basu et al. *Spatiotemporal Control of Gene Expression with Pulse-Generating Networks*. en. In: **Proceedings of the National Academy of Sciences** 101.17 (Apr. 2004), pp. 6355–6360. DOI: 10.1073/pnas.0307571101 (cit. on p. 11).

[84] S. Ishihara, K. Fujimoto, and T. Shibata. *Cross Talking of Network Motifs in Gene Regulation That Generates Temporal Pulses and Spatial Stripes*. en. In: **Genes to Cells** 10.11 (2005), pp. 1025–1038. DOI: 10.1111/j.1365-2443.2005.00897.x (cit. on p. 11).

[85] U. Alon. *Network Motifs: Theory and Experimental Approaches*. en. In: **Nature Reviews Genetics** 8.6 (June 2007), pp. 450–461. DOI: 10.1038/nrg2102 (cit. on p. 11).

[86] Y. Benenson. *Biomolecular Computing Systems: Principles, Progress and Potential*. In: **Nature Reviews Genetics** 13.7 (2012), pp. 455–468. DOI: 10.1038/nrg3197 (cit. on p. 11).

[87] U. Alon. *An Introduction to Systems Biology: Design Principles of Biological Circuits*. Chapman \& Hall/CRC Computational Biology Series. CRC Press, 2019 (cit. on p. 11).

[88] B.N. Kholodenko. *Cell-Signalling Dynamics in Time and Space*. en. In: **Nature Reviews Molecular Cell Biology** 7.3 (Mar. 2006), pp. 165–176. DOI: 10.1038/nrm1838 (cit. on p. 11).

[89] M. Howard, A.D. Rutenberg, and S. de Vet. *Dynamic Compartmentalization of Bacteria: Accurate Division in* E. Coli. In: **Physical Review Letters** 87.27 (Dec. 2001). DOI: 10.1103/PhysRevLett.87.278102 (cit. on pp. 12, 84).

[90] K.C. Huang, Y. Meir, and N.S. Wingreen. *Dynamic Structures in Escherichia Coli: Spontaneous Formation of MinE Rings and MinD Polar Zones*. en. In: **Proceedings of the National Academy of Sciences** 100.22 (Oct. 2003), pp. 12724–12728. DOI: 10.1073/pnas.2135445100 (cit. on pp. 12, 84, 158).

[91] Y. Mori, A. Jilkine, and L. Edelstein-Keshet. *Wave-Pinning and Cell Polarity from a Bistable Reaction-Diffusion System*. In: **Biophysical Journal** 94.9 (May 2008), pp. 3684–3697. DOI: 10.1529/biophysj.107.120824 (cit. on pp. 12, 15, 66, 84, 102, 113, 140).

[92] A.B. Goryachev and A.V. Pokhilko. *Dynamics of Cdc42 Network Embodies a Turing-Type Mechanism of Yeast Cell Polarity*. en. In: **FEBS Letters** 582.10 (2008), pp. 1437–1443. DOI: 10.1016/j.febslet.2008.03.029 (cit. on pp. 12, 84, 140).

[93] S. Ishihara, M. Otsuji, and A. Mochizuki. *Transient and Steady State of Mass-Conserved Reaction-Diffusion Systems*. In: **Physical Review E** 75.1 (Jan. 2007), p. 015203. DOI: 10.1103/PhysRevE.75.015203 (cit. on pp. 12, 15, 17, 84, 92, 93, 141).

[94] M. Otsuji et al. *A Mass Conserved Reaction–Diffusion System Captures Properties of Cell Polarity*. In: **PLoS Computational Biology** 3.6 (2007), e108. DOI: 10.1371/journal.pcbi.0030108 (cit. on pp. 12, 15, 17, 84, 92, 93, 141).

[95] J. Halatek and E. Frey. *Highly Canalized MinD Transfer and MinE Sequestration Explain the Origin of Robust MinCDE-Protein Dynamics*. en. In: **Cell Reports** 1.6 (June 2012), pp. 741–752. DOI: 10.1016/j.celrep.2012.04.005 (cit. on pp. 12, 70, 84, 158).

[96] B. Klünder et al. *GDI-Mediated Cell Polarization in Yeast Provides Precise Spatial and Temporal Control of Cdc42 Signaling*. In: **PLOS Computational Biology** 9.12 (Dec. 2013), e1003396. DOI: 10.1371/journal.pcbi.1003396 (cit. on pp. 12, 84, 140).

[97] P.K. Trong et al. *Parameter-Space Topology of Models for Cell Polarity*. In: **New Journal of Physics** 16.6 (June 2014), p. 065009. DOI: 10.1088/1367-2630/16/6/065009 (cit. on pp. 12, 84, 140, 154).

[98] S. Alonso and M. Bär. *Modeling Domain Formation of MARCKS and Protein Kinase C at Cellular Membranes*. In: **EPJ Nonlinear Biomedical Physics** 2.1 (Jan. 2014), p. 1. DOI: 10.1140/epjnbp14 (cit. on pp. 12, 84).

[99] A.B. Goryachev and M. Leda. *Many Roads to Symmetry Breaking: Molecular Mechanisms and Theoretical Models of Yeast Cell Polarity*. en. In: **Molecular Biology of the Cell** 28.3 (Feb. 2017). Ed. by W. Bement, pp. 370–380. DOI: 10.1091/mbc.e16-10-0739 (cit. on pp. 12, 70, 84, 140).

[100] S.M Murray and V. Sourjik. *Self-Organization and Positioning of Bacterial Protein Clusters*. In: **Nature Physics** 13.10 (Oct. 2017), pp. 1006–1013. DOI: 10.1038/nphys4155 (cit. on pp. 12, 84).

[101] J. Denk et al. *MinE Conformational Switching Confers Robustness on Self-Organized Min Protein Patterns*. In: **Proceedings of the National Academy of Sciences** 115.18 (May 2018), pp. 4553–4558. DOI: 10.1073/pnas.1719801115 (cit. on pp. 12, 84).

[102] D. Cusseddu et al. *A Coupled Bulk-Surface Model for Cell Polarisation*. In: **Journal of Theoretical Biology** (Sept. 2018). DOI: 10.1016/j.jtbi.2018.09.008 (cit. on pp. 12, 84).

[103] J.-G. Chiou et al. *Principles That Govern Competition or Co-Existence in Rho-GTPase Driven Polarization*. en. In: **PLOS Computational Biology** 14.4 (Apr. 2018), e1006095. DOI: 10.1371/journal.pcbi.1006095 (cit. on pp. 12, 15, 84, 140, 141, 152, 154).

[104] P. Glock et al. *Design of Biochemical Pattern Forming Systems from Minimal Motifs*. In: **eLife** 8 (Nov. 2019), e48646. DOI: 10.7554/eLife.48646 (cit. on pp. 12, 84).

[105] M.C. Wigbers et al. *Flow Induced Symmetry Breaking in a Conceptual Polarity Model*. en. In: **Cells** 9.6 (June 2020), p. 1524. DOI: 10.3390/cells9061524 (cit. on pp. 13, 72, 83, 141, 157).

[106] J. Halatek, F. Brauns, and E. Frey. *Self-Organization Principles of Intracellular Pattern Formation*. In: **Philosophical Transactions of the Royal Society B: Biological Sciences** 373.1747 (May 2018), p. 20170107. DOI: 10.1098/rstb.2017.0107. eprint: 1802.07169 (cit. on pp. 16, 84, 116, 141, 144, 145, 151, 161).

[107] M.C. Cross and P.C. Hohenberg. *Pattern Formation Outside of Equilibrium*. In: **Reviews of Modern Physics** 65.3 (July 1993), pp. 851–1112. DOI: 10.1103/RevModPhys.65.851 (cit. on pp. 17, 161).

[108] A. Pogan, A. Scheel, and K. Zumbrun. *Quasi-Gradient Systems, Modulational Dichotomies, and Stability of Spatially Periodic Patterns*. In: **Differential Integral Equations** 26.3/4 (2013), pp. 389–438 (cit. on pp. 17, 92, 93).

[109] A. Pogan and A. Scheel. *Instability of Spikes in the Presence of Conservation Laws*. In: **Zeitschrift für angewandte Mathematik und Physik** 61.6 (Dec. 2010), pp. 979–998. DOI: 10.1007/s00033-010-0058-3 (cit. on pp. 17, 92, 93).

[110] F. Tostevin et al. *Four Different Mechanisms for Switching Cell Polarity*. en. In: **PLOS Computational Biology** 17.1 (Jan. 2021). Ed. by Q. Nie, e1008587. DOI: 10.1371/journal.pcbi.1008587 (cit. on p. 19).

[111] J.P Campanale, T.Y. Sun, and D.J. Montell. *Development and Dynamics of Cell Polarity at a Glance*. In: **J Cell Sci** 130.7 (2017), pp. 1201–1207 (cit. on p. 20).

[112] M.T. Butler and J.B. Wallingford. *Planar Cell Polarity in Development and Disease*. In: **Nat Rev Mol Cell Biol** 18.6 (2017), pp. 375–388 (cit. on p. 20).

[113] D.G. Drubin and W.J. Nelson. *Origins of Cell Polarity*. In: **Cell** 84.3 (1996), pp. 335–344 (cit. on p. 20).

[114] D. Kaiser and R. Yu. *Reversing Cell Polarity: Evidence and Hypothesis*. In: **Curr Opin Microbiol** 8.2 (2005), pp. 216–221 (cit. on p. 20).

[115] J. Dalous et al. *Reversal of Cell Polarity and Actin-Myosin Cytoskeleton Reorganization under Mechanical and Chemical Stimulation*. In: **Biophys J** 94.3 (2008), pp. 1063–1074 (cit. on p. 20).

[116] J. Dworkin. *Cellular Polarity in Prokaryotic Organisms*. In: **Csh Perspect Biol** 1.6 (2009), a003368–a003368 (cit. on p. 20).

[117] R. Wedlich-Soldner and R. Li. *Spontaneous Cell Polarization: Undermining Determinism*. In: **Nat Cell Biol** 5.4 (2003), pp. 267–270 (cit. on p. 20).

[118] T. Freisinger et al. *Establishment of a Robust Single Axis of Cell Polarity by Coupling Multiple Positive Feedback Loops*. In: **Nat Commun** 4.1 (2013), p. 1807 (cit. on pp. 20, 140).

[119] A.H. Chau et al. *Designing Synthetic Regulatory Networks Capable of Self-Organizing Cell Polarization*. en. In: **Cell** 151.2 (Oct. 2012), pp. 320–332. DOI: 10.1016/j.cell.2012.08.040 (cit. on p. 20).

[120] E. Albrecht and H.R. Petty. *Cellular Memory: Neutrophil Orientation Reverses during Temporally Decreasing Chemoattractant Concentrations*. In: **Proc Natl Acad Sci USA** 95.9 (1998), pp. 5039–5044 (cit. on pp. 20, 21, 38).

[121] J. Park et al. *Mechanochemical Feedback Underlies Coexistence of Qualitatively Distinct Cell Polarity Patterns within Diverse Cell Populations*. In: **Proc Natl Acad Sci USA** 114 (2017), E5750–E5759 (cit. on pp. 20, 21, 23).

[122] K.D. Moran et al. *Cell-Cycle Control of Cell Polarity in Yeast*. In: **J Cell Biol** 218.1 (2018), pp. 171–189 (cit. on p. 20).

[123] Z. Hu and J. Lutkenhaus. *Topological Regulation of Cell Division in Escherichia Coli Involves Rapid Pole to Pole Oscillation of the Division Inhibitor MinC under the Control of MinD and MinE*. In: **Mol Microbiol** 34.1 (1999), pp. 82–90 (cit. on p. 21).

[124] B. Novák and J.J. Tyson. *Design Principles of Biochemical Oscillators*. In: **Nat Rev Mol Cell Biol** 9.12 (Oct. 2008), pp. 981–991 (cit. on pp. 21, 61).

[125] D.R. Zusman et al. *Chemosensory Pathways, Motility and Development in Myxococcus Xanthus*. In: **Nature Reviews Microbiology** 5 (2007), pp. 862–872 (cit. on p. 21).

[126] D. Kaiser. *Myxococcus—from Single-Cell Polarity to Complex Multicellular Patterns*. In: **Annual Review of Genetics** 42.1 (2008), pp. 109–130. DOI: 10.1146/annurev.genet.42.110807.091615 (cit. on p. 21).

[127] M. Guzzo et al. *A Gated Relaxation Oscillator Mediated by FrzX Controls Morphogenetic Movements in Myxococcus Xanthus.* In: **Nat. Microbiol** 3.8 (2018), pp. 948–959 (cit. on pp. 21–25, 27, 38, 39).

[128] S. Etienne-Manneville. *Cdc42 - the Centre of Polarity*. In: **J Cell Sci** 117.8 (Mar. 2004), pp. 1291–1300 (cit. on p. 21).

[129] A. Pikovsky and J. Kurths. *Coherence Resonance in a Noise-Driven Excitable System*. In: **Phys Rev Lett** 78 (1997), pp. 775–778 (cit. on p. 35).

[130] D. Szadkowski et al. *Spatial Control of the GTPase MglA by Localized RomR–RomX GEF and MglB GAP Activities Enables Myxococcus Xanthus Motility*. In: **Nat Microbiol** 4 (2019), pp. 1344–1355 (cit. on p. 38).

[131] L.A.M Carreira et al. *Protein-Protein Interaction Network Controlling Establishment and Maintenance of Switchable Cell Polarity.* In: **PLoS Genet** 16 (2020), e1008877 (cit. on p. 38).

[132] T. Gardner, C. Cantor, and J. Collins. *Construction of a Genetic Toggle Switch in Escherichia Coli*. In: **Nature** 403 (2000), pp. 339–342 (cit. on p. 39).

[133] P.B. Warren and P.R. ten Wolde. *Chemical Models of Genetic Toggle Switches*. In: **J Phys Chem B** 109.14 (Apr. 2005), pp. 6812–6823 (cit. on p. 39).

[134] G. Fritz et al. *Designing Sequential Transcription Logic: A Simple Genetic Circuit for Conditional Memory*. In: **Syst Synth Biol** 1 (Apr. 2007), pp. 89–98 (cit. on p. 39).

[135] C. Lou et al. *Synthesizing a Novel Genetic Sequential Logic Circuit: A Push-on Push-off Switch*. In: **Molecular Systems Biology** 6.1 (2010). DOI: 10.1038/msb.2010.2 (cit. on p. 39).

[136] P. Hillenbrand, G. Fritz, and U. Gerland. *Biological Signal Processing with a Genetic Toggle Switch*. In: **PLoS ONE** 8.7 (July 2013), e68345. DOI: 10.1371/journal.pone.0068345 (cit. on p. 39).

[137] J.-B. Lugagne et al. *Balancing a Genetic Toggle Switch by Real-Time Feedback Control and Periodic Forcing*. In: **Nat Commun** 8 (2017), p. 1671 (cit. on p. 39).

[138] C. W. Mullineaux et al. *Diffusion of Green Fluorescent Protein in Three Cell Environments in Escherichia Coli*. In: **J Bacteriol** 188.10 (May 2006), pp. 3442–3448 (cit. on p. 39).

[139] N. G. van Kampen. *Stochastic Processes in Physics and Chemistry*. North Holland, Amsterdam, 1981 (cit. on p. 40).

[140] D. T. Gillespie. *The Chemical Langevin Equation*. In: **J. Chem. Phys.** 113.1 (2000), pp. 297–306. DOI: 10.1063/1.481811 (cit. on p. 40).

[141] F. Pedregosa et al. *Scikit-Learn: Machine Learning in Python*. In: **J. Mach. Learn. Res.** 12 (2011), pp. 2825–2830 (cit. on p. 41).

[142] P. Welch. *The Use of Fast Fourier Transform for the Estimation of Power Spectra: A Method Based on Time Averaging over Short, Modified Periodograms*. In: **IEEE Trans. Audio Electroacoust.** 15.2 (1967), pp. 70–73 (cit. on p. 41).

[143] M. C. Wigbers et al. *A Hierarchy of Protein Patterns Robustly Decodes Cell Shape Information*. en. In: **Nature Physics** (Feb. 2021). DOI: 10.1038/s41567-021-01164-9 (cit. on pp. 59, 67, 115).

[144] J. Bischof et al. *A Cdk1 Gradient Guides Surface Contraction Waves in Oocytes*. en. In: **Nature Communications** 8.1 (Oct. 2017), pp. 1–10. DOI: 10.1038/s41467-017-00979-6 (cit. on pp. 60, 62, 64, 116, 118, 127, 140).

[145] W. M Bement et al. *Activator–Inhibitor Coupling between Rho Signalling and Actin Assembly Makes the Cell Cortex an Excitable Medium*. en. In: **Nature Cell Biology** 17.11 (Nov. 2015), pp. 1471–1483. DOI: 10.1038/ncb3251 (cit. on pp. 60, 68, 70, 71, 119, 127).

[146] T. Tatsumoto et al. *Human Ect2 Is an Exchange Factor for Rho Gtpases, Phosphorylated in G2/M Phases, and Involved in Cytokinesis*. en. In: **Journal of Cell Biology** 147.5 (Nov. 1999), pp. 921–928. DOI: 10.1083/jcb.147.5.921 (cit. on p. 60).

[147] A. Basant and M. Glotzer. *Spatiotemporal Regulation of RhoA during Cytokinesis*. en. In: **Current Biology** 28.9 (May 2018), R570–R580. DOI: 10.1016/j.cub.2018.03.045 (cit. on pp. 60, 69).

[148] R. G. Hodge and A. J. Ridley. *Regulating Rho GTPases and Their Regulators*. en. In: **Nature Reviews Molecular Cell Biology** 17.8 (Aug. 2016), pp. 496–510. DOI: 10.1038/nrm.2016.67 (cit. on pp. 60, 68–70, 77, 122).

[149] K.-C. Su, T. Takaki, and M. Petronczki. *Targeting of the RhoGEF Ect2 to the Equatorial Membrane Controls Cleavage Furrow Formation during Cytokinesis*. en. In: **Developmental Cell** 21.6 (Dec. 2011), pp. 1104–1115. DOI: 10.1016/j.devcel.2011.11.003 (cit. on pp. 60, 62, 77, 119).

[150] F. Niiya et al. *Phosphorylation of the Cytokinesis Regulator ECT2 at G2/M Phase Stimulates Association of the Mitotic Kinase Plk1 and Accumulation of GTP-Bound RhoA*. en. In: **Oncogene** 25.6 (Feb. 2006), pp. 827–837. DOI: 10.1038/sj.onc.1209124 (cit. on p. 60).

[151] J. Birkenfeld et al. *GEF-H1 Modulates Localized RhoA Activation during Cytokinesis under the Control of Mitotic Kinases*. en. In: **Developmental Cell** 12.5 (May 2007), pp. 699–712. DOI: 10.1016/j.devcel.2007.03.014 (cit. on pp. 60, 68, 70, 71, 77, 133).

[152] J. Bischof. *The Molecular Mechanism of Surface Contraction Waves in the Starfish Oocyte*. In: (2016). DOI: 10.11588/HEIDOK.00021578 (cit. on pp. 62, 68, 71, 116, 136).

[153] A. S. Mikhailov. *Foundations of Synergetics I: Distributed Active Systems*. In: **Foundations of Synergetics I: Distributed Active Systems.** Vol. Vol. 51. Springer Science & Business Media, 2012 (cit. on pp. 63, 65, 123).

[154] L. Gelens, G. A. Anderson, and J. E. Ferrell. *Spatial Trigger Waves: Positive Feedback Gets You a Long Way*. en. In: **Molecular Biology of the Cell** 25.22 (Nov. 2014). Ed. by D. Kellogg and J. Lippincott-Schwartz, pp. 3486–3493. DOI: 10.1091/mbc.e14-08-1306 (cit. on pp. 65, 123).

[155] S. A. Ramirez, S. Raghavachari, and D. J. Lew. *Dendritic Spine Geometry Can Localize GTPase Signaling in Neurons*. In: **Molecular Biology of the Cell** 26.22 (Sept. 2015), pp. 4171–4181. DOI: 10.1091/mbc.E15-06-0405 (cit. on p. 66).

[156] A. T. Dawes and D. Iron. *Cortical Geometry May Influence Placement of Interface between Par Protein Domains in Early Caenorhabditis Elegans Embryos*. en. In: **Journal of Theoretical Biology** 333 (Sept. 2013), pp. 27–37. DOI: 10.1016/j.jtbi.2013.04.024 (cit. on p. 66).

[157] S. Rulands, B. Klünder, and E. Frey. *Stability of Localized Wave Fronts in Bistable Systems*. In: **Physical Review Letters** 110.3 (Jan. 2013), p. 038102. DOI: 10.1103/PhysRevLett.110.038102 (cit. on pp. 66, 102, 124).

[158] P. M Müller et al. *Systems Analysis of RhoGEF and RhoGAP Regulatory Proteins Reveals Spatially Organized RAC1 Signalling from Integrin Adhesions*. en. In: **Nature Cell Biology** 22.4 (Apr. 2020), pp. 498–511. DOI: 10.1038/s41556-020-0488-x (cit. on pp. 68–70, 77, 122).

[159] M. Graessl et al. *An Excitable Rho GTPase Signaling Network Generates Dynamic Subcellular Contraction Patterns*. en. In: **Journal of Cell Biology** 216.12 (Dec. 2017), pp. 4271–4285. DOI: 10.1083/jcb.201706052 (cit. on p. 69).

[160] A. E. Golding et al. *Extraction of Active RhoGTPases by RhoGDI Regulates Spatiotemporal Patterning of RhoGTPases*. en. In: **eLife** 8 (Oct. 2019), e50471. DOI: 10.7554/eLife.50471 (cit. on p. 69).

[161] W. M Bement, H. A. Benink, and G. von Dassow. *A Microtubule-Dependent Zone of Active RhoA during Cleavage Plane Specification*. en. In: **Journal of Cell Biology** 170.1 (July 2005), pp. 91–101. DOI: 10.1083/jcb.200501131 (cit. on p. 69).

[162] A. L. Miller and W. M Bement. *Regulation of Cytokinesis by Rho GTPase Flux*. en. In: **Nature Cell Biology** 11.1 (Jan. 2009), pp. 71–77. DOI: 10.1038/ncb1814 (cit. on pp. 69, 71, 77, 133).

[163] S. Budnar et al. *Anillin Promotes Cell Contractility by Cyclic Resetting of RhoA Residence Kinetics*. en. In: **Developmental Cell** 49.6 (June 2019), 894–906.e12. DOI: 10.1016/j.devcel.2019.04.031 (cit. on p. 69).

[164] A. B. Goryachev and M. Leda. *Autoactivation of Small GTPases by the GEF–Effector Positive Feedback Modules*. en. In: **F1000Research** 8 (Sept. 2019), p. 1676. DOI: 10.12688/f1000research.20003.1 (cit. on p. 70).

[165] U. Bezeljak et al. *Stochastic Activation and Bistability in a Rab GTPase Regulatory Network*. en. In: **Proceedings of the National Academy of Sciences** 117.12 (Mar. 2020), pp. 6540–6549. DOI: 10.1073/pnas.1921027117 (cit. on p. 70).

[166] K. C. Huang and N. S. Wingreen. *Min-Protein Oscillations in Round Bacteria*. en. In: **Physical Biology** 1.4 (Dec. 2004), pp. 229–235. DOI: 10.1088/1478-3967/1/4/005 (cit. on p. 70).

[167] L. Edelstein-Keshet et al. *From Simple to Detailed Models for Cell Polarization*. In: **Philosophical Transactions of the Royal Society B: Biological Sciences** 368.1629 (Nov. 2013), p. 20130003. DOI: 10.1098/rstb.2013.0003 (cit. on p. 71).

[168] W. R. Holmes, A. E. Carlsson, and L. Edelstein-Keshet. *Regimes of Wave Type Patterning Driven by Refractory Actin Feedback: Transition from Static Polarization to Dynamic Wave Behaviour*. en. In: **Physical Biology** 9.4 (July 2012), p. 046005. DOI: 10.1088/1478-3975/9/4/046005 (cit. on p. 71).

[169] J. Allard and A. Mogilner. *Traveling Waves in Actin Dynamics and Cell Motility*. en. In: **Current Opinion in Cell Biology**. Cell Architecture 25.1 (Feb. 2013), pp. 107–115. DOI: 10.1016/j.ceb.2012.08.012 (cit. on p. 71).

[170] E. M Izhikevich. *Dynamical Systems in Neuroscience The Geometry of Excitability and Bursting*. MIT Press, 2010 (cit. on pp. 78, 126, 134).

[171] A. M Turing. *The Chemical Basis of Morphogenesis*. en. In: **Philosophical Transactions of the Royal Society of London. Series B, Biological Sciences** 237.641 (Aug. 1952), pp. 37–72. DOI: 10.1098/rstb.1952.0012 (cit. on pp. 84, 140, 161).

[172] P. K. Maini, D. L. Benson, and J. A. Sherratt. *Pattern Formation in Reaction-Diffusion Models with Spatially Inhomogeneous Diffusion Coefficients*. In: **Mathematical Medicine and Biology: A Journal of the IMA** 9.3 (Jan. 1992), pp. 197–213. DOI: 10.1093/imammb/9.3.197 (cit. on p. 85).

[173] G. B. Ermentrout and J. Rinzel. *Reflected Waves in an Inhomogeneous Excitable Medium*. In: **SIAM Journal on Applied Mathematics** 56.4 (Aug. 1996), pp. 1107–1128. DOI: 10.1137/S0036139994276793 (cit. on p. 85).

[174] M. Bär et al. *Composite Catalyst Surfaces: Effect of Inert and Active Heterogeneities on Pattern Formation*. In: **The Journal of Physical Chemistry** 100.49 (Jan. 1996), pp. 19106–19117. DOI: 10.1021/jp961689q (cit. on p. 85).

[175] X. Yuan, T. Teramoto, and Y. Nishiura. *Heterogeneity-Induced Defect Bifurcation and Pulse Dynamics for a Three-Component Reaction-Diffusion System*. In: **Physical Review E** 75.3 (Mar. 2007), p. 036220. DOI: 10.1103/PhysRevE.75.036220 (cit. on p. 85).

[176] Y. Nishiura et al. *Dynamics of Traveling Pulses in Heterogeneous Media*. In: **Chaos: An Interdisciplinary Journal of Nonlinear Science** 17.3 (Sept. 2007), p. 037104. DOI: 10.1063/1.2778553 (cit. on pp. 85, 100, 102).

[177] J. Miyazaki and S. Kinoshita. *Stopping and Initiation of a Chemical Pulse at the Interface of Excitable Media with Different Diffusivity*. In: **Physical Review E** 76.6 (Dec. 2007). DOI: 10.1103/PhysRevE.76.066201 (cit. on p. 85).

[178] K. Nishi, Y. Nishiura, and T. Teramoto. *Dynamics of Two Interfaces in a Hybrid System with Jump-Type Heterogeneity*. In: **Japan Journal of Industrial and Applied Mathematics** 30.2 (June 2013), pp. 351–395. DOI: 10.1007/s13160-013-0100-x (cit. on p. 85).

[179] A. Doelman, P. van Heijster, and F. Xie. *A Geometric Approach to Stationary Defect Solutions in One Space Dimension*. In: **SIAM Journal on Applied Dynamical Systems** 15.2 (Jan. 2016), pp. 655–712. DOI: 10.1137/15M1026742 (cit. on pp. 85, 100, 102).

[180] P. van Heijster et al. *Pinned Solutions in a Heterogeneous Three-Component FitzHugh–Nagumo Model*. In: **Journal of Dynamics and Differential Equations** 31.1 (Mar. 2019), pp. 153–203. DOI: 10.1007/s10884-018-9694-7 (cit. on pp. 85, 100, 102).

[181] A. Scheel and J. Weinburd. *Wavenumber Selection via Spatial Parameter Jump*. In: **Philosophical Transactions of the Royal Society A: Mathematical, Physical and Engineering Sciences** 376.2117 (Apr. 2018), p. 20170191. DOI: 10.1098/rsta.2017.0191 (cit. on p. 85).

[182] C.K.R.T. Jones. „Geometric Singular Perturbation Theory“. In: *Dynamical Systems*. Vol. 1609. Berlin, Heidelberg: Springer, 1995, pp. 44–118. DOI: 10.1007/BFb0095239 (cit. on p. 85).

[183] M.J. Ward. *Asymptotic Methods for Reaction-Diffusion Systems: Past and Present*. In: **Bulletin of Mathematical Biology** 68.5 (July 2006), pp. 1151–1167. DOI: 10.1007/s11538-006-9091-y (cit. on pp. 85, 102).

[184] J. Guckenheimer and P. Holmes. *Nonlinear Oscillations, Dynamical Systems, and Bifurcations of Vector Fields*. Vol. 42. Applied Mathematical Sciences. New York, NY: Springer New York, 1983. DOI: 10.1007/978-1-4612-1140-2 (cit. on pp. 85, 95).

[185] B. Krauskopf, H.M Osinga, and J. Galan-Vioque, eds. *Numerical Continuation Methods for Dynamical Systems: Path Following and Boundary Value Problems*. Understanding Complex Systems. Dordrecht: Springer Netherlands, 2007. DOI: 10.1007/978-1-4020-6356-5 (cit. on pp. 91, 109).

[186] J.D. Pryce. *Numerical Solution of Sturm-Liouville Problems*. Monographs on Numerical Analysis. Oxford; New York: Clarendon Press, 1993 (cit. on p. 95).

[187] A. Ziepke, S. Martens, and H. Engel. *Wave Propagation in Spatially Modulated Tubes*. In: **The Journal of Chemical Physics** 145.9 (Sept. 2016), p. 094108. DOI: 10.1063/1.4962173 (cit. on pp. 100, 102).

[188] S.R. Pfeffer. *Rab GTPase Localization and Rab Cascades in Golgi Transport*. In: **Biochemical Society Transactions** 40.6 (Dec. 2012), pp. 1373–1377. DOI: 10.1042/BST20120168 (cit. on p. 102).

[189] P. Novick. *Regulation of Membrane Traffic by Rab GEF and GAP Cascades*. In: **Small GTPases** 7.4 (Oct. 2016), pp. 252–256. DOI: 10.1080/21541248.2016.1213781 (cit. on p. 102).

[190] L.C. Noack and Y. Jaillais. *Precision Targeting by Phosphoinositides: How PIs Direct Endomembrane Trafficking in Plants*. In: **Current Opinion in Plant Biology** 40 (Dec. 2017), pp. 22–33. DOI: 10.1016/j.pbi.2017.06.017 (cit. on p. 102).

[191] A.S. Zadorin et al. *Synthesis and Materialization of a Reaction–Diffusion French Flag Pattern*. In: **Nature Chemistry** 9.10 (Oct. 2017), pp. 990–996. DOI: 10.1038/nchem.2770 (cit. on p. 102).

[192] A. Ziepke, S. Martens, and H. Engel. *Control of Nonlinear Wave Solutions to Neural Field Equations*. In: **SIAM Journal on Applied Dynamical Systems** 18.2 (Jan. 2019), pp. 1015–1036. DOI: 10.1137/18M1197278 (cit. on p. 102).

[193] A. Krekhov. *Formation of Regular Structures in the Process of Phase Separation*. In: **Physical Review E** 79.3 (Mar. 2009), p. 035302. DOI: 10.1103/PhysRevE.79.035302 (cit. on p. 108).

[194] M. Kotzagiannidis et al. *Stable Pattern Selection through Invasion Fronts in Closed Two-species Reaction-diffusion Systems*. In: **RIMS Kôkyuroku Bessatsu** B31 (2012), pp. 79–92 (cit. on p. 108).

[195] Z. Wu et al. *Membrane Shape-Mediated Wave Propagation of Cortical Protein Dynamics*. In: **Nature Communications** 9.1 (2018), p. 136. DOI: 10.1038/s41467-017-02469-1 (cit. on p. 116).

[196] A.P Liu et al. *Membrane-Induced Bundling of Actin Filaments*. en. In: **Nature Physics** 4.10 (Oct. 2008), pp. 789–793. DOI: 10.1038/nphys1071 (cit. on p. 116).

[197] P. Rangamani et al. *Decoding Information in Cell Shape*. en. In: **Cell** 154.6 (Sept. 2013), pp. 1356–1369. DOI: 10.1016/j.cell.2013.08.026 (cit. on p. 116).

[198] M. Théry and M. Bornens. *Cell Shape and Cell Division*. en. In: **Current Opinion in Cell Biology** 18.6 (Dec. 2006), pp. 648–657. DOI: 10.1016/j.ceb.2006.10.001 (cit. on p. 116).

[199] N. Minc, D. Burgess, and F. Chang. *Influence of Cell Geometry on Division-Plane Positioning*. en. In: **Cell** 144.3 (Feb. 2011), pp. 414–426. DOI: 10.1016/j.cell.2011.01.016 (cit. on p. 116).

[200] A.N. Gray et al. *Coordination of Peptidoglycan Synthesis and Outer Membrane Constriction during Escherichia Coli Cell Division*. en. In: **eLife** 4 (May 2015), e07118. DOI: 10.7554/eLife.07118 (cit. on p. 116).

[201] A. Mogilner and K. Keren. *The Shape of Motile Cells*. en. In: **Current Biology** 19.17 (Sept. 2009), R762–R771. DOI: 10.1016/j.cub.2009.06.053 (cit. on p. 116).

[202] W. Razzell, W. Wood, and P. Martin. *Recapitulation of Morphogenetic Cell Shape Changes Enables Wound Re-Epithelialisation*. en. In: **Development** 141.9 (May 2014), pp. 1814–1820. DOI: 10.1242/dev.107045 (cit. on p. 116).

[203] C.-P. Heisenberg and Y. Bellaïche. *Forces in Tissue Morphogenesis and Patterning*. In: **Cell** 153.5 (2013), pp. 948–62. DOI: 10.1016/j.cell.2013.05.008 (cit. on p. 116).

[204] A.C. Martin and B. Goldstein. *Apical Constriction: Themes and Variations on a Cellular Mechanism Driving Morphogenesis*. en. In: **Development** 141.10 (May 2014), pp. 1987–1998. DOI: 10.1242/dev.102228 (cit. on p. 116).

[205] E.N. Harvey and G. Fankhauser. *The Tension at the Surface of the Eggs of the Salamander, Triturus (Diemyctylus) Viridescens*. en. In: **Journal of Cellular and Comparative Physiology** 3.4 (Oct. 1933), pp. 463–475. DOI: 10.1002/jcp.1030030410 (cit. on p. 116).

[206] M. K. Kojima. *EFFECTS OF CHEMICAL REAGENTS ON THE CYCLIC CHANGES OF CORTEX AND CYTOPLASM IN THE ACTIVATED ENUCLEATED EGG-FRAGMENTS OF THE SEA URCHIN**. en. In: **Development, Growth and Differentiation** 22.3 (June 1980), pp. 415–420. DOI: 10.1111/j.1440-169X.1980.00415.x (cit. on p. 116).

[207] K. Hara, P. Tydeman, and M. Kirschner. *A Cytoplasmic Clock with the Same Period as the Division Cycle in Xenopus Eggs*. en. In: **Proceedings of the National Academy of Sciences** 77.1 (Jan. 1980), pp. 462–466. DOI: 10.1073/pnas.77.1.462 (cit. on p. 116).

[208] T. Sawai. *Wavelike Propagation of Stretching and Shrinkage in the Surface of the Newt's Egg before the First Cleavage*. en. In: **Journal of Experimental Zoology** 222.1 (July 1982), pp. 59–68. DOI: 10.1002/jez.1402220108 (cit. on p. 116).

[209] E. Houliston et al. *Axis Establishment and Microtubule-Mediated Waves Prior to First Cleavage in Beroe Ovata*. en. In: (), p. 13 (cit. on p. 116).

[210] J. Quaas and C. Wylie. *Surface Contraction Waves (SCWs) in the Xenopus Egg Are Required for the Localization of the Germ Plasm and Are Dependent upon Maternal Stores of the Kinesin-like Protein Xklp1*. en. In: **Developmental Biology** 243.2 (Mar. 2002), pp. 272–280. DOI: 10.1006/dbio.2001.0564 (cit. on p. 116).

[211] L. Wolpert. *Positional Information and Pattern Formation*. en. In: **Current Topics in Developmental Biology**. Vol. 117. Elsevier, 2016, pp. 597–608. DOI: 10.1016/bs.ctdb.2015.11.008 (cit. on pp. 118, 161).

[212] E. Wagner and M. Glotzer. *Local RhoA Activation Induces Cytokinetic Furrows Independent of Spindle Position and Cell Cycle Stage*. en. In: **Journal of Cell Biology** 213.6 (June 2016), pp. 641–649. DOI: 10.1083/jcb.201603025 (cit. on p. 124).

[213] J. B. A. Green and J. Sharpe. *Positional Information and Reaction-Diffusion: Two Big Ideas in Developmental Biology Combine*. en. In: **Development** 142.7 (Apr. 2015), pp. 1203–1211. DOI: 10.1242/dev.114991 (cit. on p. 126).

[214] T. H. Tan et al. *Topological Turbulence in the Membrane of a Living Cell*. en. In: **Nature Physics** 16.6 (June 2020), pp. 657–662. DOI: 10.1038/s41567-020-0841-9 (cit. on p. 127).

[215] J. Howard, S. W. Grill, and J. S. Bois. *Turing's next Steps: The Mechanochemical Basis of Morphogenesis*. In: **Nature Reviews Molecular Cell Biology** 12.6 (2011), pp. 392–398. DOI: 10.1038/nrm3120 (cit. on p. 127).

[216] P. Gross, K. V. Kumar, and S. W. Grill. *How Active Mechanics and Regulatory Biochemistry Combine to Form Patterns in Development*. In: **Annual review of biophysics** 46.1 (2017), pp. 337–356. DOI: 10.1146/annurev-biophys-070816-033602 (cit. on p. 127).

[217] J.B. Chang and J.E. Ferrell Jr. *Mitotic Trigger Waves and the Spatial Coordination of the Xenopus Cell Cycle*. en. In: **Nature** 500.7464 (Aug. 2013), pp. 603–607. DOI: 10.1038/nature12321 (cit. on p. 127).

[218] V.E. Deneke et al. *Self-Organized Nuclear Positioning Synchronizes the Cell Cycle in Drosophila Embryos*. en. In: **Cell** 177.4 (May 2019), 925–941.e17. DOI: 10.1016/j.cell.2019.03.007 (cit. on pp. 127, 158).

[219] M. Vergassola, V.E. Deneke, and S. Di Talia. *Mitotic Waves in the Early Embryogenesis of* Drosophila *: Bistability Traded for Speed*. en. In: **Proceedings of the National Academy of Sciences** 115.10 (Mar. 2018), E2165–E2174. DOI: 10.1073/pnas.1714873115 (cit. on p. 127).

[220] V.E. Deneke et al. *Waves of Cdk1 Activity in S Phase Synchronize the Cell Cycle in Drosophila Embryos*. en. In: **Developmental Cell** 38.4 (Aug. 2016), pp. 399–412. DOI: 10.1016/j.devcel.2016.07.023 (cit. on p. 127).

[221] H.A. Benink and W.M Bement. *Concentric Zones of Active RhoA and Cdc42 around Single Cell Wounds*. en. In: **Journal of Cell Biology** 168.3 (Jan. 2005), pp. 429–439. DOI: 10.1083/jcb.200411109 (cit. on p. 127).

[222] K.-C. Su et al. *An Astral Simulacrum of the Central Spindle Accounts for Normal, Spindle-Less, and Anucleate Cytokinesis in Echinoderm Embryos*. en. In: **Molecular Biology of the Cell** 25.25 (Dec. 2014). Ed. by T.D. Pollard, pp. 4049–4062. DOI: 10.1091/mbc.e14-04-0859 (cit. on p. 127).

[223] T. Gökirmak et al. *Localization and Substrate Selectivity of Sea Urchin Multidrug (MDR) Efflux Transporters*. en. In: **Journal of Biological Chemistry** 287.52 (Dec. 2012), pp. 43876–43883. DOI: 10.1074/jbc.M112.424879 (cit. on p. 128).

[224] M.C. Wigbers et al. *Pattern Localization to a Domain Edge*. In: **Physical Review E** 101.2 (Feb. 2020), p. 022414. DOI: 10.1103/PhysRevE.101.022414. eprint: 1908.07309 (cit. on p. 139).

[225] O.D. Weiner. *Regulation of Cell Polarity during Eukaryotic Chemotaxis: The Chemotactic Compass*. en. In: **Current Opinion in Cell Biology** 14.2 (Apr. 2002), pp. 196–202. DOI: 10.1016/S0955-0674(02)00310-1 (cit. on p. 140).

[226] D. Keilberg and L. Søgaard-Andersen. *Regulation of Bacterial Cell Polarity by Small GTPases*. en. In: **Biochemistry** 53.12 (Apr. 2014), pp. 1899–1907. DOI: 10.1021/bi500141f (cit. on pp. 140, 154).

[227] E. Bi and H.-O. Park. *Cell Polarization and Cytokinesis in Budding Yeast*. en. In: **Genetics** 191.2 (June 2012), pp. 347–387. DOI: 10.1534/genetics.111.132886 (cit. on p. 140).

[228] R. Diegmiller et al. *Spherical Caps in Cell Polarization*. en. In: **Biophysical Journal** 115.1 (July 2018), pp. 26–30. DOI: 10.1016/j.bpj.2018.05.033 (cit. on pp. 140, 141, 154).

[229] M. Mittasch et al. *Non-Invasive Perturbations of Intracellular Flow Reveal Physical Principles of Cell Organization*. en. In: **Nature Cell Biology** 20.3 (Mar. 2018), pp. 344–351. DOI: 10.1038/s41556-017-0032-9 (cit. on pp. 140, 154).

[230] R. J. Hawkins et al. *Rebuilding Cytoskeleton Roads: Active-Transport-Induced Polarization of Cells*. In: **Physical Review E** 80.4 (Oct. 2009), p. 040903. DOI: 10.1103/PhysRevE.80.040903 (cit. on p. 140).

[231] V. Calvez et al. *Non-Linear Analysis of a Model for Yeast Cell Communication*. en. In: **ESAIM: Mathematical Modelling and Numerical Analysis** 54.2 (Mar. 2020), pp. 619–648. DOI: 10.1051/m2an/2019065 (cit. on p. 140).

[232] A. Yochelis et al. *Self-Organization of Waves and Pulse Trains by Molecular Motors in Cellular Protrusions*. en. In: **Scientific Reports** 5.1 (Oct. 2015), p. 13521. DOI: 10.1038/srep13521 (cit. on p. 140).

[233] V. Ivanov and K. Mizuuchi. *Multiple Modes of Interconverting Dynamic Pattern Formation by Bacterial Cell Division Proteins*. In: **Proceedings of the National Academy of Sciences** 107.18 (2010), pp. 8071–8078. DOI: 10.1073/pnas.0911036107 (cit. on pp. 140, 158).

[234] A. G. Vecchiarelli et al. *Differential Affinities of MinD and MinE to Anionic Phospholipid Influence Min Patterning Dynamics* in Vitro*: Flow and Lipid Composition Effects on Min Patterning*. en. In: **Molecular Microbiology** 93.3 (Aug. 2014), pp. 453–463. DOI: 10.1111/mmi.12669 (cit. on p. 140).

[235] S. W. Grill et al. *Polarity Controls Forces Governing Asymmetric Spindle Positioning in the Caenorhabditis Elegans Embryo*. en. In: **Nature** 409.6820 (Feb. 2001), pp. 630–633. DOI: 10.1038/35054572 (cit. on p. 140).

[236] E. Munro, J. Nance, and J. R. Priess. *Cortical Flows Powered by Asymmetrical Contraction Transport PAR Proteins to Establish and Maintain Anterior-Posterior Polarity in the Early C. Elegans Embryo*. en. In: **Developmental Cell** 7.3 (Sept. 2004), pp. 413–424. DOI: 10.1016/j.devcel.2004.08.001 (cit. on p. 140).

[237] I. Hecht, W.-J. Rappel, and H. Levine. *Determining the Scale of the Bicoid Morphogen Gradient*. en. In: **Proceedings of the National Academy of Sciences** 106.6 (Feb. 2009), pp. 1710–1715. DOI: 10.1073/pnas.0807655106 (cit. on p. 140).

[238] R. E. Goldstein and J.-W. van de Meent. *A Physical Perspective on Cytoplasmic Streaming*. en. In: **Interface Focus** 5.4 (Aug. 2015), p. 20150030. DOI: 10.1098/rsfs.2015.0030 (cit. on p. 140).

[239] A. Mogilner and A. Manhart. *Intracellular Fluid Mechanics: Coupling Cytoplasmic Flow with Active Cytoskeletal Gel*. In: **Annual Review of Fluid Mechanics** 50.1 (2018), pp. 347–370. DOI: 10.1146/annurev-fluid-010816-060238 (cit. on p. 140).

[240] E.F. Koslover, C.K. Chan, and J.A. Theriot. *Cytoplasmic Flow and Mixing Due to Deformation of Motile Cells*. en. In: **Biophysical Journal** 113.9 (Nov. 2017), pp. 2077–2087. DOI: 10.1016/j.bpj.2017.09.009 (cit. on pp. 140, 158).

[241] A. Jilkine and L. Edelstein-Keshet. *A Comparison of Mathematical Models for Polarization of Single Eukaryotic Cells in Response to Guided Cues*. en. In: **PLoS Computational Biology** 7.4 (Apr. 2011). Ed. by J.M Haugh, e1001121. DOI: 10.1371/journal.pcbi.1001121 (cit. on p. 140).

[242] N.S. Allen and R.D. Allen. *Cytoplasmic Streaming in Green Plants*. en. In: **Annual Review of Biophysics and Bioengineering** 7.1 (June 1978), pp. 497–526. DOI: 10.1146/annurev.bb.07.060178.002433 (cit. on p. 141).

[243] E. Siero et al. *Striped Pattern Selection by Advective Reaction-Diffusion Systems: Resilience of Banded Vegetation on Slopes*. In: **Chaos: An Interdisciplinary Journal of Nonlinear Science** 25.3 (2015), p. 036411 (cit. on p. 149).

[244] A.J. Perumpanani, J.A. Sherratt, and P.K. Maini. *Phase Differences in Reaction-Diffusion-Advection Systems and Applications to Morphogenesis*. en. In: **IMA Journal of Applied Mathematics** 55.1 (Jan. 1995), pp. 19–33. DOI: 10.1093/imamat/55.1.19 (cit. on p. 149).

[245] R. Samuelson et al. *Advection and Autocatalysis as Organizing Principles for Banded Vegetation Patterns*. English (US). In: **Journal of Nonlinear Science** 29.1 (Feb. 2019), pp. 255–285. DOI: 10.1007/s00332-018-9486-6 (cit. on p. 149).

[246] *Mathematica*. Wolfram Research, Inc. Champaign, IL, 2019 (cit. on p. 149).

[247] M. Fivaz et al. *Robust Neuronal Symmetry Breaking by Ras-Triggered Local Positive Feedback*. en. In: **Current Biology** 18.1 (Jan. 2008), pp. 44–50. DOI: 10.1016/j.cub.2007.11.051 (cit. on p. 154).

[248] Y. Wang et al. *Identifying Network Motifs That Buffer Front-to-Back Signaling in Polarized Neutrophils*. en. In: **Cell Reports** 3.5 (May 2013), pp. 1607–1616. DOI: 10.1016/j.celrep.2013.04.009 (cit. on p. 154).

[249] S.-C. Wang et al. *Cortical Forces and CDC-42 Control Clustering of PAR Proteins for Caenorhabditis Elegans Embryonic Polarization*. en. In: **Nature Cell Biology** 19.8 (Aug. 2017), pp. 988–995. DOI: 10.1038/ncb3577 (cit. on p. 154).

[250] M. Loose et al. *Spatial Regulators for Bacterial Cell Division Self-Organize into Surface Waves in Vitro*. en. In: **Science** 320.5877 (May 2008), pp. 789–792. DOI: 10.1126/science.1154413 (cit. on p. 158).

[251] P. Glock et al. *Stationary Patterns in a Two-Protein Reaction-Diffusion System*. en. In: **ACS Synthetic Biology** 8.1 (Jan. 2019), pp. 148–157. DOI: 10.1021/acssynbio.8b00415 (cit. on p. 158).

[252] S. Iden and J.G. Collard. *Crosstalk between Small GTPases and Polarity Proteins in Cell Polarization*. en. In: **Nature Reviews Molecular Cell Biology** 9.11 (Nov. 2008), pp. 846–859. DOI: 10.1038/nrm2521 (cit. on p. 158).

[253] J. S. Bois, F. Jülicher, and S. W. Grill. *Pattern Formation in Active Fluids*. In: **Physical Review Letters** 106.2 (Jan. 2011), p. 028103. DOI: 10.1103/PhysRevLett.106.028103 (cit. on p. 158).

[254] M. Radszuweit et al. *Intracellular Mechanochemical Waves in an Active Poroelastic Model*. en. In: **Physical Review Letters** 110.13 (Mar. 2013), p. 138102. DOI: 10.1103/PhysRevLett.110.138102 (cit. on p. 158).

[255] K. V. Kumar et al. *Pulsatory Patterns in Active Fluids*. en. In: **Physical Review Letters** 112.20 (May 2014). DOI: 10.1103/PhysRevLett.112.208101 (cit. on p. 158).

[256] T. Nakagaki, H. Yamada, and M. Ito. *Reaction–Diffusion–Advection Model for Pattern Formation of Rhythmic Contraction in a Giant Amoeboid Cell of thePhysarum-Plasmodium*. en. In: **Journal of Theoretical Biology** 197.4 (Apr. 1999), pp. 497–506. DOI: 10.1006/jtbi.1998.0890 (cit. on p. 158).

[257] E. Frey et al. *Protein Pattern Formation*. In: **arXiv** (2018). eprint: 1801.01365 (cit. on p. 161).

[258] A. Mietke, F. Jülicher, and I. F. Sbalzarini. *Self-Organized Shape Dynamics of Active Surfaces*. In: **Proceedings of the National Academy of Sciences** 116.1 (2018), pp. 29–34. DOI: 10.1073/pnas.1810896115 (cit. on p. 162).

[259] A. Mietke et al. *Minimal Model of Cellular Symmetry Breaking*. en. In: **Physical Review Letters** 123.18 (Oct. 2019), p. 188101. DOI: 10.1103/PhysRevLett.123.188101 (cit. on p. 162).

[260] C. Tozzi, N. Walani, and M. Arroyo. *Out-of-Equilibrium Mechanochemistry and Self-Organization of Fluid Membranes Interacting with Curved Proteins*. In: **New Journal of Physics** 21.9 (2019), p. 093004. DOI: 10.1088/1367-2630/ab3ad6 (cit. on p. 162).

Acknowledgement

"We gotta fight in life for what's right,
and love what's left."
– Awolk

This work has not been possible without the help and support of many people.

Most importantly, I would like to thank my supervisor Erwin Frey, who has been a great support in many ways. Erwin, thank you for creating an amazing environment which stimulates initiative, creativity and personal development. What I value most is the enormous amount of trust you gave me to let me lead our projects. I am very happy that you asked me to join the starfish project. This project turned out to include every aspect that I hoped to find in a PhD project. It was challenging, creative, collaborative and it turned out into an elegant story. I am also thankful for all the opportunities and freedom you gave me to develop myself as a scientist, to visit conferences, and explore options to apply this to the industry of medicine development. All in all, I had a fantastic time in your group. And although it is time to move on, it is hard to leave.

I would also like to thank my colleagues Tom Burkart, Ulrich Gerland, Andriy Goychuk, Jacob Halatek, Tobias Hermann, Ching Yee Leung, Filipe Tostevin and Laeschkir Würthner. It has been lots of fun to discuss science with you and I am proud of the papers we have been writing. And, of course, my collaborators Nikta Fahkri and Tzer Han Tan. It has been amazing collaborating with you from the very start and I am proud of what we achieved.

A special thanks goes out to Fridtjof Brauns. You are an impressive scientist and I learned a lot from you. Not only, how to properly analyze reaction–diffusion systems, but so much more. Thanks for all the scientific discussions we had, and your merciless judgements on my choices on line thicknesses or font sizes in figures. They indeed look more esthetic now. I wish you all the best on your academic journey, and I am looking forward to your future ideas!

Munich also has been a fantastic place to make friends and spend my free time. I would like to thank Manu and Elina, Verena and Andi, Tim and Caro, and Heinrich for many fantastic dinner parties, for the skiing and hiking trips. I am looking forward to many more in Germany or The Netherlands. Our door is always open.

Furthermore, I would like to thank Bernard Mooij, Fred MacKintosh, Piet Mulders and Josh Shaevitz, who have been important mentors for me. Bernard found me in the corridors at my school staring at a set of coupled differential equations, describing the spreading of an infectious disease through a population. I didn't know what a differential equation was, nor how to solve them. Bernard is the type of teacher who enjoyed teaching beyond the curriculum and helped me to find an approximate analytical and numerical solution. Fred, being part of your group has been a fantastic starting point of my academic career. Thanks for giving me the opportunity to spend some time in Princeton. As I am sure you know, it is not really in the Dutch culture to try to become the best at something. Good is good enough. Going to Princeton really opened my eyes to a world of truly dedicated people, who wanted to understand the world. This has been a great inspiration for me and after this first visit to Princeton I knew I wanted to do the same. Piet, thank you for being a teacher with passion for what you teach. You once said to me: 'You always have to do it differently'. Thanks for supporting me doing it 'differently', it has been a great help. Josh, on my first day in your lab you told me your view on theoretical physics and made an interesting analogy, which I will not repeat here. Years later, you told me that you still show my results in your presentations. Have you changed you mind on theoretical physics? Spending a year in your lab was a great inspiration and it made it very clear to me that I wanted to do a PhD. There was still so much to understand and explore. Josh, you have been a great mentor to me who shows that you deeply care about your students becoming successful and happy.

My sister Fleur has always been a great inspiration to me. As a child, we liked to brainstorm whether it is possible to build life from scratch. You thought this would not be possible because it is too complex, and I argued that this should in principle work with the right ingredients. After writing this thesis, I now know that, even if it is possible in principle, it will be pretty hard to achieve. There may be easier ways. Often during my PhD, I thought back to your dedication to learn, your creativity, and your integrity and courage when you argued with your doctors as an equal about your own treatment – everybody can make a difference. I think you would also have enjoyed it a lot to do a PhD in medicine or biomedical sciences, or whatever field of research would have caught your interest. And I would have enjoyed to continue to brainstorm with you about how to build life. Fleurtje, you have been in my thoughts during the whole process of this PhD and I am sure you will join me on my next adventures.

I would also like to thank my mom and dad, Marion and Ino, and my sister Sabine. Mamma, thanks for always being proud of what I am doing and supporting the decisions I make, regardless of what it is. I would also like to thank you for making sure that I am always stocked up on dutch cheese, hagelslag and any other important dutch product that I couldn't get in Munich. Pappa, thank you for teaching me that simplicity has its charm. During my PhD, I often reminded myself about the architectural model of a gym that I wanted to build as a present for my mom. This gym had to be fully equipped with several floors, electricity, and dynamically moving fitness devices. Of course, such a huge project was way too difficult for a 9-year old to achieve. You helped me to change my project into

something that I could finish. This showed me that big ideas are great, but realistic ideas are better – an important lesson for anyone starting a PhD someday. Sabine, thank you for always visiting me wherever I moved, even when your plane did not have enough fuel. It didn't stop you, as also the pandemic didn't stop you to organize a fantastic corona-proof bachelor's party for me.

Also, many thanks to my mother in law, Inez, and the rest of the Broedersz family. Thanks for the warm welcome into the family, and for always showing interest in my research.

Finally, I would like to thank my husband Chase. As you know, the process of completing a PhD thesis can be a bumpy road, or should I say ski-route. Thanks for supporting me during all the bumps, ascends, descends, turns and 'tornanti' on this route. When I was skiing down the slopes into a direction where I thought would be a dead-end, you supported me to take a sharp turn and quit the project. When I was skiing down the "organ grinder", you encouraged me to continue, because you believed I could do it and because there is always fresh power to ski at the end of it. Thank you for insisting to always celebrate every fresh-powder moment. Chase, it is not a coincidence that I compare our time in Munich with a skiing slope, as many important moments happen with mountains in the background, contributing to the esthetic harmony.